QUANTIFYING LIMITS AND LOSSES IN NANOSCALE PHOTOVOLTAICS

Cover image: the front and back cover show a quantitative absorption and current measurement performed simultaneously on a single nanowire solar cell, as shown in Chapter 6. While the nanowire solar cell absorbs everywhere, a current is only generated locally.

Ph.D. Thesis University of Amsterdam, December 2016
Quantifying limits and losses in nanoscale photovoltaics
Sander Adriaan Mann

ISBN: 978-94-92323-10-1

A digital version of this thesis can be downloaded from http://www.amolf.nl.

QUANTIFYING LIMITS AND LOSSES IN NANOSCALE PHOTOVOLTAICS

Het kwantificeren van grenzen en verliezen in zonnecellen op nanoschaal

Academisch Proefschrift

ter verkrijging van de graad van doctor
aan de Universiteit van Amsterdam
op gezag van de Rector Magnificus
prof. dr. ir. K.I.J. Maex
ten overstaan van een door het college voor promoties
ingestelde commissie,
in het openbaar te verdedigen in de Agnietenkapel
op dinsdag 6 december 2016, te 10:00 uur

door

Sander Adriaan Mann

geboren te 's-Gravenzande

Promotiecommissie

Promotor:	prof. dr. A. Polman	Universiteit van Amsterdam
Copromotor:	dr. E.C. Garnett	AMOLF
Overige Leden:	prof. dr. A. F. Koenderink	Universiteit van Amsterdam
	prof. dr. W. C. Sinke	Universiteit van Amsterdam
	prof. dr. T. Gregorkiewicz	Universiteit van Amsterdam
	prof. dr. J. Gómez Rivas	FOM Institute DIFFER
	prof. dr. M.L. Brongersma	Stanford University, CA, USA

Faculteit der Natuurwetenschappen, Wiskunde en Informatica

This work is part of the research program of the 'Stichting voor Fundamenteel Onderzoek der Materie' (FOM), which is financially supported by the 'Nederlandse organisatie voor Wetenschappelijk Onderzoek' (NWO). It is also funded by the European Research Council (ERC).

Contents

1

Introduction

The availability of energy is an important driver for the development, wealth, and well-being of societies. However, due to the associated emission of greenhouse gasses, this driving force is currently under severe pressure. A transition to renewable energy sources is required, and just based on its sheer availability, solar power is the most promising. The total solar power incident on earth is 1.7×10^{17} W, four orders of magnitude more than the global average power consumption of 1.2×10^{13} W. Even the densely populated Netherlands receives more than 340 times its average electricity consumption and over 40 times its primary energy consumption.

For large scale deployment, solar power needs to be able to compete with other energy technologies. The cost of electricity from solar panels has fallen by 80% in the past five years alone, now in certain cases reaching the historical cost target of 0.05$/kWh. At this cost, photovoltaic modules can compete with fossil fuels, enabling more rapid expansion of installed capacity. However, this target may not be ambitious enough: at large market penetration the value of solar power is likely to decrease, as a result of the inherent intermittency of the source [1]. As a result, it is argued that a more stringent cost target of 0.01$/kWh is required, which current technologies may not reach even when extrapolating the learning curve [1].

The largest lever in reducing the cost of solar power is the power conversion efficiency: only about a third of the total installed cost is due to the solar panel itself [2], and the remaining costs scale inversely proportional to the module efficiency. For example, as the efficiency goes up, the required area, racking, and installation costs go down. Hence, to enable truly large scale application of solar panels, high efficiency photovoltaic technologies are required.

This thesis concerns the role that nanotechnology, and nanophotonics in particular, can play in high efficiency photovoltaics. Here we first introduce the limiting efficiency of a single junction solar cell, and several current approaches to

enhance the efficiency beyond this limit. We then briefly discuss nanophotonics and single nanoparticle spectroscopy, a set of important techniques for characterization of nanophotonic structures. We conclude with an outline of this thesis.

1.1 The Shockley-Queisser limit

The efficiency of a solar panel is given by its output power $P(V) = I(V) \times V$, divided by the power in the incident sunlight*. For an ideal solar cell the current-voltage behavior is given by the ideal diode equation [3], modified to take into account a photocurrent:

$$J(V) = J_0\left(\exp\left(\frac{qV}{k_B T}\right) - 1\right) - J_{\text{sc}}. \tag{1.1}$$

Here q is the electron charge, k_B is Boltzmann's constant, T is the temperature, and J_0 is the recombination current density (frequently called the reverse saturation current density). An example of a current-voltage curve for a solar cell is shown in Fig. 1.1a, which at 0 V goes through the short-circuit current density (J_{sc}) and at 0 mA/cm^2 goes through the open-circuit voltage (V_{oc}). At the "maximum power point" this solar cell produces the most power, and the corresponding product $I \times V$ is shown in Fig. 1.1a by the blue square.

Understanding the fundamental limit to the efficiency of a solar cell is important in many ways. It can guide in setting realistic goals, provide tools to direct the efficiency of devices towards that limit, and ultimately perhaps help find ways to exceed such a limit. By glancing at Fig. 1.1a we can see that the efficiency limit of a solar cell is intimately related to the highest J_{sc} and V_{oc} that that solar cell can possibly achieve. The highest J_{sc} is straightforward to find: it is just the total flux of above band gap photons in the solar spectrum,

$$J_{\text{sc}} \approx q \int_{E_g}^{\infty} a(E, \theta = \phi = 0) S(E) dE. \tag{1.2}$$

Here $a(E, \theta, \phi)$ is the absorptance resulting in photogenerated carriers, and we approximated the sun as a point source at normal incidence. The solar spectrum used for standard test conditions, $S(E)$, is shown in Fig. 1.1b [4], together with the corresponding maximum current as a function of semiconductor band gap.

Finding the maximum voltage is more tricky. We can rewrite Eq. 1.1 for the V_{oc} by setting the current to zero:

$$V_{\text{oc}} \approx \frac{k_B T}{q} \log\left(\frac{J_{\text{sc}}}{J_0}\right). \tag{1.3}$$

Finding the maximum V_{oc} thus requires a lower bound on the recombination current J_0. In device physics this current is usually calculated using device parameters

*Under standard test conditions this is taken to be 1000 W/m^2.

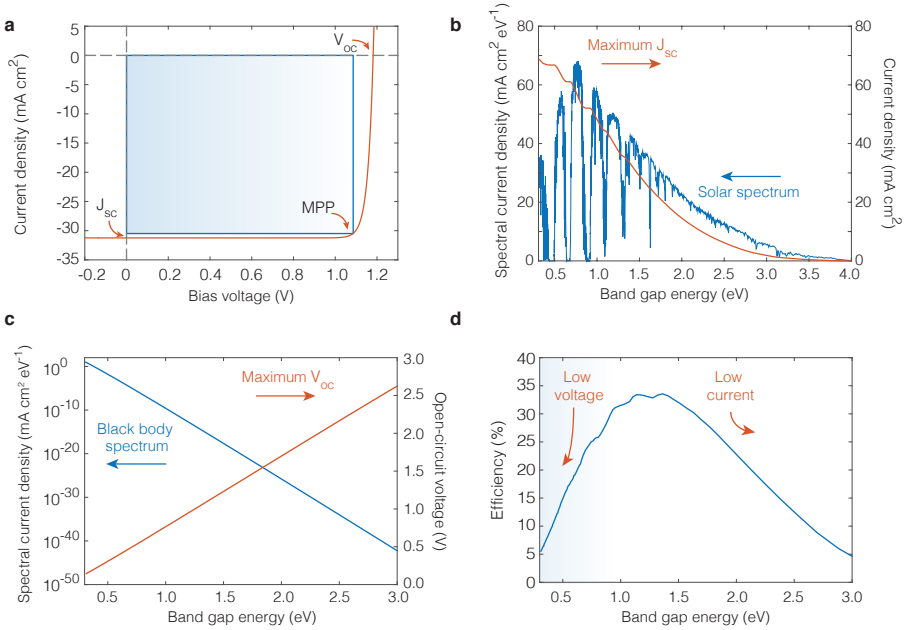

Figure 1.1: The Shockley-Queisser limit. a. A current-voltage curve of an ideal solar cell with a band gap of 1.44 eV (860 nm), corresponding to GaAs. **b.** The AM1.5 solar spectrum [4] shown as a spectral current density with the maximum short-circuit current as a function of the band gap energy. **c.** The spectral current density in the absorbed black body radiation spectrum, shown together with the maximum open-circuit voltage. The recombination current calculated with Eq. 1.4 decreases by 32 orders of magnitude when going from a band gap of 0.5 to 2.5 eV, due to the exponential decrease in the black body spectrum. However, the corresponding increase in the V_{oc} is only 1.86 V, due to the logarithmic dependence of the V_{oc} on J_0. **d.** The Shockley-Queisser limit to the efficiency of a single junction solar cell. It peaks at 33.6% for a band gap at 930 nm, corresponding to InP (1.34 eV) and close to GaAs (1.44 eV, 860 nm). On the large band gap side the J_{sc} is too low, while on the low band gap side the V_{oc} is too low.

such as the diffusion lengths of carriers, and the thickness of the p and n-type layers. The first predictions of a limiting efficiency were therefore heuristic models, based on empirical findings of material constants and estimates on how much they could be improved (see *e.g.* [5, 6]). However, these models were not strict bounds, and usually underestimated the actual limiting efficiency.

In their seminal paper from 1961, Shockley and Queisser resolved this issue by turning to thermodynamics [7]. In particular, they realized that a very small fraction of the ambient black body flux incident on the solar cell lies above the semiconductor band gap. As the solar cell can not distinguish between these photons and those coming from the sun, the incident black body radiation leads to a minute

generation rate of excited carriers. To achieve steady state, that generation rate must be balanced by a recombination rate, which gives the lower bound on the recombination current:

$$J_0^{\text{rad}} = q \int_{E_g}^{\infty} \int_0^{2\pi} \int_0^{\pi/2} a(E,\theta,\phi)\Theta(E)\sin(\theta)\cos(\theta) d\theta d\phi dE \tag{1.4}$$

where the $\cos(\theta)$ term accounts for Lambert's rule, the integral is over the hemisphere of which the solar cell faces the ambient, and $\Theta(E)$ is Planck's law for the black body spectrum, as shown in Fig. 1.1c. The superscript "rad" signifies that the lowest possible J_0 is actually found when radiative recombination is the only loss mechanism.

Equations 1.1,1.2, and 1.4 fully describe the current-voltage behavior of an ideal solar cell. This allowed Shockley and Queisser to derive the efficiency limit as a function of the semiconductor band gap, shown in Fig. 1.1d. It peaks at an efficiency of 33.6% at a band gap 1.34 eV (930 nm), similar to the band gaps of InP and GaAs. This maximum originates from a trade-off in current densities and voltages: for band gaps at higher energies the current is too low (Fig. 1.1b), and at lower band gap energies the voltage is too low (Fig. 1.1c).

1.1.1 Exceeding the Shockley-Queisser limit

There is great interest in exceeding the Shockley-Queisser limit, which indeed can be achieved in a number of ways[†]. For example, a concentrating lens can be used to collect light from a larger area and enhance the incident intensity, increasing the current-density and thus the voltage [8]. Alternatively, multiple semiconductors with different band gaps can be used in conjunction, to reduce thermalization losses. More exotic approaches are to use angle restriction filters to reduce the recombination current [9–12], or multiple exciton generation, where a single photon with sufficient energy excites multiple excitons [13–16]. Concentrator photovoltaics and multi-junction solar cells are commercially available, and efficiencies far exceeding 33.6% have been demonstrated [17]. However, for a single junction material under terrestrial conditions, the Shockley-Queisser limit has actually never been achieved, or even approached. This is due to shortcomings on both the current and voltage side, resulting from insufficient carrier and light management [18]. Nanophotonics can potentially be applied to mitigate both management problems, as we will discuss in the next section.

[†]A note on semantics: we refer to the detailed balance limit under standard test conditions as the "Shockley-Queisser" limit, which can be surpassed. However, the same detailed balance approach can be applied to find a limiting efficiency for concentrator cells, angle restriction photovoltaics, multi-junction solar cells, thermophotovoltaics, and other types of devices as well.

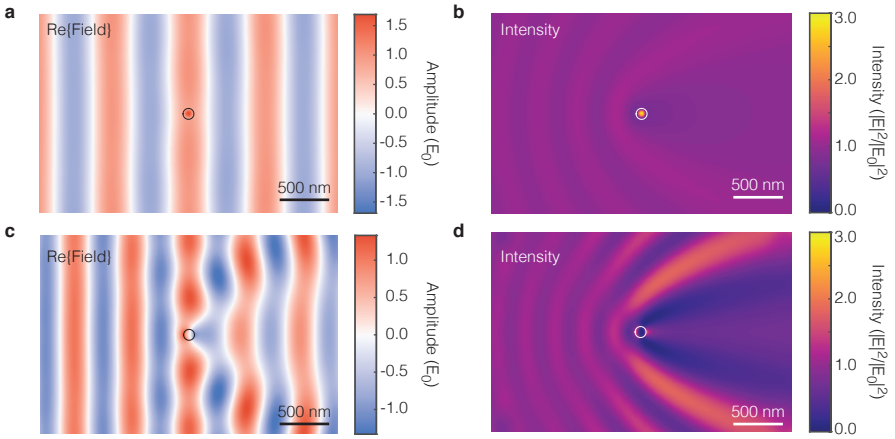

Figure 1.2: Electric field around a core-shell nanowire a,b. The electric field amplitude ($\mathrm{Re}\{E_z\}$, **a**) and intensity ($|E_z|^2$, **b**) near an 80 nm cylinder with $n = 4$ coated with 15 nm of Ag. At this particular wavelength ($\lambda = 780$ nm) the cylinder has a very small extinction cross section ($\sigma_{\mathrm{ext}} \approx dL/2$, where L is the length of the nanowire). **c,d.** The field amplitude (**c**) and intensity (**d**) near an 88 nm Ag core, coated with 18 nm of amorphous silicon at $\lambda = 640$ nm. The nanoparticle now has a extinction cross section 10 times larger, $\sigma_{\mathrm{ext}} \approx 5dL$.

1.2 Nanophotonics for photovoltaics

The field of nanophotonics utilizes the wave nature of light: while it used to be common to speak of "pencils of rays", researchers now more frequently express their wish to "control the flow of light", as if light in fact were a liquid. When materials are structured with length scales similar to the wavelength, it is no longer sufficient to consider only the surface normals, angles of incidence, and refractive indices, as in the ray optics approximation. Instead, the wave equation $(\nabla^2 + k^2)\mathbf{E} = 0$ must be considered, which enables many new phenomena not observed in the ray optics regime [19]. To name a few examples: nanophotonics can be used to manipulate the polarization and direction of beams of light with ultra-thin surfaces of nanoscale resonators [20–22], inhibit or enhance the decay rate of emitters [23–28], strongly enhance non-linear effects [29, 30], create broadband angular selectivity in transmission [31, 32], and much more. However, in light of photovoltaics, the most striking effect may be that objects with sizes comparable to the wavelength may absorb or deflect much more power than you would expect, given their geometrical size [33, 34]. The opposite is also possible: a nanoparticle can be "hidden" by applying a special coating [35–37].

The interaction magnitudes of nanoparticles with light are captured by cross sections [38]. For example, the absorption cross section (an area, m^2) determines how much power (W) a nanoparticle can absorb from an incident plane wave with

a certain intensity I_0 (W/m^2):

$$\sigma_{\text{abs}} = \frac{P_{\text{abs}}}{I_0}. \tag{1.5}$$

Similar expressions exist for the scattering cross section σ_{sca} and the extinction cross section σ_{ext}, which is the total power taken from the incident beam: $\sigma_{\text{ext}} = \sigma_{\text{abs}} + \sigma_{\text{sca}}$.

Fig. 1.2 shows both of these cases for a core-shell nanowire: in Fig. 1.2a we see the field distribution around a core-shell nanowire, where the silver shell effectively hides the high refractive index core (n=4), leading to very small disturbance even in the intensity pattern shown in 1.2b: $\sigma_{ext} \approx dL/2$, where d is the diameter of the nanowire and L is the nanowire length. However, while the nanoparticle barely scatters or absorbs incident radiation, it is clear from the intensity plot that the intensity inside the nanowire is quite high, as the nanowire temporarily stores some of the incident energy. By changing the composition of the particle, this concentration of incident light can be utilized to enhance the absorption significantly, as is shown in Fig. 1.2c and d, where the field and intensity are shown near a core-shell nanowire with a silver core and amorphous silicon shell. In this case, the nanowire absorbs all of the light in an area twice its physical size, $\sigma_{\text{abs}} \approx 2dL$ and the total extinction is $\sigma_{\text{ext}} \approx 5dL$, 10 times larger than for the "cloaked" particle. We will study these core-shell nanoparticles and their interesting ability to strongly absorb light in more detail in Chapters 7 and 8.

These examples demonstrate the large degree of manipulation of light that can be achieved with nanophotonics. Nanophotonics has therefore already been applied extensively to enhance photovoltaic devices, in particular to increase the photocurrent [34, 39–51]. For example, the property of nanoparticles to temporarily collect and store energy can be used to direct light into a photovoltaic device very efficiently, making a more effective anti-reflection coating (see Fig. 1.3a and [48, 52]). Alternatively, these large cross sections can be used to directly absorb the incident power, so that significant reductions in the material consumption can be achieved (see Fig. 1.3b and [49, 51, 53–56]). Complex photonic structures can lead to extremely high field intensities in very thin layers of material, such as in the slot waveguide shown in Fig. 1.3c [45, 57]. This geometry enables J_{sc} from an ultra thin layer of material far above what would be possible in the ray optics regime [45, 46, 58, 59]. More exotic approaches exist as well, for instance in the form of thermophotovoltaics, where nanophotonics is applied to efficiently down-convert the solar spectrum through a selective thermal emitter [60, 61].

It is clear that a lot of work has been done focused on using nanophotonics to increase short-circuit currents. More recently, researchers started to apply nanophotonics to enhance the open-circuit voltage as well. A number of chapters in this thesis build on this idea, and we will therefore also briefly elaborate on this younger field.

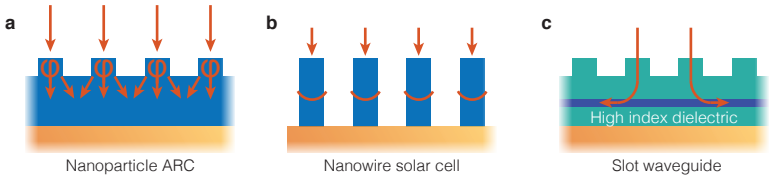

Figure 1.3: Light trapping with nanophotonics. a. An anti-reflection coating based on nanoparticles. **b.** A schematic depiction of a nanowire solar cell with excited guided modes in the nanowires. **c.** A schematic drawing of a slot waveguide solar cell, which can enable absorption significantly above the ergodic limit.

1.2.1 Enhancing voltages with nanophotonics

Because an ideal solar cell is entirely governed by the processes of absorption and emission, not only the current but also the voltage can be enhanced with nanophotonics. An easy way to visualize this is by realizing that the voltage in a solar cell is exponentially proportional to the charge carrier density:

$$\frac{np}{n_0^2} = \exp\left(\frac{qV}{k_B T}\right), \tag{1.6}$$

where n and p are electron and hole densities and n_0 is the intrinsic carrier density. Expressing the diode equation Eq. 1.1 at open-circuit directly in terms of rates and carrier densities, we find:

$$G - R_0 \frac{np}{n_0^2} = 0. \tag{1.7}$$

Enhancing the fraction G/R_0 therefore leads to larger charge carrier densities, and thus to larger voltages. A simple way to think about this is by envisioning a bucket being filled with water at a rate G, while at the same time there is a hole in the bottom with size R_0. In steady state the water level in the bucket is determined by the rate G with respect to the size of the hole R_0. In an ideal solar cell, R_0 is given by how many photons it exchanges per second with its environment in thermal equilibrium (when there is no sunlight). This rate can be calculated using Eq. 1.4, and as we see it depends strongly on the absorptance $a(E,\theta,\phi)$ of the solar cell. The absorptance can be manipulated using nanophotonics, thereby enabling enhancement of the voltage of a solar cell through optical design: making the size of the hole R_0 smaller results in a higher water level. Similarly, reducing the rate at which a solar cell exchanges photons with the ambient surroundings increases the maximum V_{oc}.

One of the first methods known to enhance the voltage of a solar cell is photon recycling (see Fig. 1.4b) [62–65]. If a material has a high radiative efficiency (much more radiative than non-radiative recombination), the photons that follow

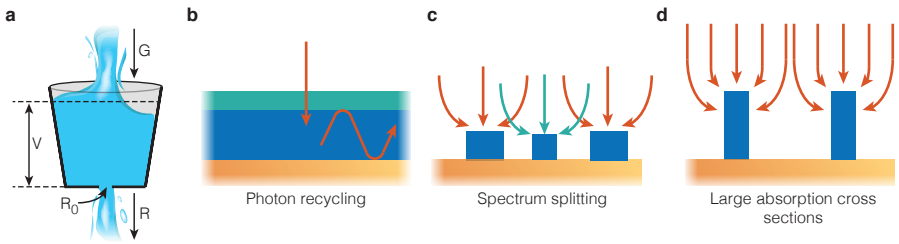

Figure 1.4: Voltage enhancements with nanophotonics. a. The V_{oc} in a solar cell can conceptually be understood from a simple bucket being filled by a steady stream of water. The water escapes again through a small hole in the bottom, and in steady state the water level reaches a height determined by the size of the hole with respect to the rate at which water flows into the bucket. This is similar to photovoltaics, where the water level is corresponds to the potential (charge carrier density), G corresponds to the incident solar flux, and R_0 to the equilibrium recombination rate. **b.** A schematic drawing of a solar cell that uses photon recycling to enhance the V_{oc}. **c.** Spectrum splitting through structures with large optical cross sections at different wavelengths. **d.** A solar cell comprising only nanophotonic structures that have absorption cross sections significantly exceeding their own size, thereby leading to drastic material consumption reductions.

an emission event can be reabsorbed in the active layer, thereby effectively reducing the net recombination rate. The photon recycling rate can be enhanced by applying an angle restriction filter to the front of the solar cell [9, 10], which reduces the critical angle inside the material. As a result, the probability that a photon emitted into a random direction escapes also becomes smaller. In fact, by applying a filter that blocks all emission in a narrow window above the material band gap, the solar cell effectively attains a new band gap - that of the filter (or photonic crystal) [66]. However, the latter approach decreases the J_{sc} simultaneously, and the overall efficiency therefore does not increase above the Shockley-Queisser limit. Finally, by enhancing the absorption near the band gap only, the opposite is achieved: J_0 becomes larger with respect to J_{sc}, leading to a decrease in the open-circuit voltage [67, 68].

To increase efficiencies beyond the Shockley-Queisser limit, nanophotonic approaches to existing concepts can be sought. For example, the multijunction solar cell reduces thermalization losses by splitting the incident spectrum over solar cells that are more appropriate for these separate spectral ranges. While in regular multijunction solar cells this is done by placing these solar cells on top of each other, the large absorption cross sections found in nanostructures can also be used to split the spectrum and absorb different colors in different positions (see Fig. 1.4c) [69–71].

It has also been proposed that these large absorption cross sections can by themselves lead to efficiencies above the Shockley-Queisser limit. The proposed

mechanism is that the large absorption cross section enhances the generation rates (G), similar to concentrator photovoltaics (see Fig. 1.4d) [53, 72]. However, due to the disparities between wave and ray optics, the actual similarities between both situations are still subject to debate. Does the concentration of light using the intrinsic optical properties of a nanostructure really lead to voltage enhancements? What does it take to achieve efficiencies above the Shockley-Queisser limit? And to what degree can efficiencies be enhanced for practical systems that also have non-radiative recombination? This thesis approaches these questions by studying the photovoltaic response of single nanoparticles, both theoretically and experimentally. To do so experimentally requires single nanoparticle spectroscopy, a set of techniques to determine the optical properties of individual nanostructures, which we introduce in the next section.

1.3 Single nanoparticle spectroscopy

The interaction cross sections of nanoparticles strongly depend on their composition, size, shape, and environment, but above all — they are *small*. A single gold particle with a 50 nm diameter has a maximum absorption cross section of $\sigma_{\text{abs}} = 2.5 \times 10^{-15}$ m^2, and as a result it would only absorb roughly one billionth (10^{-9}) of the power in the beam of a simple laser pointer.

As a result of the extremely small cross sections, nanoparticle spectroscopy is usually performed on large ensembles of nanoparticles. Already in 1857 Faraday reported a large variety of optical investigations of colloidal gold particles, like the depence of the color of scattered and transmitted light, and even the ability of these particles to permeate tissue [73]. However, ensemble spectroscopy always yields broadened spectral characteristics, due to inhomogeneities between different particles. Furthermore, in certain cases properties may be of interest that only arise in one out of many particles, such as dimerization or other specific geometrical features. In many cases it is thus desirable to characterize the nanoparticles individually, which is done with so called single nanoparticle spectroscopy techniques. In those techniques the probing light beam is typically focused down to sizes at most a few orders of magnitude larger than the optical cross section of interest. As a result, with common detection techniques the signal contrast is then sufficient to be detected, even on single nanoparticles. This is shown schematically in Fig. 1.5, where the beam waist w_0 is comparable to the size of the nanoparticle. If the nanoparticle lies in the focus, it scatters light and possibly absorbs some of the incident power. This affects the transmitted and reflected beams, which can then be used to characterize the nanoparticle. Alternatively, only the scattered light can be collected, as in dark field microscopy [74–83].

The first spectroscopic studies of single (sub)nanoscale objects were done on single atoms in ion traps [84] and cells and viruses in optical traps in solution [85]. The first absorption spectroscopy study of a single nanoscale object in a solid environment was in fact on a single molecule in an organic host, cooled to 1.6 K and

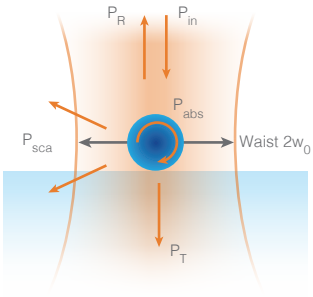

Figure 1.5: Focused beams for single nanoparticle spectroscopy. To detect single nanoparticles it is important to focus down the beam waist to a size comparable to the cross section of interest. The largest part of the beam will then still either be transmitted (P_T) or reflected (P_R), and a small part will be scattered (P_{sca}) or absorbed (P_{abs}). Single nanoparticles can be characterized by detecting either P_{sca}, P_R, or P_T, or a combination of these.

with a double modulation technique to enhance sensitivity [86]. Many experimental improvements have been made since, and single nanoparticle spectroscopy is now an established technique to investigate fluorescence, scattering, absorption, second harmonic generation, and more. For single nanoparticle photovoltaics we are particularly interested in determining the quantitative absorption cross section of a nanostructure, and we will therefore limit our discussion to the techniques enabling such measurements: extinction spectroscopy [87], photothermal spectroscopy [88], and common path interferometry [89]. For more extensive discussions of the field of single nanoparticle spectroscopy, we refer the reader to references [90–92].

1.3.1 Single nanoparticle absorption spectroscopy

If a nanoparticle is very small, its optical response will be dominated by absorption [38]. In this regime quantitative information can thus be obtained about the absorption cross section by characterizing the total extinction, as is done in extinction spectroscopy [93–101]. In fact, the first direct and quantitative measurement of absorption in a nanoscale system was performed in 2004 [102], where the absorption cross section of gold nanoparticles with diameters down to 5 nm was measured. In these types of experiments the nanoparticles are illuminated with a focused beam, and the transmitted light is then recorded (see 1.6b). From the reduction in transmitted light by the presence of the nanoparticle, the quantitative extinction cross section can be deduced if the beam waist is known.

If the nanoparticle is larger and also scatters, the extinction cross section is no longer equal to the absorption cross section. In that case a different technique

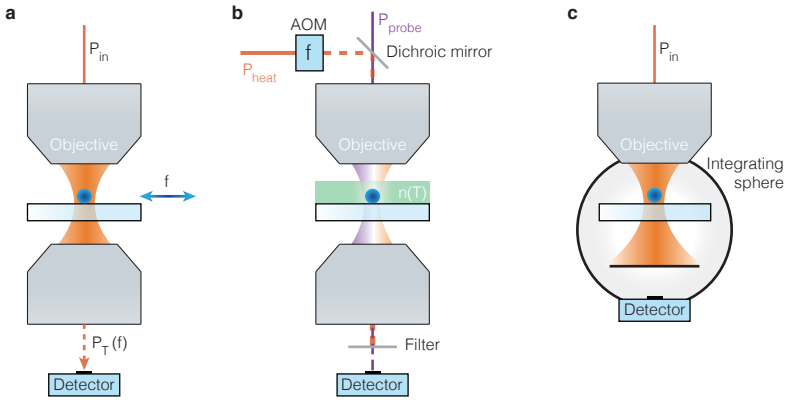

Figure 1.6: Single nanoparticle absorption spectroscopies. a. In extinction spectroscopy the transmitted beam is collected, which is reduced by the extinction of the single nanoparticle.The substrate position is frequently modulated to enhance the detection sensitivity *via* lock-in detection schemes. **b.** In photothermal spectroscopy a nanoparticle and its surroundings are periodically heated through absorption of light from a laser temporally modulated by an acousto-optical modulater (AOM). This heating leads to temporal variation in the refractive index, detected *via* the transmitted power of a detuned probe beam with a lock-in amplifier. **c.** In Chapter 5 we introduce a technique based on an integrating sphere, were we directly and quantitatively measure P_{sca}, P_{T}, and P_{R} in Fig. 1.5, so that P_{abs} remains.

is required, such as photothermal spectroscopy. This is a non-linear technique that relies on heating of the particle and its environment as a consequence of the nanoparticle absorbing light [88, 103–105]. The heating of the environment affects the transmission of a second beam, which probes the same position but is detuned so that it doesn't directly interact with the nanoparticle (see Fig. 1.6c). Determining a quantitative absorption cross section directly from the detected signal is difficult [106], and the measurements are therefore frequently shown in arbitrary units [107] or compared to a particle with a known absorption cross section [88, 108].

The last available technique relies on common path interferometry to obtain phase information of the scattered field. From this phase information the absorption and scattering cross sections can be calculated [89]. A drawback is that it requires a model to connect the cross sections to the phase and amplitude of the forward scattered field, and it only works if the response is completely dominated by a single resonance.

For nanoscale photovoltaics we are interested in the conversion efficiency of light absorbed by a structure into photocurrent or photoluminescence. With current experimental techniques these processes can not be quantified, since measuring the absorption cross section also requires assuming that the nanoparticle either does not scatter, turns all absorption into heat, or interacts with light like

a dipole. In Chapter 5 we therefore introduce integrating sphere microscopy, a new technique that allows us to determine the absorption cross section of a single nanoparticle directly, so that we can characterize its photovoltaic performance quantitatively. The technique relies on combining an integrating sphere with a long working distance microscope objective (see Fig. 1.6c), which enables us to detect the light not absorbed by the nanostructure and infer what was absorbed.

1.4 Motivation and outline

Nanophotonics offers a wide range of tools that may be utilized to enhance the efficiency of photovoltaic devices. In this thesis we aim to investigate how, and to what degree, efficiency enhancements can be achieved. This can be divided into three main questions: (1) For a given nanoscale device, what is the fundamental limiting conversion efficiency? (2) How do realistic material parameters affect the conversion efficiency? (3) How can the device performance be improved in that case? This thesis targets these questions both theoretically and experimentally.

In **Chapter 2** we extend the detailed balance framework pioneered by Shockley and Queisser to the single nanoparticle regime, to investigate how a single nanostructure may enable efficiencies above the Shockley-Queisser limit. We show that, contrary to expectations, a large absorption cross section is not equivalent to macroscopic concentration but that directivity in the absorption pattern is required. We discuss how this may affect practical device design, in particular in the presence of non-radiative recombination.

In **Chapter 3** we extend the theoretical investigation of photovoltaic devices comprising nanoscale building blocks to combinations of different materials. We investigate a new multi-junction solar cell architecture based on interlacing resonators resonant at different frequencies to achieve spatial separation of light, which can help circumvent the current and lattice matching requirements found in conventional multi-junction solar cells.

In **Chapter 4** we delve into the "photon escape probability", the probability that photons originating from radiative recombination in a semiconductor eventually escape the semiconductor. This property is of crucial importance to the efficiency of solar cells and light-emitting diodes, but it has never been rigorously calculated before. We present a rigorous method to calculate the escape probability, and discuss how nanophotonic objects and their associated resonances affect the internal and external radiative efficiencies of a semiconductor material.

In **Chapter 5** we present a new single nanoparticle spectroscopy technique, which allows direct and quantitative determination of the absorption cross section of scattering nanoparticles. The technique, integrating sphere microscopy, is based on the combination of an integrating sphere with a microscopy objective, resulting in the direct determination of absorption with high spatial resolution. We use this technique in **Chapter 6** to determine for the first time the internal quantum efficiency and photoluminescence quantum yield of a single nanowire

solar cell. These metrics are crucial to understand the performance a photovoltaic device. We also introduce a new quantity that is the nanophotonic equivalent to the external quantum efficiency, which allows us to place a thermodynamic limit on the performance of the nanowire solar cell. This quantity is a cross section, just like the cross sections discussed earlier in this chapter, to account for the strong wavelength dependence of the effective optical area of nanostructures.

In **Chapter 7** we discuss the optical properties of metal-semiconductor core-shell nanowires, which can absorb very strongly in only very thin layers of semiconductors. This makes them interesting candidates for photovoltaic applications, especially considering the presence of a local metal contact, facilitating charge extraction. Using solution chemistry we also synthesized such core-shell nanowires, which we investigate experimentally in **Chapter 8**. We measure the absorptance of a single core-shell nanowire with the technique introduced in Chapter 5 and compare the results to theoretical predictions. We also fabricate photovoltaic devices based on these nanowires, which we investigate using laser-induced current maps.

In **Chapter 9** we investigate transmission into bulk metamaterials. These metamaterials can have properties that are very interesting for optical applications, such as flat lensing, but may also have very low or even zero transmission into the material from free space. We demonstrate how to design an anti-reflection coating for such a metamaterial, which contrary to regular anti-reflection coatings, must be nanostructured to be effective.

Finally, **Chapter 10** describes two applications that are based on central concepts in this thesis. First, we propose two ways to incorporate integrating sphere microscopy into commercially available optical systems. Secondly, we demonstrate how to achieve large photon escape probabilities in structures that at the same time have very high absorption, which is crucial for any photovoltaic application.

Overall, this thesis provides new fundamental insights into nanoscale photovoltaics, their limiting efficiencies, and how to achieve those efficiencies. Many of the findings and techniques are directly applicable to other optoelectronic devices as well, in particular to light emitting diodes.

2

Opportunities and limitations for nanophotonic structures to exceed the Shockley-Queisser limit

Nanophotonic engineering holds great promise for photovoltaics, with several recently proposed approaches that have enabled efficiencies close to the Shockley-Queisser limit. Here we theoretically demonstrate that suitably designed nanophotonic structures may be able to surpass the 1 sun Shockley-Queisser limit by utilizing tailored directivity of the absorption of nanoparticles. We show that large absorption cross sections do not play a role in the efficiency enhancement, and on the contrary, directivity enhancement constitutes the nanoscale equivalent to concentration in macroscopic photovoltaic systems. Based on this principle, we discuss fundamental limits to the efficiency based on directivity bounds, and a number of approaches to get close to these limits. We also highlight that, in practice, achieving efficiencies above the Shockley-Queisser limit strongly depends on whether high short-circuit currents can be maintained. Finally, we discuss how our results are affected by the presence of non-radiative recombination, in which case both directivity and photon escape probability should be increased to achieve voltage enhancement.

2.1 Introduction

Shockley and Queisser showed that the limiting power conversion efficiency of a solar cell can be calculated using the principle of detailed balance [7]. For a single junction solar cell, this limit strongly depends on the semiconductor band gap and, under terrestrial conditions, it peaks at 33.6%. The detailed balance limit is entirely concerned with absorption and emission of photons, both of which can be controlled through nanophotonic engineering. As a result, there has been significant interest in applying nanophotonic concepts to approach or even exceed the Shockley-Queisser limit. Nanophotonics approaches have been studied to enhance the absorption in thin semiconductor layers based on light trapping [34, 39, 41–43, 45–47, 49–51, 109–111], but more recently interest has surged in applying nanophotonics to enhance the induced open-circuit voltage in a photovoltaic cell [44, 53, 66–71, 112–114]. For instance, it is possible to use nanostructures to artificially shift the semiconductor bandgap to higher photon energies [66, 67, 69, 113], or to split the solar spectrum in multijunction solar cells by interlacing detuned nanostructures with large absorption cross sections [70, 71]. However, the most promising route to high voltages and efficiencies in single junction solar cells is through concentration (enhancing the short-circuit current relative to the dark current), which increases the maximum efficiency from 33.6% to 45.1%. In macroscopic solar cells this is typically achieved with a concentrating lens (Fig. 2.1a), which focuses the incident sunlight into a much smaller active device area, or by using angle restrictive filters [9–12, 109], which enhance photon recycling (Fig. 2.1b).

In this chapter we discuss whether and how nanostructures can enable efficiencies exceeding the 1 sun Shockley-Queisser limit by enhancing the open-circuit voltage (hereafter simply referred to as the SQ limit). For both macroscopic concentration and angle restriction approaches nanophotonic analogues have been proposed: nanostructures can absorb light from an area much larger than their own size (Fig. 2.1c) and they can provide asymmetric absorption and emission patterns (Fig. 2.1d). Here, we emphasize that only anisotropy in the absorption pattern can lead to efficiencies exceeding the SQ limit, after taking into consideration the difference between geometric and wave optics. We demonstrate this by analyzing the simple case of a GaAs sphere, which has no directivity in absorption, and a single GaAs nanowire, which has weak directivity in absorption. After proving that much larger absorption directivity is required to provide voltage enhancements and larger overall efficiencies, we then discuss the fundamental limitations to directivity using nanostructures, and propose two relevant approaches for high directivity. While the role of directivity has been mentioned before [112], the implications, difficulties, and fundamental limitations of directivity for nanostructured photovoltaics have not been discussed. Finally, we discuss practical implications of how nonradiative recombination in nanoscale systems affects the possibility of enhancing the overall cell efficiency beyond the SQ limit.

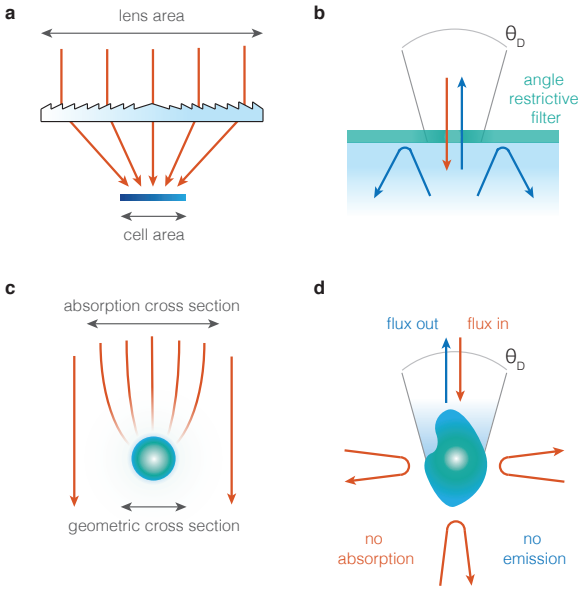

Figure 2.1: Concentration and large absorption cross sections. a. Concentrator photovoltaics use a lens to focus light on a small solar cell, thereby enhancing the generation rate of free carriers. **b.** In angle restricted photovoltaics a filter is used to enhance photon recycling and reduce the net recombination rate. **c.** Nanostructures can absorb light from an area that is much larger than their own size. **d.** Nanostructures can also have anisotropic angular absorption and emission patterns if the structure itself is geometrically asymmetric.

2.2 Open-circuit voltage in ideal nanophotonic systems

We begin our discussion on ways to achieve voltage enhancement by considering ideal photovoltaic systems, in which the only recombination mechanism is radiative. The open-circuit voltage in a solar cell is proportional to the excess carrier density in the active region of the solar cell when no carriers are extracted [7, 67], which is governed by the simple rate equation

$$G - R_0 \frac{n^2}{n_0^2} = G - R_0 \exp\left(\frac{qV}{k_B T}\right) = 0, \tag{2.1}$$

where G is the generation rate of carriers, n and n_0 are the equilibrium and excess carrier densities, k_B is Boltzman's constant, T is the temperature of the solar cell and ambient (300 K), and q is the electron charge. R_0 is the rate at which the solar cell emits photons when it is in equilibrium with its ambient surroundings (there is

no incident sunlight, only black-body radiation). Eq. 2.1 is easily solved for the V_{oc}, which leads to the familiar expression

$$V_{oc} = \frac{k_B T}{q} \ln\left(\frac{G}{R_0}\right) = \frac{k_B T}{q} \ln\left(\frac{I_{sc}}{I_0}\right), \tag{2.2}$$

where I_{sc} and I_0 are the short-circuit current and the equilibrium recombination current, respectively. From Eqs. 2.1 and 2.2 it is clear that the V_{oc} increases if G increases with respect to R_0. This is the mechanism behind the efficiency enhancement in concentrator photovoltaic systems, where the term "concentration" refers to the intensity of incident sunlight. In these systems a focusing lens enhances the intensity of incident sunlight, which increases the generation rate of carriers (G) but leaves the equilibrium recombination rate (R_0) unchanged. As a result, concentration of incident light directly leads to a larger excess carrier density in the semiconductor, and a higher V_{oc}. Semiconductor nanostructures can also concentrate light, based on their nanoantenna functionality of collecting light from a large area and temporarily storing it inside and around the nanostructure (Fig. 2.1c). As a result, the electric field intensity in the absorbing nanostructure can be orders of magnitude higher than the incident intensity. This similarity has been invoked to suggest that this effect fulfills the same role as macroscopic concentration, and that nanophotonic solar cells may therefore be intrinsic concentrator solar cells achieving efficiencies above the SQ limit. However, we point out that there is a crucial difference between the two cases: in nanostructures the enhanced intensity does not lead to a higher carrier density, because the nanoantenna functionality also increases the recombination rate R_0. To understand this we turn to the expression for R_0 in nanostructured systems in which there is only radiative recombination:

$$R_0 = \int_{E_g/\hbar}^{\infty} \int_0^{2\pi} \int_0^{\pi} \sigma_{abs}(\omega,\theta,\phi)\Theta(\omega)\sin(\theta)\, d\theta\, d\phi\, d\omega. \tag{2.3}$$

Here E_g is the band gap energy of the semiconductor, $\hbar$ is the reduced Planck's constant, ω is the optical frequency, Θ is the incident black body photon flux at 300 K and σ_{abs} is the absorption cross section as a function of incident angle and frequency. This expression can be found through Kirchhoff's law [115], which states that an object in thermal equilibrium must emit as many photons as it absorbs. Interaction with the ambient surrounding has no preferred direction, and as a result Eq. 2.3 has to be evaluated over all angles. On the other hand, the generation rate due to the sun only concerns the sun's solid angle (in the absence of diffuse light):

$$G = \int_{E_g/\hbar}^{\infty} \int_0^{2\pi} \int_0^{\theta_s} \sigma_{abs}(\omega,\theta,\phi) S(\omega)\sin(\theta)\, d\theta\, d\phi\, d\omega, \tag{2.4}$$

where $S(\omega)$ is the AM1.5 solar spectrum [4] and θ_s is the half-angle subtended by the sun. From these equations it becomes clear that if we increase σ_{abs} over all frequencies and isotropically for all angles of incidence, both G and R_0 will increase by the same amount, implying that the magnitude of σ_{abs} does not play a role.

The crucial difference between macroscopic and nanophotonic systems, leading to the disparity between concentration and large absorption cross sections, is that lenses necessarily affect the angular response of a solar cell due to conservation of étendue [8]. In fact, we show in the supplementary information to this chapter that a concentrating photovoltaic system can be described entirely from the perspective of angle restriction, where the lens is considered an integral part of the photovoltaic system and reduces the equilibrium recombination rate instead of increasing the generation rate. This is very different from nanophotonic systems, which may have large absorption cross sections from all directions.

It turns out that the only way to enable efficiencies above the SQ limit in nanophotonic systems is by reducing the absorption at oblique angles (as shown in Fig. 2.1d), which reduces R_0 but leaves G unchanged. This directivity in absorption is thus similar to angle restriction in macroscopic solar cells [9, 12, 116] (Fig. 2.1b). It is important to note that, while suppressing σ_{abs} near the band gap can also increase the V_{oc}, this simultaneously comes at a penalty in the short-circuit current. As a result, suppression of absorption cannot be used in a macroscopic device to surpass the Shockley-Queisser efficiency limit [66], unless when utilizing this effect to construct a multijunction solar cell [69].

2.2.1 Maximum voltage in a single sphere

In order to further elucidate the difference between macroscopic and nanophotonic systems, we consider as a basic example a resonant nanosphere that can have large but isotropic absorption cross sections. More specifically, we use Eqs. 2.3 and 2.4 to calculate the generation and recombination rates in a GaAs sphere under solar illumination as a function of sphere diameter. The cross section σ_{abs}, shown in Fig. 2.2a, is determined using Mie theory [38]. Resonances clearly redshift with increasing radius, eventually passing the band gap of GaAs at 860 nm (top of Fig. 2.2a). Fig. 2.2b shows the corresponding maximum V_{oc} that a spherical GaAs solar cell could achieve. It is strongly modulated by diameter variations, significantly exceeding the V_{oc} in a similar Shockley-Queisser type solar cell (defined by a sharp onset of an isotropic and constant absorption cross section above the band gap). Interestingly, by comparing the two panels, it is easy to verify that these enhancements indeed do not correspond to large absorption cross sections, but actually to the opposite: suppression of absorption near the band gap [67, 69, 70, 113]. This is seen noticing the anticorrelation of the voltage peaks and the absorption resonances moving through the band gap, which has also been observed theoretically for a single nanowire [68]. As we noted before, suppression of absorption near the band gap decreases the equilibrium recombination rate, but cannot lead to efficiencies above the SQ limit in a macroscopic device.

Microscopically, the changes in R_0 are largely due to changes in the local density of optical states (LDOS), which affect the radiative transition rate [117, 118]. Fig. 2.2c shows the volume averaged LDOS $\langle\rho\rangle$ in the sphere relative to the LDOS in a homogeneous medium with the same refractive index, n=3.64 (representative of

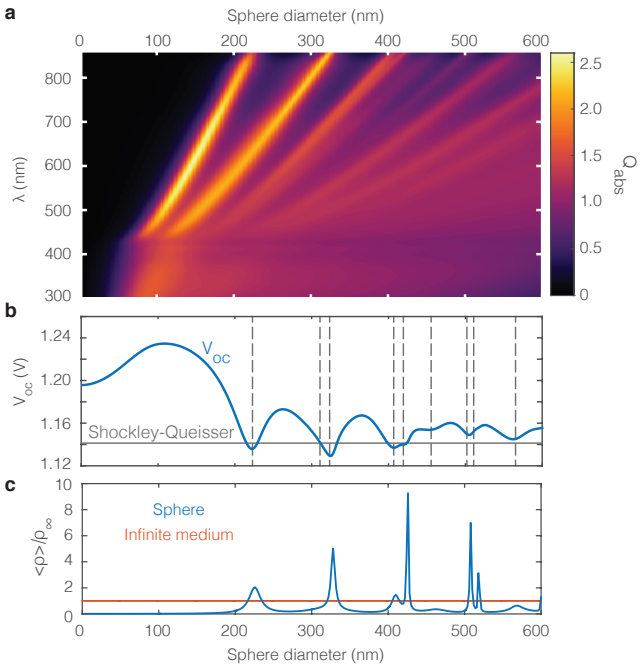

Figure 2.2: The open-circuit voltage in a single GaAs sphere. **a.** Absorption efficiency of a GaAs sphere as a function of photon energy and sphere diameter. **b.** Open circuit voltage in the sphere as a function of diameter, which shows clear dips whenever a resonance passes the band gap. Resonant sphere sizes are shown by the vertical dashed lines, in good agreement with dips in the voltage. **c.** The local density of states in a sphere with n=3.64 (representative of GaAs at the band gap, but lossless) relative to the LDOS in a homogeneous medium with the same refractive index. Whenever a resonance crosses the band gap, there is a significant increase in the LDOS, corresponding to an increase in recombination rates and a decrease in the V_{oc}. The sharp features are not visible in **c** due to averaging over the bandwidth of thermal emission and the presence of losses.

GaAs at the band gap, see Section 2.8.1 for calculation details). When a resonance crosses the band gap the LDOS at frequencies near the band gap is significantly enhanced, which corresponds to increases in the radiative recombination rate and decreases in the V_{oc} (as shown in Fig. 2.2b). Large absorption cross sections are related to LDOS enhancements, and hence by themselves they do not lead to enhanced voltages: the generation and recombination rate are both enhanced, such that the overall effect cancels out. If the LDOS is enhanced *only* in the region near the band gap, the V_{oc} actually decreases, as we saw previously.

2.3 Directivity in nanophotonic structures

The discussion in the previous section has shown that efficiencies above the SQ limit using nanostructures without external concentrating optics can only be achieved by modifying the angular dependence of the absorption pattern: reducing R_0 while maintaining G. This angular anisotropy is captured in the directivity D of the nanostructures, which in antenna theory is commonly used to describe how much power an antenna receives from or transmits into a given solid angle P_Ω, relative to the average power received or transmitted by the antenna in all directions [119]:

$$D = 4\pi P_\Omega / P_{\text{total}}. \tag{2.5}$$

It is important to distinguish between directivity in radiation or scattering and directivity in absorption. A simple homogeneous sphere may be moderately directive when it scatters a plane wave or redirects emission from a dipole inside the sphere, sending more light in a certain direction than in others, but it can never be directive in absorption since it looks identical for all directions of incidence. We will elaborate on this distinction later in this chapter, but for now it is important to keep in mind that the goal is to achieve directivity in absorption.

When the solid angle of maximum absorption directivity is pointed towards the sun, we can use the directivity to derive an expression for the open circuit voltage:

$$V_{\text{oc}}(\overline{D}) = V_{\text{oc}}^{\text{iso}} + \frac{k_B T}{q} \ln(\overline{D}), \tag{2.6}$$

where

$$\overline{D} = \frac{4\pi \int \Theta(\omega)\sigma_{\text{abs}}(\omega, \theta = \phi = 0) d\omega}{\iint \Theta(\omega)\sigma(\omega, \Omega) d\Omega d\omega}. \tag{2.7}$$

Here $V_{\text{oc}}^{\text{iso}}$ is the open circuit voltage of a nanostructure with isotropic absorption cross section equal to σ_{abs} in the solid angle facing the sun, such as for the sphere in Fig. 2.2b. Note that $\overline{D}$ is the directivity weighted to the emission spectrum, while D is the directivity at a given frequency, according to Eq. 2.5. The weighted directivity $\overline{D}$ reduces R_0 with respect to the isotropic absorber, $R_0 = R_0^{\text{iso}}/\overline{D}$, and as such is identical to the restriction factor in conventional angle restriction photovoltaics. Just as with macroscopic angle restriction, directivity is beneficial to the efficiency of a photovoltaic device until absorption within the solid angle subtended by the sun is also reduced. The sun subtends 6.83×10^{-5} sr, resulting in a maximum usable directivity equal to 1.84×10^5 and a voltage increase of 314 mV with respect to an isotropic absorber. In macroscopic angle restriction photovoltaics, the solar cell is planar, extended, and only exposed to a hemisphere, which results in a maximum angle restriction factor of 4.61×10^4 and a maximum voltage increase of 278 mV. It is important to note that the maximum V_{oc} in both cases is the same (when the solid angles of emission and absorption are the same and equal to the solid angle

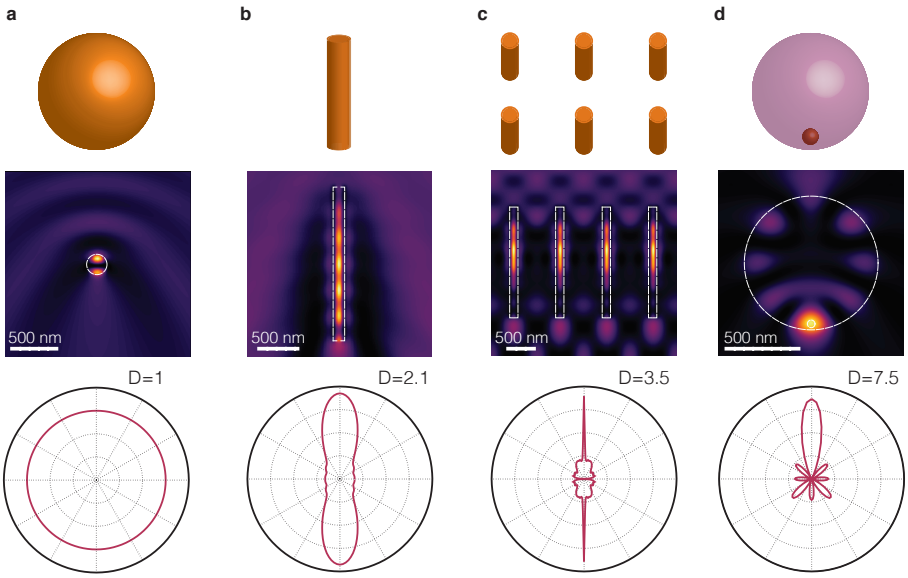

Figure 2.3: Directivity in nanostructures. a-d. Schematics showing different nanophotonic structures: a GaAs sphere (**a**), GaAs nanowire (**b**), a square array of GaAs nanowires (**c**), and a lossless sphere with a 40 nm diameter absorbing inclusion asymmetrically embedded in it (**d**). The top row shows schematic representations of each nanostructure, while the middle row shows the field intensity in the incidence plane, demonstrating the field enhancements corresponding to strong absorption. The corresponding directional absorption is shown in a polar plot in the bottom row, with directivities ranging from a directivity of 1 (no directivity) for the GaAs sphere to a directivity of 7.5 for the lossless sphere with a small absorbing inclusion.

subtended by the sun), but that the V_{oc} without concentration of the nanostructure is lower because it emits into 4π sr.

The absorption directivity of nanostructures strongly depends on their size and shape. Fig. 2.3 shows four examples of nanostructures and their calculated directivity: a simple GaAs sphere (Fig. 2.3a), a GaAs nanowire, a nanowire array, and a small lossless sphere with a GaAs inclusion. We have already discussed the GaAs sphere, which can collect light from a large area (Fig. 2.3a, middle) but is fully isotropic (Fig. 2.3a, bottom), and as a result cannot lead to efficiencies above the SQ limit. Directivity requires anisotropy in absorptance, which in turn requires an asymmetric shape. In the rest of this Chapter we will discuss the other three geometries of Fig. 2.3, which effectively concentrate electric fields (Fig. 2.3b-d, middle row), but, due to their reduced symmetry, can also provide absorption directivity (Fig. 2.3b-d, bottom row).

2.3.1 A single GaAs nanowire

An example of an anisotropic structure that frequently finds use as a nanophotovoltaic element is the nanowire [55]. This geometry has previously been suggested as a candidate for nanophotonic concentration and voltage enhancement because the absorption cross section, when illuminated along the long axis, can be very large due to excitation of weakly confined guided modes at the end facet of the nanowire [53, 112]. In addition, when illuminated perpendicular to the nanowire axis, geometrical Mie resonances can be excited [38, 47, 120, 121], which also lead to significant absorption. Figure 2.4a shows the calculated open circuit voltage (in black) of a 2 μm long GaAs nanowire as a function of its diameter, when illuminated along the long axis of the nanowire. The V_{oc} is higher than the Shockley-Queisser voltage over almost the entire range of diameters. However, Fig. 2.4a also shows a decomposition of the voltage enhancement into contributions due to absorption directivity and absorption suppression (see Section 2.8.1 for details). From this decomposition, it becomes clear that the gain in voltage is mostly due to suppression of absorption near the band gap, just as with the previous example of the sphere. In fact, for small diameters, the directivity contribution is even negative. This can be understood from Fig. 2.4b, which shows the absorption cross section of the 50 nm diameter GaAs nanowire as a function of angle of incidence (shown along the polar angle) as well as wavelength (along the radial direction). At normal incidence, absorption rises strongly at 450 nm, but it is very low at longer wavelengths. However, at larger angles and longer wavelengths the absorption cross section is significantly larger, due to excitation of the TM_{01} resonance. As a result, the recombination rate is enhanced with respect to the generation rate, which is suppressed at longer wavelengths. This in turn leads to a voltage decrease instead of a gain.

Directivity does lead to a voltage gain in the nanowire when it has a diameter around 150 nm, as shown in Fig. 2.4a. Fig. 2.4c shows the absorption cross section of the GaAs nanowire for this diameter, showing a strong peak in absorption near the band gap while absorption at oblique angles is suppressed. This peak in absorption is due to efficient excitation of the HE_{11} guided mode (note that it is not a resonance [122]), while the suppressed absorption at oblique angles is associated with the fact that the wire coincidentally does not support Mie resonances near the band gap. As a result, the absorption pattern becomes more directive, leading to an increase in the open circuit voltage. The directivity achieved here is about 2.1, which leads to a voltage gain of 19 mV. The fact that voltage enhancements due to concentration are small for nanowires has also been observed in arrays [122], where detailed balance analysis has shown that InP nanowire arrays do not surpass the regular SQ limit (but only surpass the SQ limit considering a high index passive substrate, which under normal circumstances significantly increases R_0), even though the effective filling fraction is 10 times lower than for the bulk material. Further optimization of the nanowire geometry and interference with the substrate might lead to slightly higher directivities than those observed here [123], but in the following we will show that these directivities are much lower than what can be in

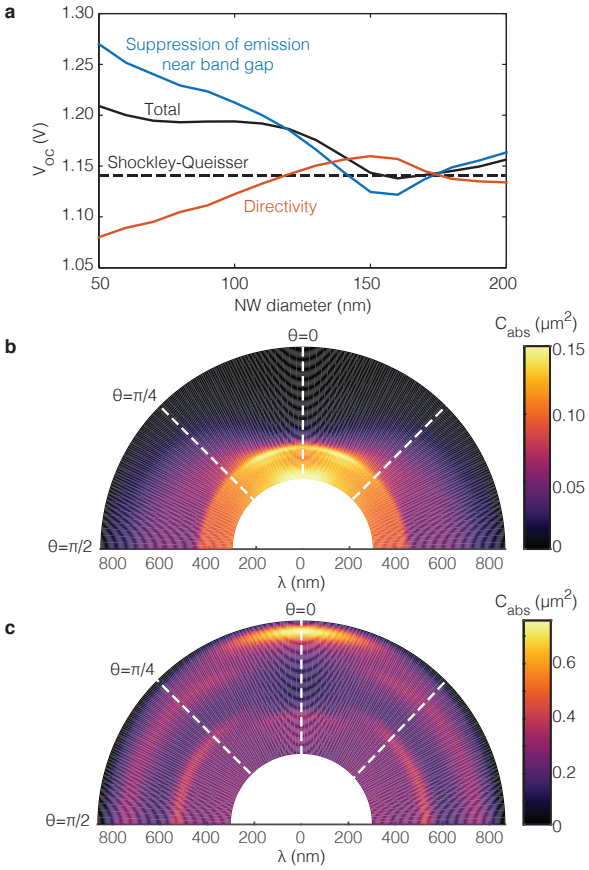

Figure 2.4: Open circuit voltage in a 2 micron long GaAs nanowire. a. The V_{oc} of a 2 μm GaAs nanowire as a function of diameter (in black) is significantly larger than the expected Shockley-Queisser V_{oc}. However, when disentangled into the component due to absorption suppression (blue) and concentration (red), it turns out that concentration contributes only weakly. **b,c.** Absorption spectra as a function of wavelength and incidence angle for 50 nm and 150 nm diameter respectively. In the 50 nm diameter wire (**b**), absorption due to Mie resonances dominates near the band gap (at $\theta = \pi/2$), while for the 150 nm (**c**) diameter wire the HE_{11} guided mode is efficiently excited (at θ=0).

principle achieved with more suitable nanophotonic structures.

2.4 Limits to directivity

We have discussed in the previous sections how the efficiency enhancement that a nanostructure can achieve is directly related to its maximum absorption directivity. In antenna theory, bounds on directivity have been actively studied for decades in the case of radiation and scattering and, although there is no fundamental limit, there are a few useful practical bounds. These bounds are derived for radiation from an antenna, but they also limit the absorption directivity, and it may therefore be instructive to investigate these bounds and in what regime they apply to absorption.

The optical response of small structures can usually be captured accurately by only a small number of spherical harmonics. This is the basis of Mie theory, which allows the calculation of the scattering and absorption response of canonical objects, such as spheres and infinite cylinders [38]. However, even if the system is not highly symmetric, the scattered and absorbed power of structures with size in the order of the wavelength can be described accurately as a superposition of only a few scattering harmonics [124].

The radiation directivity is bounded by the number of spherical harmonics that the structure supports [125]. The radiation patterns associated with the first three spherical harmonics (dipole, quadrupole, and octupole) are shown in Fig. 2.5a (top row). The octupole radiation pattern is the most directive, with a directivity of 4.5. However, by properly combining these harmonics with appropriate relative amplitudes and phases, an even more directive radiation pattern can be obtained. This is shown in the bottom row of Fig. 2.5a: the directivity clearly increases with an increase in the number of harmonics that are supported. This leads to the Harrington limit, which provides the highest possible radiation directivity for a structure that supports up to the N^{th} spherical harmonic [125]:

$$D_{max}(N) = N^2 + 2N. \tag{2.8}$$

There is also no strict limit on the number of harmonics that can be supported by a structure of a given size, but a useful approximate limit is nk_0r, where n is the refractive index of the medium, k_0 is the free space wavevector, and r is the radius of the smallest enclosing sphere. This is equivalent to the number of wavelengths that fits around the circumference of the enclosing sphere. Inserting this into Eq. 2.8 leads to the maximum directivity as a function of radius $D_{max}(r) = (nk_0r)^2+2(nk_0r)$, which for large radii is in fact approximately equal to the directivity of a uniformly illuminated circular aperture antenna, $D_{max}(r) \approx (nk_0r)^2$ [119]. Higher-order harmonics can be in principle supported by a structure of limited size, but only at the expense of very large Q-factors and sensitivity to losses and disorder [126]. Since here we focus on absorption directivity, the presence of losses is crucial, and super-directive solutions are not feasible.

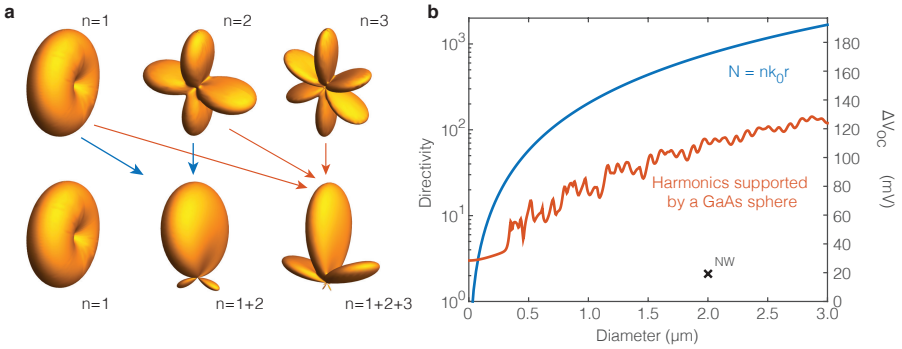

Figure 2.5: Directivity as a function of spherical harmonics. a. Radiation patterns of the first three harmonics and increased directivity due to the combination of these spherical harmonics. **b.** Maximum directivity as a function of size, assuming that the highest harmonic is given by nk_0r, or by taking the amplitudes of the harmonics as in a GaAs sphere at 860 nm. Note that we are only interested in the supported number of harmonics by a physical structure, and that the sphere itself is not directive in absorption as discussed in the previous Section. The cross depicts the directivity from the nanowire in Fig. 2.4, which is significantly lower than directivities that should in principle be achievable for structures with the same size.

Figure 2.5b shows the aperture directivity limit (in blue) as a function of diameter for n=3.66, representative of GaAs near the band gap. This figure also shows the equation for directivity, Eq. 2.8, evaluated with the harmonic amplitudes in a GaAs sphere as a function of its diameter. Although a sphere by itself is not directive in absorption, it is instructive to see how many harmonics a known nanophotonic structure supports at these diameters. Interestingly, this curve is significantly lower than the aperture limit, partially because not all harmonics that are supported have the proper amplitude and phase, but also because the highest harmonic supported is actually much lower than $N = nk_0r$. In a GaAs sphere with a diameter of 3 μm and at 860 nm the highest harmonic with a significant amplitude is $N = 13$, while based on the aperture limit one would expect $N = 39$. On the other hand, at very small diameters the nk_0r limit underestimates directivity because the lowest harmonic ($N = 1$) can lead to a radiation directivity of 3 (a so called Huygens source [127]) and the lowest harmonic has a non-zero amplitude even for very small sizes. If such a directivity of 3 can also be maintained in the absorption pattern over a significant bandwidth (such that $\overline{D} = 3$), this leads to an increase in open circuit voltage of 28.5 mV.

The maximum directivities calculated in Fig. 2.5 are much higher than what we have observed for the single nanowire, whose directivity was at most 2.1 for an object with a "'diameter" (longest dimension) of 2 microns (see cross in Fig. 2.5). In contrast, the aperture limit suggests that a directivity of 600 may be achievable, and

even the harmonics supported by a sphere imply a directivity that is significantly higher (about 70). It appears that achieving directivity in absorption is much more challenging than in scattering. To understand why, it is instructive to think of a lossless dielectric sphere and a single dipole emitter as an exemplary system. The exact placement and orientation of the emitter in the dielectric antenna yields great control over the excited harmonics, both in their phase and amplitude. With such a single feed point and control over its position and its dielectric environment, directivities close to the Harrington limit can be approached. However, achieving absorption directivity is equivalent to looking for radiation directivity from incoherent sources placed all over the absorptive nanostructure. The fact that these sources are incoherent, and placed over the entire volume, makes achieving high directivity in absorption a significant challenge.

2.5 Designing highly directive nanostructures for absorption

While the Harrington limit may not easily be achieved in an absorbing body, we can still use the limit to gain insight on how to enhance the directivity in absorption. For example, since the limit clearly depends on the effective aperture, a sensible approach to enhance the directivity is to place individual antennas in an array. This approach is already commonly taken to enhance the directivity of small antennas in so-called directional arrays. Hence, to boost the directivity of the individual GaAs nanowire, we also place it into an array (see Fig. 2.3c). This of course largely increases the overall aperture of the absorbing nanostructure, but in any case the final device layout will require using large arrangements of nanostructures to cover an entire solar cell. In this case, we use the lattice arrangement to maximize absorption directivity, making use of the fact that for certain arrangements and angles of incidence lattice resonances can be excited. These resonances result in strong absorption even at low filling fractions. By tuning the pitch to be close to the wavelength of interest (a pitch of 834 nm), the second order Bloch mode can be resonantly excited at normal incidence (see Fig. 2.6a at 860 nm and 0°). This leads to a strong directive absorption enhancement at the band edge, which, when averaged over azimuthal angles, gives the absorption/emission pattern shown in Fig. 2.3c. Although absorption at angles close to normal is significantly enhanced, the directivity is still limited to 3.5 (note that since there is no ground plane the array is exposed to free space on both sides). The main reason resides in the strong absorption of sparse nanowire arrays at larger angles [56], which in this case lies between 10% and 20%, while the absorption at normal incidence peaks at 70%. In contrast, to achieve high directivity, the absorption at off-normal angles needs to be significantly smaller than the peak absorption.

While the directivity of the single nanowire can be enhanced by placing it in an array, the obtained directivity is still small. Suppressing emission and absorption except at specific angles is clearly complicated in nanostructures that completely

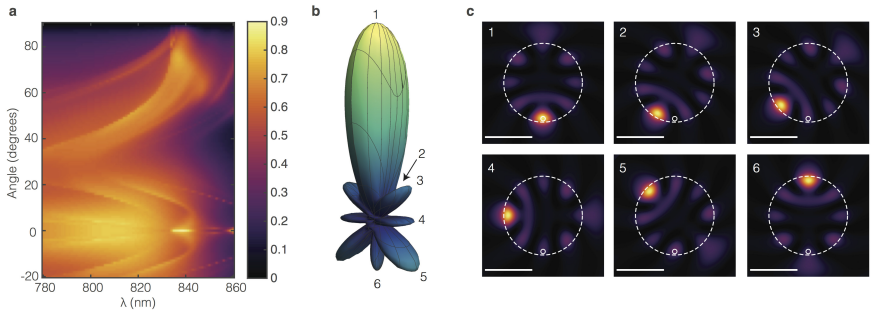

Figure 2.6: Designs for high directivity. a. Absorption of unpolarized light in a square array of nanowires with 834 nm pitch as a function of angle and wavelength for 2 micron long GaAs nanowires with a diameter of 150 nm. Excitation of Bloch modes is clearly visible. **b.** Emission/absorption pattern at λ=860 nm from a 906 nm diameter sphere with n=2, with a 60 nm diameter lossy inclusion (n=2+2i) located at 412 nm from the center of the sphere. **c.** The electric field intensity inside the sphere due to plane wave illumination as a function of incident angle, corresponding to the numerals in **b**. The peak in absorption/emission occurs when the hot spot overlaps with the lossy inclusion, and consecutive peaks and dips in emission correspond to peaks and dips in the intensity distribution. The scale bar is 500 nm.

comprise of an absorbing material. To demonstrate that reducing the absorbing volume can actually increase directivity we make use of the principle of microscopic reversibility: if it is possible to design a structure that emits directively when excited from a certain feed point in the structure, it is also possible to realize a structure that absorbs in an angularly selective fashion by concentrating the loss at that feed point. For very small lossy inclusions the absorption directivity approaches the radiation directivity from a feed point at the same location.

We explore a spherical non-absorbing antenna (refractive index $n = 2$) which is driven by spontaneous emission from a small amount of absorbing material inside the sphere ($n = 2 + 2i$, see schematic in Fig. 2.3d). The spherical harmonics are now only excited efficiently with amplitudes and phases fixed by the location of the inclusion, which can lead to much increased directivity (Fig. 2.6b), in this case up to $D = 7.5$. A simple way to understand this is by looking at the absorption of the structure when it is driven by a plane wave. For this specific size (907 nm diameter) there is a large hot spot in the sphere, at the position where we place the lossy inclusion (Fig. 2.6c). In this case, the hot spot overlaps with the lossy inclusion and absorption is strong. However, if we change the angle of incidence the hot spot rotates along the sphere and moves away from the lossy inclusion, which reduces the absorptance. Hence, the peaks and nodes in the directivity pattern correspond to the intensity maxima and minima in the sphere overlapping with the inclusion, as shown in Fig. 2.6c.

2.6 Practical implications for nanophotonic solar cells

Although the nanowire array and spherical lossy inclusion that we explored in the previous section may achieve enhanced directivity, they are not yet practical designs to achieve efficiencies above the Shockley-Queisser limit in macroscopic solar cells. Both designs suffer from low short-circuit current due to the low filling fraction of absorbing material. However, in principle directivity and large currents can be obtained at the same time, allowing for efficiencies above the Shockley-Queisser limit. This property requires designing a solar cell that achieves strong absorption between the band gap of the semiconductor and the shortest wavelength in the solar spectrum, but that at the same time is very directive in the narrow region near the band gap that is dominated by emission (a width larger than $k_B T/q$, about 26 mV). For example, an efficient directive GaAs solar cell needs to absorb all of the incident sunlight between 300 and 860 nm to achieve high current, while simultaneously being directive between about 800 and 860 nm.

The importance of maintaining high J_{sc} is evident from Fig. 2.7, which shows the efficiency relative to the SQ limit for a GaAs solar cell as a function of its J_{sc} (relative to maximum current) and directivity. Because the efficiency depends logarithmically on the directivity but linearly on the J_{sc}, small penalties in the current reduce the overall device efficiency to below the SQ limit even at reasonable directivities. For example, a weighted directivity of 10 only leads to efficiencies above the SQ limit if the J_{sc} remains above 95%. So far we have not yet demonstrated a peak directivity of 10 even in poorly absorbing structures, highlighting how challenging it may be to achieve both goals simultaneously. However, as is clear from Fig. 2.5, this outstanding design challenge may well be worth the effort since significant enhancements in efficiency can be expected. Based on our analysis it appears that the best approach to enhance intrinsic directivity in a nanophotonic solar cell is to combine an absorber with a non-absorbing nanostructured host material that enhances directivity, as in Fig. 2.3d. Such an arrangement has already been investigated to enhance absorption in small lossy nanostructures [128, 129] and would also be similar to the usual arrangement of an angle restriction solar cell, where a multilayer structure is placed on top of the absorber [9, 10]. However, these multilayer structures are required to be many microns thick to achieve significant directivity, and simultaneously achieving broadband transmission over the whole wavelength range is very challenging [9]. Hence, it is worthwhile to investigate additional approaches to angle restriction.

It is important to stress that the previous considerations hold for materials strongly dominated by radiative recombination. However, many materials appropriate for photovoltaic purposes have significant non-radiative recombination. In the presence of non-radiative recombination, the total recombination current

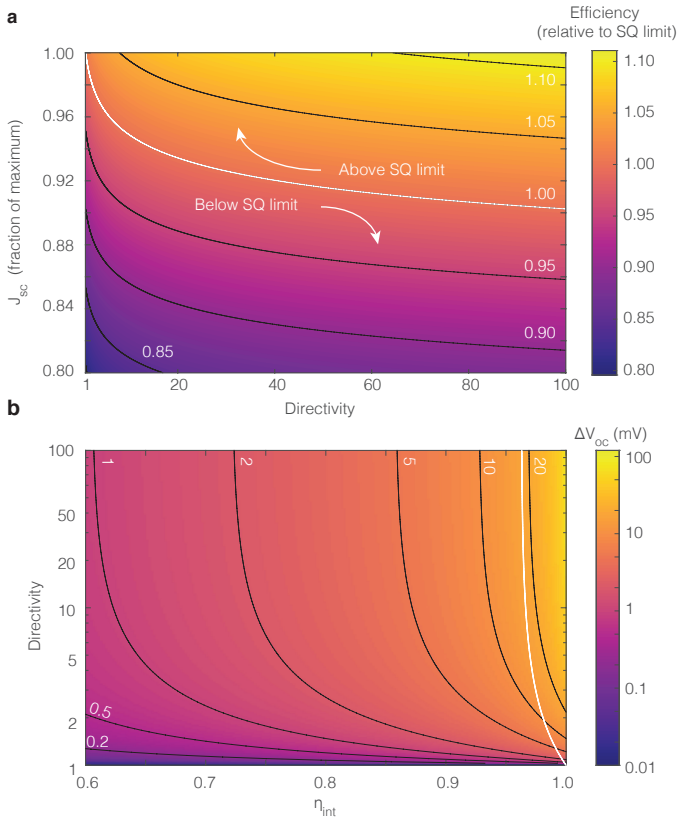

Figure 2.7: Practical implications for high-directivity designs. a. The color map shows the efficiency of a GaAs solar cell as a function of its directivity and fraction of maximum current. At very small penalties in J_{sc} the solar cell will already perform below the SQ limit, even for reasonable directivities. This indicates the importance of maintaining high currents, when trying to achieve directivity. **b.** The color map and black contour lines show the V_{oc} gain due to directivity as a function of the semiconductor internal quantum efficiency (η_{int}) for planar angle restriction systems, with respect to no angle restriction. To the right of the white contour line the SQ limit is surpassed.

increases [130, 131]:

$$R_0^{total} = R_0\left(\frac{\eta_{int}\overline{p}_{esc}}{1-\eta_{int}\overline{p}_{abs}}\right) = R_0\left(\frac{\Gamma_r\overline{p}_{esc}}{\Gamma_{nr}+\Gamma_r(1-\overline{p}_{abs})}\right) \tag{2.9}$$

where $\overline{p}_{abs}$ and $\overline{p}_{esc}$ are the reabsorption and escape probabilities of radiative recombination events in the semiconductor averaged over the semiconductor volume, η_{int} is the internal quantum efficiency, and Γ_r and Γ_{nr} are the radiative and

non-radiative recombination rates. The term in parentheses in Eq. 2.9 is known as the external radiative efficiency (η_{ext}), and it directly reduces the open-circuit voltage:

$$V_{\text{oc}} = V_{\text{oc}}^{\text{rad}} + \frac{k_B T}{q} \ln(\eta_{\text{ext}}). \tag{2.10}$$

In the following we assume that there is no parasitic absorption, so that $\overline{p}_{\text{esc}} = 1 - \overline{p}_{\text{abs}}$.

In the traditional approach to angle restriction, which relies on external multilayer structures, the angle restriction factor and photon escape probabilities are intrinsically linked due to conservation of momentum along the multilayer interfaces. From Snell's law one can show that the probability that a photon escapes a sufficiently thin solar cell with ideal back reflector is given by:

$$\overline{p}_{\text{esc}} = \frac{\Omega_c}{2\pi} = 1 - \sqrt{1 - \sin^2(\theta_D)/n^2} \approx \frac{\sin^2(\theta_D)}{2n^2}, \tag{2.11}$$

where Ω_c is the solid angle subtended by the critical angle in the substrate and θ_D is the angle to which emission is limited by the angle restriction filter. Eq. 2.18 gives an upper limit to the escape probability for planar solar cells, which is achieved only if the cell is sufficiently thin (such that $\alpha d \ll 1$, where α is the absorption coefficient and d is the thickness of the active layer). See e.g. Refs. [10, 130, 132] for a discussion of escape probabilities in the presence of larger αd.

By restricting the emission angle the escape probability decreases simultaneously, due to the fact that the critical angle decreases. In fact, if η_{int} is sufficiently low (so that $\eta_{\text{ext}} \approx \eta_{\text{int}} \overline{p}_{\text{esc}}$), the decrease in R_0 and $\overline{p}_{\text{esc}}$ due to angle restriction cancel out completely [10, 133]. This is clearly visible in Fig. 2.7b, where the color map shows the gain in V_{oc} due to angle restriction, relative to a planar cell with the same η_{int} but no directivity. Even for η_{int} as high as 0.6 the enhanced directivity and reduced $\overline{p}_{\text{esc}}$ still cancel out, with only negligible enhancements of $\Delta V_{\text{oc}} < 1$ mV. To achieve voltage enhancements larger than 10 mV, an η_{int} of at least 93% is required, which so far only GaAs has achieved [132]. In fact, due to the high rate of photon recycling, even small amounts of non-radiative recombination lead to large voltage drops when compared to ideal materials: for a directivity of 10 an η_{int} of 95% reduces the open-circuit voltage by 69 mV, and at a directivity of 100 the voltage drop is 127 mV. To surpass the SQ limit with a planar angle restriction system (shown by the white contour line in Fig. 2.7b), $\eta_{\text{int}} > 0.94$ is required. Note that this is an optimistic scenario for planar films; in real systems where $\alpha d \approx 1$ the requirement on η_{int} is even more stringent.

To reap the benefits of directivity, the relationship between the photon escape probability and directivity thus has to be broken. This is automatically done in nanostructures, where the absence of planar interfaces relaxes the constraints placed by momentum conservation along the interfaces on the escape probability. If directivity and the photon escape probability are uncorrelated, significant increases can be achieved in the open circuit voltage even in the presence of

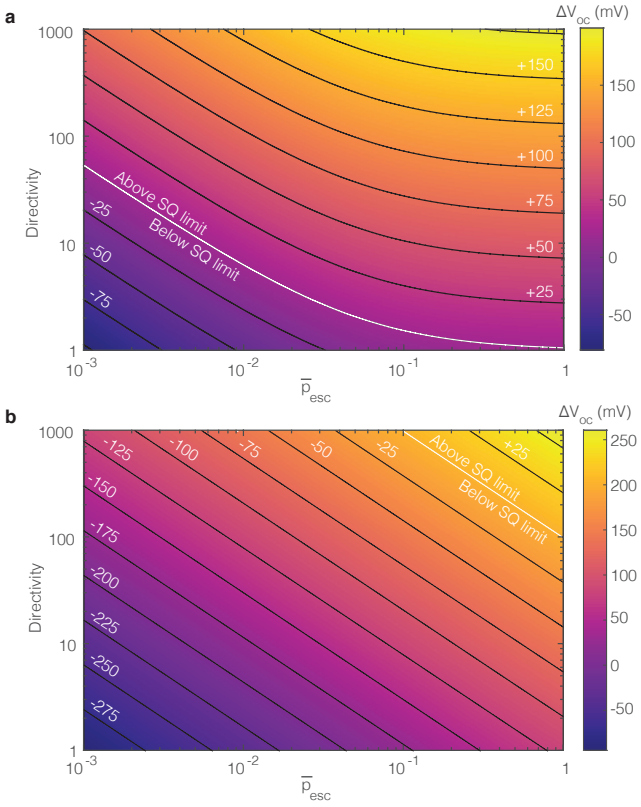

Figure 2.8: Achieving large V_{oc} in systems with non-radiative recombination. The color maps show the gain in V_{oc} for different combinations of $\overline{D}$ and $\overline{p}_{esc}$ with respect to a planar cell with $\eta_{int} = 0.95$ (**a**) and $\eta_{int} = 0.01$ (**b**), representative of GaAs and Si or CIGS, respectively. The contour lines in both figures are now not related to the color maps, but show the absolute distance in V_{oc} to the SQ limit, highlighting that in both cases the SQ limit can still be broken.

non-radiative recombination. This is shown in Figs. 2.8a and 2.8b for $\eta_{int} = 0.95$ and $\eta_{int} = 10^{-2}$, which are η_{int} representative of the best GaAs (2.8a) and Si and CIGS (2.8b) solar cells, respectively [134]. These color maps show the increase in V_{oc} relative to a planar cell with escape probability $1/2n^2$. Clearly, for both values of η_{int} significant increases in V_{oc} with respect to the planar reference case can be achieved by enhancing simultaneously the directivity and photon escape probability. Superimposed on these color maps are contour lines that show the absolute difference in V_{oc} to the SQ limit, highlighting that the SQ limit can still be surpassed as long as both $\overline{p}_{esc}$ and the directivity are sufficiently enhanced. In general, from Eq. 2.9 one can derive the lowest η_{int} for which the SQ limit can still

be beaten given a combination of directivity and $\overline{p}_{\mathrm{esc}}$:

$$\eta_{\mathrm{int}} > \left(1-(1-\overline{D})\overline{p}_{\mathrm{esc}}\right)^{-1}. \tag{2.12}$$

From Fig. 2.8b it is apparent that, even for low η_{int}, increases in directivity and $\overline{p}_{\mathrm{esc}}$ both contribute to enhanced V_{oc}, as long as an increase in one parameter does not come at the expense of the other parameter.

The photon escape probability can also be increased in planar angle restriction solar cells by texturing the back surface, as discussed in the supporting information of Ref. [10]. However, utilizing nanostructures to enhance directivity and $\overline{p}_{\mathrm{esc}}$ may have additional benefits. For example, nanophotonics offers control over the LDOS, which means that the radiative recombination rate Γ_{rad} and thus η_{int} itself can be increased. Additionally, through control over the LDOS, light trapping can also be enhanced even beyond the $1/4n^2$ limit [45, 46]. As a result, the total number of bulk defect centers in the solar cell can be reduced by reducing the amount of bulk material, without sacrificing current. If simultaneously the surface recombination velocity does not increase, Γ_{nrad} decreases and η_{int} increases again [135, 136]. This means that, even if the degree of directivity attainable in broadband absorbing nanostructures is limited, these nanostructures can perhaps be used to enhance η_{ext} in conjunction with *e.g.* concentrating lenses, angle restriction filters [9, 10, 12, 32, 137], or even external cavities [10, 12, 138] to achieve directivity. However, in the latter two external approaches care must be taken not to reduce $\overline{p}_{\mathrm{esc}}$ too much, or the benefit of nanostructuring is undone.

2.7 Conclusion

In this chapter we have discussed efficiency enhancement above the Shockley-Queisser limit using nanophotonic principles. We showed that the increase in absorption cross section available in nanoparticles cannot help break the Shockley-Queisser limit, but that increased directivity in absorption can provide such an efficiency gain. Achieving directivity in a small absorbing nanostructure is challenging, and it requires careful engineering. Fruitful ways to achieve directivity in actual nanophotonic solar cells may be to use arrays or combinations of absorbing and lossless nanostructures. However, while designing a directive solar cell, care should be taken that the penalty in short-circuit current is minimal. Furthermore, in the presence of non-radiative recombination, efficiencies above the Shockley-Queisser limit can still be realized as long as both the directivity and photon escape probabilities are enhanced. These photon escape probability and directivity enhancements are additive to traditional voltage enhancement strategies, such as concentrating lenses, which make nanostructuring a powerful approach even in combination with other more traditional schemes.

2.8 Supplementary Information

2.8.1 Methods

The calculations for the sphere were performed using Mie theory [38], except for the sphere LDOS calculations. LDOS calculations rely on evaluating the imaginary part of the Green's dyadic, $\mathrm{Im}\left\{\overleftrightarrow{\mathbf{G}}(\mathbf{r},\mathbf{r})\right\}$, at the source location, which we averaged over the sphere volume:

$$\frac{\langle\rho\rangle}{\rho_\infty} = \frac{6\pi}{Vk}\iiint \frac{1}{3}\mathrm{Tr}\left(\mathrm{Im}\left\{\overleftrightarrow{\mathbf{G}}(\mathbf{r},\mathbf{r})\right\}\right)d^3\mathbf{r}. \tag{2.13}$$

Here V is the sphere volume, we take the trace of the Green's dyadic to account for dipole orientation, and we used the fact that the homogeneous Green's dyadic evaluates to $\mathrm{Im}\left\{\overleftrightarrow{\mathbf{G}}(\mathbf{r},\mathbf{r})\right\} = \mathbf{I}k/6\pi$ (where $\mathbf{I}$ is the identity matrix and k is the wavenumber in the medium). Ref. [139] gives convenient formulas for normalized transition rates of dipoles located inside a sphere (Eqs. 10 and 11 in Ref. [139]), which readily enable evaluation of Eq. 2.13.

Fig. 2.4a shows disentanglement of the contributions to the V_{oc} due to suppression or enhancement of absorption near the band gap and due to the angular distribution of the absorption cross section. To distinguish between the different contributions, we first calculate the total "concentration factor"

$$X = \frac{4\pi\int\Theta(\omega)f(\omega-\omega_{\mathrm{bg}})d\omega}{\iint\Theta(\omega)\sigma_{\mathrm{abs}}(\omega,\Omega)d\Omega d\omega}, \tag{2.14}$$

where $f(\omega-\omega_{\mathrm{bg}})$ is a step function with onset at the band gap frequency ω_{bg}, normalized so that integrating f over the solar spectrum yields the same G as follows from Eq. 2.4. $\Theta(\omega)$ is the black body spectrum at ambient temperatures. The numerator with the Heaviside step-function is thus proportional to the standard isotropic Shockley-Queisser emission rate, while the denominator is proportional to the actual emission rate. The ratio of the two rates naturally gives the enhancement factor. We can rewrite Eq. 2.14 as

$$X = \frac{\int\Theta(\omega)f(\omega-\omega_{\mathrm{bg}})d\omega}{\int\Theta(\omega)\sigma_{\mathrm{abs}}(\omega,\theta=\phi=0)d\omega} \times \frac{4\pi\int\Theta(\omega)\sigma_{\mathrm{abs}}(\omega,\theta=\phi=0)d\omega}{\iint\Theta(\omega)\sigma_{\mathrm{abs}}(\omega,\Omega)d\Omega d\omega} \tag{2.15}$$

where now the first term only corresponds to the spectral shape of σ_{abs}, but σ_{abs} is assumed to be isotropic, while the second term captures the contribution of the angle dependence of σ_{abs}. The first term gives the enhancement factor due to suppression of emission near the band gap, A, while the second term indeed corresponds to $\overline{D}$ as given by Eq. 2.7. To calculate the contributions to the voltage explicitly, we use:

$$\Delta V_{\mathrm{oc}} = \frac{k_B T}{q}\log(X) = \frac{k_B T}{q}\left(\log(A)+\log(\overline{D})\right) = \Delta V_{\mathrm{oc}}^{A} + \Delta V_{\mathrm{oc}}^{D}, \tag{2.16}$$

where ΔV_{oc}^{A} and ΔV_{oc}^{D} are the contributions to the V_{oc} due to the absorption edge and directivity respectively.

The simulations for the single nanowire and lossy inclusion were performed with Lumerical FDTD [140], and the simulations of the array of nanowires were performed using S^4, a free package for the Fourier modal method [141].

2.8.2 Equivalence of angle restriction and concentration

It is instructive to take a closer look at concentration and angle restriction in macroscopic photovoltaic systems, to further elucidate why large absorption cross sections are not necessarily comparable to concentration. The limiting efficiency of a photovoltaic device can be calculated by considering fluxes entering and exiting the solar cell, where the solar cell itself is considered a "black box" with a given absorptance and quantum efficiency. It should not matter whether we consider a flux surface just above the solar cell or above the concentrator lens, in which case the lens is considered an integral part of the solar cell and resides inside the black box. However, this leads to an apparent paradox: the intensity of sunlight incident on the solar cell is much higher than the one incident on the lens, yet in both cases we should find the same increase in V_{oc}. This paradox is resolved by considering the angular response of the lens/solar cell system, as shown in Fig. 2.9a. If we consider the lens as an active part of the photovoltaic system the generation rate per unit area is identical to that of a regular solar cell without a lens, but the recombination rate is strongly affected by the presence of the lens. For flat, extended systems Eq. 2.3 becomes [7, 67]:

$$R_0 = \int_{E_g/\hbar}^{\infty} \int_0^{2\pi} \int_0^{\pi/2} A(\omega,\theta,\phi)\Theta(\omega)\sin(\theta)\cos(\theta)\, d\theta\, d\phi\, d\omega \tag{2.17}$$

where the $\cos(\theta)$ follows from Lambert's rule and A is the absorptance. From Fig. 2.9b it is clear that for certain angles ($\theta_s < \theta \leq \theta_L$, where θ_L is the angle of the edge of the cell to the edge of the lens) black-body radiation does not generate carriers in the semiconductor at all, because the action of the lens directs the radiation next to the solar cell. At very large angles the solar cell is directly exposed to black-body radiation, but because it doesn't pass the lens the intensity is lower by a factor X, where the concentration factor of the lens is given by $X = \sin^2(\theta_L)/\sin^2(\theta_s)$. If we evaluate Eq. 2.17 according to Fig. 2.9b, we find:

$$R_0^L = \pi\left(\sin^2(\theta_L) + \frac{1}{X}\cos^2(\theta_L)^2\right)\int_{E_g/\hbar}^{\infty} \Theta(\omega)\, d\omega \tag{2.18}$$

When comparing this to the recombination rate of a solar cell without a concentrating lens to find the angle restriction enhancement factor X_{AR}, we find

$$X_{AR} = \left(\sin^2(\theta_L) + \frac{1}{X}\cos^2(\theta_L)^2\right)^{-1} = X \tag{2.19}$$

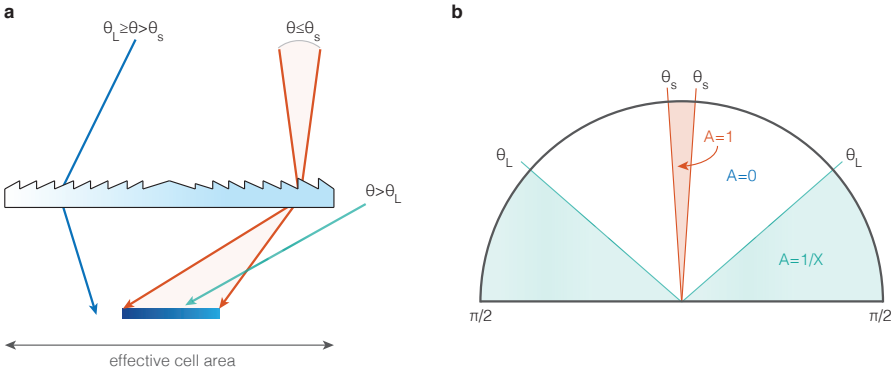

Figure 2.9: Equivalence of angle restriction and concentration. a. A lens also acts as an angular filter for a solar cell, which only transmits light into the solar cell that is incident within the solid angle of the sun, while light that is incident with larger angles is focused next to the solar cell. Light incident at very oblique angles still hits the solar cell, but with lower intensity. **b.** Polar plot representation of the absorptance of an ideal solar cell when considering the lens as an integral part of the system. A refers to the absorptance of the solar cell and lens system in each angular range. The lens has a concentration factor of X.

where we used the expression for X given above. Hence, as one would expect, the voltage enhancement due to a lens can be described both from the perspective of concentration and angle restriction, and both lead to the same result. This even holds in the presence of non-radiative recombination: a lens does not affect the escape probability or internal quantum efficiency, and as a result η_{ext} is independent of the concentration factor X. The total recombination rate given in Eq. 2.9 therefore still scales with $1/X$. Note that in practice a lens and an angle restriction filter block different angles, and they can therefore be used in conjunction with additive voltage enhancements, as long as the angle restriction filter does not block angles incident from the lens [133].

3

Nanophotonic spectrum splitting for ultra-thin multijunction solar cells

We present an approach to spectrum splitting for photovoltaics that utilizes the resonant optical properties of nanostructures for simultaneous voltage enhancement and spatial separation of different colors of light. Using metal-insulator-metal resonators commonly used in broadband metamaterial absorbers, we show theoretically that output voltages can be enhanced significantly compared to single junction devices. However, the approach is general and works for any type of resonator with a large absorption cross section. Due to its resonant nature the spectrum splitting occurs within only a fraction of the wavelength, as opposed to traditional spectrum splitting methods where many wavelengths are required. Combining nanophotonic spectrum splitting with other nanophotonic approaches to voltage enhancements, such as angle restriction, may lead to highly efficient but deeply subwavelength photovoltaic devices.

3.1 Introduction

The conversion efficiency of solar cells is an important factor in the cost per kWh, and improving it has therefore been a key goal of photovoltaic research. For a single junction solar cell, such an efficiency enhancement can come from improving the

current or voltage output, or both. Nanophotonic engineering has so far mostly been applied to solar cells with the goal of enhancing the absorption and thereby current of a thin semiconductor layer. This has been achieved using optical resonances in plasmonic [43] or dielectric structures [39]. By eliminating reflection and maximizing light trapping, such resonances can bring the solar cell short-circuit current (J_{sc}) close to that expected under the Shockley-Queisser limit [7]. More recently, interest has shifted towards using nanophotonics to enhance the open circuit voltage (V_{oc}) of a solar cell [44]. In general, this is achieved when the recombination rate is reduced with respect to the generation rate, resulting in higher carrier densities which correspond to a larger Fermi-level splitting and thus higher output voltage [142]. Nanophotonic modification of the recombination rate is possible via three different mechanisms: optical concentration, angle restriction, and optical band gap engineering. Optical concentration occurs when nanostructures act as antennas for light. This means that nanostructures absorb photons from an area much larger than their physical cross section, leading to lower material consumption and thus lower bulk recombination rates without the need for focusing lenses or external optics [51, 53]. However, as discussed in Chapter 2, such an effect can only be beneficial in the presence of non-radiative recombination. Alternatively, for cells that are strongly dominated by radiative recombination, limiting the angles of emitted light through for instance a nanophotonic multilayer structure leads to photon recycling and as a result to higher carrier concentrations [9, 10].

In addition to intrinsic optical concentration and angle restriction, nanophotonics can also be used to suppress absorption near a material's electronic band gap to create an effective photonic band gap that is higher in energy [66–68, 113]. This works because due to reciprocity, reducing absorption near the band gap also makes it harder for carriers to recombine and emit a photon to the far field. Instead, photons are recycled in bulk cells [66] or the recombination rate is actually reduced due to changes in the local density of optical states (LDOS, see Chapter 2).

While this third approach increases the voltage output of the solar cell, the higher effective optical band gap also reduces the maximum current; it therefore cannot lead to a power conversion efficiency above the single cell Shockley-Queisser limit. The standard method to exceed this limit is to build a solar cell where materials with different band gaps are stacked on top of each other. This is the multijunction solar cell concept, where a top cell only absorbs high energy photons, but transmits lower energy photons into the next layer (see Fig. 3.1a). In each subcell the thermalization losses are small, so the overall conversion efficiency of photons is high. Efficiencies as high as 46% have been achieved using four different semiconductor layers that are grown on top of each other epitaxially [17]. It has recently been shown theoretically that, with a two-layer multijunction architecture as in Fig. 3.1a, the single-junction SQ limit can actually be surpassed even if both layers are made of the same material [69]. This is achieved by increasing the voltage output of the top layer through photonic engineering, as described above.

Although multijunction solar cells are a proven concept for high efficiencies,

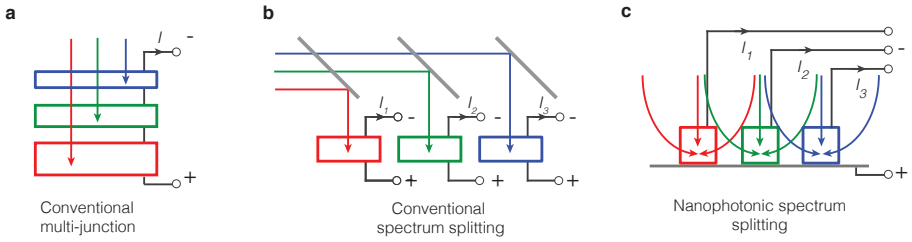

Figure 3.1: Different approaches to multijunction solar cells. a. The conventional tandem geometry, in which light is separated through sequential absorption. **b.** A conventional spectrum splitting approach based on spectrally selective filters. **c.** Nanophotonic spectrum splitting, where light is separated spatially in parallel. In each case the contacting scheme is shown as well, with in **a** a series connection, in **b** each cell is connected independently, and in **c** a four-terminal connection with a shared positive contact.

their design and fabrication is complicated. Since the standard multijunction solar cell is grown epitaxially, each layer has to be lattice matched and produce the same current (which puts constraints on the band gap). The difficulty involved in finding the ideal combination of band gaps and lattice constants makes spectrum splitting multijunctions - where the subcells are not placed on top of each other but next to each other - quite appealing (see Fig. 3.1b) [143–145]. This spectral splitting is typically done on macroscopic length scales using external optics, such as dichroic mirrors.

Just as focusing optics can be replaced by nanoscale resonances to provide optical concentration (as described above), nanostructures also provide an opportunity for spectrum splitting without external macroscopic optics. In this chapter we propose such an alternative approach to spectrum splitting, where the resonant optical properties of nanoparticles are responsible for both the voltage enhancement (due to an increased optical band gap) and the actual spectrum splitting (see Fig. 3.1c). This approach is based on the fact that nanoparticles can have very large absorption cross sections and that sufficiently detuned resonators operate independently, even if they are closely spaced. As opposed to the approaches in Fig. 3.1a and 3.1b, where colors are separated over distances of many wavelengths, nanophotonic spectrum splitting occurs within a fraction of the wavelength. As a result, the multijunction solar cell can have a subwavelength height, significantly reducing material consumption.

3.2 Identical resonators

We begin by investigating an array of identical resonant particles, to gauge the voltage enhancements that can be achieved through nanophotonic manipulation of the band gap alone. We will then move on to an array of detuned resonators

in one unit cell, to investigate nanophotonic spectrum splitting. Since the resonators are spatially separated, we are not restricted to certain materials or lattice constants. Hence, we will also look at nanophotonic spectrum splitting when resonators are made from different semiconductors. Although in this study we investigate metal-insulator-metal patch resonators, the results are general and apply to any nanostructured resonator with a large absorption cross section. We believe that this approach to spectrum splitting facilitates further integration with other nanophotonic concepts for voltage enhancements such as angle restriction [9, 10] and, in the presence of non-radiative recombination, concentration [51, 53].

Nanostructures, particularly at resonance, can have an absorption cross section that is much larger than their geometrical cross section [38]:

$$Q_{abs} = \frac{\sigma_{\text{abs}}}{\sigma_{\text{geo}}} \gg 1 \tag{3.1}$$

where Q_{abs} is called the absorption efficiency. As a result, an array of identical nanostructures with large spacing in between can still absorb all of the incident light at the resonance wavelength [146, 147]. An example of such an array is depicted in Fig. 3.2a, where a small metal-insulator-metal (MIM) resonator is shown in a 400 by 400 nm unit cell. The metal-insulator-metal (MIM) configuration supports so-called MIM waveguide modes, which reflect off of the sides of the disk and form a Fabry-Perot like resonance [148–151]. In our case the metal substrate and top hat are silver (Ag) and in between is a disk of aluminum gallium arsenide ($Al_{0.3}Ga_{0.7}Sb$). Using finite-difference time-domain simulations (Lumerical FDTD, [140]) we calculated the absorption in the semiconductor under normal incidence illumination for a range of wavelengths and MIM disk diameters (Fig. 3.2b, see Fig. 3.6 for full spectrum and total absorptance including in silver). A strong absorption peak corresponding to the fundamental MIM resonance is shown redshifting and increasing in intensity for larger diameters, until the peak amplitude starts to decrease close to the band gap (1130 nm/1.1 eV [152]). This variation in amplitude is due to changes in the absorption loss rate of the resonance, which depends on the extinction coefficient of $Al_{0.3}Ga_{0.7}Sb$. Resonances absorb most strongly when their radiative loss rate and absorption loss rate are equal (the so-called called critical coupling condition), and an increase or decrease in the absorption loss rate reduces the peak amplitude [34]. The radiative loss rate of the MIM resonator is low (its bandwidth is small), so counterintuitively it absorbs most when the extinction coefficient is also low (close to the band gap).

If the absorptivity of a geometry such as an array of nanostructures is known over the whole range of the solar spectrum and all angles, one can calculate the maximum open circuit voltage (V_{oc}) using the detailed balance framework [67]:

$$V_{\text{oc}} = \frac{k_B T}{q} \ln\left(\frac{J_{\text{sc}}}{J_0}\right) \tag{3.2}$$

where q is the electron charge, k_B is the Boltzmann constant, T is the temperature of the solar cell, and J_{sc} and J_0 the short circuit and reverse saturation current

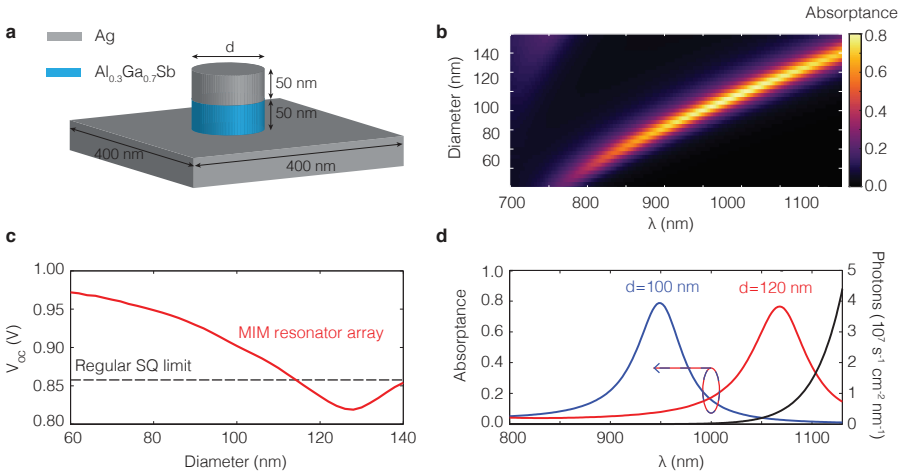

Figure 3.2: The V_{oc} of a lattice of identical gap-plasmon resonators a. Schematic diagram of the MIM resonator array with a unit cell size of 400 by 400 nm. **b.** Absorption spectrum of periodic array of identical MIM resonators, for different diameters d (see **a**). **c.** V_{oc} of the MIM array (red), compared to the Shockley-Queisser V_{oc} for a perfectly absorbing solar cell (dashed black) with the same band gap. **d.** Absorption spectrum of the MIM array for two diameters and the black body spectrum at 300 K for unity emissivity in black.

density, respectively. The J_{sc} is obtained simply by integrating the semiconductor absorptance of the array under normal incidence and over the solar spectrum (i.e. assuming 100% internal quantum efficiency), while calculation of J_0 is a little more involved. In the dark, a very small amount of carriers are generated because of above band gap blackbody radiation, and in equilibrium the same amount of carriers must recombine (the principle of detailed balance) [7, 67]. In the presence of other absorbing materials near the semiconductor, parasitic absorption must also be taken into account because it reduces $\overline{p}_{esc}$, the photon escape probability*. However, such gap resonator structures can actually be very bright, with large probability of emitting a photon to the far-field [153] and even enhance the total external radiative efficiency [154, 155]. For simplicity we therefore assume that the recombination current J_0 can simply be found by integrating the full hemisphere absorption spectrum over the blackbody spectrum at ambient temperatures, and

*See Section 2.6 on page 39 for extensive discussion on how $\overline{p}_{esc}$ affects the V_{oc}.

that parasitic absorption can be neglected. This gives for J_{sc} and J_0:

$$J_{sc} \approx q \int_{\omega_g}^{\infty} S(\omega) A(\omega, \theta = 0, \phi = 0) d\omega \tag{3.3a}$$

$$J_0 \approx q \int_{\omega_g}^{\infty} \int_0^{2\pi} \int_0^{\pi/2} \Theta(\omega) A(\omega, \theta, \phi) \sin(\theta) \cos(\theta) d\theta d\phi d\omega \tag{3.3b}$$

Here $S(\omega)$ is the AM1.5 solar spectrum [4], and $\Theta(\omega, T)$ is the black body spectrum at ambient temperature (T_a =300 K). A is the unpolarized absorbtance of the total array in the semiconductor, thus excluding absorption in silver, as a function of incident angle. In Eq. 3.3b the $\cos(\theta)$ term is due to Lambert's cosine rule and the term accounts for the solid angle. We've assumed that the illumination only occurs at normal incidence (Eq. 3.3a), which is a good approximation considering the small solid angle occupied by the sun, while for recombination we integrate over the full hemisphere (Eq. 3.3b). Furthermore, as mentioned earlier, we have assumed that there is only radiative recombination and no parasitic absorption. Finally, we have assumed that the absorption is in fact isotropic ($A(\omega, \theta, \phi) = A(\omega)$), which is a good assumption [156] (see Supporting Information Fig. 3.7).

The V_{oc} of this array, shown in red in Fig. 3.2c, varies with diameters and for small diameters is significantly higher than the regular Shockley-Queisser V_{oc} (dashed black line). As the absorptance is isotropic, this voltage enhancement is not due to angle restriction effects (see Supporting Information), but instead the origin lies in the suppression of absorption near the band gap [66, 67, 113]. As thermal emission peaks near the band gap and then decays exponentially for higher energies, moving a resonance to shorter wavelengths reduces J_0 dramatically. For example, Fig. 3.2d shows the absorption spectra of 100 and 120 nm diameter MIM resonator arrays together with the 300K black body spectrum. Because the integrated product of the 100 nm disk absorption and the black body spectrum is much smaller, the equilibrium thermal emission is lower and the V_{oc} is increased.

Although voltages are enhanced significantly, the absorption bandwidth is small and as a result, so is the current. However, because Q_{abs} is large enough, this can leave ample room to interdigitate a second (or third, forth, *etc.*) array detuned from the first to absorb strongly at another wavelength. This is the basic principle of some broadband metamaterial absorbers, where it is used to enhance the absorbing bandwidth of an array [147, 151, 156–158]. Since at different wavelengths light is absorbed in physically different positions, this phenomenon has also been suggested for photon sorting [157, 159]. Photon sorting is exactly what is required in a multijunction solar cell, where photons are directed to and absorbed in a subcell where they are converted most efficiently. We can thus use the resonant properties of these nanoscale resonators to simultaneously enhance the voltage and split the spectrum.

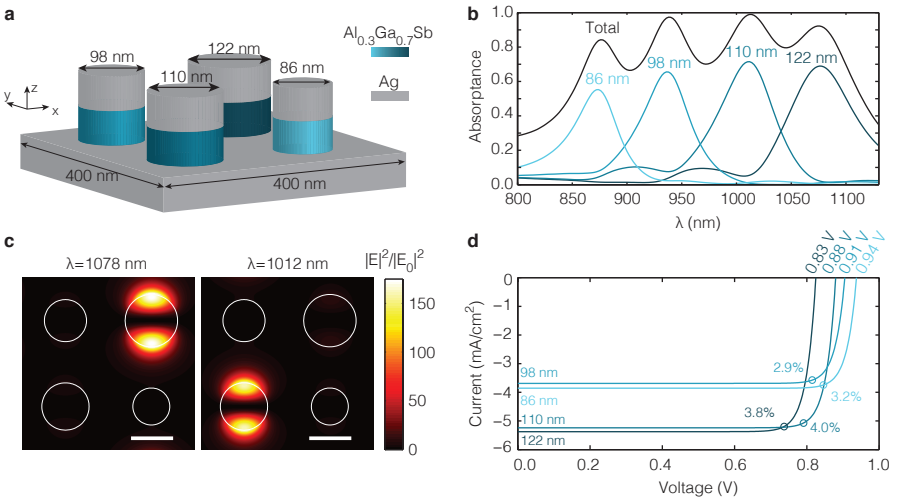

Figure 3.3: A lattice of detuned resonators a. Diagram of the MIM resonator array, now with four resonators in a unit cell. They are positioned on a square lattice with 200 nm spacing between centers. **b.** Absorption spectrum of this array, where black is total absorption and shades of blue are the different size resonators individually, excluding absorption in the silver. **c.** Field enhancement plots showing the electric field density at different wavelengths corresponding the resonant frequencies of the different resonators. The scale bar is 100 nm. The plot depicts the 400 by 400 nm x-y plane in the middle of the semiconductor cylinder (z = 25 nm above the Ag substrate). Polarization is along the y-axis in both **b** and **c** (the other polarization is shown in Fig. 3.6). **d**. The current-voltage curves for the four independent resonators shown schematically in **a**.

3.3 Detuned resonators

To achieve nanophotonic spectrum splitting we place multiple detuned resonators in the same subwavelength unit cell (see Fig. 3.3a). The absorption spectrum of the array is shown in Fig. 3.3b, with in solid black the total absorption, and in colors the different semiconductor disks. The spectra over the whole solar range for both polarizations are shown in Fig. 3.6. The absorption spectrum shows that this geometry spatially separates colors: at different wavelengths absorption peaks in different resonators (total absorption reaches over 90% in three out of four resonators), which are physically separated, without the need for external optics. This is even more clearly visible in Fig. 3.3c, where the electric field intensity enhancement $|E|^2/|E_0|^2$ is shown (E_0 is the incident field amplitude). The two plots correspond to the peak wavelengths of the two larger resonators in Fig. 3.3b. At the different wavelengths high field intensities are visible in the resonant nanostructures while the off-resonance nanostructures remain dark, which visualizes how light is captured and the spectrum is split by the resonators.

Using Eqs. 3.2 and 3.3 we can calculate the open circuit voltage and short circuit current from each resonator in the array. We can then calculate the J-V curve corresponding to each resonator, which is given by the ideal diode equation [7, 67]. From these curves, shown in Fig. 3.3d, it is clear that again the V_{oc} for each resonator has increased: 825, 880, 905, and 937 mV for the largest to smallest resonators respectively. This remarkable increase of more than 100 mV in the V_{oc} (14%) using exactly the same material arises only through careful engineering of the nanophotonic resonances. The current of each resonator is relatively small due to the narrow bandwidth, as mentioned above, which limits the efficiency. Although in the current design this limits the total power conversion efficiency to 13.91%, we can show that spectrum splitting does actually improve the efficiency of the array by making two comparisons. First of all, if each resonator in the array has the same size, the efficiency would be comparable to the single resonator array discussed before. Due to significantly lower currents this efficiency is below 6% (see Supplementary Information, Fig. 3.5). Secondly, we can compare it to a configuration where all resonators are connected in parallel. In that case the voltage over each cell is equal, and the advantage of spectrum splitting is lost. For the device in Fig. 3.3a this leads to an efficiency of 13.41%, so spectrum splitting has led to an increase in efficiency of almost 4% relative.

3.4 Detuned resonators comprising different materials

Although we have demonstrated that nanophotonic spectrum splitting can lead to a multijunction solar cell using only a single material by proper resonance engineering, the improvement in efficiency is still modest (4%). Further gains in V_{oc} are possible by making the different resonators from materials with different band gaps. Fig. 3.4a shows a unit cell with two detuned $Al_{0.3}Ga_{0.7}Sb$ resonators (band gap = 1.1 eV), one indium phosphide (InP, band gap = 1.34 eV [152]), and one aluminum gallium arsenide ($Al_{0.2}Ga_{0.8}As$, band gap = 1.67 eV [152]) resonator. The absorption spectrum of the array is shown in Fig. 3.4b, with absorption in each semiconductor disk shown as a colored curve. Fig. 3.4c shows the J-V curves of the different resonators, and we immediately notice that higher V_{oc} values are indeed achieved: the AlGaAs subcell has a V_{oc} of 1.39 V and the InP subcell has a V_{oc} of about 1.06 V. This enhanced voltage compared to the AlGaSb resonators is due to the fact that the AlGaAs and InP resonators naturally do not absorb at all below their band gap, leading to a lower J_0. This increase in output voltage positively affects the efficiency: it has increased by 27% from 13.91% for the AlGaSb array to 17.53%, while the total J_{sc} has only increased by 12% to 20.3 mA/cm^2.

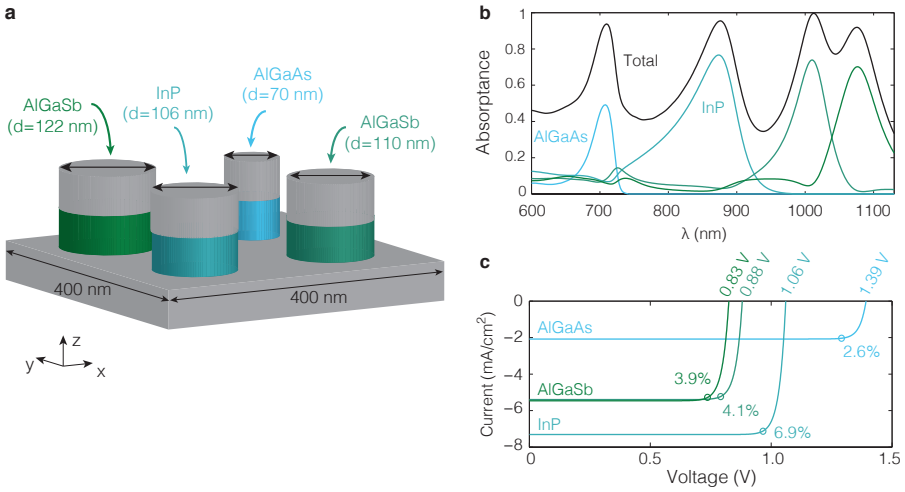

Figure 3.4: A lattice of detuned resonators comprising different materials. a. Diagram of the MIM resonator array, now with four resonators in a unit cell. Two resonators comprise AlGaSb as an absorber, one InP and one AlGaAs. They are positioned equally far from each other (200 nm spacing between centers). **b.** Absorption spectrum of this array, where black is total absorption and the colored curves show absorption in the semiconductor material of the individual resonators (unmarked curves correspond to the AlGaSb pair). The incident polarization is along the y axis, see Fig. 3.6 for the other polarization. **c.** Current-voltage curves for the four independent resonators in **a**.

3.5 Conclusion and discussion

To conclude, we have investigated theoretically spectrum splitting for photovoltaic applications utilizing arrays of nanoscale antennas with different resonant frequencies. This allows for simultaneous voltage enhancement and spatial separation of different colors of light. Such an intrinsic spectrum splitting mechanism relaxes the lattice and current-matching requirements compared to the typical multijunction solar cells, while also eliminating the need for external splitting optics. Additionally, this was achieved in an array with a deeply subwavelength height. Efficiency enhancements are observed for a multijunction spectrum splitting design that uses only a single semiconductor, due to suppression of absorption near the band gap in some of the resonators, leading to higher voltages. Much larger efficiency enhancements are observed when the different resonators are made from different semiconductors, due to the more stringent reduction of reverse saturation currents that comes with increasing electronic band gaps.

In all array solar cells discussed in this chapter, the efficiency is limited by the generated current, due to the narrow bandwidth resonances. To increase the efficiency, the current has to be increased either by including more resonators in

the lattice, or by using resonators with a larger bandwidth. Ideally one would increase the number of narrowband resonators to keep thermalization losses as low as possible, but it may be more practical to use larger bandwidth resonances or a nanostructure that supports multiple resonances in the same frequency window [34, 160]. However, there is a trade-off between the size of the absorption cross section and the bandwidth of the resonance: the larger the absorption cross section, the narrower the bandwidth [125, 126, 161] and increasing the absorption cross section at some point also requires increasing the physical size of the resonator [161]. As a result, for very large currents the traditional sequential approach, or nanophotonic interpretations of the multilayer approach [71], may be more suitable. Furthermore, the large metal-semiconductor interfaces present in the current geometry might lead to high interface recombination rates, which have to be taken into account through for instance interfacial contact passivation. Purely dielectric nanophotonic structures might therefore be more favorable to achieve high internal quantum efficiencies, and to avoid ohmic absorption losses, but a contact to extract carriers is always required.

In conclusion, the nanophotonic approach to spectrum splitting, in particular in combination with other nanophotonic approaches to voltage enhancements such as angle restriction, may lead to deeply subwavelength, yet efficient photovoltaic devices with very low material consumption.

3.6 Supplementary Information

Efficiency of a single resonator periodic device

For completeness, below we show the efficiency and short circuit current together with the same V_{oc} plot shown in the main text in Fig. 3.2. Clearly, although the voltage shows significant shifts, the efficiency is still dominated by the current. The plateau between 90-100 nm diameter is due to shifting of the resonance over an atmospheric absorption band in the solar spectrum.

Full absorption spectra

Here we show the full absorption spectra as determined with FDTD for completeness. To calculate the short circuit current we integrated the absorption from 300 nm to the band gap of the material. Hence, in this section we show those full absorption spectra of all the simulations that are used in the main text.

In Figs. 3.6a,b the absorption spectra are shown for the array comprising a single resonator. On the left side the absorptance in the semiconductor is shown, while on the right side in b the absorption in the total array is shown. Note that the absorption in the total array, calculated as $1-R$ where R is the reflection, goes slightly over one (to 1.02) at around 400 nm. This is due to a very strong lattice resonance, and convergence studies show that this result can be reduced closer to one by decreasing the mesh size. However, this does not affect our results because the simulation is converged at all other wavelengths and it does not noticeably affect integrated absorption in the semiconductor.

The absorption remains strong right up to the band gap because the reported

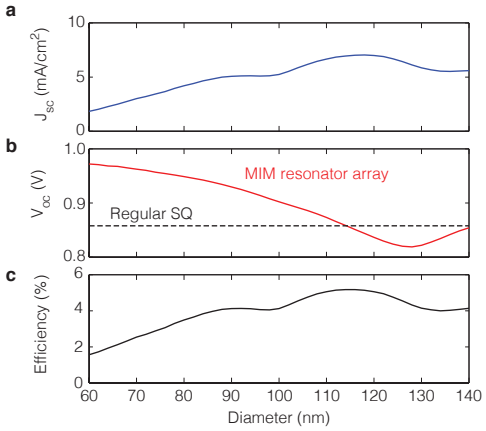

Figure 3.5: The efficiency of a solar cell comprising an array of identical resonators. Short circuit current (**a**), voltage (**b**), and efficiency (**c**) for the array with a single resonator, shown in Fig. 3.2 in the main text.

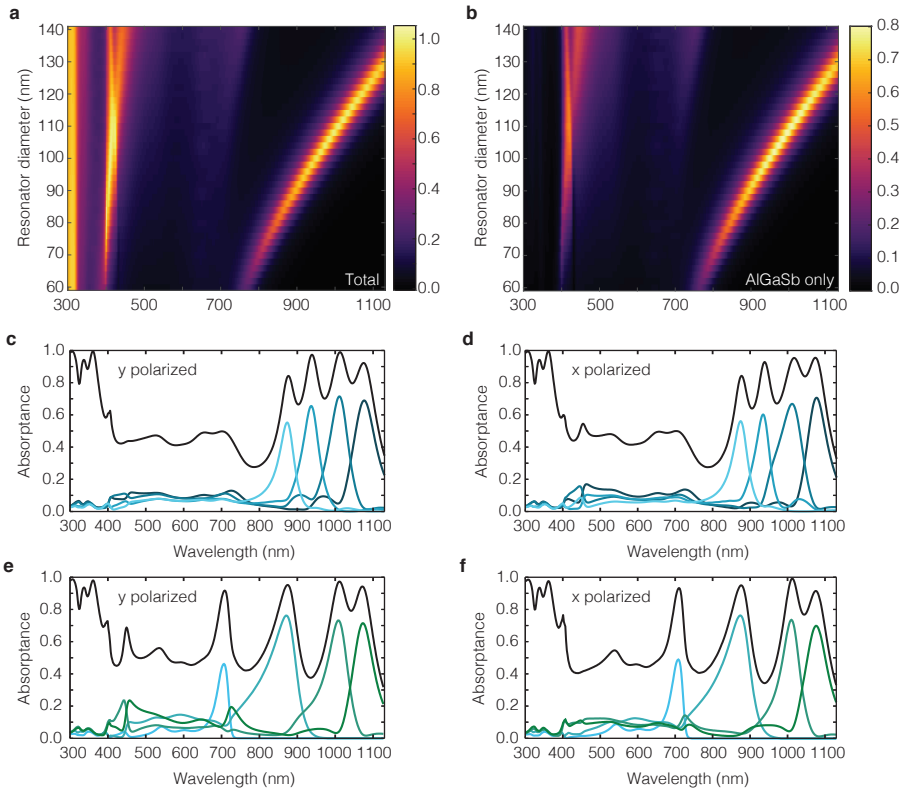

Figure 3.6: Full absorption spectra for the resonator arrays. a,b. Absorptance in the single resonator array (Fig. 3.2) as a function of diameter and wavelength in the total array (**a**) and in the semiconductor alone (**b**). **c,d.** Absorption over the full solar range for the AlGaSb resonator array, with the electric field polarized along the y (**c**) and x (**d**) directions, as shown in the schematic in Fig. 3.3a. **e,f.** Absorption over the full solar range for the resonator array comprising different materials, with the electric field polarized along the y (**e**) and x (**f**) directions (see Fig. 3.4a).

refractive index has few data points near the band gap (0.1 eV spacing), so we used the band gap reported in [152] as a hard cut off. A change in band gap only affects absolute numbers, and since we are mostly interested in relative enhancements, this does not change the conclusions of this chapter.

Fig. 3.6c,d show the full absorption spectra corresponding to Fig. 3.3 in the main text. Because in this case the array is no longer rotation symmetric, there are two polarizations that are described by the axis shown in the cartoon in Fig. 3.3a. As shown in Fig. 3.6 the spectra are slightly different, which is due to the difference between “closest particle" when the polarization is changed. For example, the 98 nm resonator (absorption in blue) seems to be affected more by the 110 nm res-

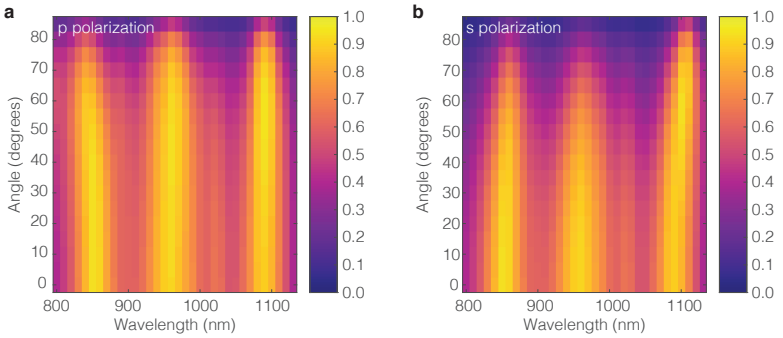

Figure 3.7: Angle dependence of absorption Absorption as a function of angle for p (**a**) and s (**b**) polarized light for an array with two 84 nm, one 104 and one 124 nm diameter resonators in the unit cell. The absorption is only affected by the angle of incidence if it is sufficiently large.

onator (absorption in green) when the polarization is perpendicular to the spacing in between them.

Similarly we have the full absorption spectrum for the multijunction array described in Fig. 3.4 in the main text, as shown in Fig. 3.6e,f. Again the difference in polarization is very small, and the majority of the current in each resonator is due to the resonance.

Angle dependence of absorption

To probe the angular response of our array we used the fourier modal method (S^4, [141]), because of its convenience for angular calculations. The absorption of an array of AlGaSb particles as a function of angle is shown in Fig. 3.7 for s and p polarizations. This particular array had two resonators with 84 nm diameter, one with 104 nm diameter and one with 124 nm diameter. The degenerate pair leads to full absorption at 780 nm, where a single resonator would not achieve this (see Fig. 3.6 in this Supporting Information).

Clearly the absorption only starts to deviate at angles larger than 80 degrees, which is consistent with literature reports on MIM resonators [147]. Calculating the difference in recombination rate using Eq. 3.3b in the main text we find that due to the increased reflection of the array at large angles the recombination rate in fact is reduced compared to a truly isotropic absorption spectrum, but only by 2.5%. Since the V_{oc} goes with the natural logarithm of the ratio of generation over recombination rate, this small decrease barely affects the results and can thus safely be ignored.

4

Photon recycling in nanostructured photovoltaics

The performance of a photovoltaic device with non-radiative recombination strongly depends on the probability that luminescence can escape the solar cell. While this escape probability is important, there is no known method to calculate it rigorously. Here we present such a method, based on the fluctuation-dissipation theorem, and apply it to a GaAs sphere. We demonstrate that the volume averaged escape probability can be at least 85% in a sphere with diameter of 230 nm, which is over 20 times higher than the escape probability in a planar layer. Furthermore, we demonstrate that in these semiconductors there can be a net benefit from the enhanced local density of states to the internal quantum efficiency. Overall, these results strengthen the case for nanophotonic photovoltaics.

4.1 Introduction

Optoelectronic devices such as light emitting diodes (LEDs) and solar panels rely on the emission of light for their efficient operation [162–164]. In a photovoltaic device, for example, the open circuit voltage (V_{oc}) depends on the external radiative efficiency (η_{ext}) [162, 163]:

$$V_{\mathrm{oc}} = V_{\mathrm{oc}}^{\mathrm{rad}} + \frac{k_B T}{q} \ln(\eta_{\mathrm{ext}}), \tag{4.1}$$

where k_B is Boltzmann's constant, T is the solar cell and ambient temperature, q is the electron charge, and $V_{\mathrm{oc}}^{\mathrm{rad}}$ is the V_{oc} in case all recombination events lead to a photon in the far field. η_{ext} is defined as the actual probability that a recombination event in the semiconductor leads to a photon in the far field, and thus reduces the V_{oc} from the limiting value $V_{\mathrm{oc}}^{\mathrm{rad}}$. It naturally depends on the internal quantum efficiency η_{int}, a material parameter that gives the fraction of recombination events that are radiative, but also on the probabilities that a photon escapes the solar cell, $\overline{p}_{\mathrm{esc}}$, or is reabsorbed inside the semiconductor, $\overline{p}_{\mathrm{abs}}$:

$$\eta_{\mathrm{ext}} = \frac{\eta_{\mathrm{int}}\overline{p}_{\mathrm{esc}}}{1-\eta_{\mathrm{int}}\overline{p}_{\mathrm{abs}}}, \tag{4.2}$$

where $\overline{p}_{\mathrm{abs}}$ and $\overline{p}_{\mathrm{esc}}$ are related through $\overline{p}_{\mathrm{abs}} + \overline{p}_{\mathrm{esc}} + \overline{p}_{\mathrm{par}} = 1$, with $\overline{p}_{\mathrm{par}}$ the parasitic absorption in *e.g.* a back reflector. In recent years there has been a lot of progress in theoretically understanding why high $\overline{p}_{\mathrm{esc}}$ are required [162, 164], and in implementing ways to achieve large external radiative efficiencies [130, 134, 165]. However, to date there is no rigorous method to calculate $\overline{p}_{\mathrm{esc}}$ and $\overline{p}_{\mathrm{abs}}$ directly.

In the ray optics regime, when the solar cell is large with respect to the wavelength of light, the emission and reabsorption processes are frequently modelled using the Lambert-Beer law [64, 65, 114, 130, 135, 166], but this approximation may not fully capture the near-field of the emission process, nor is it strictly correct when the local density of optical states (LDOS) varies with position such as near interfaces [118, 167, 168]. In the nanophotonic regime this approximation completely breaks down, because the LDOS variations become very strong and the reabsorption process no longer follows a Lambert-Beer law, but is strongly affected by *e.g.* guided modes and resonance field profiles.

Recently there has been significant process on the rigorous modeling of photovoltaic devices, even when the solar cell has subwavelength dimensions. The performance of a photovoltaic device is strongly connected to its thermal emission when it is in equilibrium with its surroundings. Niv *et al.* [113] realized that they could calculate this thermal emission even for complex structures by making use of the fluctuation-dissipation theorem, which connects the microscopic stochastic fluctuations of charges to averaged current densities. These current densities can then be used in conjunction with a Green's function for the structure to calculate the radiated electromagnetic fields. This approach fully takes into account the optical environment of the solar cell, including spatial variations in the LDOS, and the probability that photons are reabsorbed. As a result, this approach can in principle be used to determine η_{ext}, but it cannot separate the contribution arising from $\overline{p}_{\mathrm{esc}}$ and η_{int}. In the case that there is no parasitic absorption elsewhere in the solar cell ($\overline{p}_{\mathrm{par}} = 0$), the approach can be considerably simplified by invoking Kirchoff's law of thermal radiation [67].

Here, we extend the approach introduced by Niv. *et al.* to calculate the escape and reabsorption probabilities for photons originating from emission events at any position $\mathbf{r}$ in the solar cell. Furthermore, we can now calculate local variations in η_{int} due to variations in the LDOS. As a result we can gain insight into

the physical mechanisms that underly η_{ext}. We will first discuss the application of the fluctuation-dissipation theorem to calculate the external emission rate from a nanostructure, and then discuss how the total radiative recombination rate inside the semiconductor can be calculated. By comparing the two rates we find the escape probability, which we show can be as high as 85%, over 20 times the escape probability in a planar film. We then use this technique to disentangle the contributions from η_{int} and $\overline{p}_{\text{esc}}$ to η_{ext} in the same GaAs sphere, and show that η_{int} in the sphere can increase by a factor of 1.6 with respect to a homogeneous environment with the same quality material due to LDOS enhancements.

4.2 Thermal emission from semiconductor nanostructures

The maximum open-circuit voltage $V_{\text{oc}}^{\text{rad}}$ of a solar cell is intimately related to the rate R_0 at which the solar cell emits and absorbs photons when it is in thermal equilibrium with its surroundings:

$$V_{\text{oc}}^{\text{rad}} = \frac{k_B T}{q} \log\Big(\frac{G}{R_0}\Big). \tag{4.3}$$

Here G is the total generation rate due to solar insolation. The thermal emission rate R_0 is naturally related to the thermal electromagnetic fields emanating from the structure, which in turn originate from the chaotic thermal motion and spontaneous decay of charged particles. The connection between these stochastic microscopic processes and macroscopic electromagnetic fields is made by the fluctuation-dissipation theorem, which describes the stochastic processes as averaged current densities [115, 169, 170]. Using a Green's function for the structure of interest, and integrating over the volume of the semiconductor then allows calculation of *e.g.* the total emission rate R_0 [113]. More specifically, we can write for electric field at position $\mathbf{r}$ due to a current density $\mathbf{j}$ [118]:

$$\mathbf{E}(\mathbf{r}) = i\omega\mu_0 \int_{\mathcal{V}} \mathbf{G}(\mathbf{r},\mathbf{r}')\mathbf{j}(\mathbf{r}')\, d\mathcal{V}', \tag{4.4}$$

where the integral runs over the volume $\mathcal{V}$ that contains the sources and the thermal current density $\mathbf{j}$ is given by the fluctuation-dissipation theorem [115, 169, 170]:

$$\langle j_k(\mathbf{r},\omega)\, j_l^*(\mathbf{r}',\omega')\rangle = \frac{\omega\Theta(\omega,T,V)}{\pi} \operatorname{Im}\{\varepsilon\}\, \delta_{kl}\delta(\mathbf{r}-\mathbf{r}')\delta(\omega-\omega'). \tag{4.5}$$

Here the subscripts k and l refer to the dipole orientation, ε is the permittivity, and $\Theta(\omega,T)$ is the mean energy of the quantum oscillator [113, 142, 170]:

$$\Theta(\omega,T,V) = \frac{\hbar\omega}{e^{(\hbar\omega - qV)/k_B T} - 1} + \frac{\hbar\omega}{2}, \tag{4.6}$$

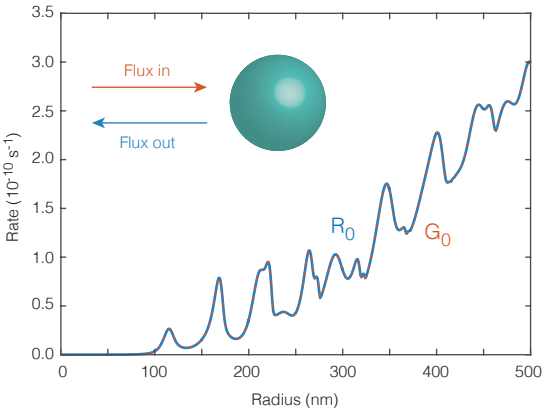

Figure 4.1: Thermal emission and absorption rates for a GaAs sphere. This figure shows the emission rate of a GaAs sphere calculated by integrating over the far field, using the fluctuation-dissipation theorem. We compare it to the absorption of photons due to black-body emission incident on the solar cell, using the absorption cross section of the sphere as calculated with Mie theory.

where qV is the chemical potential. In the following we will omit the zero point energy $\hbar\omega/2$, because ultimately we are interested in net fluxes at elevated potentials (non-equilibrium processes), to which the zero point energy does not contribute. From Eq. 4.5 it is clear that the thermal currents are uncorrelated in frequency, position, and orientation. Using Eq. 4.4 we can thus define an expression for the total emission rate:

$$R_0 = \iint \frac{\mathbf{S}(\mathbf{r},\omega)\cdot\hat{\mathbf{n}}}{\hbar\omega} d\omega dA = \frac{1}{2\eta}\iint \frac{|\mathbf{E}(\mathbf{r},\omega)|^2}{\hbar\omega} d\omega dA, \tag{4.7}$$

for $r \to \infty$. In this equation $\mathbf{S}(\mathbf{r},\omega)$ is the Poynting vector at position $\mathbf{r}$ for frequency ω, $\hat{\mathbf{n}}$ is the surface normal on the integration surface A, and η is the free space impedance. Further calculation details are given in the Supplementary Information, but for now it is mostly important to realize that the fields are evaluated *outside* the structure, while the sources are *inside* the structure: $\mathbf{r} \notin \mathcal{V}$.

Using Eq. 4.7 we can calculate the total emitted flux from a semiconductor body. As an exemplary system we calculate the rate of photon emission from a semiconductor sphere at $T = 300$ K and zero potential. This result is shown in Fig. 4.1, and shows clear correlation with resonances in the nanostructure: if the structure is resonant, the rate of thermal emission is enhanced.

Since we are describing a structure that is in thermal equilibrium with its surroundings, the rate of emission should be equal to the rate of absorption of thermal photons. We can calculate the rate at which photons are absorbed due to incident

black body radiation using:

$$G_0 = 4\pi \int_0^\infty \sigma_{\text{abs}}(\omega) \frac{\omega^2}{4\pi^3 c^2} \frac{1}{\exp(\hbar\omega / k_B T) - 1} d\omega, \tag{4.8}$$

where $\sigma_{\text{abs}}(\omega)$ is the absorption cross section of the sphere, and the fraction corresponds to the spectral photon flux in Planck's law for black body radiation. G_0 is also shown in Fig. 4.1, and indeed R_0 and G_0 are exactly equal. This also means that it is often much simpler to deduce the value of R_0 from G_0, than it is to calculate R_0 from first principles. This approach to determine the radiative recombination rate is therefore more frequently taken, such as in Chapter 2 in this thesis and in references [67, 68, 171]. However, it only works if there is no additional absorbing body present, because then only the total flux emanating from both bodies to the far field can be determined using Eq. 4.8. To find the emitted flux from one of the two bodies, the fluctuation-dissipation theorem has to be used. This for example holds for a solar cell with a slightly absorbing back contact, where we are only interested in the emission from the semiconductor [113]. Note that G_0 and R_0 are still equal also if the zero point energy is included [172].

4.3 Photon recycling

In the previous section we saw that the thermal emission of an absorbing body is governed by local thermal current densities inside that body. Since the body is absorbing, photons originating from any position within that absorbing body have a finite probability of escaping. We can quantify this by defining the radiative recombination rate per unit volume and unit frequency inside the absorbing body, $\Gamma_{\text{inj}}(\mathbf{r}, \omega)$. Here the subscript "inj" signifies the number of *injected* photons, which we want to distinguish from the photons that actually escape the absorbing body and are *radiated* to the far field:

$$\Gamma_{\text{rad}}(\mathbf{r}, \omega) = p_{\text{esc}}(\mathbf{r}, \omega) \Gamma_{\text{inj}}(\mathbf{r}, \omega), \tag{4.9}$$

where p_{esc} is the probability that a photon escapes the absorbing body. The emission rate density $\Gamma_{\text{rad}}(\mathbf{r}, \omega)$ is connected to the total emission rate R_{rad}, which we discussed in the previous section, *via*:

$$R_0 = \iint \Gamma_{\text{rad}}(\mathbf{r}, \omega) d\omega d\mathcal{V}, \tag{4.10}$$

where the volume integral runs over the absorbing body. An explicit equation for $\Gamma_{\text{rad}}(\mathbf{r}, \omega)$ in a spherical body is given in Eq. 4.41 in the Supplementary Information.

To calculate the escape probability p_{esc}, we thus need to know the rate of injection: $p_{\text{esc}} = \Gamma_{\text{rad}} / \Gamma_{\text{inj}}$. To find the total power radiated by a dipole one commonly evaluates the Green's function at the source position $\mathbf{r}$ [118]:

$$P = \frac{\omega}{2} \mathbf{p}^\dagger \text{Im}\{\mathbf{G}(\mathbf{r}, \mathbf{r})\} \mathbf{p}, \tag{4.11}$$

where $\mathbf{p}$ is the dipole moment. Calculating the total radiated power in this way is particularly important if the dipole is located near an absorbing structure, as an integral over the far field power (as in Eq. 4.5) then does not yield the total radiated power, but the radiated power minus the absorbed power. Note that we are now required to evaluate the Green's function at the source position, and no longer outside of the emitting body. In lossless media this is no problem: evaluating Eq. 4.11 yields $\mathrm{Im}\{\mathbf{G}(\mathbf{r},\mathbf{r})\} = (k/6\pi)\mathbf{I}$ if the medium is homogeneous, and in lossless heterogeneous media this value is affected by the local density of optical states [173]. However, when the medium hosting the dipole itself is lossy, the imaginary part of the Green's function diverges at the source position (see Supplementary Information).

To resolve this we will consider the decay process in more detail. Using the Helmholtz decomposition any vector field $\mathbf{F}$ can be decomposed into a component that has no divergence and a component that has no rotation, $\mathbf{F}(\mathbf{r}) = \mathbf{F}^{\perp}(\mathbf{r}) + \mathbf{F}^{\parallel}(\mathbf{r})$. We call these the longitudinal and transverse components [174]:

$$\nabla \cdot \mathbf{F}^{\perp}(\mathbf{r}) = 0, \tag{4.12a}$$

$$\nabla \times \mathbf{F}^{\parallel}(\mathbf{r}) = 0. \tag{4.12b}$$

In the Green's function the divergence at the source position is contained in the longitudinal part $\mathbf{G}^{\parallel}$, which in lossless materials is purely real and therefore does not affect $\mathrm{Im}\{\mathbf{G}(\mathbf{r},\mathbf{r})\}$. However, spontaneous emission events are associated with the *transverse* electromagnetic fields [175, 176], for which we only need to consider the transverse Green's function $\mathbf{G}^{\perp}$. For the decay rate in a lossy medium, one then finds $\mathrm{Im}\left\{\mathbf{G}^{\perp}(\mathbf{r},\mathbf{r})\right\} = (\mathrm{Re}\{k\}/6\pi)\mathbf{I}$ [177].

In the Supplementary Information we outline how to find the transverse Green's function in spherical harmonics, but to find $\Gamma_{\mathrm{inj}}(\mathbf{r},\omega)$ we actually do not need the full transverse Green's function. Instead, we will make use of a proof that considerably simplifies the procedure to calculate $\Gamma_{\mathrm{inj}}(\mathbf{r},\omega)$. The total Green's function in an inhomogeneous environment is given by:

$$\mathbf{G}(\mathbf{r},\mathbf{r}') = \mathbf{G}_{\mathrm{h}}(\mathbf{r},\mathbf{r}') + \mathbf{G}_{\mathrm{s}}(\mathbf{r},\mathbf{r}'), \tag{4.13}$$

where $\mathbf{G}_{\mathrm{h}}$ is the homogeneous Green's function and $\mathbf{G}_{\mathrm{s}}$ is the scattered Green's function due to the presence of heterogeneities. To find the transverse Green's function we can thus subtract the longitudinal part from the total Green's function, which allows us to make use of the following identity [178]:

$$\mathbf{G}^{\parallel}(\mathbf{r},\mathbf{r}') = \frac{\varepsilon_h}{\varepsilon(\mathbf{r})}\mathbf{G}_h^{\parallel}(\mathbf{r},\mathbf{r}'), \tag{4.14}$$

where ε_h is the permittivity corresponding to $\mathbf{G}_h$ and $\varepsilon(\mathbf{r})$ is the piecewise constant permittivity. Eq. 4.14 states that the longitudinal Green's function is not affected by

heterogeneities, except for a factor given by the permittivities. Using this identity we can write for the transverse Green's function at the source position **r**:

$$\mathbf{G}^{\perp}(\mathbf{r},\mathbf{r}) = \mathbf{G}_{\mathrm{h}}^{\perp}(\mathbf{r},\mathbf{r}) + \mathbf{G}_{\mathrm{s}}(\mathbf{r},\mathbf{r}). \tag{4.15}$$

This simplifies the evaluation of $\mathrm{Im}\left\{\mathbf{G}^{\perp}(\mathbf{r},\mathbf{r})\right\}$, since:

$$\mathrm{Im}\left\{\mathbf{G}^{\perp}(\mathbf{r},\mathbf{r})\right\} = \mathrm{Im}\left\{\mathbf{G}_{\mathrm{h}}^{\perp}(\mathbf{r},\mathbf{r}) + \mathbf{G}_{\mathrm{s}}(\mathbf{r},\mathbf{r})\right\} = \frac{\mathrm{Re}\{k\}}{6\pi}\mathbf{I} + \mathrm{Im}\{\mathbf{G}_{\mathrm{s}}(\mathbf{r},\mathbf{r})\}. \tag{4.16}$$

Hence, we do not need $\mathbf{G}^{\parallel}$ explicitly to find Γ_{inj}. To demonstrate, we will now compare Γ_{inj} to Γ_{rad} in a GaAs sphere.

4.3.1 Internal and external luminescence spectrum

We show the injected rate density of photons originating from the center of a 115 nm radius GaAs sphere in Fig. 4.2a, in blue. A fraction of these photons will be escape the absorbing sphere and make it to the far-field, which shown in orange. A red-shift of the peak value is observed due to stronger reabsorption at shorter wavelengths. Note that these rates are markedly different from those in a homogeneous environment, which is given by the van Roosbroeck-Shockley equation [179]. This demonstrates how important it is to take into account the full optical environment of the material.

In Fig. 4.2b we show the escape probability p_{esc} for photons originating from the center of the 115 nm radius sphere (solid, blue) and the 221 nm sphere (solid, green). In both cases the escape probability increases to 1 for wavelengths at the band gap, where the absorption coefficient vanishes. For the larger radius the escape probability is generally lower, which may just be due to the larger size of the absorbing body, but could also be due to properties of the specific resonances that are excited by the recombination events.

To emphasize again the importance of taking into account the full optical environment of the semiconductor body, we also calculated p_{esc} but using the van Roosbroeck-Shockley equation for the injected power. This equation thus assumes that the medium is homogeneous, and ignores variations in the local density of optical states. The resulting curves are shown as dashed blue and green curves for the 115 and 221 nm spheres respectively, and either severely overestimate or underestimate the actual p_{esc}. In fact, for the 115 nm sphere, this naive calculation of p_{esc} leads to values above 1 over all wavelengths, which is unphysical without gain.

4.3.2 Spatial dependence of reabsorption

Fig. 4.2c shows the total per unit volume rates of injection and emission in the same two spheres as a function of position along the radius. This is the integrated

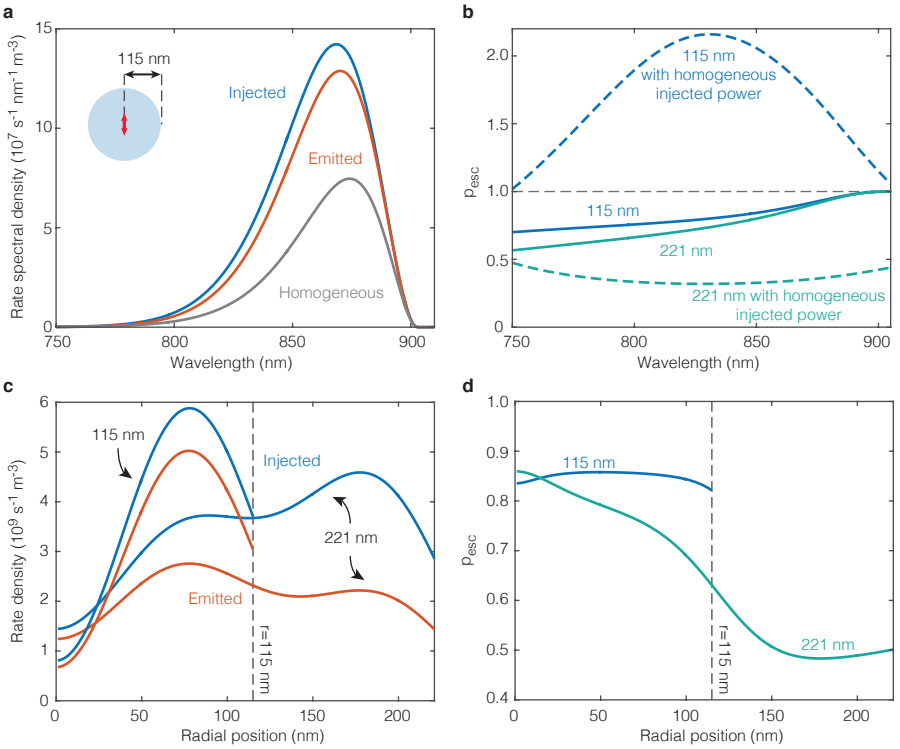

Figure 4.2: Emission and reabsorption in a GaAs sphere. a. The emission rate per unit volume and unit frequency Γ_{rad} for photons originating from recombination events at the center of a GaAs sphere (orange), compared to the rate density Γ_{inj} that is injected at the center of the sphere (blue). The injected spectrum in a homogeneous medium is shown in gray for comparison, highlighting the difference due to the nanophotonic nature of the sphere. **b.** The probability that a photon emitted in the center escapes the sphere, calculated by dividing the far field emitted spectrum by the injected spectrum in panel **a** (solid lines). The dashed lines show the same calculation, but using the homogeneous spectrum in panel **a**. This results in erroneous estimates of p_{esc}, emphasizing the importance of taking into account the full optical environment. **c.** The injection and emission rate densities r_{inj} and r_{rad} as a function of position inside the sphere, for the 115 and 221 nm radius spheres. **d.** The escape probability as a function of position for both spheres, demonstrating very large values.

emission over the spectra in Fig. 4.2a:

$$r_{\text{inj}}(\mathbf{r}) = \int \Gamma_{\text{inj}}(\mathbf{r},\omega)\,d\omega \tag{4.17a}$$

$$r_{\text{rad}}(\mathbf{r}) = \int \Gamma_{\text{rad}}(\mathbf{r},\omega)\,d\omega. \tag{4.17b}$$

Clear "hot spots" of emission are visible along the radius, corresponding to the field profiles of resonances supported by the sphere. The lowest order resonance, supported by the 115 nm sphere, has a single field intensity maximum in the radial direction. The resonance supported by the 221 nm sphere is of higher order, and supports two peaks in the radial direction.

The ratio of the emitted and injected rate densities gives the local photon escape probability averaged over frequency, $\overline{p}_{\mathrm{esc},\omega}$. This probability is shown in Fig. 4.2d for both spheres as a function of position along the radius of the sphere. For the small sphere the escape probability is almost constant over the size of the sphere, and approximately 85%. This is very high, especially compared to planar semiconductors, and provides evidence that nanophotonic structures may benefit the V_{oc} by enabling efficient outcoupling of light. Interestingly, while in the larger sphere the probability of escape is still large, it decreases instead of increases as the emitter approaches the interface. This is because there is a second higher order resonance in the same spectral window of emission, which is strongly confined to the interface. This resonance radiates less strongly, as it is most likely overdamped and therefore leads to larger reabsorption of injected power [126].

4.4 The total escape probability

We will now discuss the total escape probability as a function of sphere radius. Assuming again that the sphere is in equilibrium, we can define the escape probability averaged over frequency *and* volume as:

$$\overline{p}_{\mathrm{esc}} = \frac{R_0}{R_{\mathrm{inj}}}. \tag{4.18}$$

Here R_0 is the total emission rate in equilibrium as calculated with Eq. 4.7, and R_{inj} is given by:

$$R_{\mathrm{inj}} = \iint \Gamma_{\mathrm{inj}}(\mathbf{r},\omega)\, d\omega\, d\mathcal{V}. \tag{4.19}$$

Although for simplicity we assume that the sphere is in thermal equilibrium and $V = 0$, this equation for p_{esc} is in fact valid as long as the potential V is constant throughout the absorbing body. This is because the potential in Eq. 4.6 only scales the magnitude of recombination processes and therefore divides out in $\overline{p}_{\mathrm{esc}}$. We will briefly discuss situations with spatially varying potentials in Section 4.5.

Fig. 4.3 shows $\overline{p}_{\mathrm{esc}}$ as a function of sphere radius, together with dashed lines indicating the presence of a resonance. The escape probability increases at lower order resonances, but for larger sphere sizes the correlation between resonance and escape probability becomes more complicated. This is most likely due to the excitation of overdamped resonances that do not radiate well, as also seen in the previous section.

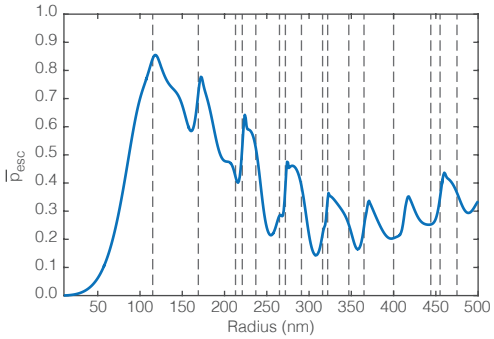

Figure 4.3: Total escape probability in a GaAs sphere. This figure shows the escape probability of thermal radiation in a GaAs sphere, which is characterized by a constant carrier density throughout the sphere. The vertical dashed lines correspond to peaks in the total emission shown in Fig. 4.2. The escape probability peaks at a value of 85%, which corresponds to the first resonance in the sphere. However, at larger sphere sizes the correlation between resonances and the escape probability is more complicated, and sometimes the presence of a resonance significantly reduces the escape probability. At very small sphere sizes $\overline{p}_{\text{esc}}$ is severely underestimated, so this curve should be interpreted as a lower bound on $\overline{p}_{\text{esc}}$.

For very small sizes, $\overline{p}_{\text{esc}}$ tends to zero. Mathematically this originates from the divergence of $\mathbf{G}_h$ near the source position, which affects $\mathbf{G}_s$ even though we removed $\mathbf{G}_h^{\parallel}$ through Eq. 4.16. In fact:

$$\lim_{a\to 0}\Big(\text{Im}\{\mathbf{G}_s(\mathbf{r},\mathbf{r},a)\}\Big) = \infty, \tag{4.20}$$

where a is the sphere radius and $\mathbf{r}$ lies inside the sphere. This divergence is also known, and is usually interpreted as non-radiative energy transfer from emitter to absorber in the case that a single atom is embedded in an absorbing medium [180]. However, as the emitter and absorber in this case are the same, it is not immediately clear how to interpret this contribution with regards to the decay rate. However, to find only the radiative injection rate, $\text{Im}\{\mathbf{G}_s(\mathbf{r},\mathbf{r},a)\}$ can be expanded in powers of a for small a. The term independent of a is finite and exactly corresponds to the emitted flux, suggesting that actually the escape probability tends to 1, not 0, for small sizes. This is also the more intuitive result, and the $\overline{p}_{\text{esc}}$ in Fig. 4.3 should therefore be taken as a lower bound on $\overline{p}_{\text{esc}}$.

4.4.1 Internal and external radiative efficiency

As we saw in the previous sections, the radiative recombination rate depends strongly on its environment [118]. This is known to affect the quantum yield of many systems, including atoms [181], molecules [23, 182], quantum dots [28, 183],

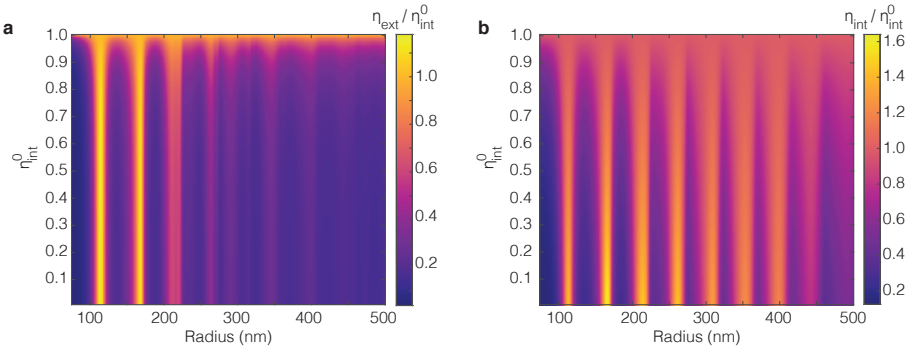

Figure 4.4: The external and internal quantum efficiencies of radiation. a. η_{ext} as a function of the internal quantum efficiency in a homogeneous medium, η^0_{int}, and the sphere radius. η_{ext} can actually exceed η^0_{int} due to enhancements in the LDOS, despite the probability that photons are reabsorbed. **b.** η_{int} as a function of η^0_{int} and the sphere radius, demonstrating that indeed η_{int} reaches values over 1.6 η^0_{int}. For high η^0_{int} the fluctuations in both η_{int} and η_{ext} vanish, as both also tend to 1.

2D materials [154, 155], and semiconductors [184]. We can write for the volume averaged probability that a recombination event is radiative:

$$\eta_{int} = \frac{\overline{\gamma} r^0_{inj}}{\overline{\gamma} r^0_{inj} + r_{nrad}}, \tag{4.21}$$

where r^0_{inj} is the injection rate density in the homogeneous medium and r_{nrad} is the non-radiative recombination rate density. We define $\overline{\gamma}$ as the volume averaged LDOS enhancement with respect to the LDOS in the homogeneous medium, $\overline{\gamma} = \langle\rho\rangle/\rho_\infty$. The probability that, out of *all* recombination events, a photon makes it to the far field is then given by η_{ext}:

$$\eta_{ext} = \frac{\overline{p}_{esc}\overline{\gamma}\eta^0_{int}}{1 + (\overline{p}_{esc}\overline{\gamma} - 1)\eta^0_{int}}. \tag{4.22}$$

Here we have assumed that there is no parasitic absorption ($\overline{p}_{par} = 0$), and η^0_{int} is the internal quantum yield corresponding to a homogeneous medium ($\overline{\gamma} = 1$). While in principle η_{ext} can be calculated using existing approaches, it was not possible to discern between enhancements in η_{int} and $\overline{p}_{esc}$. Here we investigate how η_{ext} changes with changing sphere radius, and to what degree this is due to changes in η_{int} and $\overline{p}_{esc}$. The external radiative efficiency is shown in Fig. 4.4a as a function of η^0_{int} and sphere radius, also normalized to η^0_{int}. Interestingly, η_{ext} is seen to exceed η^0_{int} by a factor of almost 1.2 at the two lowest order resonances. This indicates that even semiconductor structures that exhibit photon recycling, such as this GaAs

sphere, can benefit from enhancements in η_{int} through LDOS enhancements. This LDOS enhancement is crucial, because enhancements in $\overline{p}_{\text{esc}}$ alone could never lead to $\eta_{\text{ext}}/\eta_{\text{int}}^0$ above one. In fact, using Eq. 4.22 we can make the requirement on $\overline{\gamma}$ to achieve $\eta_{\text{ext}} > \eta_{\text{int}}^0$ explicit:

$$\eta_{\text{ext}} > \eta_{\text{int}}^0 \quad \text{for} \quad \overline{\gamma} > \frac{1}{\overline{p}_{\text{esc}}}. \tag{4.23}$$

In Fig. 4.3 we show η_{int} as a function of sphere radius. Again clear enhancements are seen, correlating with the lowest order resonances. We omitted small radii due to the underestimation of $\overline{p}_{\text{esc}}$, which would lead to unrealistically high enhancements of η_{int}. However, even at larger radii the quantum efficiency enhancements are significant, reaching values over 1.6. At very high η_{int}^0 the effect vanishes both in η_{ext} and η_{int}, as in this case photon recycling barely leads to increased non-radiative recombination. In the limit of $\eta_{\text{int}}^0 = 1$, we therefore also find $\eta_{\text{ext}} = \eta_{\text{int}} = 1$.

At very low η_{int}^0, the enhancement factor approaches $\overline{\gamma}$, which in this case is thus at most slightly over 1.6. It is interesting to compare the LDOS enhancements we see here with the LDOS enhancements that we observed for the GaAs sphere in Fig. 2.2c on page 30. In that case the LDOS enhancements were much higher, in particular for higher order resonances, but we see here that these higher order resonances are in fact severely damped due to the presence of absorption losses. This difference emphasizes the importance of taking into account the absorption losses in the semiconductor.

4.5 Application to solar cell modelling

Modelling a solar cell is a complicated task, because the charge carriers in a photovoltaic device are subject to various currents, generation rates, and recombination rates. For example, writing the continuity equation for the electron density [166]:

$$\frac{\partial n}{\partial t} = \frac{1}{q}\nabla \cdot \mathbf{J} + g_{\text{th}} + g_{\text{nr}} + g_{\text{s}} + g_{\text{pr}}(V) - r_{\text{nr}}(V) - r_{\text{rad}}(V). \tag{4.24}$$

Here $\mathbf{J}$ is the current density, g_{th}, g_{s}, and g_{pr} are the generation rate densities due to thermal radiation from the surroundings, due to sunlight, and due to reabsorption of photons following a recombination event elsewhere, respectively. g_{nr} is the generation rate density due to non-radiative processes (such as impact ionization), and r_{nr} is the non-radiative recombination rate density. Finally, r_{rad} is the radiative recombination rate density, given by Eq. 4.17b. Some of these processes are schematically shown in Fig. 4.5.

To solve Eq. 4.24 some simplifying assumptions have to be made. As we mentioned in the introduction of this chapter, $r_{\text{rad}}(V)$ and $g_{\text{pr}}(V)$ can be approximated by assuming that the recombination rate is given by the van Roosbroeck-Shockley

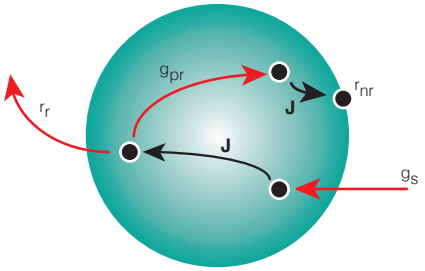

Figure 4.5: Schematic depiction of microscopic processes in a semiconductor. In a semiconductor body under solar irradiation charges are photogenerated, which may then diffuse and recombine. This recombination can be radiative r_r, resulting in either an escaped photon, or a recycling event, where it reincarnates as a new electron-hole pair (g_{pr}). This recombination may also be non-radiative (r_{nr}), *e.g.* due to surface recombination, in which case the recombination event leads to heat.

equation for an infinite medium [179], and that the reabsorption process is governed by Lambert-Beer type behavior [64, 65, 114, 130, 135, 166]. Alternatively, one can also assume that the charge carrier density is constant throughout the entire device, not only in thermal equilibrium but also at elevated potentials V. As we mentioned earlier in this chapter, due to this assumption local processes do not have to be taken into account anymore, and the solar cell performance can be evaluated based solely on total rates. This assumption is frequently made, for example by Shockley and Queisser in their derivation of the detailed balance limit [7], but also by Niv *et al.* and others [67, 113, 135].

With the approach we presented in this Chapter, we can now calculate g_{pr} and r_{rad} without assuming Lambert-Beer type behavior, and therefore in complex photonic environments. This enables investigating *e.g.* the role that photon recycling can take in charge transport in nanophotonic structures, which can be an important factor in materials with a high internal quantum efficiency [185]. Furthermore, deviations from a constant charge carrier density can be investigated numerically, which may offer important insights for practical nanophotonic devices.

4.6 Conclusion and discussion

In this chapter we demonstrated an approach to evaluate the radiative recombination rates inside a semiconductor, so that the probability that a photon escapes can be calculated. Likewise, our approach also yields the photon recycling probability. These probabilities has important consequences for the ultimate performance of a photovoltaic device, as well as for carrier transport through the device. We find that both the radiative recombination rate and the recycling probability in a GaAs

sphere depend strongly on position, and that the net external radiative efficiency of such a sphere may actually be larger than the internal radiative efficiency of the same medium when infinitely extended. This confirms that nanophotonics has great potential to improve photovoltaic devices: not only can nanostructures lead to very high escape probabilities (we observed $\overline{p}_{\mathrm{esc}} > 0.8$), the η_{int} can be enhanced at the same time.

For future work it is important to further investigate the divergence at very small sphere sizes, and exactly how this diverging contribution to the total decay rate should be interpreted. Furthermore, using the presented approach it is interesting to investigate quantitatively how charge carrier transport is affected by photon recycling. Once a spatial distribution of reabsorption probabilities as a function of emission locations is obtained, this can also be used to investigate regimes where the potential is not constant throughout the device, by numerically solving the charge continuity equations. Additionally, the emission and reabsorption probabilities can be disentangled into the different dipole moment orientations, which may offer more insight in the interaction with resonances.

4.7 Supplementary Information

4.7.1 Dipoles in lossy media

The power injected by a dipole is proportional to $\mathrm{Im}\{G(\mathbf{r},\mathbf{r})\}$ at the source position $\mathbf{r}$, as given in Eq. 4.11. To investigate what happens in a medium with complex refractive index we consider the homogeneous Green's function, given by [118]:

$$\mathbf{G_h}(\mathbf{r},\mathbf{r}') = \frac{\exp(ikR)}{4\pi R}\left(\left(1+\frac{ikR-1}{k^2R^2}\right)\mathbf{I}+\frac{3-3ikR-k^2R^2}{k^2R^2}\frac{\mathbf{R}\otimes\mathbf{R}}{R^2}\right), \tag{4.25}$$

with $\mathbf{R} = \mathbf{r}-\mathbf{r}'$, $R = ||\mathbf{R}||$, and $\mathbf{I}$ the identity matrix. To evaluate this function at the source position, we consider the xx component of the Green's function and choose the dipole positioned at the origin, so that we can take the limit $R \to 0$ as $x \to 0$:

$$\mathbf{G}_{xx}(x,0) = \frac{\exp(ikx)}{4\pi x}\left(1+\frac{ikx-1}{k^2x^2}+\frac{3-3ikx-k^2x^2}{k^2x^2}\right) \tag{4.26}$$

$$= \frac{\exp(ikx)}{4\pi x}\left(\frac{2-2ikx}{k^2x^2}\right). \tag{4.27}$$

This still diverges, so to obtain a useful value we use the series expansion of the exponent $[\exp(ikx) = 1+ikx+(1/2)(ikx)^2+(1/6)(ikx)^3+\cdots]$, and obtain for very small x:

$$\mathbf{G}_{xx}(x,0) = \frac{1}{4\pi}\left(\frac{2ik}{3}+\frac{2}{k^2x^3}+\frac{1}{x}-\frac{k^2x}{3}\right). \tag{4.28}$$

Now, only the real part diverges, and we find for the imaginary part of the Green's function:

$$\mathrm{Im}\{\mathbf{G}(\mathbf{r},\mathbf{r})\} = \frac{k}{6\pi}\mathbf{I}. \tag{4.29}$$

However, this is only true if $k \in \mathbb{R}$. For materials with a complex index of refraction, $\tilde{n} = n + i\kappa$, we see from Eq. 4.28 that the imaginary and real parts of the Green's function become mixed. The divergence that in lossless media is contained in the real part now bleeds into the imaginary part, which therefore diverges as well. This problem can be averted by considering only the transverse Green's function, as we will see next.

The transverse Green's function

The Green's function can be split into its longitudinal and transverse parts, which have no curl and divergence respectively (see Eqs. 4.30). These can be found for example through reciprocal space [174, 177, 186]:

$$\begin{aligned}\mathbf{G}_h^{\perp}(\mathbf{r},\mathbf{r}') = \frac{\exp(ikR)}{4\pi R}\Bigg(\Bigg(\mathbf{I} - \frac{\mathbf{R}\otimes\mathbf{R}}{R^2}\Bigg) \\ + \Bigg(\Big(\frac{i}{kR^2} - \frac{1}{k^2R^3}\Big)\frac{\exp(ikR)}{4\pi} + \frac{1}{4\pi k^2R^3}\Bigg)\Bigg(\mathbf{I} - 3\frac{\mathbf{R}\otimes\mathbf{R}}{R^2}\Bigg)\end{aligned} \tag{4.30a}$$

$$\mathbf{G}_h^{\parallel}(\mathbf{r},\mathbf{r}') = -\frac{1}{3k^2}\delta(R) + \frac{1}{4\pi k^2R^3}\Bigg(3\frac{\mathbf{R}\otimes\mathbf{R}}{R^2} - \mathbf{I}\Bigg). \tag{4.30b}$$

Here it is immediately clear that the longitudinal Green's function is real for real k and diverges for $R \to 0$. For the transverse Green's function we can follow the same procedure as before, by assuming a source at $\mathbf{R} = \mathbf{0}$ and evaluating the function at position x:

$$\mathbf{G}_{xx}^{\perp}(x,0) = \frac{1}{4\pi}\Bigg(\frac{1}{k^2x^3} + \exp(ikx)\frac{k^2x^2 + ikx - 1}{k^2x^3}\Bigg). \tag{4.31}$$

Again expanding the exponent near the origin, we find:

$$\mathbf{G}_{xx}^{\perp}(x,0) \approx \frac{3 + 2ikx - k^2x^2}{12\pi x}. \tag{4.32}$$

This enables us to calculate the limit for $x \to 0$:

$$\lim_{x\to 0}\Big(\mathrm{Im}\left\{\mathbf{G}_{xx}^{\perp}(0,x)\right\}\Big) = \frac{\mathrm{Re}\{k\}}{6\pi}. \tag{4.33}$$

4.7.2 Green's function for spheres

The Green's function for dipoles in the vicinity of spheres can be constructed from spherical harmonics that form a complete basis. Examples are given in the classic text books by Chew or Tai [187, 188], but in both cases they comprise even and odd harmonics that together form a complete basis. It is also possible to form a complete basis with a single harmonic that is summed over positive and negative indices. We will use this approach here, as it requires less terms and is therefore easier to implement. The solution to the scalar wave equation is given by:

$$\psi(r,\theta,\phi) = z_n(kr)P_n^{|m|}(\cos(\theta))e^{im\phi}, \tag{4.34}$$

where z_n is the Bessel j_n or Hankel $h_n^{(1)}$ function, and P_n^m is the Legendre polynomial. The vector spherical harmonics are then formed using:

$$\mathbf{M} = \nabla \times (\mathbf{r}\psi) \tag{4.35a}$$

$$\mathbf{N} = \frac{1}{k}\nabla \times \mathbf{M}. \tag{4.35b}$$

The Green's function is then given by:

$$\mathbf{G}_h(\mathbf{r},\mathbf{r}') = -\frac{\delta(R)}{k^2}(\hat{r}\otimes\hat{r}) + \frac{ik}{4\pi}\sum_{n=1}^{\infty}\sum_{m=-n}^{n} C_{nm}\Big(\mathbf{M}_{n,m}^{(1)}\otimes\mathbf{M}'_{n,-m} + \mathbf{N}_{n,m}^{(1)}\otimes\mathbf{N}'_{n,-m}\Big), \tag{4.36}$$

where the superscript (1) means that $h_n^{(1)}$ is the radial function, and without superscript j_n is the radial function. This particular expression is valid for $r > r'$, to find the expression for $r < r'$ the radial functions should be switched. The prime denotes that this harmonic is the harmonic for the source position $\mathbf{r}'$. The normalization constant C_{nm} is given by:

$$C_{nm} = \frac{2n+1}{n(n+1)}\frac{(n-|m|)!}{(n+|m|)!}. \tag{4.37}$$

The scattered Green's function outside of the sphere can be found following the procedure in Tai [187], and the scattered field coefficients A_n and B_n are the same in both formalisms:

$$\mathbf{G}_s(\mathbf{r},\mathbf{r}') = \frac{ik_2}{4\pi}\sum_{n=1}^{\infty}\sum_{m=-n}^{n} C_{nm}\Big(A_n\mathbf{M}_m^{(1)}\otimes\mathbf{M}'_{-m} + B_n\mathbf{N}_m^{(1)}\otimes\mathbf{N}'_{-m}\Big), \tag{4.38}$$

where k_2 is the wavenumber in the source medium.

The radiated power density

Here we will now derive a direct expression for Γ_{rad} which does not require integrating over a spherical surface in the far field. Because the thermal current densities

are uncorrelated spatially, in frequency, and in dipole orientation, we can write:

$$\Gamma_{\mathrm{rad}}(\mathbf{r}',\omega) = \frac{\mu_0\omega}{2\hbar c}\sum_{k,l}\int_A \mathbf{G}_{kl}(\mathbf{r},\mathbf{r}')\langle j_l(\mathbf{r}')\, j_l^*(\mathbf{r}')\rangle \mathbf{G}_{lk}^{\dagger}(\mathbf{r},\mathbf{r}')\, d\mathbf{r}. \tag{4.39}$$

Here we integrate $\mathbf{r}$ over the far field to obtain the radiated power due to current densities at $\mathbf{r}'$. In Eq. 4.39 we have already taken into account the delta functions in Eq. 4.5, but we can can simplify the equation further inserting the rest of Eq. 4.5:

$$\Gamma_{\mathrm{rad}}(\mathbf{r}',\omega) = \frac{\mu_0\omega^2}{2\pi\hbar c}\Theta(\omega,T)\mathrm{Im}\{\varepsilon\}\int_A \mathrm{Tr}\Big(\mathbf{G}(\mathbf{r},\mathbf{r}')\mathbf{G}^{\dagger}(\mathbf{r},\mathbf{r}')\Big)d\mathbf{r}. \tag{4.40}$$

To integrate this expression over the far field we can make use of the orthogonality of the vector harmonics [187]. This allows us to find a direct expression for the rate density $\Gamma_{\mathrm{rad}}(\mathbf{r}',\omega)$ which just requires summing over the scattered field coefficients:

$$\Gamma_{\mathrm{rad}}(\mathbf{r}',\omega) = \frac{\omega^2\mu_0|n|^2}{2\hbar c}\mathrm{Im}\{\varepsilon\}\,\Theta(\omega,T)\times \sum_{n=1}^{\infty}\sum_{m=-n}^{n} C_{nm}\Big(|A_n|^2\mathbf{M}'_{n,m}\cdot\mathbf{M}'^{*}_{n,m} + |B_n|^2\mathbf{N}'_{n,m}\cdot\mathbf{N}'^{*}_{n,m}\Big). \tag{4.41}$$

Integrating this expression over the volume of the sphere and all frequencies yields the total emission rate R_{rad}. The local dependence of the emitted power $r_{\mathrm{rad}}(\mathbf{r}')$, shown in Fig. 4.2, is calculated by integrating the equation above only over frequency.

The longitudinal Green's function

To find the transverse Green's function it is most convenient to subtract the longitudinal one from the total Green's function, which we gave in the previous section. We need the longitudinal Green's function as an expansion of vector harmonics. A general equation is given by Howard [189]:

$$\mathbf{G}^{\parallel}(\mathbf{r},\mathbf{r}') = -\frac{\nabla\nabla'}{k^2}g(\mathbf{r},\mathbf{r}'). \tag{4.42}$$

Here g is the electrostatic Green's function [190]:

$$g(\mathbf{r},\mathbf{r}') = \sum_{n=1}^{\infty}\sum_{m=-n}^{n}\frac{1}{2l+1}C_{nm}Y_{nm}^{*}(\theta',\phi')Y_{nm}(\theta,\phi)\frac{(r')^n}{r^{(n+1)}}. \tag{4.43}$$

The angular functions Y_{nm} are given by:

$$Y_{nm}(\theta,\phi) = P_n^m(\cos(\theta))e^{im\phi}. \tag{4.44}$$

5

Integrating sphere microscopy for direct absorption measurements of single nanostructures

Nanoscale materials are promising for optoelectronic devices because their physical dimensions are on the order of the wavelength of light. This leads to a variety of complex optical phenomena, that for instance enhance absorption and emission. However, quantifying the performance of these nanoscale devices frequently requires measuring absolute absorption at the nanoscale and, remarkably, there is no general method capable of doing so directly. Here we present such a method based on an integrating sphere, but modified to achieve diffraction-limited spatial resolution. We explore the limits of this technique by using it to measure spatial and spectral absorptance profiles on a wide variety of nanoscale systems including different combinations of weakly and strongly absorbing and scattering nanomaterials (Si and GaAs nanowires, Au nanoparticles). This measurement technique provides quantitative information about local optical properties that are crucial for improving any optoelectronic device with nanoscale dimensions or nanoscale surface texturing.

5.1 Introduction

A number of techniques to measure quantitative absorptance on single nanostructures exist [90–92], such as photothermal spectroscopy [88, 106, 107, 191], (spatial modulation) extinction spectroscopy [94, 99, 102], and scattered field interferometry [89]. Although some of these techniques are extremely sensitive and can even measure single molecules [87], they also rely on at least one of the following assumptions: all absorbed power is converted into heat, the nanoparticle doesn't scatter light, or it interacts with light as an ideal dipole. Hence, to date there is no generally applicable method available for quantitative absorption measurements of nanostructures, even though for instance nanostructured semiconductor and plasmonic hot-electron optoelectronic devices [192, 193] require such a technique to quantify their performance.

Here we show that by combining an integrating sphere with an ultra-long working distance microscope objective, we can achieve submicron spatial resolution inside the integrating sphere. As a result, quantitative local absorptance measurements can be obtained, even on single nanostructures. In this chapter we detail the working mechanism and explore the limits of integrating sphere microscopy using weakly absorbing but strongly scattering structures (a silicon nanowire and a large gold nanoparticle), a weakly absorbing and weakly scattering structure (a small gold nanoparticle), and a strongly absorbing and strongly scattering structure (a GaAs nanowire). Additionally, we demonstrate the spatial resolution with absorption maps on a highly tapered nanowire where resonances can be seen moving along the length as a function of wavelength.

5.2 Integrating sphere microscopy

Single nanoparticle spectroscopy relies on illumination with a focused beam to enhance the interaction with the nanoparticle. When illuminating a nanoparticle, part of the power will be absorbed or scattered by the nanoparticle (P_{abs} and P_{sca}, see Section 1.3 on page 19). Additionally, even for a focused beam the majority of the incident power will typically not interact with the nanoparticle and be either transmitted or reflected (P_{T} and P_{R}). Just as with the standard integrating sphere method [194, 195], integrating sphere microscopy relies on determining the scattered, transmitted, and reflected light, such that the absorbed power can be inferred: $P_{\mathrm{abs}} = P_{\mathrm{in}} - P_{\mathrm{R}} - P_{\mathrm{T}} - P_{\mathrm{sca}}$. To do so with submicron resolution, we combined an integrating sphere with a ultra-long working distance microscope objective, which focuses the light on the sample inside the integrating sphere (see Fig. 5.1a). The sample is mounted on a 3D piezoelectric stage, which allows scanning of the sample to obtain quantitative local information of the absorptance. The ability to scan the focus with respect to the sample is crucial: without scanning, integrating sphere microscopy can only be used in a wide field configuration, which does not allow for quantitative spatial information [196]. Finally, broadband char-

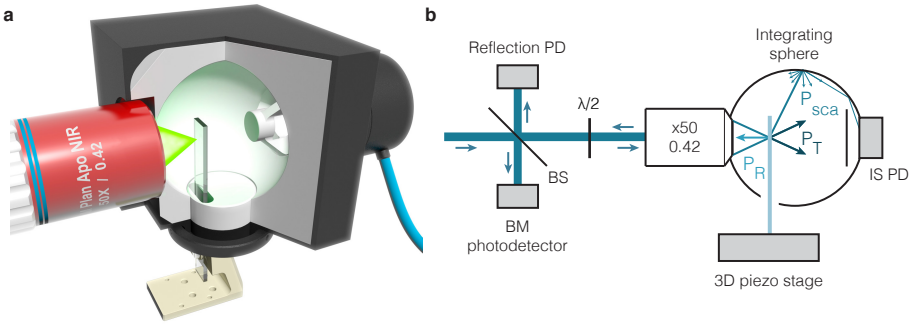

Figure 5.1: Schematic of the integrating sphere set-up. a. Schematic depiction of the combination of microscope objective and integrating sphere. The objective focuses light on the sample holder inside the integrating sphere, and the photodetector is behind a baffle on the backside of the integrating sphere. **b.** Schematic diagram for the experimental set-up, including reflection photodetector (PD) and half-wave plate to control the polarization. BS stands for beam splitter and BM for beam monitor, which we use to account for fluctuations in laser power.

acterization is possible, since we use a supercontinuum laser as a light source (400-2000 nm), and the integrating sphere inner surface remains Lambertian from 250-2500 nm.

A detector behind a baffle on the backside of the integrating sphere measures transmitted and most of the scattered power, while the reflected and backscattered power is collected back through the objective and measured by a second photodetector (see Fig. 5.1b). For the absorptance we then obtain:

$$A = 1 - \frac{R}{R_{\text{ref}}} - \frac{IS}{IS_{\text{ref}}} - C, \tag{5.1}$$

where R and R_{ref} are the reflection signal and reference measurement, and IS and IS_{ref} are the integrating sphere signal and reference measurement. Calibration of the technique is thus extremely simple: it only requires two reference measurements, usually a mirror for R_{ref} and a small hole in the substrate for IS_{ref} (meaning that the beam misses the sample, but the sample is still in the integrating sphere). C in Eq. 5.1 is an offset that arises from the reflection of the second interface of the glass sample holder, which is collected by the objective but so far out of the focal plane that it is not imaged on the photodetector. For glass $C \approx 0.04$ (the reflection of a single air-glass interface), but it depends slightly on how much power is transmitted and scattered forward, and assuming that it is constant therefore introduces a small source of error. The accuracy of the technique additionally depends on the detection efficiency of all non-absorbed light: *e.g.*, if some light is scattered but not detected by either photodetector, it will appear as absorption. Based on measurements on non-absorbing but strongly scattering silica beads we

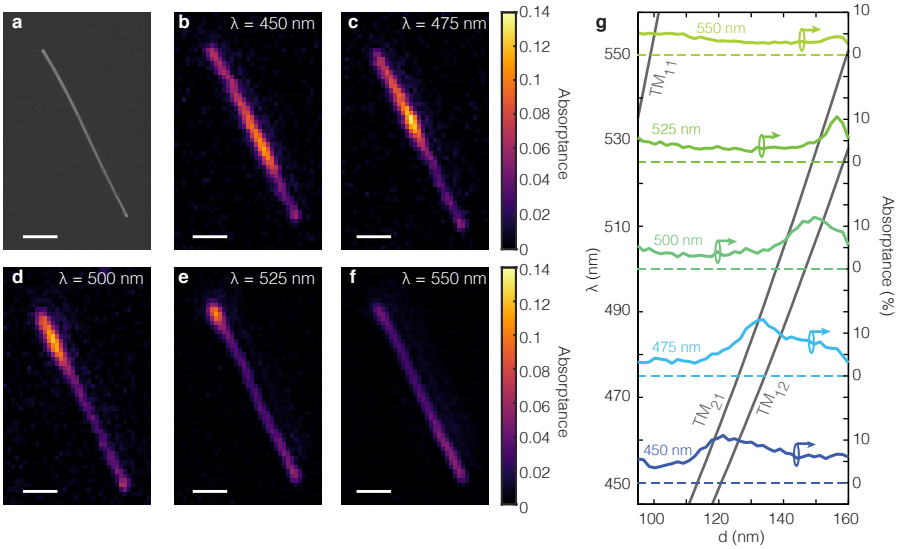

Figure 5.2: Absorptance maps of a silicon nanowire. a. SEM image of the silicon nanowire under consideration. Its diameter ranges from 95 (bottom) to 160 nm (top). The scale bar is 2 μm. **b-f.** Absorptance maps over the same spatial range for different wavelengths. For all maps the laser polarization is aligned with the long axis of the nanowire. The absorption peak shows how the TM_{12} and TM_{21} resonances shift position along the wire as the wavelength increases, and the TM_{11} is seen to appear on the bottom side of the wire. **g.** Wavelength dispersion of the resonances of a circular silicon nanowire in vacuum as a function of diameter, with the absorptance spectra at different wavelengths superimposed. The peaks in absorption along the length of the wire clearly correspond to the presence of resonances.

estimate that 95 ± 1.2% of the total scattered power is collected (see Supplementary Information, Section 5.6.3).

5.3 Nanowire absorption measurements

5.3.1 Silicon nanowires

We will now demonstrate this technique by showing local variation in the absorptance of a tapered silicon nanowire. Semiconductor nanowires are important building blocks for optoelectronics applications [197], including nanowire solar cells [51, 53], light-emitting diodes [123, 198, 199], lasers [200], and quantum information technology [201]. Fig. 5.2a shows an SEM image of a 10 μm long silicon nanowire on a glass substrate. The nanowire is slightly tapered, with a diameter that varies from 160 nm at the top of the image to 95 nm at the bottom. Fig. 5.2b displays the

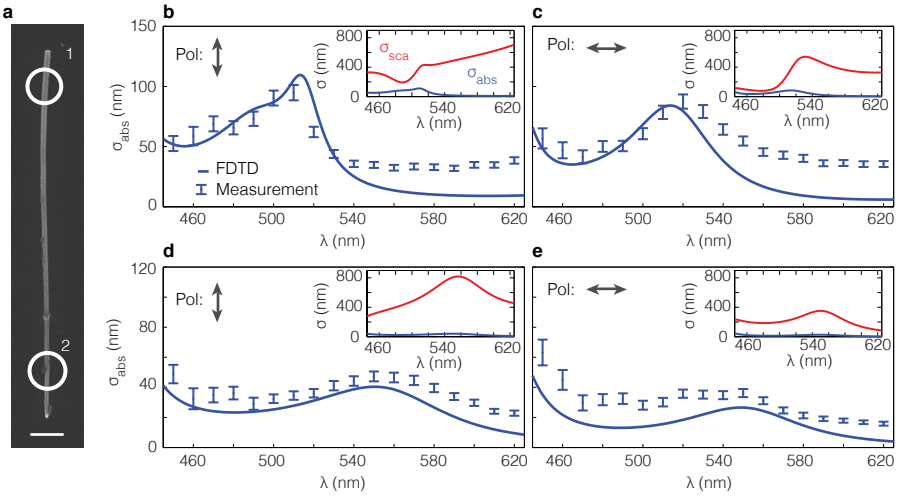

Figure 5.3: Absorption spectra of a silicon nanowire. **a**, SEM image of the silicon nanowire indicating the positions at which spectra were measured. The scale bar is 1 μm. **b.** The measured absorption cross section of the silicon nanowire at position 1 with the electric field polarized along the nanowire axis, compared to simulations of a hexagonal nanowire on glass with an apothem of 68 nm (blue line, see Supplementary Information Section 5.6.5 for details). The inset shows the simulated absorption cross section (blue) compared to the scattering cross section (red), indicating that the wire scatters much more strongly than it absorbs. **c.** Same as in panel **b** but with the electric field polarized perpendicular to the axis. **d-e.** Same as panels **b** and **c**, but measured at position 2 and with 48 nm apothem hexagonal nanowire simulation. In **b-e** the error bars are due to variance in the absorptance and uncertainty in the conversion to cross section.

absorptance A (absorbed fraction of the incident power, $A = P_{\text{abs}}/P_{\text{in}}$) at a wavelength of 450 nm, measured while scanning over the area shown in the SEM image using the 3D piezoelectric stage. In the center of the wire a peak in absorptance is visible, which corresponds to resonantly enhanced absorption via a Mie (geometrical) resonance. Mie resonances shift to longer wavelengths as the radius of the wire is increased, as they occur for fixed values of the product nk_0r, where n, k_0, and r are the refractive index, free space wavenumber and radius [202]. The absorption maps in Fig. 5.2c-f show the peak moving from smaller to larger diameter along the tapered nanowire as the illumination wavelength increases, providing a direct visualization of these diameter-dependent resonance phenomena.

Fig. 5.2g plots absorption intensity line cuts along the tapered nanowire in Fig. 5.2c-f, together with calculated dispersion relations to identify the relevant Mie resonances (see Chapter 7, Section 7.6.2). These resonances can be specified with the notation TM_{ml}, where TM indicates the magnetic field is transverse to the long axis of the nanowire, m is the azimuthal mode number, corresponding to the

number of field maxima around the nanowire circumference, and l indicates the number of radial field maxima. From these calculations shown in Fig. 5.2g it is clear that we observe the TM_{21} and TM_{12} resonances. These resonances are nearly degenerate and hard to disentangle spatially.

In addition to measuring nanoscale absorption maps at a fixed wavelength, we can also fix the laser position and measure local absorption spectra. Fig. 5.3a shows an SEM image of the same nanowire (but rotated) and indicates two positions where spectra were measured. Figs. 3b-e show the wavelength-dependent absorption cross sections of the nanowire at the two different positions, with the laser polarized either along or orthogonal to the nanowire axis. A geometric scaling factor is used to convert from absorptance to cross section: $\sigma_{abs} = A\sqrt{\pi w_0^2/2}$, where A is absorptance and w_0 is the beam radius. This factor can be derived by assuming that the nanowire is infinitely thin, and integrating the Gaussian spot intensity over the nanowire length. While the nanowire is not infinitely thin, agreement with full-wave simulations is good (see Supplementary Information, Section 5.6.1). However, because the scattered power significantly exceeds the absorption by up to a factor of 75, disagreement between the measurement and full-wave simulations is likely due to the small fraction of scattered light that is not detected.

5.3.2 GaAs nanowires

Due to the indirect band gap of silicon, these nanowires scatter very strongly, and they therefore provide a particularly challenging test case. Agreement with theory is even better for more strongly absorbing materials such as GaAs, as we will show now. Fig. 5.4a shows an SEM image of a GaAs nanowire with a radius ranging from 110 nm at the top of the image to 84 nm at the bottom. Figures 5.4b-f show absorption maps for different wavelengths, just as for the silicon nanowire. However, since this nanowire has a lower tapering angle the resonances do not appear localized along the nanowire length. Additionally, the nanowire has a smaller diameter, which means that a lower order resonance is excited (the TM_{11} resonance), which has a broader linewidth and, interestingly, therefore also a larger spatial extent in a tapered nanowire than a resonance with a narrower linewidth would have. Fig. 5.4g and 5.4h show the cross section versus wavelength, compared to full-wave simulations of the nanowire absorption and extinction cross section for parallel and perpendicular incident polarizations, measured at the top of the wire. Both spectra show a resonance at 480 nm, which are the TM_{11} and TE_{01} resonances in the parallel and perpendicular polarization respectively. Since GaAs has a direct band gap, the scattering cross section is reduced and the absorption cross section is increased, indeed improving the agreement with numerical predictions.

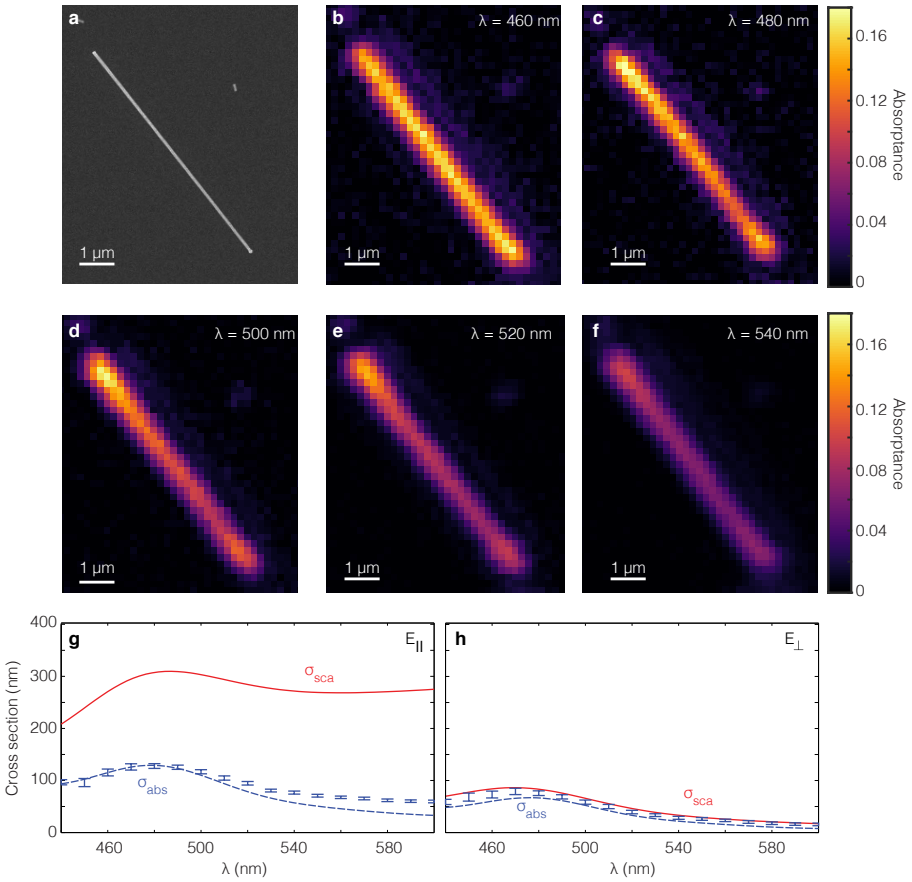

Figure 5.4: Absorption measurements of a GaAs nanowire. a. SEM image of the GaAs nanowire. The scale bar is 1 μm. **b-f.** Absorption maps from 460 to 540 nm. Due to the smaller diameter of the nanowire and the lower tapering angle the resonances appear to be less confined along the length of the nanowire. **g,h.** Absorption spectra with the electric field parallel (**g**) and perpendicular (**h**) to the nanowire axis. The solid red and dashed blue lines show full-wave simulations of the extinction and absorption cross sections for a GaAs nanowire with the same diameter (110 nm).

5.4 Au nanoparticles

Due to the linear extent of the nanowire, the intersection with the focused spot is significant and measurements above the noise floor are therefore easily achieved. To probe the detection limits of our set-up, we also investigate small spherical gold nanospheres with a plasmon resonance near 500 nm. While the absorptance of

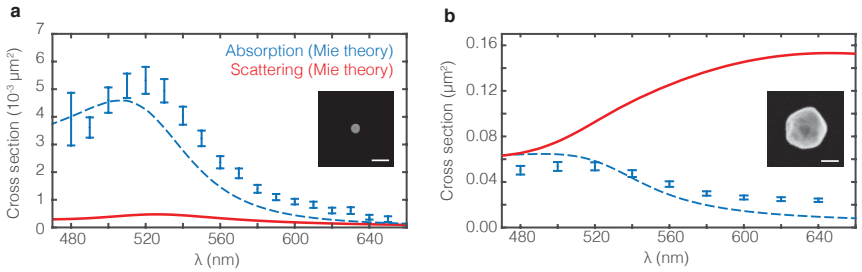

Figure 5.5: Absorption measurements of gold nanospheres. a. Absorption spectrum of a 60 nm Au nanoparticle compared to Mie theory predictions for absorption (dashed blue line) and scattering (red line). **b.** Absorption spectrum of a 220 nm Au nanoparticle compared to Mie theory calculations for absorption and scattering (dashed blue and red line respectively). The insets in both figures show representative gold particles along with a 100 nm scale bar.

the nanowires reaches >10% easily, the absorptance of a 60 nm gold sphere will lie below 1% due to the small absorption cross section. Since the nanoparticle is localized in three dimensions, we now obtain for the absorptance (assuming that the nanoparticle can be treated as a point): $A(x,y) = \sigma_{\text{abs}} I(x,y)$, where $I(x,y)$ is the intensity distribution in the Gaussian spot. If the nanoparticle lies exactly in the focus, we find $\sigma_{\text{abs}} = A \times \pi w_0^2/2$, where we used $I(x=0,y=0) = 2P_{\text{in}}/\pi w_0^2$ and $A = P_{\text{abs}}/P_{\text{in}}$. This absorption cross section is shown in Fig. 5.5a for a 60 nm diameter gold sphere and in Fig. 5.5b for a 200 nm diameter gold sphere.

Even though the absorptance peaks at 0.5% for the 60 nm diameter nanosphere, the noise floor is low enough for accurate determination of the absorption cross section. In fact, the error margin shown in Fig. 5.5 arises largely due to the determination of the Gaussian beam radius w_0. For the absorptance measurements the signal-to-noise ratio (determined as the peak absorptance relative to the standard deviation of the baseline) is 530 for the 200 nm diameter sphere and 30 for the 60 nm sphere. The noise level relative to the total measured power is 5×10^{-5}, which is comparable to the relative intensity noise (RIN) of supercontinuum lasers (1.5×10^{-5}) as reported in Ref. [95]. These measurements were done using lock-in amplifiers with a measurement bandwidth of 780 mHz (100 ms time constant and 24 dB/oct roll-off). The noise floor can be reduced further by using low noise lasers, but at the cost of the broad bandwidth, since supercontinuum lasers are inherently noisy [203]. Furthermore, tighter foci, longer integration times, or balanced detection schemes can also help, but the noise floor is clearly already is sufficiently low to measure the absorption of a single small gold particle.

5.5 Conclusion

To conclude, we have introduced a new technique to perform quantitative and spatially resolved absorption spectroscopy on single scattering nanoparticles. The technique uses an integrating sphere to measure directly the transmitted, reflected, and scattered power, allowing for determination of the absorbed power. Calibration of the absorption measurement is very straightforward and no assumptions on the nature of the scattering particle are required. We demonstrated integrating sphere microscopy by mapping the absorption cross section of tapered silicon and GaAs nanowires. These are essential characteristics for many optoelectronic devices, in particular for LEDs and solar cells, but can not be measured on the nanoscale with photothermal spectroscopy or any other known method. We therefore believe that this extension of the standard integrating sphere measurement to nanoscale systems can be of great utility in nanoscale optoelectronics, single nanoparticle spectroscopy, and other fields where quantitative and high spatial resolution measurements are desired.

5.6 Supplementary Information

5.6.1 Conversion from absorptance to cross section

The equation to convert from absorptance to cross section can be found by considering the Gaussian intensity distribution of the focused spot:

$$I(x,z) = I_G \exp\left(-2\left(\frac{x^2+z^2}{w_0^2}\right)\right) = \frac{2P_{\text{in}}}{\pi w_0^2} \exp\left(-2\left(\frac{x^2+z^2}{w_0^2}\right)\right), \tag{5.2}$$

where I_G is the Gaussian peak intensity and P_{in} is the total power carried by the beam. The beam waist w_0 is defined as the radius at which the intensity is I_G/e^2. When the wire is subject to inhomogeneous illumination, as with a Gaussian spot, the total absorbed power is found by integrating the intensity along the nanowire, where we assume that we can ignore the field gradient over the width of the nanowire (i.e. the wire is infinitely thin):

$$P_{\text{abs}} = \int \sigma_{\text{abs}} I(x=0,z)\,dz = \sigma_{\text{abs}} P_{\text{in}} \sqrt{\frac{2}{\pi w_0^2}}, \tag{5.3}$$

where for simplicity we assume that the wire is aligned along the z-axis, and that the cross section does not depend on position along the nanowire. Note that for tapered wires this is an approximation. From Eq. 5.3 we obtain:

$$\sigma_{\text{abs}} = \frac{P_{\text{abs}}}{P_{\text{in}}} w_0 \sqrt{\frac{\pi}{2}} = A w_0 \sqrt{\frac{\pi}{2}}. \tag{5.4}$$

This formula has been applied before to carbon nanotubes [94]. Although the assumption is made that the wire is infinitely thin, the agreement between

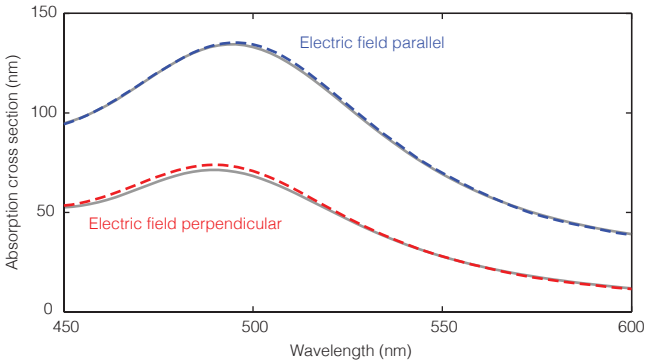

Figure 5.6: Numerical verification of the conversion from absorptance to cross section. Using finite-difference time-domain (FDTD, Lumerical [140]) we determined the absorption in a hexagonal GaAs nanowire with apothem of 46 nm on a glass substrate when positioned in the focus of a Gaussian beam (NA=0.25), as shown in blue and red dashed lines. We compare this to total-field scattered-field plane wave simulations to obtain the actual cross section σ_{abs} (gray solid lines), which shows excellent agreement with the Gaussian beam simulations.

Gaussian beam and plane wave simulations using this formula is excellent even for nanowires with a diameter of 100 nm and a beam waist of 570-760 nm (see Fig. 5.6).

Knife edge measurements

To determine the spot size we performed standard knife edge measurements, as described in *e.g.* Ref. [204]. The measurements were performed on a gold film with sharp edges on glass. The reflectivity is recorded as a function of position, resulting in a curve with the typical error function shape (see blue circles in Fig. 5.7a). The derivative of the reflectance (shown in red circles) is fit with the Gaussian intensity along one axis:

$$f(x) = a\exp\left(-2\left(\frac{x-x_0}{w_0}\right)^2\right), \tag{5.5}$$

where a is a fitting parameter for the height, x_0 for the position of the knife edge, and w_0 for the beam waist. The fit is also shown in Fig. 5.7a (red solid line), and is in good agreement with the measurement. This fitting procedure is performed for different wavelengths and for two directions (horizontal and vertical), the results of which are shown in Fig. 5.7b. The measurements indicate a slightly elliptical spot size, with the spot elongated in the vertical direction. The error bars in Fig. 5.7b indicate the 68% confidence interval.

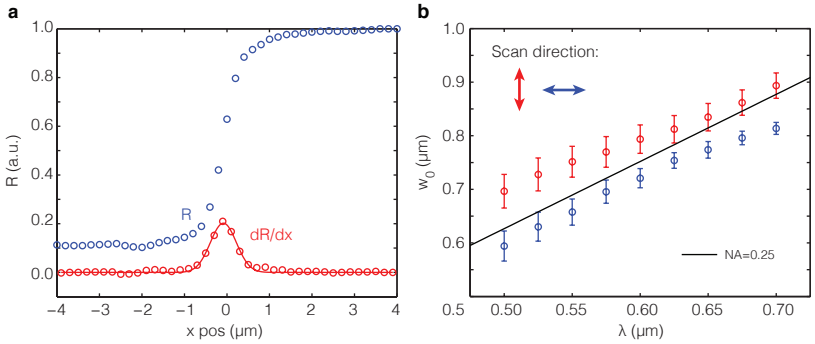

Figure 5.7: Knife edge measurements to determine the beam waist. a. Recorded reflection while scanning over a sharp edge of a gold film on glass (blue) at 500 nm wavelength. The derivative (red dots) shows the beam profile together with the fit (red solid line). **b.** Retrieved spot sizes as a function of wavelength for two scanning directions (vertical in red and horizontal in blue). This indicates that the spot is slightly elliptical. The increase in spot size is linear with an NA of 0.25 averaged over both scan directions.

5.6.2 Error propagation

The error on the measured absorption cross sections in Figs. 5.3, 5.4, and 5.5 in the main text is due to noise in the measured absorptance values δA, as well due to uncertainty in the spot size conversion. Since the absorption measurements themselves can be too lengthy to repeat many times we estimate the uncertainty in the measurement from the standard deviation in 50 values of R and IS that were measured next to a nanoparticle. Then, we obtain for the uncertainty in the absorption measurement [205]:

$$\delta A = \sqrt{(\delta IS)^2 + (\delta R)^2}. \tag{5.6}$$

For the conversion to cross section we assume that the 68% confidence interval from the fit algorithm (see previous section) is representative of the uncertainty. This then gives for the total error:

$$\delta\sigma_{\text{abs}} = \sigma_{\text{abs}} \sqrt{\left(\frac{\delta A}{A}\right)^2 + \left(\frac{\delta w_0}{w_0}\right)^2}. \tag{5.7}$$

5.6.3 Non-absorbing silica bead measurements

To examine the detection efficiency of scattered light in the integrating sphere microscopy setup, we have measured these detection losses on a SiO_2 nanosphere with a 460 nm diameter (see Fig. 5.8a), which strongly scatters but does not absorb. Figs. 5.8b and 5.8c show the reflection and integrating sphere maps, respectively,

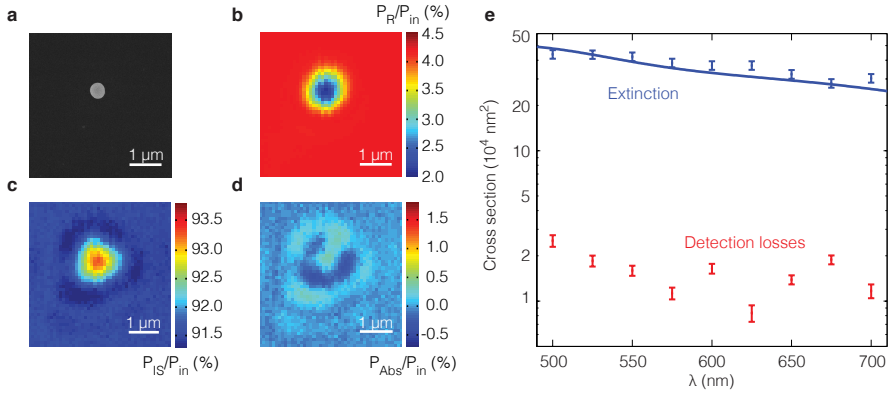

Figure 5.8: Examination of accuracy based on a non-absorbing particle. a. SEM image of a silica nanosphere with a diameter of 460 nm. **b,c.** Reflection and integrating sphere signal of the same nanosphere at 600 nm wavelength. **d.** Maps in **b** and **c** combined to give the absorptance map, showing that only a small fraction of the scattered power is not detected. The scale bar in **a-d** is 1 μm. **e.** The extinction cross section of the nanosphere (blue dots) together with the Mie theory cross section (blue line). Red dots show the measured detection losses, indicating that 95.2 $\pm$ 1.2% of the scattered light is detected. Error is due to variance and uncertainty in the cross section conversion (see Section 5.6.2).

for the nanosphere. The 2% decrease in reflection is matched by an analogous increase in the integrating sphere signal, but as shown in Fig. 5.8d a small difference remains when reflection and integrating sphere signals are combined. The maximum of this detection loss is shown as an effective detection loss cross section for a range of wavelengths in Fig. 5.8e. This figure also shows the extinction cross section measured on the same nanosphere (blue points), which we determined by measuring transmission of the focused light using a second microscope objective facing the excitation objective (see Section 5.6.6). Following the same approach as for σ_{abs} for the gold nanospheres, we find $\sigma_{\mathrm{ext}} = (\Delta T/T) \times \pi w_0^2/2$. The extinction measurements agree very well with the theoretical extinction cross section from Mie theory for a 460 nm SiO_2 sphere in vacuum (blue line, equal to the scattering cross section since the nanoparticle does not absorb). Based on the ratio of detection loss to extinction we estimate that 95 $\pm$ 1.2% of the scattered power is collected. This is higher than what can be detected with other methods. For example, for microscope objectives with the highest possible numerical aperture, the acceptance half-angle is practically limited to about 75 degrees. As a result, in the standard extinction setup with two objectives facing each other, only 80% of the power scattered by a simple dipole in a homogeneous environment can be collected [206].

Although the collection efficiency is already quite high, we believe it can be further increased. In our current set-up, there appear to be two major loss mechanisms: 1) the outer few millimeters of the objective front lens do not contribute to

laser light focusing or collection, but are also not covered by the integrating sphere; and 2) light that is scattered within the critical angle of the glass substrate might be guided out of the integrating sphere through the sample port. We believe that both losses can be mitigated with an improved integrating sphere and sample holder design, such that collection efficiencies even higher than 95% may be achieved.

5.6.4 Sample preparation

The silicon nanowires are grown epitaxially on a silicon substrate by the vapor-liquid-solid growth mechanism using an atmospheric-pressure chemical vapor deposition system. 40 nm gold particles were used as catalysts. The growth was conducted at 800 °C for 5 minutes with silicon tetrachloride ($SiCl_4$) as the precursor. The carrier-gas flows during growth are Ar=200 Standard Cubic Centimeters per Minute (SCCM) and H_2=50 SCCM, while only 75 SCCM Ar gas flows directly through the silicon tetrachloride precursor bubbler (held at 0 °C in a temperature-controlled bath). Self-catalyzed GaAs nanowires were grown by solid-source III-V MBE directly on p-type Si(100) substrates by solid-source III-V Veeco molecular beam epitaxy (MBE) GEN-930. The nanowires were grown with a Ga beam equivalent pressure of 8.7×10^{-8} Torr, a V/III flux ratio of 50, a substrate temperature of 630 °C, and a growth duration of 1 hour. The substrate temperature was measured with a pyrometer. The gold nanoparticles (60 nm and 200 nm diameter) were acquired from BBI solutions.

5.6.5 Simulations

The nanowire cross section simulations were performed with Lumerical FDTD [140]. The nanowire had a hexagonal shape and was assumed to be infinitely long (the simulations were 2D). The refractive index of silicon and GaAs was based on tabulated data from Palik [207]. In both the calculations of the dispersion diagrams and simulations the parallel momentum was assumed to be zero, treating the wire as if illuminated under normal incidence. Considering the low NA (0.42) in the experiment this is an accurate assumption.

5.6.6 Experimental setup

The light source in the experiment was a supercontinuum laser (Fianium WL-SC-390-3), which was made monochromatic using an acousto-optical tunable filter (AOTF, Crystal Technologies). Power in the focused laser beam is on the order of several to tens of μW. The microscope objective is a 17 mm working distance Mitutoyo M Apo Plan NIR 50x with NA=0.42. The integrating sphere is a LabSphere GPS-020-SL, modified so that it can accommodate our objective lens. The photodetectors are Thorlabs amplified Si detectors (PDA100A), read out by Stanford Research Systems SR830 lock-in amplifiers. For the Au NP measurements the IS photodetector was replaced by a passive Newport 818-UV photodetector, which

has a lower noise level than the Thorlabs transimpedance amplifiers. The transmission of the AOTF was digitally modulated at 20 kHz with a 50 percent duty cycle for the nanowire measurements, and at 700 Hz for the Au NP measurements. The sample holder is mounted on a Piezojena Tritor400 3D piezoelectric stage for high resolution scanning of the sample, while for rough alignment the piezoelectric stage itself is mounted on a Newport mechanical stage. For the extinction measurements on the silica beads in Fig. 5.8 we used a Nikon T Plan EPI SLWD 50X 0.4 NA objective for collection, which imaged the transmitted light on a PDA100A amplified photodetector.

6

Quantifying losses and thermodynamic limits in a single nanowire solar cell

Due to the large absorption cross section of nanostructures the interaction of a nanoscale solar cell with light is markedly different compared to macroscopic solar cells. As a result, metrics such as power conversion efficiency and external quantum efficiency, used for all macroscopic solar cells, have become meaningless. Furthermore, experimental metrics such as the internal quantum efficiency and photoluminescence quantum yield have never been determined, because an experimental technique enabling direct absorption measurements on individual nanosystems was lacking. Using integrating sphere microscopy, the technique we presented in Chapter 5, we now determine the performance of a single nanowire device based on intrinsic metrics like the absorption cross section, internal quantum efficiency, and photoluminescence quantum yield. We then introduce the nanoscale equivalent to the external quantum efficiency, enabling us to quantify the losses and thermodynamic limit of nanoscale solar cells.

6.1 Introduction

Nanophotonic engineering holds great promise for photovoltaics: the record conversion efficiencies of nanowire solar cells are increasing rapidly [51, 208], and the record open-circuit voltages are becoming comparable to record planar equivalents [165, 209]. Furthermore, several authors have suggested that nanophotonic effects could help photovoltaics surpass the fundamental efficiency limits of planar solar cells [44, 53]. These effects are particularly pronounced in single nanowire devices, where two out of the three dimensions are subwavelength. Therefore, single nanowires provide an ideal platform to study how nanophotonics affects photovoltaics [53, 120, 210–215]. However, in isolated nanophotonic systems the standard definition of power conversion efficiency no longer applies, because the device can absorb light from an area much larger than its own size. Additionally, while a thermodynamic bound on the photovoltage still exists, it is *a priori* unknown and may be very different from that of a planar solar cell. This complicates characterization of such nanoscale devices: it is unclear how well they perform with respect to fundamental limits and to other devices, how much can be gained through optimization, and whether the efficiency limits of planar devices can be surpassed by understanding and applying nanophotonics to photovoltaics. Here we analyze a record InP single nanowire solar cell using intrinsic metrics to place its performance on an absolute thermodynamic scale. Determining these metrics requires novel integrating sphere microscopy, which combines spatially resolved quantitative absorption, photocurrent, and photoluminescence measurements. We measure a photocurrent collection efficiency of >90% and a record open-circuit voltage (850 mV) that is 73% of the thermodynamic limit (1.16 V).

6.2 The internal quantum efficiency

The single nanowire device consists of a 310 nm diameter wurtzite InP nanowire with a 50 nm SiO_2 coating used to prevent oxidation and enhance stability (see Fig. 6.1a and the Methods section in the Supplementary Information to this chapter). It has a short-circuit current of I_{sc} = 450 pA, an open-circuit voltage of V_{oc} = 850 mV, and a fill factor of FF = 0.76 under AM1.5 solar spectrum illumination (Fig. 6.1b), all of which are high compared to previous nanowire devices. However, to understand the origin of the obtained I_{sc} and V_{oc} we need to determine intrinsic metrics like the device internal quantum efficiency (IQE) and photoluminescence quantum yield (PLQY)*. To date the primary experimental challenge in determining intrinsic performance metrics for single nanowire devices has been measuring quantitative absorption during solar cell operation, which is not possible with existing techniques. These methods assume that absorbed power is converted into heat (photothermal spectroscopy [88, 106, 107, 191]), that scattering does not oc-

*Note that in other chapters the PLQY is referred to as "external radiative efficiency" (ERE).

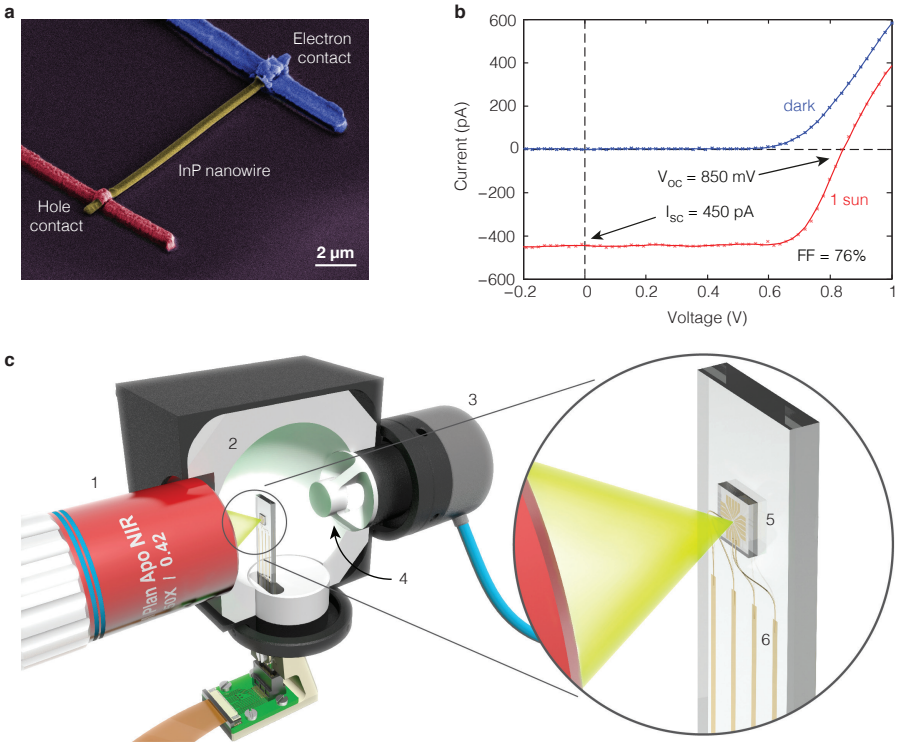

Figure 6.1: Characterization of a record single nanowire solar cell. A single nanowire solar cell is characterized with integrating sphere microscopy. **a.** False-color SEM image of the InP nanowire device (yellow) with hole contact (red) and electron contact (blue). **b.** The nanowire I-V curve in the dark (blue) and under the solar simulator at 1 sun intensity (red). The solid line is a smoothed fit to the data points (shown as small crosses). **c.** A schematic depicting the integrating sphere microscopy setup. A microscope objective (1) focuses light from a monochromated supercontinuum laser source on the nanowire solar cell inside the integrating sphere. The integrating sphere (2, only half is shown) collects transmitted as well as scattered light via a photodetector (3) behind a baffle (4), while the objective directs the reflected light to another photodetector (not shown here, see Fig. 6.6a). Subtracting these calibrated signals from the input gives the local absorptance (fraction of incident light that is absorbed) with submicron resolution. The device is connected to electrode pads (5) and current leads (6) to simultaneously measure photocurrent is measured simultaneously, enabling determination of the IQE. With a long-pass filter in front of the detector (3), photoluminescence can be collected quantitatively to give the PLQY. The sample is mounted on a piezoelectric stage, enabling spatial mapping of all these output parameters.

cur (extinction spectroscopy [94, 99, 102]), or that the particle is an ideal dipole (scattered field interferometry [89]). As discussed in Chapter 5, integrating sphere microscopy circumvents these assumptions by combining the standard tool for measuring absorptance of macroscopic samples [194] or ensembles of nanoparticles [196], with a long working distance microscope objective (see Fig. 6.1c). A photodetector placed behind a baffle on the integrating sphere collects scattered and transmitted light while the microscope objective collects reflected light (sent to another photodetector). Simply calibrating and subtracting these signals from the input gives the quantitative absorptance (see Section 5.2, p. 80). The sample has current collecting leads and is mounted on a piezoelectric stage, which enables two-dimensional scans of the absorptance and IQE for the first time.

Two-dimensional maps of the absorptance (fraction of incident power that is absorbed) and IQE (fraction of absorbed light converted to current) are shown in Fig. 6.2. A plan view SEM image of the device is shown in Fig. 6.2a for comparison to the absorptance and IQE maps in Fig. 6.2b and 6.2c, measured at an excitation wavelength of 600 nm. The IQE reaches a peak value of 100% and is strongly localized to the upper half of the wire, as is more clearly visible in the line profile of the IQE along the nanowire in Fig. 6.2d. The color shading in Fig. 6.2d shows the intended doping profile during growth. It should be noted that the p-type dopant zinc might have diffused further into the nanowire during growth as it is very mobile in InP at high concentrations [216]. Carrier collection is most efficient near the n-type/intrinsic interface, and collection occurs over a length of 3.4 microns. In the p-type region the IQE is essentially zero, indicating short electron diffusion lengths. This is confirmed by an electron-beam induced current (EBIC) measurement shown above the IQE line profile, from which we determine the electron diffusion length in the intrinsic/p-type segment to be 285 nm (see Supplementary Information, Section 6.6.5). The IQE is nearly independent of polarization and wavelength, with values >90% over the whole wavelength range up to the band gap (Fig. 6.2e). The difference in band gap depending on excitation polarization is caused by the anisotropic nature of wurtzite InP and has previously been observed with photoluminescence excitation spectroscopy [217].

6.3 The photoluminescence quantum yield

With integrating sphere microscopy we can probe not only the IQE to understand the current collection efficiency, but also directly measure the PLQY [195, 196]. In absence of non-radiative recombination, PLQY=1 and the open-circuit voltage reaches the thermodynamic limit $V_{\mathrm{oc}}^{\mathrm{rad}}$. For a PLQY below 1, the V_{oc} is reduced from the radiative limit to the implied $V_{\mathrm{oc}}^{\mathrm{imp}}$ [134, 162, 218]:

$$V_{\mathrm{oc}}^{\mathrm{imp}} = V_{\mathrm{oc}}^{\mathrm{rad}} - V_T|\ln(\mathrm{PLQY})|, \tag{6.1}$$

where V_T is the thermal voltage (25.9 mV). Hence, the PLQY plays a crucial role in understanding the photovoltage. To measure the PLQY, we place a filter in

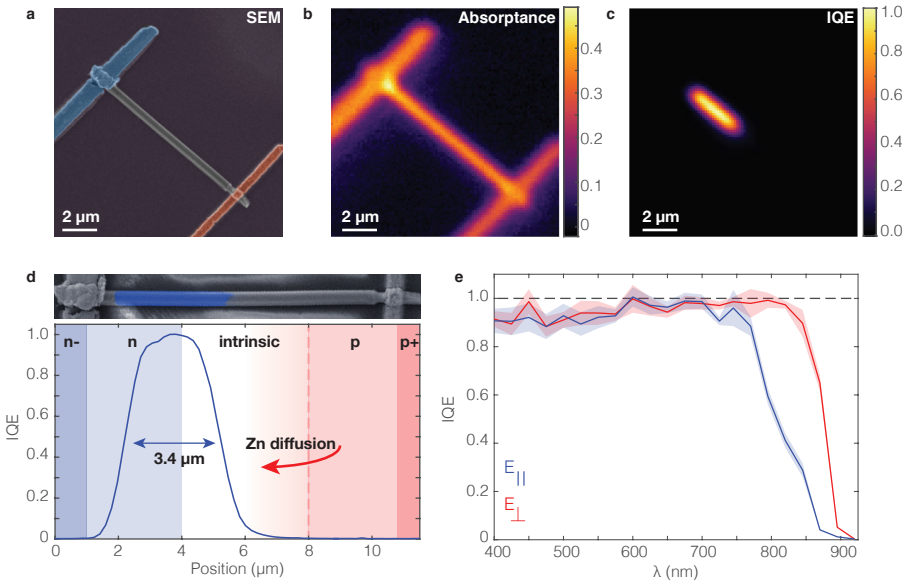

Figure 6.2: Internal quantum efficiency of a single nanowire photovoltaic. By measuring quantitative absorption and photocurrent simultaneously the IQE can be determined with high spatial resolution. **a.** False color scanning electron microscopy (SEM) image of the single nanowire device (InP nanowire diameter = 310 nm, length = 12.1 μm, SiO_2 shell thickness = 50 nm). The p-i-n doped InP nanowire device is visible in the center with an electron contact (blue) and hole contact (red). **b**,**c.** Absorptance and internal quantum efficiency (IQE) as a function of position for the nanowire device. **d.** The IQE as a function of position along the nanowire length, convoluted with the focused spot size (beam radius 730 nm). The color shading shows the nanowire doping profile as intended during growth, but it should be noted that the p-type dopant zinc may have diffused further into the nanowire during growth [216]. The SEM image on top has an electron beam-induced current (EBIC) measurement (blue shade) in good agreement with the IQE profile. **e.** The peak IQE spectrum for light polarised perpendicular (red) and parallel (blue) to the nanowire axis lies between 90% and 100% up to wavelengths close to the band gap, where the anisotropic nature of wurtzite InP becomes apparent. The shading displays the measurement uncertainty, which arises largely due to noise in the photodetectors (see Supplementary Information, Section 6.6.3).

front of the integrating sphere photodetector, such that only photoluminescence is detected (see Section 6.6.1 for details). Our spatially-resolved measurements show that the nanowire PLQY peaks in the same region where the IQE is highest (Fig. 6.3a), with an average PLQY over the active area of 0.9% at an excitation intensity of 1 μW 600 nm light ($\approx 1.4 \times 10^3$ suns, note that the PLQY is independent of excitation wavelength as shown in Fig. 6.5). To determine the average PLQY at 1 sun intensity, we measure at a range of lower excitation powers (Fig. 6.3b). The

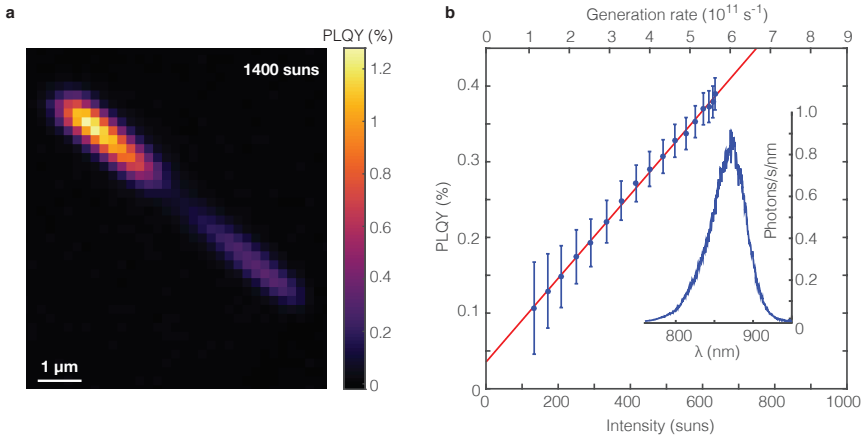

Figure 6.3: Photoluminescence quantum yield, power dependence, and recombination mechanism. a. The photoluminescence quantum yield (PLQY) as a function of position, indicating that the PLQY peaks where IQE is also highest. The PLQY was measured at 1400 suns to increase the signal to noise ratio. **b.** To determine the PLQY at 1 sun intensity we measured it for a range of intensities lower than in panel **a**. The PLQY clearly shows linear behavior with intensity, which indicates that Shockley-Read-Hall recombination dominates. The inset shows the nanowire photoluminescence (PL) spectrum at the brightest position in panel **a**, also at 1400 suns. All PLQY measurements were performed with 600 nm excitation light polarized parallel to the nanowire axis.

PLQY decreases linearly with excitation intensity, indicating that in this regime Shockley-Read-Hall recombination dominates (see Supplementary Information, Section 6.6.1). Assuming linearity down to 1 sun intensity, the average PLQY is 4.0×10^{-4} (0.040%). This value corresponds to a loss of 210 mV from the thermodynamic limit, and is comparable to what is observed in world record planar crystalline Si, Cu(In,Ga)Se_2, and InP solar cells [134].

6.4 The collection cross section

The PLQY can provide the V_{oc} loss from the thermodynamic bound V_{oc}^{rad}, but in order to calculate the latter value for our device we must know the recombination current corresponding to radiative thermal emission, I_0^{rad}. This emission current together with the I_{sc} determines $V_{oc}^{rad} = V_T \ln(I_{sc}/I_0^{rad})$ [162]. In a macroscopic solar cell, the I_{sc} and I_0^{rad} can be calculated by integrating the external quantum efficiency (EQE, fraction of incident photons converted to current) over the solar and blackbody spectra (T=300 K), respectively [134]. However, for nanoscale solar cells the standard definition of the EQE is not valid, because the absorption cross

section (σ_{abs}) can be much larger than the device area. To solve this important issue, we define a new quantity called the collection cross section that takes on the same role:

$$\sigma_{\text{EQE}}(\lambda,\Omega) = \int \text{IQE}(\lambda,z)\sigma_{\text{abs}}^{\text{1D}}(\lambda,\Omega)dz, \tag{6.2}$$

where IQE(λ,z) is the spatially resolved internal quantum efficiency (shown in Fig. 6.2e) and $\sigma_{\text{abs}}^{\text{1D}}$ is the effective absorption width of the nanowire (see Section 6.6.4 for a derivation and additional details). Fig. 6.4a shows σ_{EQE} for the nanowire device studied here, in both polarizations. Note that σ_{EQE} requires units of area, while the conventional EQE is a unitless quantum efficiency. This is a crucial difference, because for macroscopic solar cells the area collecting photons is independent of the incident wavelength and simply equal to the geometric area. In contrast, for nanostructures the interaction area with the incident light can be strongly wavelength dependent [53], e.g. due to resonances [120]. Additionally, in contrast to the IQE and PLQY, σ_{EQE} can be determined directly from the photocurrent measurement, incident flux, and laser spot size, and an integrating sphere is thus not required (see Section 6.6.4).

Integrating σ_{EQE} over the black body spectrum and all angles we find I_0^{rad}, which leads to a maximum open-circuit voltage for our nanowire device (see Section 6.6.4). The difference between the ideal voltage ($V_{\text{oc}}^{\text{rad}}$) and the measured (850 mV) is 310 mV: the V_{oc} is 73% of the thermodynamic limit. The measured V_{oc} is 100 mV smaller than the implied open-circuit voltage $V_{\text{oc}}^{\text{imp}}$ in the semiconductor nanowire, suggesting that the contact selectivity plays a significant role in the V_{oc} loss, likely due to diffusion of the highly mobile Zn out of the p-type doped region [216] and/or Fermi level pinning due to the surface oxide [219]. Additionally, knowledge of I_{sc} and I_0^{rad} allows us to determine the ideal fill factor, which is 89.5%, compared to 76% in our InP nanowire device. The deficit is likely due to large series resistance, which can be observed from the slope of the I-V curve in Fig. 6.1b and is supported by a fit of the I-V curve (see Supplementary Information Section 6.6.6). The series resistance can most likely be reduced by increasing the contact quality and reducing the length of the intrinsic nanowire segment.

The V_{oc} for this device is significantly higher than the Shockley-Queisser V_{oc} for a planar cell with an absorption onset at 890 nm (like our nanowire device, see Fig. 6.4a), which is 1.13 V [7]. The difference arises due to suppressed absorption near the band gap, which thus leads to reduced emission and a lower radiative recombination current [68]. It is important to note that such a voltage enhancement due to suppressed absorption necessarily comes at a cost in current, and can therefore not lead to efficiencies above the Shockley-Queisser limit in macroscopic devices [66, 69].

Integrating the EQE over the AM1.5 solar spectrum [4] is a common procedure used in macroscopic solar cells to verify the I_{sc} from solar simulator measurements. Here we find that an analogous procedure using σ_{EQE} instead of EQE gives a calculated short-circuit current of 320 pA, which is 29% lower than the value measured

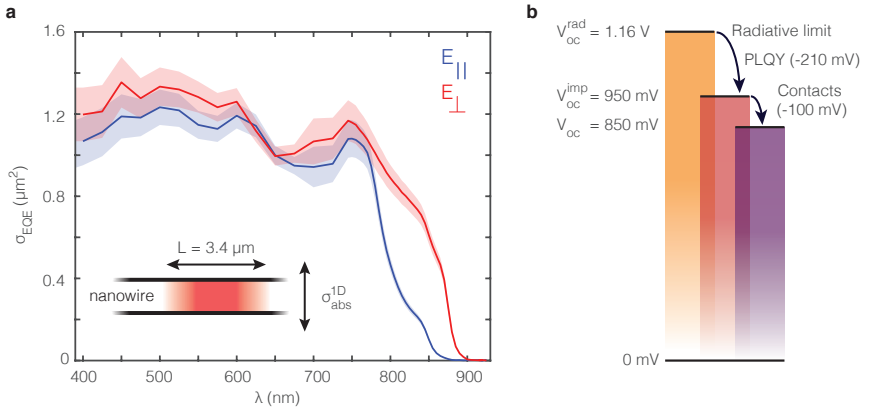

Figure 6.4: Measuring thermodynamic limits and quantifying loss mechanisms in single nanowire solar cells. To determine the thermodynamic limit to the in a nanoscale solar cell we introduce the collection cross section σ_{EQE}, the nanophotonic equivalent of the external quantum efficiency (EQE). **a.** σ_{EQE} for polarizations perpendicular (red) and parallel (blue) to the nanowire axis as a function of wavelength. σ_{EQE} is the nanophotonic equivalent to the standard external quantum efficiency (EQE) for a macroscopic solar cell, but takes into account the effective area over which photons are absorbed. As shown schematically in the inset, this area is determined by multiplying the absorption cross section $\sigma_{\mathrm{abs}}^{\mathrm{1D}}$ (see Methods) by the internal quantum efficiency (IQE) integrated over the nanowire length (see Fig. 6.2d). The shading displays the uncertainty, which is largely due to determination of the focused beam waist (see Methods in the Supplementary Information). **b.** Based on σ_{EQE} we estimate the different contributions to the open-circuit voltage. The thermodynamic limit is $V_{\mathrm{oc}}^{\mathrm{rad}}$ = 1.16 V, which is reduced by 210 mV due to the PLQY (non-radiative recombination in the semiconductor) to $V_{\mathrm{oc}}^{\mathrm{imp}}$=950 mV, and further reduced by 100 mV due to losses at the contacts, to a final V_{oc}= 850 mV.

under the solar simulator (450 pA). We attribute the difference to light trapping in the glass substrate, which leads to an overestimation of the actual photocurrent of nanowire photovoltaic devices when measured on glass substrates with a solar simulator. This is supported by the fact that covering almost the entire sample, including the nanowire, with opaque foil still results in a short-circuit current of ~100 pA (22% of total, see Section 6.6.8). This suggests that just as with macroscopic solar cells, measurements under the solar simulator require proper masking to avoid artefacts. We therefore used the I_{sc} value based on σ_{EQE} for the calculation of $V_{\mathrm{oc}}^{\mathrm{rad}}$ (see Section 6.6.4).

6.5 Conclusion and discussion

In conclusion, integrating sphere microscopy measurements and analysis allow us to place nanoscale solar cell performance on an absolute thermodynamic scale and pinpoint loss mechanisms. These measurements may direct our efforts to make more efficient integrated power sources for autonomous nanoelectronic applications [210] or macroscopic nanowire solar cells that can beat record planar cell efficiencies. In terms of photocarrier collection, these nanowires are already close to the limit, reaching IQE values >90% in both polarizations for a 3.4 micron segment of the nanowire. In a vertical nanowire geometry, with the n-type segment facing the sun, this is enough to absorb all incident light and collect the generated carriers. Regarding the photovoltage, we determined three different values for the V_{oc} that can help us pinpoint remaining loss mechanisms (Fig. 6.4b): (1) the thermodynamic limit calculated from wavelength-dependent measurements (1.16 V), which only includes radiative recombination; (2) the material limit extracted from local PLQY measurements (950 mV), that includes non-radiative recombination in the nanowire; and (3) the device limit extracted from solar cell operation (850 mV), that also includes losses at the contacts. The 210 mV (18%) loss related to non-radiative recombination in the nanowire could be reduced by lowering the surface recombination velocity (surface passivation) or material defect density (purification). Improvements in contact selectivity alone could lead to a 100 mV (12%) increase in the V_{oc} compared to our record single nanowire results. Combining both makes $V_{oc} > 1$ V for InP nanowire solar cells — far above world record planar InP solar cell performance — certainly within reach.

6.6 Supplementary Information

6.6.1 Quantitative photoluminescence measurements

An integrating sphere is also commonly used to measure photoluminescence quantum yield (PLQY) quantitatively, either by connecting a spectrometer to the integrating sphere or by using a combination of long- and shortpass filters [195]. To measure the PLQY on the nanowire we use a longpass filter in front of the integrating sphere detector (Thorlabs FELH0750). The PLQY at low intensities is not high enough to require a shortpass filter for accurate absorption measurement. The photoluminescence collection efficiency of the integrating sphere is determined by sending monochromatic light over the wavelength range of photoluminescence into the integrating sphere, but missing the sample. The total photoluminescence detection efficiency η_{PL} (Coulombs/emitted photon) can then be calculated using:

$$\eta_{PL} = \frac{\int S(\lambda)\eta(\lambda)d\lambda}{\int S(\lambda)d\lambda}. \tag{6.3}$$

Here $S(\lambda)$ is the PL spectrum (shown in the inset in Fig. 6.3b), and η is the wavelength dependent collection efficiency of the integrating sphere (also in Coulombs/photon). The PLQY is then calculated as the number of emitted photons divided by the number of absorbed photons.

Verification with R6G$^+$

To verify that with integrating sphere microscopy we can indeed also quantify the PLQY we measured the PLQY of a quantum yield standard. We used rhodamine 6G (R6G$^+$), which in low concentrations in ethanol has a quantum yield of 95% [220]. Since this integrating sphere setup is not capable of cuvette measurements we sealed a few μL of 0.1 mM R6G$^+$ between two microscope cover slips using transparent nail polish. We then placed this sample in the integrating sphere to measure the PLQY following the procedure described above, although the contribution of photoluminescence emitted through the objective was not recorded but estimated to be 4.6% based on the solid angle of collection. Additionally, a "miss" was not possible without significantly moving the sample. The absorption and photoluminescence measurements were done with Thorlabs FELH0500 and FESH0500 long pass and short pass filters. The resulting PLQY is shown in Fig. 6.5a for wavelengths between λ =460 and 490 nm, with an average PLQY of 86%. This is slightly lower than the reported quantum yield of R6G$^+$ in ethanol (95%), which may be due to a number of reasons:

- The dye concentration is too high, since calibration typically occurs at μM concentrations to prevent photoluminescence reabsorption and dye aggregation. However, due to the short path length of the laser through the solutions, high concentrations are required for sufficient signal.
- The nail polish slightly reduces the PLQY. We added a drop of nail polish to a cuvette of R6G$^+$, and did not observe strong quenching of emission. However, we could not rule out small variations.
- The calibration of the photoluminescence and absorption collection efficiencies were not accurate enough, as the "miss" measurement required significantly displacing the sample.

It is important to resolve this discrepancy to make sure that it does not originate from a systematic error. However, even with the current underestimation of the PLQY the $V_{\mathrm{oc}}^{\mathrm{imp}}$ would only be underestimated by $\sim V_T \log(0.95/0.86) = 2.6$ mV.

Excitation photoluminescence spectroscopy

In Fig. 6.3 we have determined the PLQY with an excitation wavelength of 600 nm. Here we verify that the PLQY is wavelength independent, which is expected for semiconductors in the linear regime (where one photon creates one electron-hole pair). The result of the excitation spectroscopy is shown in Fig. 6.5b, where the

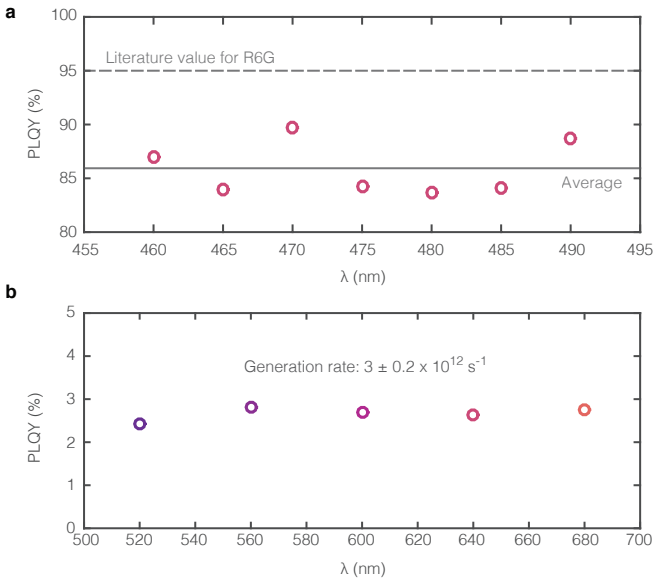

Figure 6.5: Photoluminescence quantum efficiency calibration and wavelength dependence. a. Measurement of the PLQY of Rhodamine 6G dissolved in ethanol (0.1 mM) using integrating sphere microscopy. The average PLQY (86%) is in reasonable agreement with the literature value of 95%. **b.** The PLQY of an InP nanowire from the same batch as the nanowire under investigation in the main text is shown as a function of the excitation wavelength ranging from 520 to 680 nm. The PLQY does not depend significantly on excitation wavelength.

PLQY is shown for a range of excitation wavelengths. While the luminescence intensity will depend on wavelength due to variation in the absorption cross section, this dependence is removed by correcting for the absorptance and calculating the PLQY. The generation rate is almost 6 times higher than the highest rate shown in Fig. 6.3, and as a result the PLQY is also higher, but it was roughly the same for each wavelength to be able to compare the results.

Excitation power dependence of the PLQY

In Fig. 6.3b in the main text we show the slope of the PLQY versus the generation rate, which has a linear slope. This slope can be explained by examining the ABC model for the semiconductor carrier density [221]:

$$G = AN + \overline{p}_{\mathrm{esc}} BN^2 + CN^3. \tag{6.4}$$

Here N is the carrier density (assuming that holes and electrons have the same density, such that we are in the high injection regime), G is the generation rate

of carriers, A is Shockley-Read-Hall coefficient, B is the radiative recombination coefficient, and C is the Auger coefficient. $\overline{p}_{\mathrm{esc}}$ is the probability that a photon from a radiative recombination event actually escapes the semiconductor structure and is emitted, instead of reabsorbed. The PLQY can then be written as:

$$\mathrm{PLQY} = \frac{\overline{p}_{\mathrm{esc}} B N^2}{G} = \frac{\overline{p}_{\mathrm{esc}} B N^2}{AN + \overline{p}_{\mathrm{esc}} B N^2 + C N^3}. \tag{6.5}$$

If Shockley-Read-Hall recombination dominates (A $\gg$ (BN, CN^2)), the rate equation simplifies to $G = AN$, which indicates that the carrier density now increases linearly with the generation rate. Inserting this into the expression of the PLQY, we find that:

$$\mathrm{PLQY} = \frac{\overline{p}_{\mathrm{esc}} B N^2}{AN} = \frac{\overline{p}_{\mathrm{esc}} B}{A} N. \tag{6.6}$$

Hence the slope of the PLQY is linear with the generation rate, while the radiative recombination rate goes with the generation rate squared. As noted in Chapter 4, $\overline{p}_{\mathrm{esc}}$ can be controlled by modifying the photonic environment of the emitting semiconductor, and in this way the total PLQY and thus thus the V_{oc} can be increased. For the nanowire case, luminescence might end up in a waveguide mode, reducing the probability that this photon escapes. By tuning the nanowire diameter and silica coating thickness this probability may be modulated, enabling further control over the device efficiency.

6.6.2 Integrating sphere microscopy

Integrating sphere microscopy is described in detail in Chapter 5. In this case the set-up is slightly different because a near infrared arm was required for characterization near the InP band gap, as shown in Fig. 6.6a. A supercontinuum laser (Fianium WL-SC-390-3) is fiber coupled into an acousto-optical tunable filter (AOTF), which has a visibile output for wavelengths 400-750 nm and a near IR output for wavelengths 700-1100 nm. We use polarizing beam splitters to ensure proper polarization, after which the light is sent through a 50:50 beam splitter to a beam monitor photodetector (to measure long-term fluctuations in incident power) and towards the integrating sphere. The light going towards the integrating sphere passes through a half-wave plate to control the incident polarization. The objective focuses the light on the sample inside the integrating sphere, and collects reflected light that goes towards the reflection photodetector. Light inside the integrating sphere is monitored by the integrating sphere photodetector. The sample is moved by a 3D piezo stage (Piezojena Tritor400). The incident intensity was controlled with ND filters (Thorlabs, not shown in the schematic) and the AOTF RF power. We used Newport 818-UV calibrated photodiodes as photodetectors, and modulated the acousto-optical tunable filter (AOTF) output with a 50 percent duty cycle at 195Hz. The laser output power was further controlled using the AOTF RF power and through neutral density (ND) filters.

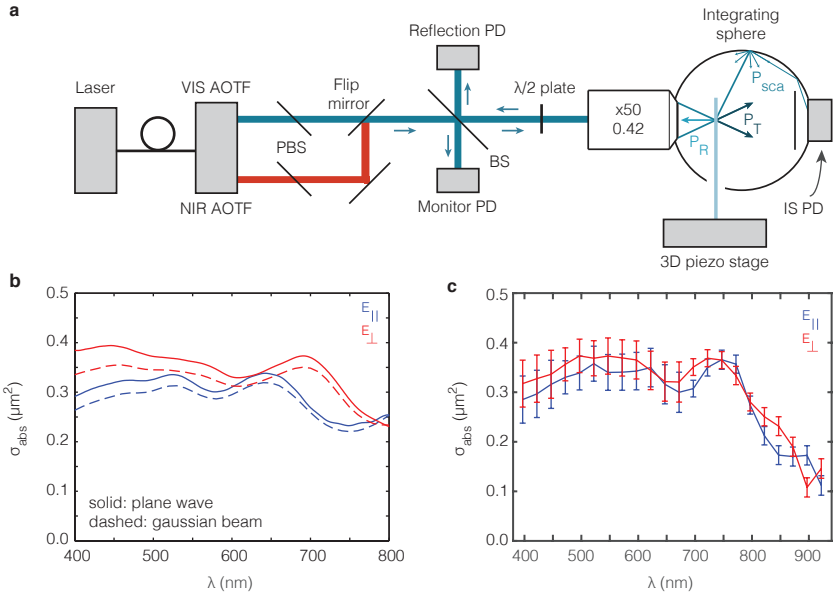

Figure 6.6: Schematic of the integrating sphere microscopy setup. a. A schematic diagram of the integrating sphere microscopy setup. PD stands for photodiode, BS for beam splitter, PBS for polarizing beam splitter, and AOTF for acousto-optical tunable filter. **b.** The absorption cross section of a zincblende InP nanowire (300 nm diameter with 50 nm SiO_2 shell) as a function of wavelength for both polarizations of light calculated with finite-difference time-domain simulations (FDTD, Lumerical [140]), compared to the converted absorption cross section from a Gaussian beam simulation (also FDTD) following the procedure in the main text. There is about a 5% difference between the two, which becomes smaller for longer wavelengths. **c.** The wurtzite InP nanowire absorption cross section converted from the absorptance measurements using the same procedure. The magnitude of the absorption cross section shows good quantitative agreement with the simulated absorption cross section for zincblende InP in panel **b**, but since the crystal structure is different a direct comparison is not possible. Additionally, the absorption cross section does not appear to vanish near the band gap, which is most likely due to the finite collection efficiency of scattered light. As absorption in the nanowire decreases, scattering increases strongly, and some of this light will not be collected (see Section 5.6.3 on page 89).

Absorption cross section spectra

To determine $\sigma_{\text{abs}}^{\text{1D}}$ from the absorptance A we assume that the nanowire is infinitely thin, so that we can derive a conversion factor $\sigma_{\text{abs}}^{\text{1D}} = A w_0 \sqrt{\pi/2}$. This is discussed in detail in Section 5.6.1 (p. 87), where we showed numerically that indeed even for nanowires with a diameter of ~ 100 nm and focused beams with an NA=0.25 this approximation is still valid. However, in the present case the nanowire has a diameter roughly 4 times larger, and as a result the agreement will most likely

be less good. This is verified again numerically in Fig. 6.6b, which shows a direct comparison between the absorption cross section of a zincblende InP nanowire (300 nm diameter, 50 nm SiO_2 shell) from a plane wave simulation and a Gaussian beam simulation using the conversion factor. The Gaussian beam underestimates the real absorption cross section by about 5%. This underestimation can be understood qualitatively from the Mie theory expansion: a tightly focused spot requires fewer harmonics than a plane wave, and for large nanowires the contribution from higher harmonics can be substantial. As a result, these harmonics contribute more to absorption when excited by a plane wave than when excited by a tightly focused spot.

To avoid underestimating the absorption cross section the beam waist can be expanded, such that the focused spot again becomes much larger than the nanowire. However, experimentally we did not observe a dependence of the absorption cross section on the spot size, which we checked by underfilling our objective until the spot size was increased by 60%. This experimentally obtained absorption cross section for the InP nanowire is shown in Fig. 6.6c. Although a direct comparison with theory is not possible, because the refractive index of wurtzite InP is not known, the magnitude of the absorption cross section is in quantitative agreement with the cross section for the zincblende InP nanowire in Fig. 6.6b. The absorption cross section does not appear to vanish near the band gap, which is most likely due to parasitic absorption from scattered light: as absorption in nanowires decreases, scattering increases strongly (see Section 5.6.3 on page 89 for additional discussion). This may also explain why the IQE decreases near the band gap.

6.6.3 Measurement uncertainty

Figs. 6.2e, 6.3b, and 6.4a show shaded areas corresponding to the measurement uncertainty in each of these measurements. These areas indicate the standard deviation, which were determined following regular error propagation rules for each of the individual signals [205]. For example, the IQE (shown in Fig. 6.2e) is given by $\mathrm{IQE} = \hbar\omega I_{\mathrm{sc}}/(qP_{abs})$, where $\hbar\omega$ is the photon energy, I_{sc} is the photocurrent, q is the electron charge, and P_{abs} is the absorbed power. Denoting the standard deviation by δ, we find for the measurement uncertainty:

$$\delta\mathrm{IQE} = \mathrm{IQE}\sqrt{\left(\frac{\delta I_{\mathrm{sc}}}{I_{\mathrm{sc}}}\right)^2 + \left(\frac{\delta P_{\mathrm{abs}}}{P_{\mathrm{abs}}}\right)^2}. \tag{6.7}$$

For the absorptance a similar procedure is followed, which is described in Section 5.6.2 (p. 89). Due to the low incident power, the photodetector noise contained in P_{abs} dominates for Figs. 6.2e and 6.3b, while for the cross sections in Fig. 6.4a fitting of the spot size dominates the measurement uncertainty, which can be further improved.

6.6.4 The collection cross section σ_{EQE}

To derive a nanoscale equivalent to the external quantum efficiency (EQE), it helps to define the EQE rigorously first. The EQE is a quantum number that relates the generated photocurrent to the incident photon flux:

$$\mathrm{EQE}(\lambda) = \frac{hc}{\lambda q}\frac{I_{\mathrm{sc}}}{P_{\mathrm{in}}}, \tag{6.8}$$

where $P_{\mathrm{in}} = aI_0$, with a the solar cell area and I_0 the incident intensity. To simplify notation somewhat we will only consider plane waves under normal incidence, but this derivation can readily be generalized to take into account more complicated P_{in}. Microscopically, the actual photocurrent that is generated depends on the generation profile of carriers in the semiconductor volume and the probability that these carriers are collected (the local IQE($\mathbf{r}$)). If we denote the absorbed power density by u_{abs}, we can then write the generated current as [162]:

$$I_{\mathrm{sc}}(\lambda) = \frac{\lambda q}{hc}\iiint \mathrm{IQE}(\mathbf{r})\, u_{\mathrm{abs}}(\mathbf{r})\, d^3\mathbf{r}. \tag{6.9}$$

Combining these equations, we can relate the local IQE to the EQE:

$$\mathrm{EQE}(\lambda) = \iiint \mathrm{IQE}(\lambda,\mathbf{r})\frac{u_{\mathrm{abs}}(\mathbf{r})}{P_{\mathrm{in}}}d^3\mathbf{r}. \tag{6.10}$$

What distinguishes the EQE from σ_{EQE} is how the total absorbed power $P_{\mathrm{abs}} = \iiint_V u_{\mathrm{abs}} d^3\mathbf{r}$ is related to P_{in}. For example, in planar thin film solar cells of sufficiently high quality the IQE is only weakly dependent on $\mathbf{r}$, in which case we can approximate Eq. 6.10 as:

$$\mathrm{EQE}(\lambda) \approx \frac{P_{\mathrm{abs}}}{P_{\mathrm{in}}} \times \mathrm{IQE}(\lambda) = (1 - R(\lambda)) \times \mathrm{IQE}(\lambda), \tag{6.11}$$

where $R(\lambda)$ is the reflection coefficient of the thin film solar cell. In nanoscale systems, however, the incident power loses its meaning since the geometrical area of the solar cell is no longer related to its absorption or extinction. We therefore need to rewrite Eq. 6.10:

$$\sigma_{\mathrm{EQE}}(\lambda) = \iiint \mathrm{IQE}(\lambda,\mathbf{r})\frac{u_{\mathrm{abs}}(\mathbf{r})}{I_0}d^3\mathbf{r}. \tag{6.12}$$

Since the area is left out from the denominator, it is now immediately clear that Eq. 6.12 indeed has units of area. If the IQE equals unity, σ_{EQE} simply becomes equal to the absorption cross section. This also elucidates the physical meaning of the collection cross section: for a given incident photon flux F (photons per unit area), $F \times \sigma_{\mathrm{EQE}}$ gives the generated photocurrent.

To derive Eq. 6.2 from Eq. 6.12 we need to assume that the IQE in the cross section of the nanowire is constant: $\mathrm{IQE}(r,\theta,z) = \mathrm{IQE}(z)$, where the nanowire is

aligned along the z axis. Then, writing the effective absorption width as an integral over the absorbed power density,

$$\sigma_{\mathrm{abs}}^{\mathrm{1D}}(z) = \iint \frac{u_{\mathrm{abs}}(\mathbf{r})}{I_0} r\,dr\,d\theta, \tag{6.13}$$

we find Eq. 6.2:

$$\sigma_{\mathrm{EQE}}(\lambda) = \int \mathrm{IQE}(\lambda, z)\sigma_{\mathrm{abs}}^{\mathrm{1D}}(\lambda, z)\,dz. \tag{6.14}$$

Note that here we only considered plane waves under normal incidence, and that the angle dependence is contained in $\sigma_{\mathrm{abs}}^{\mathrm{1D}}$. This is explicitly captured in Eq. 6.2 by adding the Ω dependency.

Experimental determination of σ_{EQE}

While σ_{EQE} can be determined using Eq. 6.2, it is important to note that σ_{EQE} can also be determined directly from the beam waist, the incident photon flux, and the laser induced photocurrent:

$$\sigma_{\mathrm{EQE}}(\lambda) = w_0\sqrt{\frac{\pi}{2}}\int \frac{I_L(z)}{S_{\mathrm{in}}}\,dz, \tag{6.15}$$

where I_L is the laser induced photocurrent, S_{in} is the total incident photon flux, and the integral again is over the nanowire length. This approach has two benefits: (1) since it does not rely on the absorptance, σ_{EQE} can be determined with any laser-beam induced current (LBIC) setup and no integrating sphere is thus required; and (2) the experimental error will be smaller since both S_{in} and I_L can be determined accurately. For the latter reason we have determined σ_{EQE} in Fig. 6.4 using Eq. 6.15. We will also apply this approach in Chapter 8, where the absorptance of the nanowire is actually unknown.

Angle dependence of σ_{EQE}

The highest possible open-circuit voltage is obtained for the lowest possible recombination current I_0^{rad}, which is normally calculated by integrating the EQE over the black-body spectrum [134]. Hence, for a nanostructure we obtain:

$$I_0^{\mathrm{rad}} = \int\int \sigma_{\mathrm{EQE}}^{\mathrm{U}}\Theta(T, \lambda)\cos(\theta)\,d\lambda\,d\Omega. \tag{6.16}$$

Here the integration over the black-body photon flux density $\Theta(T, \lambda)$ (where T is the temperature, 300K) is over all angles (taking into account a factor n^2 for the higher density of states when integrating over the glass hemisphere), and the $\cos(\theta)$ is the Lambertian factor. Because thermal radiation is unpolarized we use the absorption cross section $\sigma_{\mathrm{abs}}^{\mathrm{U}}$ averaged over both polarizations, signified by the superscript U. We assume that between 300 and 400 nm the absorption cross section stays

constant, which is a good approximation given the weakly varying nature of σ_{EQE} at shorter wavelengths. Additionally, the fraction of the photon flux in the solar spectrum contained below 400 nm is very small. Assuming that the nanowire absorbs light isotropically, we find a minimum recombination current of $I_0^{\mathrm{rad}} = 3.1 \times 10^{-17}$ pA, resulting in an open-circuit voltage of $V_{\mathrm{oc}}^{\mathrm{rad}} = 1.16$ V in the radiative limit.

To validate the assumption of an isotropic absorption cross section, we used finite-difference time-domain (Lumerical FDTD, [140]) to investigate the angle dependent absorption cross section. Because the refractive index of wurtzite InP is not known, we investigated two comparable materials, zincblende InP and GaAs (both also have direct band gap in the same energy range), with the same diameter and coating thickness as the nanowire we investigated in the main text. We determined the absorption cross section averaged over both polarizations ($\sigma_{\mathrm{abs}}^{\mathrm{U}}$) in a series of single wavelength 2D simulations, using a total-field scattered-field source and perfectly matched layers (PML) as boundary conditions. The results are shown in Fig. 6.7a for zincblende InP and in Fig. 6.7b for GaAs. These figures show a polar plot of the absorption cross section weighted by the black body spectrum, $\sigma_{\mathrm{abs,w}}^{\mathrm{U}}(\theta)$ where the angle θ of the incident wave vector lies in the plane perpendicular to the nanowire axis:

$$\sigma_{\mathrm{abs,w}}^{\mathrm{U}}(\theta) = \int_{300}^{\lambda_{BG}} \sigma_{\mathrm{abs}}^{\mathrm{U}}(\lambda,\theta)\Theta(T,\lambda)d\lambda. \tag{6.17}$$

The dashed lines show the isotropic $\sigma_{\mathrm{abs,w}}^{\mathrm{U}}(\theta = 0)$ (where the absorption cross section is equal to the absorption cross section under normal incidence for all angles), while the solid lines show the actual $\sigma_{\mathrm{abs,w}}^{\mathrm{U}}(\theta)$. To assess the difference between the isotropic assumption and the actual angle dependence in this plane, we calculate the relative difference in recombination rate:

$$\Delta R = \frac{\int_0^{\pi} \sigma_{\mathrm{abs,w}}^{\mathrm{U}}(\theta) n^2(\theta)\sin(\theta)d\theta}{\sigma_{\mathrm{abs,w}}^{\mathrm{U}}(\theta = 0)\int_0^{\pi} n^2(\theta)\sin(\theta)d\theta}. \tag{6.18}$$

Here $n^2(\theta)$ is the squared refractive index of the medium (glass or air) to account for the different intensity of black body radiation. Evaluating this factor for zincblende InP and GaAs we find that they are $\Delta R = 0.91$ and $\Delta R = 0.96$ respectively. Interestingly, while the angular distribution of $\sigma_{\mathrm{abs,w}}^{\mathrm{U}}$ is modified by the presence of the glass, the integrated $\sigma_{\mathrm{abs,w}}^{\mathrm{U}}$ does not change significantly. This is in good agreement with emission of dipoles near glass interfaces: while the angular distribution of the emission may change dramatically in the presence of a substrate, in particular near the critical angle of the substrate [222], the total decay rate does not change as strong when the refractive index of the substrate is low [168]. Hence, the influence of the glass substrate on the angular distribution can safely be ignored. In the other plane of incidence (parallel to the nanowire axis) we observe similar behavior for both nanowires (validating our initial assumption that $\sigma_{\mathrm{EQE}}^{\mathrm{U}}(\lambda,\theta)$ can be approximated as isotropic), but it should be pointed out that in this plane of incidence the nanowire may have resonances with momentum parallel to the nanowire axis. As a

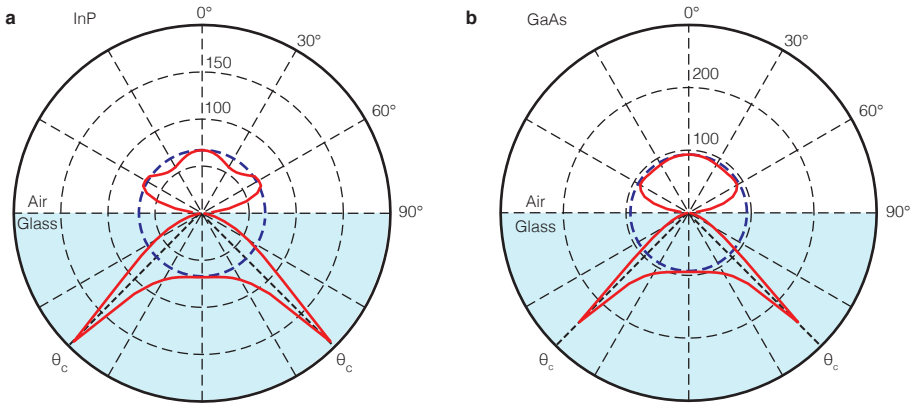

Figure 6.7: Absorption cross section versus angle of incidence. Absorption cross section in nm of a zincblende InP nanowire (**a**) and GaAs nanowire (**b**) (300 nm diameter with 50 nm SiO_2 shell), averaged over both polarizations and wavelengths, weighted by the blackbody spectrum. The strong lobes in the absorption cross section when incident from the glass side coincide with the critical angle in the glass, which is also observed for dipole emission near an interface [222]. These simulations were performed using Lumerical FDTD.

result, one would ideally determine the angle dependence of emission experimentally, for instance through Fourier microscopy [223], especially when modelling of the nanowire system is not possible (*e.g.* if the refractive index is unknown).

The I_{sc} can also be calculated using Eq. 6.16, but $\Theta(T,\lambda)$ has to be replaced by the AM1.5 spectrum [4] and the integral is not carried out over all angles, but just over normal incidence (or the angle subtended by the sun).

6.6.5 Electron beam-induced current measurement

The electron beam-induced current (EBIC) measurements are conducted with a beam current of 100 pA and 5 kV acceleration voltage. The integration time per pixel is 10 μs. The position of the electron beam is synchronised with the read-out of the current signal which allows the superposition of the extracted current signal with the SEM image. Supplementary Fig. 6.8 shows a profile of the EBIC intensity along the length of the nanowire, which shows that only the part next to the electron contact is active (at 0.5-4 μm). By fitting an exponential decay curve to the tail between 4-6 μm, a diffusion length of $L_d = 285 \pm 10$nm in the p-doped part of the wire is extracted.

6.6.6 Series resistance and diode ideality factor

Based on a fitting method described in Ref. [224] we have determined the diode ideality factor and the series resistance (see Fig. 6.8b). The shunt resistance was too

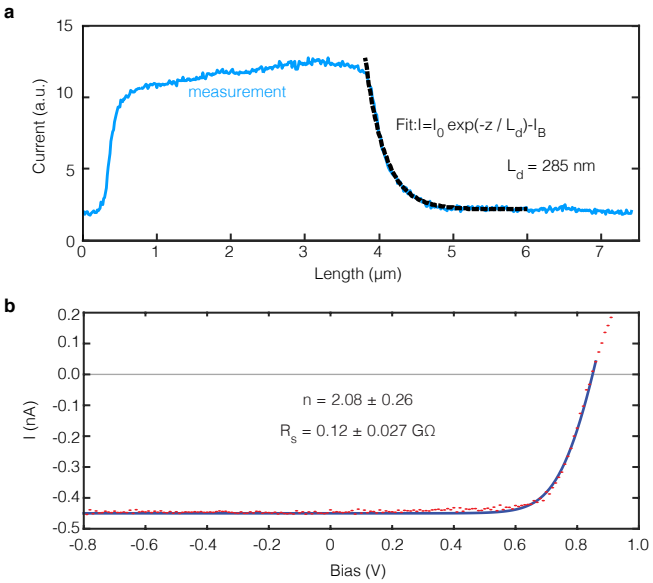

Figure 6.8: Electron beam-induced current profile and I-V curve fit. a. Electron beam-induced current (EBIC) profile along the length of the wire, oriented as shown in Fig. 6.2d in the main text. **b.** By fitting the I-V curve we determined the series resistance and diode ideality factor, both of which contribute to the fill factor FF=0.76 being below the maximum FF=0.895. The uncertainty in fitted values gives the 95% confidence interval.

high to be able to determine accurately. The ideality factor (n = 2.08) and series resistance ($R_s = 0.12 \times 10^9 \Omega$) both reduce the fill factor from its highest possible value, $FF_{rad} = 0.895$. The series resistance can possibly be reduced by improving contact resistivity and reducing the length of the intrinsic part of the nanowire.

6.6.7 Sample Fabrication

Nanowires are grown in a low-pressure Aixtron 200/4 Metal-Organic Vapor Phase Epitaxy (MOVPE) reactor, with the Selective Area MOVPE growth method. A 50 nm thick silicon nitride layer is used as Selective Area growth mask, patterned by the Soft Contact Nanoimprint Lithography technique [225, 226] on a (111)A oriented p-doped InP substrate (Zn doping carrier concentration 2×10^{18} cm^{-3} from AXT, USA). Hydrogen (H_2) is used as a carrier gas for precursors, with a total flow of 15 L/min. Growth is performed at 730 °C with a pressure of 100 mbar, using trimethyl-indium (TMI) and phosphine (PH_3) as precursors with molar fractions X_i (TMI) = 4.7×10^{-5} and X_i (PH_3) = 3.9×10^{-3}, resulting in a molar ratio of group III and group V element fluxes in the MOVPE reactor of 83. The total growth time is 11 minutes with a doping profile p^{++} / p / i / n / n^{--}, with respective segment

growth times of 0.5 min/3 min/4 min/3 min/0.5 min (1 μm/3 μm/4 μm/3 μm/1 μm). We use diethyl-zinc (DEZn) as p-dopant, with molar fractions 1.3×10^{-5} in the p^{++} region and 6.4×10^{-6} in the p region. Di-tert-butylsilane (DTBSi) is used as n-dopant, with molar fractions 9.5×10^{-6} and 4.9×10^{-7} for n^{--} and n regions, respectively. After the growth, the wires were coated with a conformal SiO_2 shell by plasma enhanced chemical vapor deposition (PECVD), performed with silane and nitrous oxide as precursors at 300 °C. The nanowire measured in this chapter had a total diameter of 410 nm (310 nm diameter InP), a length of 12 μm (9.8 μm between the contacts) and SiO_2 shell thickness of 50 nm.

Au electrode patterns (see Section 6.6.8) with alignment markers are fabricated on plasma cleaned glass substrates by UV lithography and metal evaporation. The nanowires are transferred from the arrays ($\sim 200 \times 200$ μm^2) via a pipette in ethanol and are randomly dropcast on the substrates. Electron beam lithography and metal evaporation are used to contact the single nanowires to the Au electrodes (see details below). It was found that the exact placement of the contact position on the highly doped end-segments of the nanowires is a crucial step to allow good ohmic contact and prevent extraction barriers. Then, the glass substrates are wire-bonded to glass holders, which have prefabricated metal contact lines (also by UV lithography and metal evaporation). The bottom of the glass holder is connected to a printed-circuit-board socket which also connects to a flat electrical cable extending outside of the integrating sphere (see Fig. 6.1c).

The metals used to contact the single nanowires were Ti (200 nm) and Au (30 nm) for the electron contact (on the n^{--} doped part) and Cr ($\sim$ 3 nm), Zn (15 nm), Au (215 nm) for the hole contact (on the p^{++}-doped part). Before the metal was evaporated, the exposed and developed substrates were etched in buffered HF (1:7, HF (49%):NH_4F (40%)) for 10s to remove the protective SiO_2 shell and the native oxide of the InP under the contact. The latter is known to cause Fermi-level pinning under the conduction band, which creates extraction barriers for the hole-contact [219]. The etched samples were transferred into the evaporation chamber immediately to minimise the regrowth of the native oxide. It is common to use an additional annealing step at high temperatures to diffuse Zn into the p-type InP nanowire and create a highly p-doped layer [215]. We found this treatment to be damaging to our nanowires (a strong decrease in photoluminescence efficiency was observed) and therefore omitted this step, as the in situ doping of our nanowires allowed the formation of ohmic contacts even without annealing. Nevertheless, we chose to evaporate Zn for the hole-contact to prevent diffusion of Zn from the nanowire into the contact metal at elevated temperatures during the evaporation and lift-off steps.

For the electron contact, Ti and Au were evaporated with an electron beam evaporator at a pressure of $\sim 5 \times 10^{-7}$ mbar at an evaporation rate of 0.3-2 Å/s and acceleration voltage of 10 keV. For the hole contact Cr, Zn and Au were evaporated with a thermal evaporator at $\sim 2 \times 10^{-6}$ mbar at a rate of 0.2-1.5 Å/s.

Device statistics

Table 6.1 shows the statistics of four different nanowire batches, that were grown with a different pitch (**p**) and doping profile (**d**). Batch **p2-d1** shows not only the maximum V_{oc} = 850 mV and I_{sc} = 609 pA, but also the highest means can be found in that batch. The second and third highest V_{oc}'s in that batch were 820 mV and 800 mV, respectively. Even though the doping profile of batch **p2-d1** (described above) was the same as for batch **p1-d1** the results show a clear difference in performance. To understand the influence of a different nanowire pitch (density) on the growth conditions, more studies are needed. The low yield of batch **p2-d1** can be mainly ascribed to the lower density of nanowires. However, during the contacting process several additional steps are potentially lowering the yield of the devices. Transferring the wires from the array can lead to cleavage of the wires from the substrate in a detrimental way. If the wire breaks not at the bottom, directly above the substrate, the broken end-facet does not correspond to the highly p-type doped part of the wire, that easily facilitates ohmic contacts. Furthermore, prior to the contacting the orientation of the nanowire doping profile is not known. And finally, even a slight misalignment during the electron beam-lithography will lead to metal contacts that are placed onto the lower doped regions of the wire (or are missing the nanowire altogether). In all those cases, the placement of the contacts on a region with a wrong doping type and density will lead to a strong extraction barrier in the final devices. In summary, great care has to be taken to yield any meaningful number of single nanowire devices, even for arrays with a large density of wires, while low densities almost certainly translate into low numbers of final devices.

Batch	$\overline{I_{sc}}$	δI_{sc}	I_{sc}^{max}	$\overline{V_{oc}}$	δV_{oc}	V_{oc}^{max}	# nanowires
p1-d1	54 pA	22 pA	90 pA	228 mV	117 mV	512 mV	18
p1-d2	61 pA	20 pA	93 pA	285 mV	49 mV	320 mV	8
p1-d3	210 pA	83 pA	398 pA	329 mV	146 mV	640 mV	22
p2-d1	321 pA	175 pA	609 pA	696 mV	105 mV	850 mV	12

Table 6.1: Statistics of single nanowire devices from different growth batches. The nanowires were grown under different growth conditions (array pitch (**p**) and doping profile (**d**)). The device shown in the paper comes from batch **p2-d1**. While the statistical interpretation of the results is limited due to the small number of total devices for that batch (low density of nanowires), not only the maximum open-circuit voltages and short-circuit currents but also the highest means can be found in that batch. The second and third highest open-circuit voltages from that batch were 820 mV, and 800 mV, respectively. and are the standard deviations, while and are the average values.

6.6.8 Macroscopic contact pads and solar simulator measurement

The I-V trace of the nanowire device is measured with a solar simulator (Oriel SOL2 94062A (6X6) Class ABA, Newport) with the AM1.5G spectrum at 1 sun (100 mW/cm^2) illumination intensity and an operating temperature of at most 50 °C, based on the temperature of a silicon reference cell. The lamp intensity of the solar simulator is adjusted with the same silicon reference cell. Electrical probes are used to contact the contact pads on the glass substrate with a source-measure unit (Agilent B2910). The voltage is scanned with a positive and negative scan rate between -1V and 1V in 2001 steps while the current is recorded (60 ms aperture and 70 ms delay between measurements). We observed no hysteresis in any of our measurements.

Au electrode with alignment markers were fabricated on plasma cleaned glass substrates by UV lithography and metal evaporation. The nanowires are transferred from the arrays ($\sim 200 \times 200$ μm^2) via a pipette in ethanol and are randomly drop-cast on the substrates. Electron beam lithography and metal evaporation are used to contact the single nanowires to the Au electrodes (see Fig. 6.9a). It was found that the exact placement of the contact position on the highly doped end-segments of the nanowires is a crucial step to allow good ohmic contact and prevent extraction barriers. Then, the glass substrates are wire-bonded to glass holders, which have prefabricated metal contact lines (also by masking and metal evaporation). The bottom of the glass holder is connected to a printed-circuit-board socket which also connects to a flat electrical cable extending outside of the integrating sphere (see Fig. 6.1c).

Fig. 6.9b shows a top-down view on the electrode glass substrate under the solar simulator. The connected nanowire (red, not to scale) is placed in the center and black, fully opaque foil covers a large part of the substrate. Even though the nanowire is fully covered the solar simulator measurement results in a short-circuit current of ($I_{sc} \sim 100$ pA). We note that this amounts approximately to the difference between the short-circuit current determined with the solar simulator (450 pA) and the one determined with the integrating sphere setup (320 pA). Fig. 6.9c shows as a schematic the side view on the setup configuration. The light is scattered into the glass substrate at the glass and Au electrode edges and trapped inside the thin glass slab. As a result the nanowire is not only illuminated from the top, but also partially from the bottom, which results in an inaccurate measurement. Given the common usage of glass substrates for single optoelectronic nanoscale device measurements, we stress the importance of using appropriate setups or masking conditions to avoid measurement errors.

The 28% higher intensity in the solar simulator measurement may lead to an overestimation of the V_{oc} under 1 sun of up to 8 mV. However, given that the V_{oc} seems limited by contact selectivity, it is not clear by how much exactly the V_{oc} would decrease.

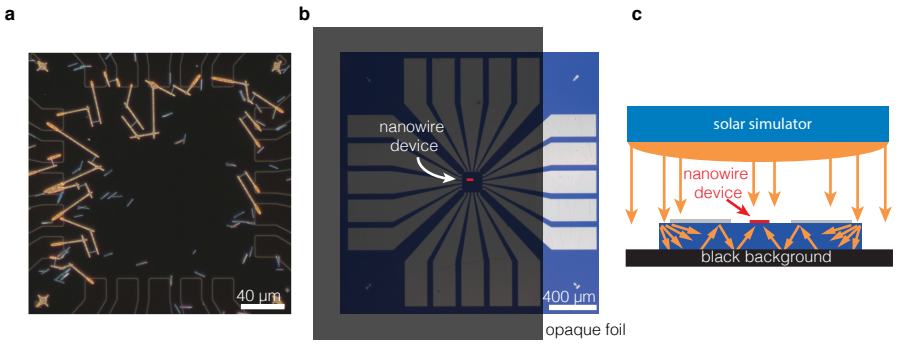

Figure 6.9: Contact pads and solar simulator measurements. a. Dark-field microscope image showing the center of the substrate after nanowires (white) have been drop-casted and contacted (gold). **b.** Schematic of top-down view on electrode glass substrate under solar simulator. The connected nanowire (red, not to scale) is placed in the center and black opaque foil covers a large part of the substrate. Even though the nanowire is fully covered the solar simulator measurement results in a short-circuit current of I_{sc} = 100 pA. **c.** Schematic of side view, showing the solar simulator and the glass substrate with the single nanowire device. The light is scattered into the glass substrate at the glass and Au electrode edges and trapped inside the thin glass slab. As a result the nanowire is not only illuminated from the top, but also partly from the bottom, which results in overestimation of the I_{sc}.

7

Superabsorption in thin semiconductor films wrapped around metal nanowires

Metallic and dielectric nanostructures have highly tunable resonances that have been used to increase light absorption in a variety of photovoltaic materials and device structures. Metal nanowires have also emerged as a promising candidate for high-performance transparent electrodes. In this chapter we propose combining these electrical and optical functions. While absorption in semiconductor nanowires is typically limited by the so-called "single channel limit", we show that metal-semiconductor core-shell nanowires can absorb significantly more than this limit. Even when weighted to the broadband solar spectrum, core-shell nanowires absorb more light than their solid counterparts, while at the same time the semiconductor volume is significantly reduced.

7.1 Introduction

Light trapping enables strong absorption of light in thin semiconductor layers, which is crucial for low-cost yet high efficiency photovoltaics. Over the past decade, light trapping research has shifted focus from large-scale texturing, intended to increase scattering within the ray-optics limit, to nanoscale patterning, designed to confine photons in the active layer via optical resonances and waveguide modes [49, 120, 211, 227, 228]. This shift has been enabled by the flourishing

field of nanophotonics, which has demonstrated impressive control over photon confinement using both metallic [43, 229] and dielectric resonators [118]. By making the resonator from an absorbing material, the high field intensities inside the structure can directly contribute to improved absorption [47, 228] and even photocurrent [55].

As discussed in the Introduction (Chapter 1), the strength of the absorption in a nanostructure is typically described by the absorption cross section $\sigma_{\text{abs}} \equiv P_{\text{abs}}/I_0$, where P_{abs} is the absorbed power and I_0 is the intensity of the incident plane wave. For resonances in systems with cylindrical geometry, such as nanowires, the absorption cross section of a single resonance is fundamentally limited to $\lambda/2\pi$. In this chapter we show that, while a single resonance can not absorb more than $\lambda/2\pi$, the absorption cross section of the cylindrical nano-object itself can actually significantly exceed this limit. We will first discuss absorption in simple semiconductor nanowire systems. We will then elaborate on how metal-semiconductor core-shell nanowires can create "superabsorbers", with $\sigma_{\text{abs}} > \lambda/2\pi$ with low polarization dependence.

7.2 Absorption in nanowires

We begin our discussion by investigating a solid semiconductor nanowire as a simple model system. Analytical calculations for such systems rely on Mie theory, a powerful and well-known tool to analyze the optical properties of spheres and (infinitely long) nanowires [38]. Mie theory relies on decomposing the electric and magnetic fields into an orthogonal basis set of vector harmonics, and matching the boundary conditions for each harmonic. It then turns out that the total scattering cross section is simply given by:

$$\sigma_{\text{sca}} = \sum_{m=0}^{\infty} (2-\delta_{m,0})|a_m|^2, \tag{7.1}$$

where a_m is called the Mie coefficient or scattering coefficient. Similarly, the extinction and absorption cross sections is given by:

$$\sigma_{\text{ext}} \equiv \sigma_{\text{abs}} + \sigma_{\text{sca}} = \sum_{m=0}^{\infty} (2-\delta_{m,0})\text{Re}\{a_m\} \tag{7.2}$$

$$\sigma_{\text{abs}} = \sigma_{\text{ext}} - \sigma_{\text{sca}}. \tag{7.3}$$

These equations can be derived by integrating the Poynting vector over a surface surrounding the nanowire [38], or directly through energy conservation [33].

From Eqs. 7.1-7.3 it is clear that the absorption cross section can be decomposed into independent contributions $\sigma_{\text{abs}}^{(m)}$, where m referes to the angular momentum channel. In other words, m describes the number of angular nodes in the field distribution. Note that channels with $m \geq 1$ contribute twice as much to the

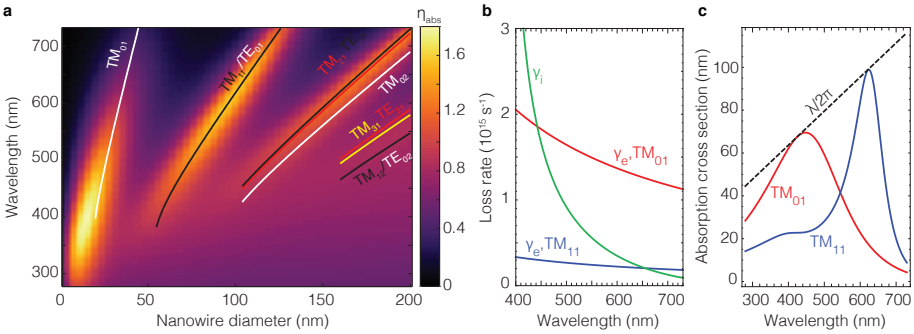

Figure 7.1: The magnitude of the absorption cross section depends on the radiative and absorption loss rates. a. 2D color plot of the absorption efficiency for a range of wavelengths and a-Si nanowire diameters. The white, black, red and yellow lines correspond to resonances (see Supplementary Information Section 7.6.1 for details). **b.** The absorption loss rate γ_i (green) and radiative loss rates γ_e for the TM_{01} (red) and TM_{11} (blue) resonances. The intersections indicate where the resonances are critically coupled. **c.** Absorption cross sections for the TM_{01} (red) and TM_{11} (blue) resonances in 22 and 102 nm diameter a-Si nanowires, respectively. The dashed line is the fundamental absorption limit for a single channel, $\lambda/2\pi$.

total cross section as the lowest order, $m = 0$ channel, due to degeneracy in the azimuthal phase (clockwise and counterclockwise propagation).

Within each channel there are "leaky mode resonances", which have previously been shown to correspond to peaks in the scattering and absorption spectra of nanowires [120, 223]. Aside from the azimuthal mode number m these are characterized by a radial mode number l, which signifies the number of radial field maxima within the nanowire. This notation is similar to the one used for atomic orbitals to designate principle and angular quantum numbers, which also are related to the number of radial and angular nodes, respectively. These geometrical resonances occur for approximately fixed values of nk_0r, where n is the refractive index of the nanowire material, k_0 is the free space wavevector and r is the radius of the cylinder [202]. Thus, one can tune the resonant wavelength by changing the diameter of the nanowire. This is clearly visible in Fig. 7.1a, where the unpolarized absorption efficiency spectrum of an amorphous silicon nanowire under normal incidence is shown as a function of the nanowire diameter. The absorption efficiency is defined as the σ_{abs} normalized to the diameter of the nanowire.

The white, black, red, and yellow lines in Fig. 7.1a show the resonance dispersion calculated with mode-solver calculations for the 0^{th}, 1^{st}, 2^{nd}, and 3^{rd} order azimuthal channels, respectively (see Supplementary Information for details on the calculations). Note that a distinction is made between the TE and TM polarizations, which have the electric field perpendicular or parallel to the nanowire axis respectively. In cylindrical coordinates the TM_1 and TE_0 channels are degenerate.

From Fig. 7.1a it is clear that the absorption efficiency of a specific resonance is not constant for a given nk_0r value, but always has a maximum at a particular diameter/wavelength combination ($d = 16/\lambda = 400$ nm for TM_{01}, $d = 110/\lambda = 600$ nm for TM_{11}/TE_{01}). To understand this behavior, we turn to temporal coupled mode theory [33, 230], which gives expressions for the resonance lineshapes [231]:

$$\sigma_{\text{abs}}^{(m,l)} = \frac{2\pi}{\lambda} \frac{\gamma_e \gamma_i}{(\omega - \omega_0)^2 + (\gamma_e + \gamma_i)^2}, \tag{7.4}$$

where ω_0 is the resonance frequency and γ_i and γ_e are the absorption and radiative loss rates of the resonance. This equation gives a lorentzian lineshape, which has a maximum absorption cross section when $\omega = \omega_0$ and $\gamma_e = \gamma_i$:

$$\max\left(\sigma_{\text{abs}}^{(m,l)}\right) = \frac{\lambda}{2\pi}. \tag{7.5}$$

This condition ($\gamma_e = \gamma_i$) is called critical coupling: the direct and scattered contributions to the outgoing field destructively interfere completely, such that all power is absorbed inside the cavity. This fundamental limit to absorption in a single channel can also be derived starting from Mie theory [232]. Note that these equations are strictly only valid when $\omega_0 \gg \gamma_e + \gamma_i$, but as we will see, the critical coupling condition is a good indicator for the frequency of the maximum cross sections in Fig. 7.1a nonetheless.

We estimate the absorption loss rates γ_i for the TM_{01} and TM_{11} resonances by calculating the power loss per unit time:

$$\gamma_i = \alpha \frac{c}{n_g}, \tag{7.6}$$

where c is the speed of light, $n_g$is the material group index, and $\alpha = 2k_0\kappa$ is the absorption coefficient with κ the material extinction coefficient. We thus find $\gamma_i = 2\kappa\omega/n_g$. When only a fraction f of the modal energy is confined within the absorbing medium, the absorption loss rate is reduced linearly with that fraction. Here, for simplicity, we assume that confinement $f = 1$. We estimate the radiative loss rates from mode solver calculations, as discussed in Supplementary Information Section 7.6.2. Both loss rates are shown in Fig. 7.1b.

The critical coupling condition is met when the radiative and absorption loss rates cross. For comparison, Fig. 7.1c shows the absorption spectrum of the critically coupled TM_{01} and TM_{11} resonances together with the fundamental limit to absorption in a single channel ($\lambda/2\pi$, dashed line). Indeed, while coupled-mode theory is strictly only valid in the low loss regime, the condition $\gamma_e = \gamma_i$ predicts the maximum absorption cross sections quite well.

Note that the higher radiative loss rate for the TM_{01} resonance is directly related to the broader bandwidth in Fig. 7.2c. All higher order resonances have radiative loss rates much lower than that of the TM_{01} mode. Paradoxically, this means that for these higher order modes, *absorption in the semiconductor increases when the absorption coefficient decreases.* This counterintuitive result means that these optical

resonances are especially effective at improving absorption in exactly the spectral regions that can benefit the most from light trapping (for example near the band edge).

7.3 Broadband and unpolarized absorption

So far we have discussed single resonances that contribute to a finite absorption band in only one polarization, but in photovoltaic and solar fuel applications we want to achieve broadband absorption in both polarizations. For a given geometry we therefore calculate the integrated weighted absorption efficiency over the solar spectrum:

$$\overline{\eta}_{\text{abs}} = \frac{\int S(\lambda)\eta_{\text{abs}}(\lambda)d\lambda}{\int S(\lambda)d\lambda}. \tag{7.7}$$

Here η_{abs} is the absorption efficiency and $S(\lambda)$ is the photon flux density in the AM1.5 solar spectrum [4]. The weighted absorption efficiency reflects the total number of photons absorbed in a single nanowire compared to the total above band gap photon flux through the geometrical cross section. As noted earlier, the absorption cross section in a single nanowire can exceed the geometrical cross section, due to the well-known antenna effect in subwavelength structures [233]. This benefit becomes more complex in large-scale nanowire array devices, where coupling between nanowires must also be considered.

Fig. 7.2a shows $\overline{\eta}_{\text{abs}}$ for a solid a-Si nanowire as a function of the nanowire diameter (in red). We integrated over the solar spectrum from 280 to 730 nm (1.7 to 4.4 eV), which are the shortest wavelength in the AM1.5 solar spectrum and the band gap of a-Si, respectively. The peaks that appear at 25, 110 and 180 nm diameters are close to the diameters at which each of the resonances reach their maximum absorption cross section: first the TM_{01}, then the degenerate TM_{11}/TE_{01}, and so forth.

The maximum weighted absorption of 0.9 is achieved close to where the TM_{11}/TE_{01} resonances are maximally absorbing (110 nm diameter). While the TM_{01} resonance absorbs extremely efficiently at small diameters, in that size range there is no absorption in the TE polarization (solid and dashed blue curves in Fig. 4.3a respectively). This emphasizes the importance of a good response in both polarizations. Furthermore, below 200 nm a solid nanowire is more strongly absorbing in the TM polarization because the TE_0 channel only contributes once to the absorption cross section (not degenerate, Eq. 7.1), while the TM_1 channel contributes twice (it is doubly degenerate, Eq. 7.1).

A key strategy to enhance the absorption efficiency of a nanostructure is to increase the number of supported resonances, while maintaining the same particle size [45, 160]. This strategy is most effective when one maximizes the number of resonances that are critically coupled. In a regular nanowire or sphere described by a single size parameter this can not be done, because all resonances scale with the

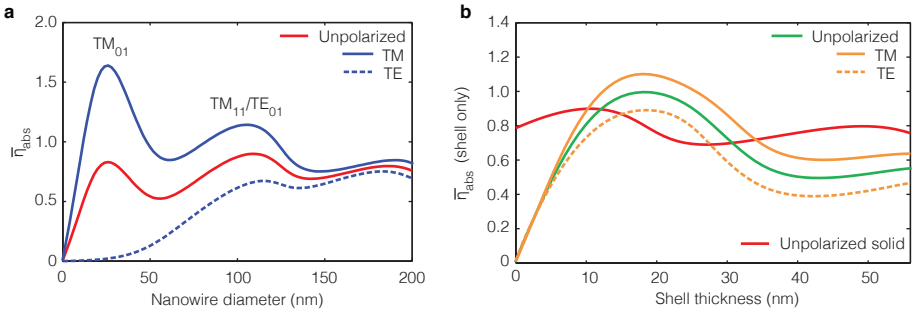

Figure 7.2: The broadband absorption efficiency of solid nanowires compared to metal-semiconductor core-shell nanowires. a. The weighted absorption efficiency of a solid a-Si nanowire for unpolarized light (red), in TM (blue, solid) and TE (blue, dashed), as a function of diameter. The peaks correspond to critically coupled resonances. **b.** The weighted absorption efficiency in an a-Si shell wrapped around an 88 nm diameter Ag nanowire as a function of shell thickness for unpolarized light (green), in TM (orange, solid) and in TE (orange, dashed). The red curve is the unpolarized weighted absorption efficiency in a solid a-Si nanowire with the same outer diameter (i.e. from 88 to 200 nm).

size parameter. In contrast, by adding an additional degree of freedom, resonances can be tuned spectrally with respect to each other. This can be done for instance through breaking the spherical or cylindrical symmetry and moving to ellipsoidal, rectangular or other shapes [234]. In fact, in terms of absorption per unit volume of a nanoscale object, spherical and cylindrical shapes are most likely not the most efficient [235, 236].

Here, we will not break cylindrical symmetry but instead move to a core-shell geometry. In particular, we will insert a metal nanowire into a semiconductor nanowire, which aside from increased tunability has an additional benefit: while the nanowire geometry itself already allows for excellent charge extraction [210, 212, 237], metal nanowires have higher conductivity and should therefore provide a more effective local contact. In fact, metal nanowire networks have already been demonstrated as high-performance transparent electrodes in touch-screen, display and photovoltaic applications [238]. One of the limiting factors for such next generation electrodes is the parasitic optical absorption loss caused by reflected and scattered light [51, 239, 240]. By embedding metal nanowires in ultrathin semiconducting shells these parasitic losses may be reduced.

To calculate the optical properties we extended Mie theory for cylinders to core-shell nanowires (see Supplementary Information Section 7.6.1). Note that we want to maximize absorption in the shell, because absorption in the metal core does not contribute to photocurrent generation. In this case, we investigate a Ag nanowire coated with an a-Si shell. To calculate only the absorbed power in the shell we make

use of the explicit expressions of the electric field [190]:

$$P_{abs} = -\iint \nabla \cdot \langle \mathbf{S} \rangle \, r \, d^2\mathbf{r} = \frac{\omega \varepsilon_0}{2} \iint \mathrm{Im}\{\varepsilon(\mathbf{r})\} |\mathbf{E}(\mathbf{r})|^2 \, r \, d^2\mathbf{r}. \tag{7.8}$$

Here the ε_0 is the permittivity of free space, ω is the frequency, $\langle \mathbf{S} \rangle$ is the time-averaged Poynting vector, and $\varepsilon(\mathbf{r})$ is the relative permittivity. By integrating over the shell and normalizing to the incident intensity and diameter, the partial absorption efficiency in the shell can be obtained. We again weight the absorption efficiency to the solar spectrum using Eq. 7.7. The result for increasing a-Si shell thickness coated on an 88 nm diameter Ag core is shown in Fig. 7.2b. An unpolarized weighted absorption efficiency of 1 is observed at a shell thickness of only 18 nm (Fig. 7.2b, green). This extraordinary absorption is higher than what can be attained in solid semiconducting nanowires (red, Fig. 7.2a and 7.2b). By comparing the dashed curves from Figures 7.2a and 7.2b it becomes clear that the absorption efficiency boost stems primarily from enhanced absorption in the TE polarization.

7.4 Superabsorption

To understand why absorption increases in the core-shell structure despite the significant decrease in semiconductor volume, it is instructive to examine the absorption spectra of these nanowires. Fig. 7.3a shows the absorption efficiency spectra in the TE polarization for the most efficiently absorbing solid nanowire (110 nm diameter). It is clear that for this diameter the largest contribution to broadband absorption stems from the critically coupled TE_{01} resonance (blue). This is interesting, because it has previously been pointed out that the largest contribution of a single resonance to broadband absorption is in the strong overcoupling limit ($\gamma_e \gg \gamma_i$) [45]. However, this is only true of the radiative loss rate γ_e can be tuned independently of the absorption loss rate γ_i, and can be made arbitrarily large. In contrast, in the present system the only way in which overcoupling can be achieved is by enhancing the nanowire diameter and redshifiting the resonance (see Fig. 7.1b), which at some point reduces absorption again due to a vanishing γ_i.

In the previous section we observed that single resonances can absorb at most $\lambda/2\pi$, the single-channel limit, which is shown in Fig. 7.3 as a dashed line. However, a straightforward approach to enhance the absorption is by enhancing the spectral resonance density [202]. This is in fact the origin of the strong absorption in the core-shell nanowire, as is shown in Fig. 7.3b: the TE_{01} and TE_{11} modes overlap, causing the absorption peak to be significantly higher than the single-channel limit. In this optimal configuration absorption is strongest near the band gap, which is due to the almost critically coupled resonances. In the shorter wavelength region where a-Si is strongly absorbing it is hard to enhance the absorption significantly with resonances, because the absorption loss rate is so high that these resonances are all undercoupled. It is also important to note that there is still a small amount of light lost to absorption in the metal (Fig. 7.3c), but that we omitted this absorption for the weighted absorption efficiency in Fig. 7.2 as it does not contribute

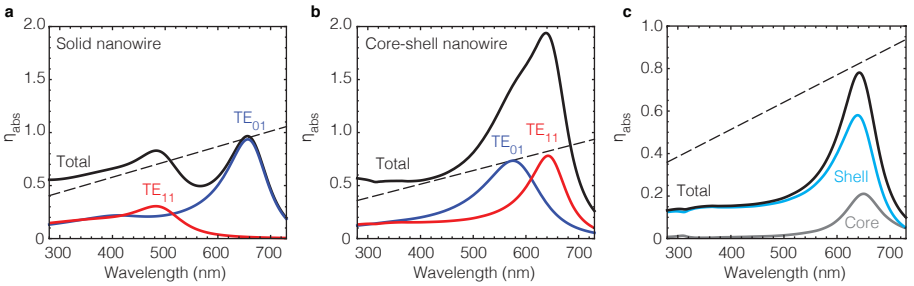

Figure 7.3: The absorption efficiency in solid and core-shell nanowires decomposed into angular momentum channels. **a.** Absorption efficiency spectra for a 110 nm diameter a-Si nanowire in the TE polarization. Black shows the total absorption, blue and red the 0th and 1st order channel contributions. The TE_{11} resonance is very close to being critically coupled. **b.** Absorption efficiency for 88 nm silver core with a 18 nm a-Si shell, demonstrating that the $\lambda/2\pi$ limit is now significantly surpassed due to closely spaced and strongly absorbing resonances in the $m = 0$ and $m = 1$ channels. **c.** Absorption efficiency spectrum in TE_1 channel for the same core-shell nanowire, but broken down into absorption in the shell (blue) and core (grey). In all figures the dashed line shows the fundamental limit to absorption in a single channel (resonant mode), $\lambda/2\pi$, normalized to the diameter of the nanowire.

to photocurrent. In the TM polarization, absorption in the solid and core-shell nanowires is almost the same: in both cases the TM_{11} resonance dominates (see Supplementary Information Fig. 7.6).

The nature of the optical resonances in these core-shell nanowires can be understood intuitively by considering the ratio of the inner to outer radius. For example, in solid nanowires in the TM polarization the electric fields are strongest near the semiconductor-air interface, except for the lowest order azimuthal modes in TM_0 where the fields peak in the center. For the higher order azimuthal modes this means that a small metal core can be inserted into the center of the nanowire without perturbing the resonance. This is shown in Fig. 7.4a: the scattering efficiency ($\eta_{sca} \equiv \sigma_{sca}/d$) of a core-shell nanowire with silver core and dielectric shell ($n = 3$) is shown as a function of wavelength and core size for a fixed outer diameter. The TM_{11}, TM_{21}, and TM_{31} resonances are visibly perturbed at a core diameter that increases with increasing mode number. This can be understood from the field profiles of these modes, which are shown in Fig. 7.4b: the larger the mode number, the stronger the confinement to the semiconductor-air interface, and the larger the core can be without perturbing the mode. Because the metal inclusion squeezes the fields outwards and reduces the mode size the modes blueshift.

If the core is large with respect to the shell, the modes are strongly perturbed and the nature of the resonances essentially changes from Mie resonances to waveguide modes or Fabry-Pérot resonances travelling around the circumference of the nanowire. In a simplified geometrical optics picture, the difference between the

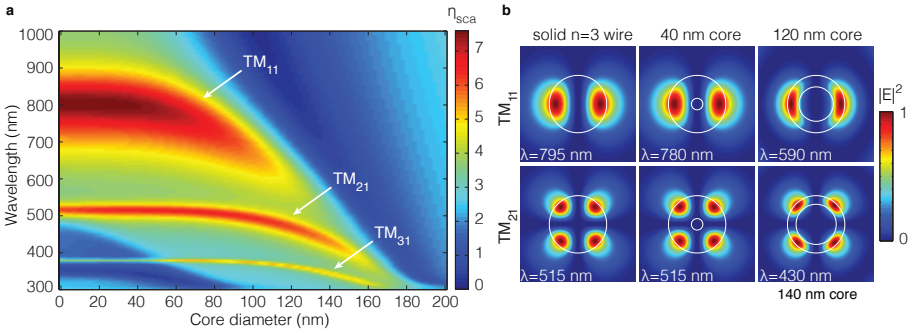

Figure 7.4: Perturbation of the resonances due to the metal core. a. The scattering efficiency as a function of wavelength and core diameter for a core-shell nanowire with fixed total diameter of 200 nm and shell refractive index $n = 3$. For higher angular momentum channels the mode starts to be perturbed at larger core diameters. **b.** Field intensity plots of the resonance profiles for the TM_{11} and TM_{21} resonances for no core, a 40 nm core, and a 120 nm core. For resonances in higher angular momentum channels the fields are more confined to the shell-air interface, explaining why the core can be larger before the resonance is perturbed.

two regimes is that in the unperturbed case light only experiences total internal reflection from the semiconductor-air interface, while in the latter case it also reflects off of the metal core [241]. This connection between planar waveguide modes and resonances in the cylindrical structure has been observed before for coaxial nanowires and metal-insulator-metal waveguides [242].

Interestingly, utilizing these different resonance types, resonances can also be made almost degenerate across polarizations. Fig. 7.5a shows the TM_{11} and TE_{11} resonances for a 180 nm Ag core with a 10 nm a-Si shell. The TE_{11} resonance is the plasmon resonance, redshifted due to the high-index shell, while the TM_{11} resonance most closely resembles a waveguide mode resonance in the shell. The dispersion of these resonances is different: the TM_{11} resonance shifts with total circumference and shell thickness, while the plasmon resonance only shifts with shell thickness, and hence they can be tuned with respect to each other. This is markedly different from the solid nanowire case, where these two resonances are always spectrally separated.

Finally, it is important to note that while enhancing the density of resonances can significantly increase the total absorption cross section, it is important to keep in mind that resonances in the same angular momentum channel can not be brought arbitrary close. Resonances in the same angular momentum channel are not orthogonal to each other (see Supplementary Information, in Section 7.6.1), and as a result they will couple. This coupling will be strong due to the large field overlap of resonances in the same channel, and as a result these resonances will repel and demonstrate avoided crossings [243, 244]. This is for example clearly

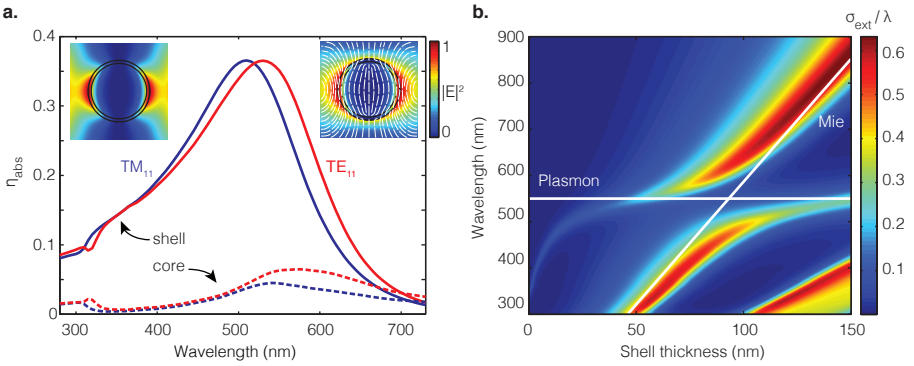

Figure 7.5: Near-degeneracies across polarizations and avoided crossings in the same channel. a. Absorption efficiency in TM_{11} (blue) and TE_{11} (red) for a 180 nm silver core with a 10 nm a-Si shell. The near-degeneracy indicates the Fabry-Pérot-like behavior. The solid lines indicate absorption in the shell, the dashed lines absorption in the core. The insets show the electric field intensities (with the stream plot indicating the direction of the field) for the TM_{11} (left) and TE_{11} (right) resonances. **b.** Two resonances within the same angular momentum channel are not orthogonal, resulting in coupling between the resonances if they are brought close together in frequency. The strong coupling between these resonances results in avoided crossings, as shown in the color map. In this case, an n=3 shell is added to a 100 nm diameter silver nanowire. The white lines show the resonance frequencies of the plasmon resonance in a homogeneous medium with n=3 and the dispersion of the TE_{11} Mie resonance without the metal core.

visible in Fig. 7.5b, where the dipolar plasmon resonance and first Mie resonance in the TE_1 channel are shown as a function of dielectric ($n = 3$) shell thickness for a fixed core diameter. For very thin shells the plasmon resonance rapidly redshifts, untill the redshift saturates when the evanescent fields of the plasmon are contained entirely in the shell. In contrast, the TE_{11} Mie resonance shifts linearly with total diameter, and hence at a certain diameter the resonances would cross. However, due to the strong coupling rate, they display an avoided crossing, and can not be brought arbitrarily close. Strong coupling is observed in many other systems, such as particle arrays coupled to waveguides [245] and even single molecules coupled to plasmonic spheres [246].

We have thus far shown results for systems involving perfect Ag cylinders coated with a-Si. The high symmetry of such model systems allows us to use Mie theory to break down the total absorption into the constituent channels. This provides deep insight into the underlying physics while minimizing calculation time. However, real nanowire core-shell structures will have a number of deviations from our ideal calculations. First, the cross sectional shape will likely not be circular; metal nanowires grown by the polyol process typically have a pentagonal cross section [247], while semiconducting nanowires often have hexagonal or other

complex cross sectional shapes [248]. We have used finite-difference time-domain simulations (FDTD, Lumerical [140]) to confirm that as with solid semiconducting nanowires [202] the cross sectional shape only has minor effects on the resonant properties and absorption results. We have also used FDTD to confirm that placing core-shell nanowires on low-index substrates like glass or plastic only leads to minor perturbations, primarily by increasing the radiative loss rate in the cavity and thus requiring a different shell thickness to maintain critically coupled resonances. Both of these results are shown in the Supplementary Information at the end of this chapter, Fig. 7.8.

These results are not limited to a-Si; silver nanowires with a CdTe shell show very similar behavior, although the optimal shell thickness is 46 nm due to a lower band gap energy and lower refractive index (see Supplementary Information, Fig. 7.7). In fact, any combination of metals and semiconductors should benefit from this geometry as long as the metal loss is low, the semiconductor absorption coefficient has a rapid increase near the band gap (typically direct band gap materials), and the shell refractive index is high (most inorganic semiconductors).

7.5 Conclusion and discussion

We have shown that the key to increasing absorption in nanoscale systems is to increase the strength and number of resonances. We have demonstrated that a given resonance is strongest when the loss rates due to absorption and radiation (leakage from the cavity) are equal. For light-trapping purposes this leads to the counter-intuitive but fortunate conclusion that most resonances are typically strongest in spectral regions where the material absorbs the weakest. We have also demonstrated that inserting a silver core into semiconducting nanowires can lead to enhanced absorption in the shell material. This occurs because the core-shell geometry can increase the number of nearly degenerate resonances and lead to super-absorption, absorption cross sections significantly exceeding the single-channel limit. An added benefit of such a structure is that the metal core would provide an ideal local contact for photogenerated carrier extraction, which we explore experimentally in Chapter 8.

For future work it may be interesting to investigate in more detail the dispersion relation of these resonances depending on core and shell radii. In particular, a connection between the planar metal-insulator-insulator geometry and the metal-semiconductor core-shell nanowire may be unearthed, just as is the case for the planar metal-insulator-metal geometry [242].

7.6 Supplementary Information

7.6.1 Mie theory

To facilitate the discussion of the mode solver calculations it is useful to briefly derive the Mie coefficients for the scattered field. For simplicitly we consider a nanowire illuminated perpendicular to the long axis of the nanowire, with the electric field polarized along the nanowire axis. In this case the electric field reduces to a simple scalar field [38]:

$$E(\mathbf{r}) = E_0\Big(e^{i\mathbf{k}\cdot\mathbf{r}} + \sum_{m=-\infty}^{\infty}(-i)^m b_m h_m^{(1)}(k_0 r)e^{im\theta}\Big). \tag{7.9}$$

Here the first term is the incident electric field (with $\mathbf{k}$ the wavevector) and the second term is the scattered field. a_m is the amplitude of the scattered field (or "Mie coefficient"), $h_m^{(1)}$ is the m^{th} order Hankel function of the first kind, and r and θ are the polar coordinates. The incident and internal fields can also be expressed in terms of vector harmonics:

$$E_{\text{inc}}(\mathbf{r}) = \sum_{m=-\infty}^{\infty}(-i)^m j_m(k_0 r)e^{im\theta} \tag{7.10a}$$

$$E_{\text{int}}(\mathbf{r}) = \sum_{m=-\infty}^{\infty}(-i)^m f_m n j_m(nk_0 r)e^{im\theta}. \tag{7.10b}$$

Boundary conditions for the electric field require that the tangential field is continuous across the boundary, which allows us to write (after combining Eqs. 7.9 and 7.10):

$$n f_m j_m(nk_0 r) - b_m h_m^{(1)}(k_0 r) = j_m(k_0 r). \tag{7.11}$$

This equation has two unknown field coefficients, b_m and f_m. However, a similar equation can be obtained from the boundary conditions for the magnetic field, which allows us to set up a system of linear equations:

$$\begin{pmatrix} h_m(k_0 r) & n j_m(nk_0 r) \\ h_m'(k_0 r) & n^2 j_m'(nk_0 r)\end{pmatrix}\begin{pmatrix} b_m \\ f_m\end{pmatrix} = \begin{pmatrix} j_m(k_0 r) \\ j_m'(k_0 r)\end{pmatrix}. \tag{7.12}$$

Such a system of equations $\mathbf{M}\cdot\mathbf{x} = \mathbf{u}$ is easily solved through Cramer's rule for the coefficients b_m and f_m. For the core-shell nanowires the approach is exactly the same, except that there is an additional region with fields for which the coefficients have to be solved. In the shell region the fields are generally given by:

$$E_{\text{shell}} = n_2 \sum_{m=-\infty}^{\infty}(-i)^m\Big(v_m j_m(n_2 k_0 r) - w_m h_m^{(1)}(n_2 k_0 r)\Big)e^{im\theta}. \tag{7.13}$$

Here n_2 is the shell refractive index. From the two interfaces one now obtains a 4×4 matrix which can be solved using Cramer's rule again. The same approach

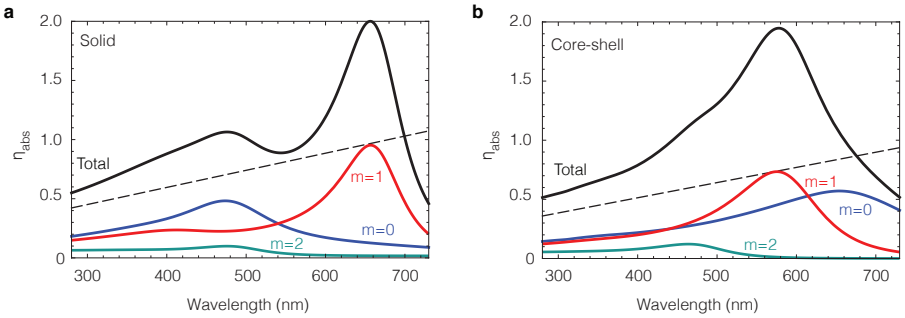

Figure 7.6: Absorption efficiency in the solid and core-shell nanowire for the TM polarization. a. Absorption efficiency in a 110 nm diameter solid a-Si nanowire decomposed into its angular momentum channels. The numbers near the colored curves indicate the order of the angular momentum channel. **b.** The absorption efficiency of the core-shell nanowire in the TM polarization, with the same color coding as in panel **a**. The dashed black line in both panels shows the single channel limit, $\lambda/2\pi$.

can be followed for electric fields polarized perpendicular to the nanowire axis, in which case a scalar equation is obtained for the magnetic field. The response of the nanowire in the TM polarization is shown in Fig. 7.6. It is clear that the optical response between the solid and core-shell nanowires differs less strongly than it does in TE (see Fig. 7.3). The main difference is the strong redshift of the lowest order resonance in the core-shell geometry, which is because the maximum field intensity in the lowest order mode is in the center of the nanowire, resulting in strong perturbation of the resonance. Note that all dielectric functions used in this Chapter come from Palik [207].

7.6.2 Mode solver calculations

To find the eigenmodes we remove the incident field from the linear systems of equations in Eq. 7.12, which results in a homogeneous system of equations $\mathbf{M}\cdot\mathbf{x} = 0$. Such a system only has a solution when the determinant vanishes, which leads to the transcendental equation:

$$|\det[\mathbf{M}(\frac{\omega}{c})]| = 0. \tag{7.14}$$

Here we are solving for ω to emphasize that we are not interested in guided modes, as $k_{\|} = 0$. The values of ω for which this transcendental equation vanishes are complex. The real part of this complex frequency is the resonance frequency ω_0, the imaginary part is the loss rate $\gamma = \gamma_i + \gamma_e$. To obtain the radiative loss rates only, we set $\gamma_i = 0$ so that $\gamma = \gamma_e$. In practice, this means that we solve the transcendental equation with only the real part of the refractive index. Here we thus implicitly

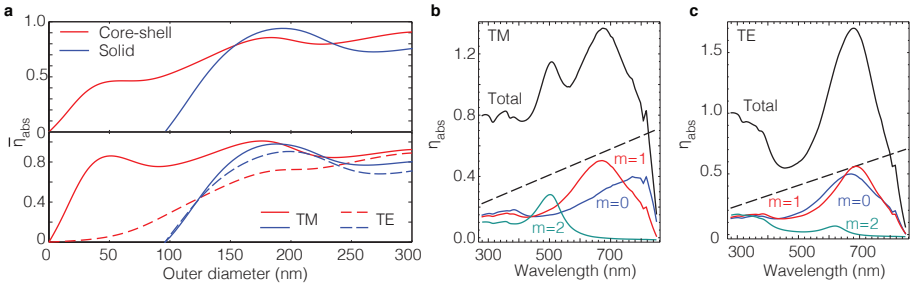

Figure 7.7: Core-shell nanowires with a CdTe shell. a. Weighted absorption comparison for a solid CdTe nanowire (red) and a CdTe shell wrapped around a 96 nm silver core (blue). The bottom plot shows the weighted absorption broken down into TM (solid lines) and TE (dashed lines) polarizations for the solid nanowire (red) and core-shell (blue). **b,c.** Absorption efficiency spectra for a 96 nm silver core with a 46 nm thick CdTe shell in TM and TE polarization, respectively. The total absorption is shown in grey, contributions from $m = 0$ in blue, $m = 1$ in red, and $m = 2$ in green. The black dashed line shows the $\lambda/2\pi$ limit, normalized to the diameter of the nanowire.

make the assumption that the presence of absorption losses does not affect the radiative loss rate.

7.6.3 CdTe core-shell nanowires

In Fig. 7.7a we see that, again, a core-shell with CdTe shell absorbs more efficiently than a solid CdTe nanowire. Because of the lower refractive index and higher band gap the total diameter at which absorption peaks is larger than with the a-Si shell, as a redshift of the resonances is required to achieve critical coupling. Fig. 7.6b and 7.6c show absorption efficiency spectra for the most efficiently absorbing core-shell nanowire in TE and TM respectively. In TM we see a clearly visible contribution to absorption from the TM_{21} resonance (green curve) due to the larger diameter. In TE, the near degeneracy of TE_{01} and TE_{11} is even clearer than with an a-Si shell. The peak absorption cross section of the a-Si and CdTe systems is roughly the same, but the absorption efficiency of the latter is lower due to the larger diameter of the wire.

7.6.4 FDTD calculations

In Fig. 7.8a and b we compare the absorption spectrum of a pentagonal Ag wire conformally coated with a-Si, as calculated with FDTD, to absorption in a cylindrical configuration. The cylindrical Ag, a-Si core-shell nanowire has the optimal configuration (88 nm diameter core, 18 nm thick shell) as discussed in the main text of this Chapter. The pentagonal wire has apothems (distance from the midpoint to the center of one of the sides) equal to the radius of the cylindrical wire (44

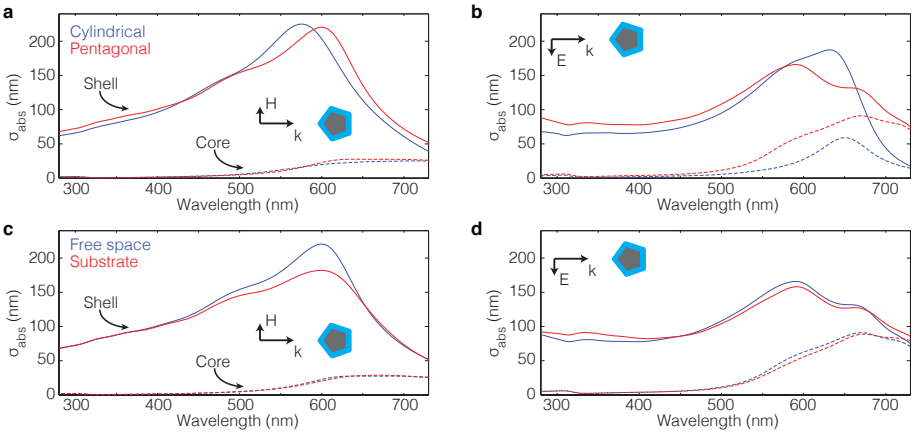

Figure 7.8: The influence of non-cylindrical shapes and substrates on superabsorption. a,b. The absorption cross section for the cylindrical core-shell nanowire discussed in the main text of this chapter, compared to a pentagonal core-shell nanowire with comparable sizes, for the TM (**a**) and TE (**b**) polarization. **c,d.** The absorption cross section for the same pentagonal core-shell nanowires in free space (**a**) and on a quartz substrate ($n = 1.5$) (**b**).

and 62 nm). There are only slight differences between the two configurations, and in general the main conclusions of this work hold: there is reduced polarization dependence compared to solid nanowires, and geometrically induced resonance degeneracy which in TE can be seen even more clearly from the two bumps in the absorption spectrum.

Furthermore, the influence of a substrate is important to take into account. In Fig. 7.8c and d, we show a comparison between a pentagonal wire on a quartz substrate (n=1.5) and in vacuum. Again, the differences are very small, justifying our approach to use Mie theory.

8

Au-Cu_2O core-shell nanowire photovoltaics

Semiconductor nanowires are among the most promising candidates for next generation photovoltaics. This is due to their outstanding optical and electrical properties which provide large optical cross sections, while simultaneously decoupling the photon absorption and charge carrier extraction length scales. These effects relax the requirements for both the minority carrier diffusion length and the amount of semiconductor needed. In Chapter 7 we found that metal-semiconductor core-shell nanowires show even better optical absorption than solid semiconductor nanowires, and offer the additional advantage of a local metal core contact. Here, we fabricate and analyze such a geometry using a single Au-Cu_2O core-shell nanowire photovoltaic cell as a model system. Spatially resolved photocurrent maps reveal that although the minority carrier diffusion length in the Cu_2O shell is less than 1 μm, the radial contact geometry with the incorporated metal electrode still allows for photogenerated carrier collection along an entire nanowire. Current-voltage measurements yield an open-circuit voltage of 600 mV under laser illumination and a dark diode turn-on voltage of 1V. This study suggests the metal-semiconductor core-shell nanowire concept could be extended to low-cost, large-scale photovoltaic devices, utilizing for example, metal nanowire electrode grids coated with epitaxially grown semiconductor shells.

8.1 Introduction

Nanophotonic engineering may facilitate the use of cheaper and lower quality semiconductors by ameliorating the constraints placed on photovoltaic device operation by these materials. For example, some semiconductors have a diffusion length that is shorter than the absorption length, which limits the extractable current from the device. Through light trapping the device thickness can be reduced significantly, such that the diffusion length no longer poses a problem. For example, in Chapter 7 we introduced metal core-semiconductor shell nanowires, which simultaneously enhance absorption in ultra-thin semiconductor shells and facilitate charge extraction through a local metal electrode.

In this chapter we experimentally investigate the optical and photovoltaic properties of metal-semiconductor core-shell nanowires. Core-shell nanoparticles with a metal core have been investigated previously for plasmon mediated charge carrier dynamics for photovoltaics and photocatalysis [249–255]. In these examples, however, the semiconductor materials were not used for strong absorption of light explicitly, and the particles were frequently nanospheres or nanorods suspended in solution. Here we synthesize a thin layer of cuprous oxide (Cu_2O) on silver nanowires and investigate their optical response. We then synthesize Cu_2O on gold nanowires and investigate and photovoltaic response of single core-shell nanowires.

Cu_2O is a direct band gap semiconductor ($E_g \approx 2$ eV), which can be synthesized from earth-abundant and non-toxic materials using many different fabrication methods (*e.g.* by evaporation, sputtering, and from solution). Due to the high band gap, solar cells comprising only Cu_2O can potentially reach power conversion efficiencies of up to 20% [256]. However, when combined with silicon as the bottom absorber ($E_g \approx 1.1$ eV), Cu_2O is a great candidate for the top absorber in a high efficiency multijunction solar cell because its band gap is close to ideal [257–259]. Current research on Cu_2O photovoltaics is largely targeted at thin-films and the interfacial properties of Cu_2O [260–267]. By using interfacial layers such as Ga_2O_3 and ZnO combined with transparent conducting oxides, the open-circuit voltage (V_{oc}) was recently increased to 1.204 V [268], which is 71% of the Shockley-Queisser limit to the V_{oc} (see Chapter 1). In contrast, the short-circuit current (J_{sc}) in the record device (7.37 mA/cm^2) is only 51% of the maximum J_{sc}. This implies that indeed charge-carrier extraction in Cu_2O devices can benefit from nanophotonic engineering.

8.2 Optical characterization of a core-shell nanowire

We begin our characterization of these core-shell nanowires by investigating their optical properties. The metal nanowires were synthesized using the polyol process and subsequently coated with a Cu_2O shell at room temperature in aqueous solution, adapting a protocol originally developed for core-shell nanoparticles [247,

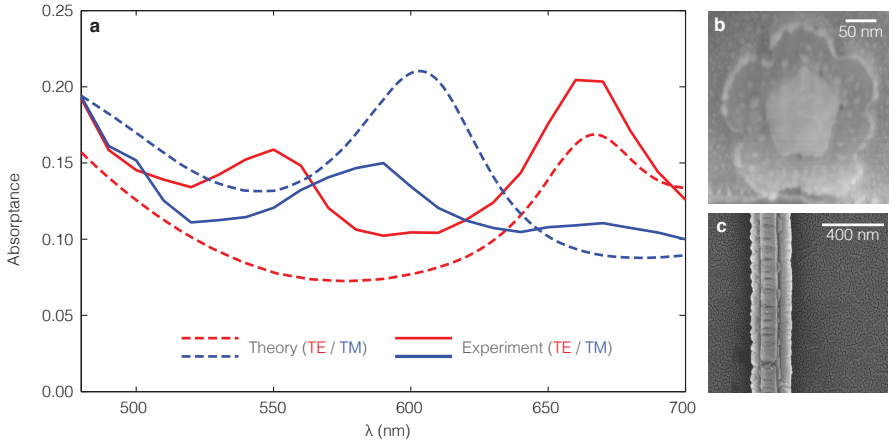

Figure 8.1: Optical characterization of Au-Cu_2O core-shell nanowires. **a.** Absorption spectra of the core-shell nanowire in both polarizations compared to theory. **b.** FIB cross section of a core-shell nanowire that we synthesized and investigated optically. **c.** Top view of the core-shell nanowire before making the FIB cross section, to highlight the surface roughness.

269]. This specific Cu_2O synthesis route was chosen over other methods to produce Cu_2O nanowires because it allowed for epitaxial growth on metal nanowires suspended in solution [270, 271]. The synthesis procedure and materials characterization on the obtained core-shell nanowires are described in detail in Ref. [272].

Nanowires grown in solution were dropcast randomly on a glass substrate prepared with markers to be able to identify the nanowires. We measured the absorption of the core-shell nanowires using integrating sphere microscopy, the experimental technique that we describe in Chapter 5. The fraction of incident light that is absorbed for a certain core-shell nanowire is shown in Fig. 8.1a for both polarizations of incident light. This particular nanowire is shown in SEM images in Fig. 8.1b and c. The pentagonal shape of the metal core is readily recognizable in the FIB cross section in Fig. 8.1b, while from the shape of the shell it appears that the epitaxial growth is seeded from the corners of the pentagonal nanowire.

Fig. 8.1a also shows Mie theory predictions for the core-shell nanowire absorptance, as discussed in detail in Chapter 7. The absorption cross section σ_{abs} as obtained with Mie theory is converted to absorptance using $A = \sigma_{\mathrm{abs}}\sqrt{2/(\pi w_0^2)}$, where w_0 is the beam radius as determined with knife edge measurements (see Chapter 5). Two of the resonant peaks observed in the spectrum correspond to the TE_{21} and TM_{21} resonances observed in Mie theory calculations, but interestingly, the experimental absorption spectrum shows an additional resonance in the TE polarization that does not appear in the Mie theory spectrum. Naturally, Mie theory

assumes perfect cylindrical interfaces, which in this case do not accurately capture the behavior of the core-shell nanowire. However, simulating the cross-section of the nanowire more truthfully to the FIB cross section using finite-difference time-domain simulations also does not yield an additional resonance in the spectrum (Lumerical FDTD, [140]). The solution may lie in the surface roughness of the nanowire, which is hard to capture accurately in a modelling environment. However, surface roughness can enhance the magnitude of an overdamped resonance significantly, due to a larger radiative loss rate (see *e.g.* Section 7.2 on page 120).

8.3 Core-shell nanowire solar cells

To fabricate photovoltaic devices we contacted the core-shell nanowires with two separate electrodes: one that collects photogenerated holes and one that is selective for photogenerated electrons. A simple and effective method to induce this carrier selectivity is to use metal contacts with different work functions such that one metal makes an Ohmic contact to the semiconductor, and the other creates a Schottky junction [273]. Here we have chosen Au as the metal nanowire core because it has a large work function (~5.4 eV; similar to that of Cu_2O) and makes an Ohmic contact to Cu_2O. Furthermore Au has a high chemical stability, low lattice mismatch with Cu_2O (~4%), and a simple nanowire synthesis route [272, 274, 275]. As the Schottky contact we have chosen Ti, which has a low work function (~4.3 eV), excellent adhesion to many materials, and a stable surface oxide [276].

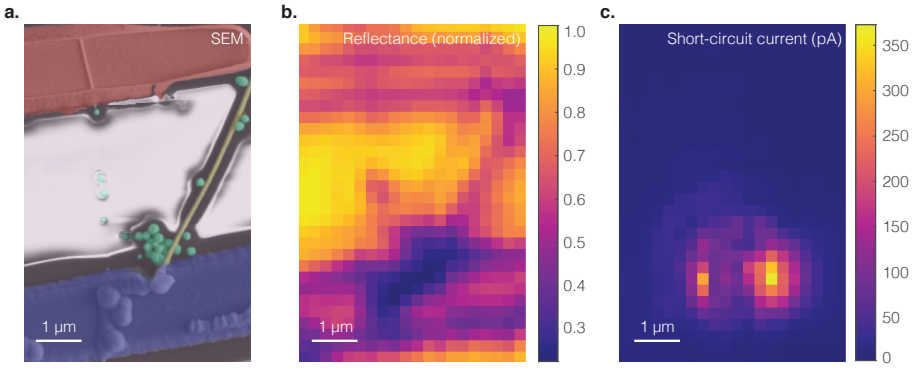

Figure 8.2: Photocurrent and reflection maps of a single Au-Cu_2O nanowire device. a. SEM image of a nanowire (yellow) connected between Ti and Au contacts (blue and red respectively). The green particles are particles of Cu_2O. **b.** Reflection measured at λ = 405 nm over the same area as shown in the SEM image. **c.** Photocurrent map for the same area, measured simultaneously with the reflection map in **b**. The incident laser power is 42 μW, the polarization perpendicular to the nanowire axis, and the spot radius is about 1 μm. From these maps it is clear that photocurrent collection occurs only near the Ti contact.

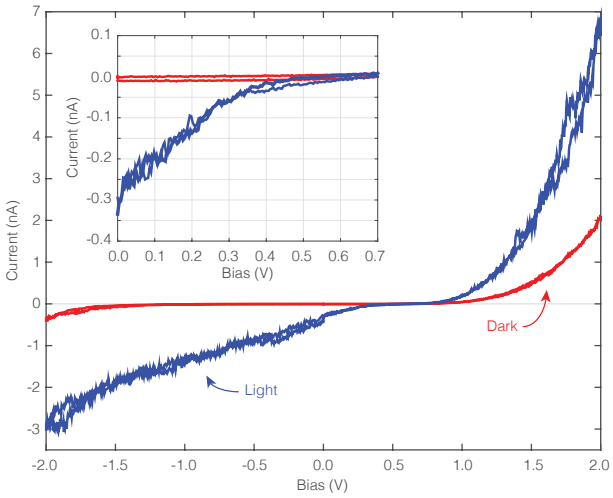

Figure 8.3: Current-voltage behavior of a single Au-Cu_2O nanowire. The I-V curve of the photovoltaic cell in the dark (red line) and under laser illumination (blue line) at 405 nm with a power of 42 μW and polarization perpendicular to the nanowire axis. The inset shows a magnified view of the region 0 - 0.7 V of the I-V curves.

In contrast to the optical measurements, which were performed on glass, we started with Si_3N_4 covered Si substrates with evaporated macroscopic Au electrodes. The core-shell nanowires were contacted using electron beam lithography and subsequent metal evaporation. Details on the fabrication procedure can be found in the Supplementary Information to this chapter (page 142). Fig. 8.2a shows a false color scanning electron microscope (SEM) image of a typical single nanowire photovoltaic cell. The reflection map in Fig. 8.2b shows the reflectance of the sample over the same area as in the SEM, measured at λ = 405 nm with an incident power of 42 μW. Fig. 8.2c shows simultaneously measured photocurrent generation, which peaks at over 300 pA under these conditions. Comparing the different images reveals that charge carrier collection only occurs near the Ti contact finger, where the Schottky junction induces a built-in electric field, such that the minority charge carriers don't have to travel long distances to get extracted. In contrast, carriers excited further away from the Ti contact are not collected. This suggests that the minority carrier diffusion length is less than the beam spot size of ~0.6 μm, consistent with reported values for Cu_2O synthesized by different methods [277, 278].

By placing the illuminating spot at the location where the nanowire device has the highest responsivity, we were able to measure current-voltage (I-V) curves under illumination as well as in the dark (see Fig. 8.3). This nanowire device showed clear rectifying behavior in the dark, with a turn on voltage of ~1V in the dark. Under laser illumination conditions similar to those in Fig. 8.2 an $I_{sc} > 300$

pA and a V_{oc} of 600 mV were observed. These results demonstrate that single metal-semiconductor core-shell nanowires show a photovoltaic response. The photocurrent increases at higher reverse voltages and reaches reverse break down before saturating. We attribute this slope to a higher carrier collection efficiency at larger reverse bias voltages due to an increased depletion region. Furthermore, from the strongly S-shaped I-V curve we deduce a substantial charge carrier extraction barrier, which is a well-known phenomena that can be attributed to accumulated space charges at the material interfaces or a non-ideal Ohmic contact [279–282]. This observation can be explained by the non-optimized metal semiconductor interfaces, which are likely to induce recombination-active trap states and accumulated space charges, resulting in a charge carrier extraction barrier at one or both of the metal interfaces. Furthermore, it is possible that a redox reaction under the Ti contact converts the Cu_2O to TiO_2 and Cu at the interface [283].

We note that the photocurrent under the AM 1.5 spectrum was below the detection limit (~1 pA) of the source measure unit, and we could therefore not analzye our devices under the full solar spectrum. One of the reasons for the the low photocurrent is the localized Schottky region close to the Ti contact: only a small fraction at the edge of the contact can contribute to the photocurrent. To extend the active area of the device, we will now cover part of the nanowire with an optically thin layer of Ti.

8.4 Extended titanium contacts

To directly probe the importance of the radial built-in field and carrier diffusion lengths, we compare the results in Fig. 8.2 to the case where a 10 nm thin Ti pad covers approximately 2/3 of the nanowire, as shown schematically in Fig. 8.4a. This arrangement is closer to a realistic large-scale device, where the whole nanowire would be covered with an additional contact (either a transparent conductive oxide or a continuous thick metal layer with illumination through a transparent substrate). Fig. 8.4b shows a false color SEM image of the nanowire device, similar to the device studied in Fig. 8.2, but now with a Ti pad on top of the nanowire. Fig. 8.4c shows the reflection image and Fig. 8.4d the respective photocurrent map under 15 μW laser illumination at λ =405 nm, which reveals photocurrent collection from an extended elongated area along the entire length covered by the Ti pad. This supports the hypothesis that charge carriers generated by light passing through the 10 nm Ti pad can be separated and collected at the metal core and the Ti top contact. Normalized for incident power the maximum photocurrent is about 4 times lower than in the axial collection case shown in Figure 8.2, which is most likely due to the presence of the extended Ti pad and other geometrical differences. These results indicate that indeed the short diffusion lengths can be mitigated to some degree by extending the electron contact along the nanowire length. However, in absolute terms the collection efficiency of excited carriers remains low, which we

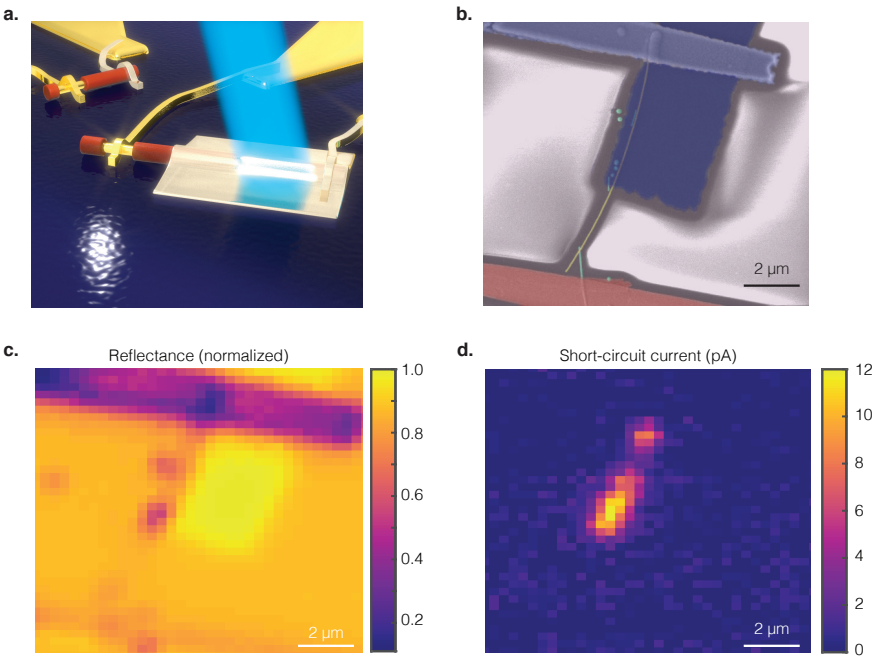

Figure 8.4: Metal-semiconductor core-shell nanowire photovoltaic cell with radial charge carrier collection. a. Schematic depiction of the photovoltaic device layout and measurement, with a thin titanium pad covering a large part of the nanowire. **b.** False color SEM image of a nanowire connected between Ti and Au contacts (blue and red respectively) and partially covered by a 10 nm thin Ti pad (darker blue). The nanowire is shown in yellow and the green particles are Cu_2O spheres. **c.** A reflection map of the same area as shown in the SEM image. **d.** A photocurrent map measured simultaneously with the reflection map. In both measurements the incident laser power is 7 μW, the polarization is perpendicular to the nanowire axis, the beam radius is < 1 μm, and the illumination wavelength is 405 nm.

can quantify using the collection cross section σ_{EQE} introduced in Chapter 6.

Fig. 8.5 shows the quantitative photocurrent response of the core-shell nanowire for four different wavelengths: 405, 520, 620, and 700 nm. The photocurrent response is quantified as the local $\sigma^{(L)}_{\mathrm{EQE}}$, which is different from the unit used in Chapter 6 because it is not yet integrated over the length of the nanowire. In this instance σ_{EQE} is thus given by the product of the IQE and σ_{abs}:

$$\sigma^{(L)}_{\mathrm{EQE}}(\mathbf{x}) = \mathrm{IQE}(\mathbf{x})\sigma_{\mathrm{abs}}(\mathbf{x}), \tag{8.1}$$

where $\mathbf{x}$ is the position. In each of the maps in Fig. 8.5 the polarization is perpendicular to the nanowire axis (TE). In the other polarization the photocurrent response

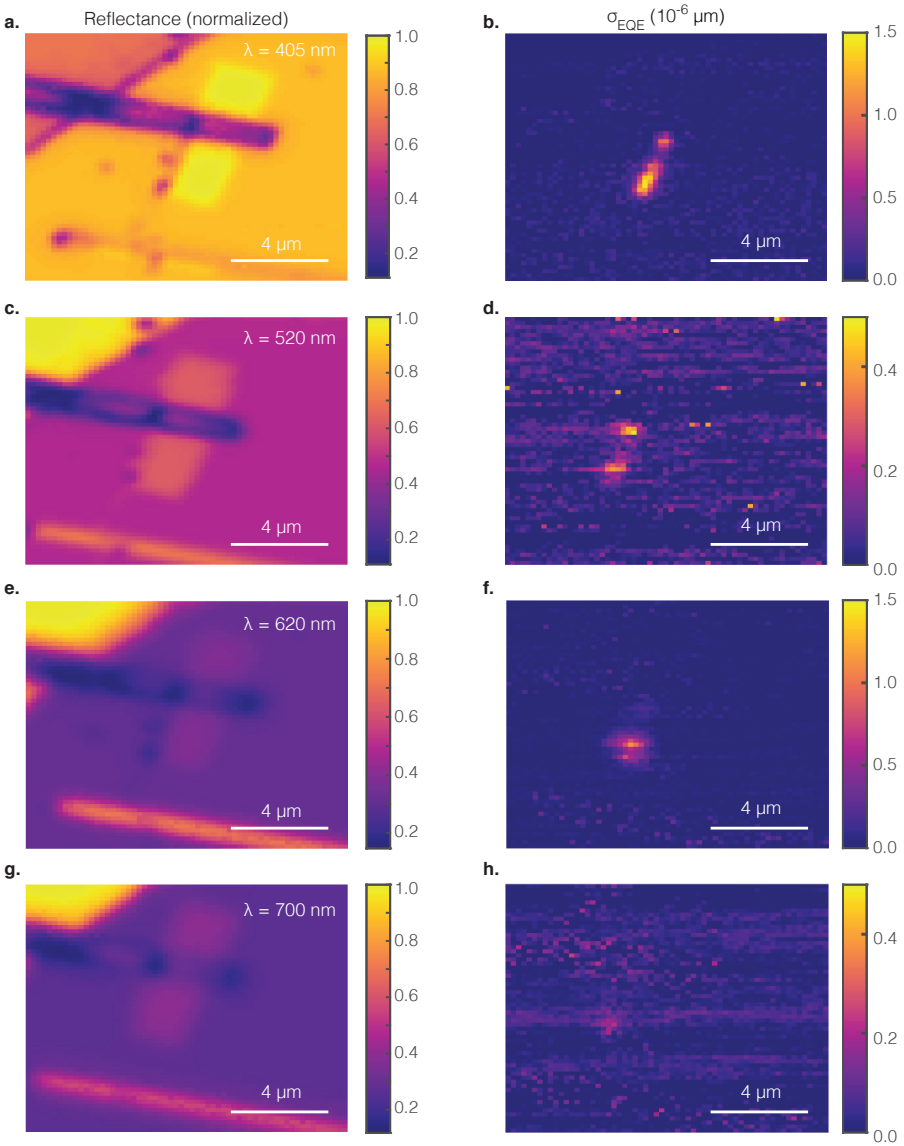

Figure 8.5: Spectral response of a metal-semiconductor core-shell nanowire photovoltaic cell. a. Reflectance map of the nanowire solar cell at $\lambda = 405$ nm. **b.** $\sigma_{\mathrm{EQE}}^{(L)}$ for the nanowire solar cell at $\lambda = 405$ nm. The subsequent color maps show the reflectance and σ_{EQE} raster scans for $\lambda = 520$ (**c,d**), $\lambda = 620$ (**d,e**), and $\lambda = 700$ (**g,h**).

is significantly weaker, most likely due to suppression of absorption. Note that the magnitude of $\sigma_{\mathrm{EQE}}^{(L)}$ peaks at $\sim 1.5 \times 10^{-6}$ μm, which means that if $\sigma_{\mathrm{abs}} = 0.15$ μm, the IQE $\sim 10^{-5}$. This is very low, in particular when compared to the IQE > 0.9 observed in Chapter 6. This low extraction efficiency may be due to *e.g.* a extraction barrier, which is also observed in the I-V curve in Fig. 8.3, as discussed earlier. At λ = 700 nm the photocurrent has disappeared altogether, which is consistent with the literature value of the optical band gap (2 eV or 620 nm) and photoluminescence measurements done on these core-shell nanowires [272, 284].

8.5 Conclusions and discussion

We have synthesized and characterized metal-semiconductor core-shell nanowires for the first time, and used them to create a photovoltaic device. Optical measurements on core-shell nanowires clearly show resonances, which show relatively good agreement with theoretical predictions. However, a third resonance appeared that is not at all visible in the theoretical spectra, possible due to enhanced radiative loss rates as a result of large surface roughness. While the effect of surface roughness on cavities with very high quality factors or waveguides is well known, it may be interesting to investigate the effect of surface roughness on low quality factor resonators such as the nanowires presented here in more detail.

In the photovoltaic device study we show that a V_{oc} of 0.6 V and an I_{sc} of 300 pA can be achieved without any detailed contact optimization, but only at very high illumination intensities. By depositing a thin (10 nm) Ti layer on top of the wire we demonstrate that two conductive radial metal contacts allow for improved photogenerated carrier collection in semiconductors with short minority carrier diffusion lengths <1 μm. However, the IQE in the photovoltaic devices is estimated to be around 10^{-5}, which is very low compared to high efficiency devices such as the single nanowire device discussed in Chapter 6. We observe a strongly S-shaped IV curve, which is also indicative of a charge carrier extraction barrier at one of the two metal interfaces. Possible explanations may be that a redox reaction under the Ti contact converts the Cu_2O to TiO_2 and Cu at the interface [283], or that there is significant mid-bandgap Fermi-level pinning due to the direct contact between the metal and a semiconductor. Performance may therefore be improved if interfacial passivation layers can be incorporated into the geometry, as already shown in thin-film Cu_2O devices and for other material systems [262, 285, 286]. Ultimately a spacer layer may also be required to prevent quenching of the photogenerated carriers due to the presence of the metal nanowire [287, 288], which as discussed in Chapters 2 and 3 would adversely affect the V_{oc}.

Interestingly, given the plasmonic nature of the device and the low IQE, we can not exclude that plasmon mediated charge transfer mechanisms such as resonance energy transfer, direct energy transfer, and hot electron carrier injection contribute to some degree to the optoelectronic response of the device [192, 193, 249, 289, 290].

While the limitations discussed above explain the overall low photovoltaic per-

formance of our device, they do not present insurmountable obstacles on the way to high efficiency metal-semiconductor core-shell nanowire solar cells. We note that the metal-semiconductor core-shell nanowire geometry is not limited to the materials used for this proof-of-concept study. An ideal structure would employ low cost metals with appropriate interfacial layers, replacing Au and Ti. Therefore, we propose metal-semiconductor core-shell nanowire photovoltaics as a promising geometry for solar cells made from low-cost and earth-abundant materials with very short minority carrier diffusion lengths.

8.6 Supplementary Information

8.6.1 Fabrication

Au-Cu_2O core-shell nanowires were prepared in solution as described in detail by Sciacca *et al.* [272]. The nanowires used for the photovoltaic devices had a Au core diameter of ~ 50 nm and a Cu_2O shell thickness of ~ 30 nm and were then dropcast onto 3 x 3 mm^2 low-stress LPCVD-Si_3N_4 covered Si chips with evaporated Au electrodes (~ 150 nm thick). The core-shell nanowires were contacted using a 2 or 3 - step electron beam lithography and metal evaporation scheme (depending on whether a thin Ti pad covering the nanowire was added). The Cu_2O shell was locally etched for 1-2 min with 0.1 mM sulfuric acid prior to Au evaporation (~ 200 nm) to expose the core contact, while the Ti contact (~ 200 nm) was directly evaporated on the Cu_2O shell. For the multi-step electron beam lithography process, pre-patterned alignment markers on the substrates were used to align subsequent exposure patterns to the correct nanowire and electrode locations.

8.6.2 Characterization

The optical characterization was conducted with a home-built optical setup discussed in Chapters 5 and 6, except for the photovoltaic device measurements, where the integrating sphere was omitted. For the characterization at 405 nm a Thorlabs S1FC405 fiber-coupled laser was used. For the other wavelengths a supercontinuum laser (Fianium WL-SC390-3) was sent through an acousto-optic tunable filter (Fianium AOTF-V1-N1) to select wavelengths in the range of 405 nm - 750 nm. The polarization was controlled with a $\lambda/2$ plate (Thorlabs) before the light was focused through an objective lens (Mitutoyo M PLAN APO NUV 50X) to a spot with waist w_0 ~ 600 nm on the electrically connected single nanowire photovoltaic cells. The substrate was mounted on and wire bonded to a custom designed printed circuit board to facilitate the electrical connections. Then the substrate was scanned relative to the focused beam position with a 3-axis piezoelectric stage (Piezosystem Jena Tritor 400 CAP). The photocurrent was measured with an Agilent B2902A Source-Measure Unit, while simultaneously recording the reflected and incident beam power (both measured with Thorlabs amplified photodiodes model PDA100A) to correlate the current with the position

of the laser spot and to normalize to variations in the laser power during a single measurement. The absolute beam power was measured using a calibrated silicon photodetector (Newport model 818-UV-L). The I-V curves were also measured with the source-measure unit (Agilent B2902A).

9

Generalized anti-reflection coatings for complex bulk metamaterials

Efficient utilization of optical power is of crucial importance not only in photovoltaic devices, but in many other optical applications as well. For this reason solar cells, optical elements, and even spectacles are frequently equipped with anti-reflection coatings to enhance transmission. A new generation of optical elements has recently been introduced that uses metamaterials, which may for instance form flat lenses that rely on a bulk negative refractive index. In this chapter we show that regular anti-reflection coatings will not always work for such materials, and we present the optimized design of a metamaterial anti-reflection coating that solves this problem. We show that such an anti-reflection coating must enable spatial engineering of the field profiles at the coating/metamaterial interface to achieve high transmission, and therefore it is required to be inhomogeneous. As a demonstration we investigate theoretically a waveguide-based negative-index metamaterial, which under normal incidence cannot be excited, due to an antisymmetric propagating eigenmode. Through careful engineering of the field profile, lateral position, and thickness of the coating layer we enhance the transmission under normal incidence from 0% to 100%. This principle may generally be applied to overcome low coupling efficiency between incident plane waves and complex mode profiles in metamaterials.

9.1 Introduction

Optical metamaterials, structures of which the effective properties are derived from sub-wavelength elements, have recently attracted a lot of attention [291, 292]. Metamaterials can be used to achieve hyperbolic dispersion [293–297], epsilon-near-zero response [298], or an effective negative index response [299–302]. While the effective optical properties of these metamaterials can be very interesting, the excitation of such media is often quite poor. This is a direct result of the fact that the propagating eigenmodes of such bulk metamaterials can have complex field profiles, which are not excited efficiently by simple plane waves. In this chapter, for instance, we focus on the interesting optical properties that arise from antisymmetric eigenmodes supported by waveguide metamaterials. These antisymmetric waveguide modes may support a negative refractive index [303], which can *e.g.* be utilized to realize a flat lens, but cannot be excited from free space under normal incidence due to their asymmetry.

To enhance transmission into bulk media, many optical systems use anti-reflection coatings, which lead to reflection cancellation through destructive interference between the reflected light from the air-coating and coating-medium interfaces. However, the simple homogeneous anti-reflection coatings that are used in conventional optical systems cannot solve the spatial field mismatch between plane waves and antisymmetric metamaterial eigenmodes: in the homogeneous coating the incident field profile is still symmetric.

Here, we propose structuring the coating layer to achieve very large coupling into complex bulk metamaterials. The use of nanoscale structures to enhance transmission into homogeneous media has been demonstrated before [47, 48, 304, 305]. Aside from impedance matching, we simultaneously utilize the more complicated field profiles in such a nanostructured anti-reflection coating to achieve significant field overlap with the substrate eigenmodes of interest, enabling perfect transmission even for an extreme mismatch between the incident wave and the substrate eigenmodes, as in the case of a plane wave coupling to antisymmetric modes.

9.2 Excitation of metamaterial waveguide modes

The proposed approach is demonstrated in the case of a multilayer stack formed by metal and dielectric thin films. There has been a lot of interest in light propagation through such multilayer geometries [306–311]. For example, a metal/air grating was first considered to explain the observed phenomenon of extraordinary optical transmission [312, 313]. The special dispersive characteristics of these multilayer metamaterials are due to coupled surface plasmon polaritons that propagate along the metal/dielectric waveguide interfaces. Furthermore, multilayer structures allow the derivation of analytical formulas for their eigenmodes, and in several cases for their transmission and reflection properties as well.

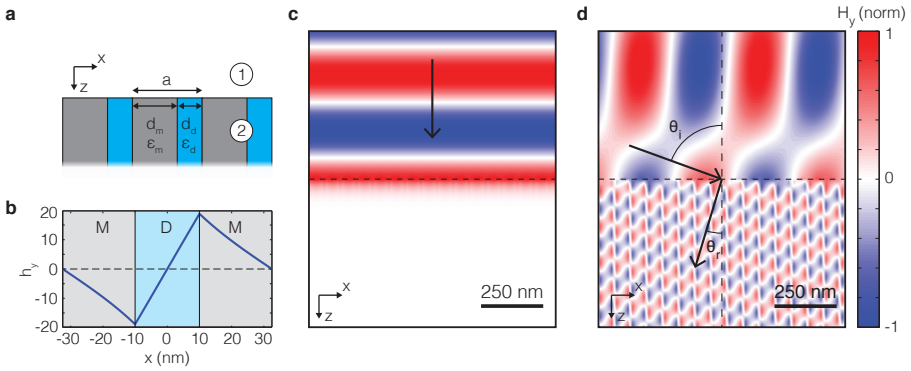

Figure 9.1: A negative index metamaterial based on an antisymmetric propagating eigenmode. a. Sketch of the metal-dielectric metamaterial geometry with metal and dielectric regions depicted as grey and blue respectively. **b.** The negative-index waveguide mode fieldprofile $h_y(x)$ ($d_m = 45$ nm, $\varepsilon_m = -3.5$, $d_d = 20$ nm, and $\varepsilon_d = 6.25$ for $\lambda_0 = 450$ nm). The field profile is antisymmetric across the dielectric core. **c.** The calculated field profile due to a plane wave ($\lambda_0 = 450$ nm) incident on the metal dielectric waveguide array at normal incidence. The spatial field profile shown is composed of 15 repetitions of the unit cell. **d.** Field profile due to a plane wave at an angle of incidence of 70°. Negative refraction is evident in the phase fronts, indicated by θ_i and θ_r.

Figure 9.1a shows a sketch of the geometry under consideration. Our metamaterial is formed by a periodic array of thin metallic layers (with thickness d_m and permittivity ε_m) and thin dielectric layers (with thickness d_d and permittivity ε_d), with unit cell size $a = d_m + d_d$. We take the direction of periodicity as the $\hat{x}$ direction, and $x = 0$ to coincide with the center of the dielectric layer of the unit cell. The waveguides are infinitely extended in the $\hat{y}$ direction, and interfaces between different regions are normal to $\hat{z}$.

For our demonstration, we investigate a lossless configuration which has a single propagating mode with an antisymmetric profile and a negative mode index: $\beta_1^{(2)}$. Following the sketch in Fig. 9.1a, the parameters of the structure are: $d_m = 45$ nm, $\varepsilon_m = -3.5$, $d_d = 20$ nm, and $\varepsilon_d = 6.25$ for $\lambda_0 = 450$ nm. All other modes supported by the metamaterial are either evanescent or anomalous [310, 314]. Fig. 9.1b shows the field profile of the negative index mode, confirming the odd symmetry with respect to the dielectric core. We denote the field by $h_y(x)$, to differentiate the waveguide mode field profile from the total magnetic field $H(x,z)$, which is the sum of all incident, reflected and transmitted modes. Fig. 9.1c shows the total magnetic field distribution near the interface when the multilayer structure is illuminated with an incident plane wave at normal incidence, calculated analytically with the exact modal method as described in the appendix. The propagating mode is clearly not excited at all, but evanescent modes with exponentially decaying field profiles are visible near the interface. Since the propagating mode is not excited and the

system is lossless, all power is reflected.

As mentioned in the introduction, systems supporting only an antisymmetric propagating mode cannot be excited by a symmetric mode, such as a plane wave at normal incidence. In order to excite an antisymmetric mode, the symmetry of the incident wave has to be broken, which can be achieved by exciting the structure from an oblique angle of incidence. Fig. 9.1d shows the calculated field distribution near the interface for a plane wave incident at 70°. Two features are evident: due to a low coupling efficiency at the interface the incident plane wave is partially reflected, leading to an interference pattern observed in free space. Secondly, for this geometry the propagating waveguide mode is excited with a significant amplitude. Since the waveguide mode has a negative mode index, the wavefronts refract negatively, as can be clearly seen in the figure. For an angle of incidence of $\theta_i = 70°$, the waveguide mode index is $\beta/k_0 = -3.12$, where β is the propagation constant in the metamaterial and $k_0 = 2\pi/\lambda_0$ is the wavenumber in free space. This mode index results in a refraction angle of $\theta_i = -17.5°$. Nevertheless, the high gradients of the mode field profile, as can be seen in Fig. 9.1b, limit the excitation efficiency of this waveguide mode by a plane wave. As discussed above, at normal incidence the transmitted power $T = (\beta_1/\beta_2)|t_{12}|^2$ equals zero, where t_{12} is the complex transmission coefficient. At around an angle of 70° transmission is maximum at approximately $T = 0.5$.

9.3 Antireflection coating design

9.3.1 Normal incidence

To improve transmission into the multilayer structure for arbitrary angles of incidence, we use a dielectric grating structure between the air half space and the waveguide array as an intermediate coupling layer that allows us to tailor the overlap between the incident field and the waveguide mode. A general expression for the reflectivity of a two interface system is given by Airy's formula for reflection [315]:

$$r_{total} = \frac{r_{12} + r_{23}\exp(2i\beta_1^{(2)}d_2)}{1 + r_{12}r_{23}\exp(2i\beta_1^{(2)}d_2)}. \tag{9.1}$$

In Eq. 9.1 $\beta_1^{(2)}$ is the propagation constant in region 2 (which now refers to the coating) and the subscripts ij on r refer to the reflection coefficient from medium i into medium j (i.e. r_{12} is the reflection coefficient from air to coating, and r_{23} is the reflection coefficient from the interface between coating and metamaterial). From Eq. 9.1 it is clear that total destructive interference is achieved when $|r_{12}|$ and $|r_{23}|$ are equal and the thickness d_2 is properly chosen so that the two terms in the numerator are π out of phase [305]. For homogeneous planar media, this condition is satisfied when the coating has a quarter wavelength thickness and the refractive index equals $n_2 = \sqrt{n_1 n_3}$. In our case, however, an inhomogeneous geometry is required. Figure 9.2a shows a sketch of the proposed coupling layer geometry: a

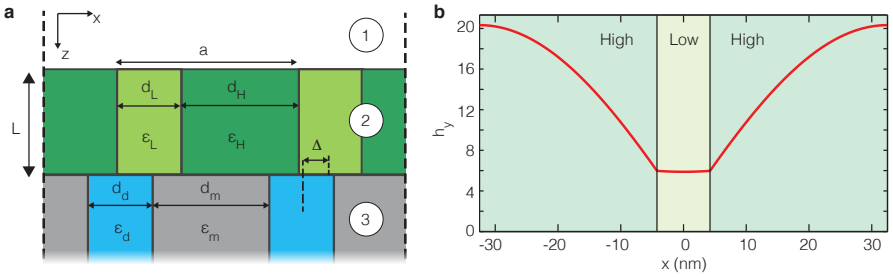

Figure 9.2: Properties of the metamaterial anti-reflection coating. a. Schematic of the anti-reflection coating metamaterial in contact with the metal-dielectric metamaterial. The displacement between the two metamaterials is signified by Δ and measures the distance from the center of the two low dielectric cores. **b.** The magnetic field profile of the propagating mode in the coupling layer with $\varepsilon_H = 20.25$, $\varepsilon_L = 1$, $\rho_H = 0.87$, and a 65 nm unit cell size. The propagation constant of the eigenmode is $\beta_1^{(2)} = 43.85\ \mu m^{-1}$.

periodic multilayer with high-permittivity dielectric blocks with width d_H and permittivity ε_H, alternated with low-permittivity blocks with width d_L and permittivity ε_L in a unit cell with size a. If we match the unit cell size to the metamaterial, $a = 65$ nm, we find that for $\varepsilon_H = 20.25$ and $\varepsilon_L = 1$ there is only one propagating mode. This mode is symmetric, and as a result it can be efficiently excited from free-space. By varying the filling fraction of the high-index dielectric ($\rho_H = d_H/a$) the reflectivity of the air/coupling layer interface can be controlled, which gradually changes from $R = 0$ when $\rho_H = 0$ to $R = 0.4$ as $\rho_H = 1$, where R is the reflected power ($R = |r_{12}|^2$). We take an air/coupling layer reflectivity of $R = 0.2$, which corresponds to a filling fraction $\rho_H = 0.87$. The field profile of the corresponding eigenmode is shown in Fig. 9.2b and has a propagation constant of $43.85\ \mu m^{-1}$.

The reflectivity of the coupling layer/metal-dielectric waveguide array interface may be controlled by displacing the coupling layer with respect to the metal-dielectric waveguide array. Such a displacement is necessary, considering that the propagating mode in the coupling layer is still symmetric, and as a result it cannot excite the antisymmetric mode if the unit cells of the two regions are symmetrically aligned. However, if we displace the coupling layer with respect to the substrate, this symmetry is broken, and the negative index waveguide mode can be excited. This displacement Δ is defined as the shift between the center of the low index layer of the dielectric grating and the center of the dielectric slab in the metal-dielectric array (see Fig. 9.2a). The reflectivity of the coupling layer/metal-dielectric waveguide array interface is determined through numerical finite-difference time-domain simulations (Lumerical FDTD, [140]), because the exact modal method does not converge well for this problem (see appendix for discussion). The results are shown in Fig. 9.3a, where the reflectivity r_{23} is plotted as a function of the displacement Δ. A small imaginary part of the dielectric constant of the metal ($\varepsilon =$

$-3.5+0.01i$) was required for the stability of the simulations. This small amount of loss in the metal does not significantly affect the coupling process compared to the lossless system.

It is clear from Fig. 9.3a that the reflectivity is strongly modulated by the displacement, with reflections in the range of $|r_{23}|^2 = 0.1-1$. We observe particularly strong variations in reflection for a displacement between 5 and 7 nm, where the interface between the high and low index region of the dielectric grating crosses the metal/dielectric interface in the substrate. For $\Delta = 0$ nm and $\Delta = a/2 = 32.5$ nm, the coupling layer is symmetrically oriented to the substrate, indeed preventing excitation of the antisymmetric mode.

For a displacement $\Delta = 7.8$ nm the reflectivity $|r_{23}|^2 = 0.2$, which matches the reflectivity of the air/coupling layer interface. Then, in order to achieve full transmission of the incident wave to the metamaterial array, the thickness of the coating layer has to be tuned such that the roundtrip phase pick-up is π. Contrary to simple lossless homogeneous media, the phase shift upon reflection at the interfaces of the system under study generally will be different than 0 or π, because energy is temporarily stored in evanescent fields close to the interfaces. Figure 9.3b shows the simulated reflectivity $|r_{total}|^2$ as a function of the coupling layer thickness. As expected, a clear periodic modulation of reflectivity is observed. Based on the propagation constant of the waveguide mode in the coating ($\beta_1^{(2)} = 43.85\ \mu m^{-1}$), we expect a modulation period of $\pi/\beta_1^{(2)} = 72$ nm, which agrees well with Fig. 9.3b.

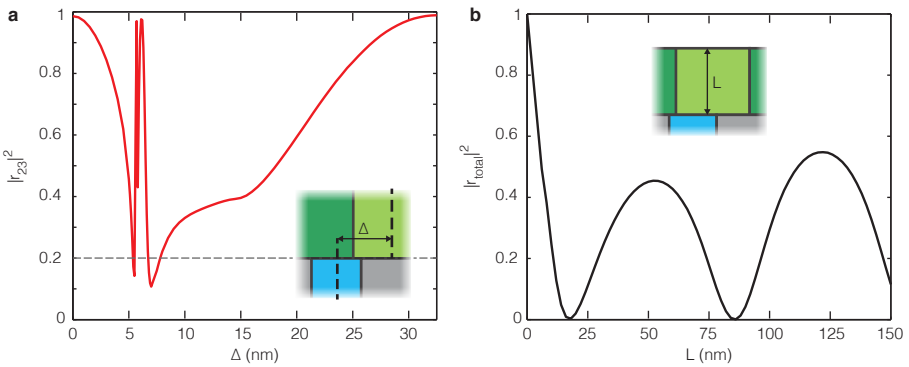

Figure 9.3: Reflection as a function of metamaterial coating displacement and thickness. a. Simulated reflectivity (at $\lambda_0 = 450$ nm) of the coupling layer/waveguide array interface as a function of displacement Δ. The coupling layer is defined by $\varepsilon_H = 20.25$, $\varepsilon_L = 1$, $\rho_H = 0.87$, and the unit cell size is $a = 65$ nm. The waveguide array is the same as in the above. **b.** Simulated reflectivity of the combined coupling layer and waveguide array for $\Delta = 7.8$ nm with changing coupling layer thickness L. Clear oscillations are visible, corresponding to a standing wave in the coupling layer. The two local maxima in reflection are not equal in amplitude due to the influence of evanescent waves in the coupling layer.

Because of the very small thickness of the coupling layer, the evanescent fields do not completely decay between the two interfaces, resulting in a different peak reflectivity for the two local maxima. For a coating layer thickness of $L = 86$ nm, a normally-incident plane wave is completely transmitted to the antisymmetric mode of the metal-dielectric waveguide array. In contrast, without coupling layer this waveguide mode cannot be excited at all at normal incidence.

The complete transmission into the metal-dielectric waveguide array is clearly visible in Fig. 9.4a, which shows a normally-incident plane wave incident on the optimized geometry. The dashed lines indicate the locations of the interfaces. The incident field is visible above the coupling layer. The magnetic field distribution in the coupling layer shows a periodic modulation with maxima in the high-index dielectric, and is clearly symmetric. In contrast, the field distribution in the metamaterial substrate is clearly antisymmetric. Due to the displacement of the symmetric field distribution in the coating with respect to the antisymmetric fields in the substrate, the symmetry constraint is relaxed and efficient excitation of the antisymmetric mode is possible. By tuning the coating layer thickness a condition can be found where destructive interference prevents any reflection, leading to perfect transmission.

9.3.2 Angle dependence

Just as with a regular anti-reflection coating, transmission remains large up to very high angles: Fig. 9.4b shows the magnetic field distribution for an angle of incidence of 70°, in which case 85% of the incident power is transmitted into the

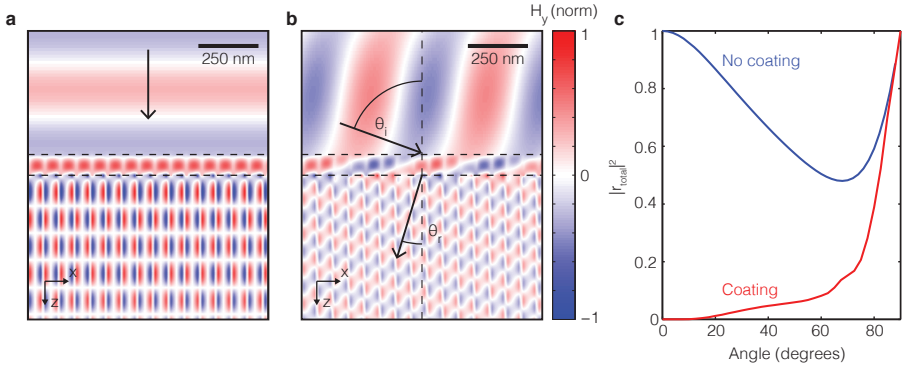

Figure 9.4: The angle dependence of the metamaterial anti-reflection coarting. a. Simulated field profile at normal incidence. As is clear, the incident plane wave now very effectively couples to the antisymmetric waveguide mode. **b.** Field profiles for a plane wave at an angle of incidence of 70°. **c.** Reflectivity from the total system as a function of angle of incidence (red). As a reference, the reflectivity of the bare multilayer substrate is also shown (blue).

substrate. Fig. 9.4c shows that the reflectivity indeed remains low for a large range of angles: $|r_{\text{total}}|^2 < 0.15$ for $\theta_i < 70°$. In contrast, reflection off of the bare waveguide array does not go below 50% and is minimum at 70° (see also Fig. 9.1d). Interestingly, the reason for the low reflectivity over a broad angular range in the presence of the coupling layer is that the field overlap between the dielectric grating and the multilayer substrate is affected very little by changing the angle of incidence, due to the subwavelength periodicity: the field profile in all layers experiences the same lateral phase gradient $\exp(ik_x x)$. On the other hand, the increase in reflectivity at oblique angles is because the condition for destructive interference is no longer fulfilled due to: (1) the angle dependence of the mode index, which changes the optical path length , and (2) the reflection coefficient of the first interface increases. These reasons also cause higher reflectivity at oblique angles in regular anti-reflection coatings.

While the proposed structure behaves very similar to a regular anti-reflection coating in terms of the angle response, the frequency response will most likely be different. For homogeneous media anti-reflection coatings typically operate over a broad frequency range, given that material dispersion is limited (as is the case in e.g. glass and silicon above 500 nm). Here, however, the reflectivity of in particular the coating-metamaterial interface may be expected to vary more strongly with frequency due to mode dispersion, thereby possibly limiting the operation bandwidth of the anti-reflection coating.

9.4 Discussion and conclusion

We have demonstrated that it is possible to achieve perfect transmission into the bulk metamaterial, as long as a coating layer can be found that satisfies $|r_{12}| = |r_{23}|$. However, even in the case that this condition is not satisfied, significant transmission enhancements can be achieved. This becomes evident if we look at the equation for minimum reflectivity R_{min} of such a multilayer system [315]:

$$R_{\text{min}} = \left| \frac{r_{12} - r_{23}}{1 + r_{12} r_{23}} \right|^2 . \tag{9.2}$$

For example, it is possible that the coating/metamaterial interface remains very reflective ($r_{23} = 0.99$) due to extremely high field gradients that cannot be efficiently matched by the low field gradients in a dielectric coating layer. Even if the reflectivity of the air/coating interface is very low ($r_{12} = 0.2$, like glass), a total transmission of $1 - R_{min} = 0.56$ is still achieved. Hence, even if perfect transmission is not attainable, significant transmission enhancements can still be achieved.

Finally, it is interesting to note that the two functions of the metamaterial anti-reflection coating (spatial engineering of the fields at the interface and tuning the propagation length to achieve destructive interference) does not necessarily require that the entire coating is inhomogeneous. For instance, one can also engineer the fields at the interface through *e.g.* a plasmonic metasurface [171], which

allows for strong field gradients, and use a homogeneous coating on top of the metasurface to achieve destructive interference. Such an approach may also be more straightforward to realize experimentally.

To conclude, we have proposed a method to enhance transmission from a plane wave into a planar complex metamaterial with a complex field profile. We achieve this by using an appropriately structured anti-reflection coating, which allows for efficient excitation of complex field profiles through spatial engineering of the field profile at the interface. In an example we show that by optimizing the relative displacement between a coupling layer and a waveguide array, and by changing the coupling layer thickness, even perfect transmission into the antisymmetric mode of the waveguide array can be achieved at normal incidence. High transmission is also observed for a broad range of angles: 100% at normal incidence and as high as 85% at a 70° angle of incidence. Our results show that a thin metamaterial layer can be used as an efficient anti-reflection coating, enabling efficient transmission into structures with a complex field profile. In this chapter we have shown how this may be applied to facilitate coupling to a waveguide array, but this approach may generally apply to any structure with a non-uniform field profiles, such as plasmonic waveguides, metamaterials with hyperbolic dispersion, epsilon-near-zero response, materials with an effective negative index response, and optical interconnects.

9.5 Supplementary Information

9.5.1 The modal method

Here we describe the modal method used to numerically calculate the transmission and reflection from an interface between a homogeneous and a stratified medium, or between two stratified media [188]. To calculate the reflection and transmission coefficients for inhomogeneous media, we need to expand the field in each region j into its eigenmodes $|\psi_n^{(j)}\rangle$, as:

$$H_y^{(j)}(x,z) = H_0 \sum_{n=0}^{\infty} a_n e^{i\beta_n^{(j)} z} |\psi_n^{(j)}\rangle . \tag{9.3}$$

In Eq. 9.3, the superscript refers to the region j, $\beta_n^{(j)}$ is the propagation constant of the nth eigenmode and a_n is the corresponding complex amplitude. Using Ampere's law we find for **E**:

$$E_x^{(j)}(x,z) = E_0 \frac{i}{\varepsilon_j(x)} \sum_{n=0}^{\infty} a_n \beta_n^{(j)} e^{i\beta_{n,j} z} |\psi_n^{(j)}\rangle . \tag{9.4}$$

These eigenmodes in each region j are defined such that they are orthonormal under the pseudo-inner product [316, 317]:

$$\begin{aligned} \langle \psi_m^{(j)} | \psi_n^{(j)} \rangle_\varepsilon = \langle \psi_n^{(j)} | \frac{1}{\varepsilon_j(x)} | \psi_m^{(j)} \rangle = \\ \int_{-a/2}^{a/2} \frac{1}{\varepsilon_j(x)} (h_{y,n}^{(j)}(x))^* h_{y,m}^{(j)}(x) dx = \delta_{nm}, \end{aligned} \tag{9.5}$$

where $\varepsilon_j(x)$ is the dielectric constant as a function of position and the asterisk denotes complex conjugation. Note that the pseudo-inner product differs from the normal inner product because it includes $1/\varepsilon_j(x)$ as a weighting function. In free space the eigenmodes are simply plane wave harmonics for normal incidence: $|\psi_n^{(j)}\rangle = \exp(in\frac{2\pi}{a}x)/\sqrt{a}$, where a is the periodicity. In the stratified medium, the expansion is performed using the waveguide modes of the geometry, which are found by solving the interface boundary conditions in a periodic unit cell [311, 318]. Note that this orthonormality condition holds only for lossless systems, but that systems with significant losses can also be treated analytically by applying the modal expansion method through an adjoint definition of the pseudo-inner product [319].

The transmission and reflection amplitudes of a wave impinging on an interface at $z = 0$ can then be calculated by making use of the continuity of tangential fields [190]:

$$\mathbf{H}^{(1)}(z=0) \times \hat{\mathbf{n}} = \mathbf{H}^{(2)}(z=0) \times \hat{\mathbf{n}} \tag{9.6a}$$

$$\mathbf{E}^{(1)}(z=0) \times \hat{\mathbf{n}} = \mathbf{E}^{(2)}(z=0) \times \hat{\mathbf{n}}. \tag{9.6b}$$

Here $\hat{n}$ is the normal vector to the interface and the superscripts refer to the two half spaces. By substituting Eqs. 9.3 and 9.4 into the continuity Eqs. 9.6a and 9.6b we find the following equations:

$$\sum_{m=0}^{\infty} (a_m^+ + a_m^-) |\psi_m^{(1)}\rangle = \sum_{n=0}^{\infty} b_n^+ |\psi_n^{(2)}\rangle \tag{9.7a}$$

$$\frac{i}{\varepsilon_1(x)} \sum_{m=0}^{\infty} \beta_m^{(1)} (a_m^+ - a_m^-) |\psi_m^{(1)}\rangle = \frac{i}{\varepsilon_2(x)} \sum_{n=0}^{\infty} b_n^+ \beta_n^{(2)} |\psi_n^{(2)}\rangle . \tag{9.7b}$$

Here a_n and b_n are the mode amplitudes in medium 1 and 2 respectively, and the upper sign identifies forward and backward propagating amplitudes. Making use of the orthonormality condition in Eq. 9.5 we can transform Eq. 9.7 into coupled

equations for the amplitudes:

$$a_m^+ + a_m^- = \sum_{n=0}^{\infty} b_n^+ \langle \psi_m^{(1)} | \frac{1}{\varepsilon_1(x)} | \psi_n^{(2)} \rangle \tag{9.8a}$$

$$a_m^+ - a_m^- = \sum_{n=0}^{\infty} b_n^+ \frac{\beta_n^{(2)}}{\beta_m^{(1)}} \langle \psi_m^{(1)} | \frac{1}{\varepsilon_2(x)} | \psi_n^{(2)} \rangle . \tag{9.8b}$$

To solve this system numerically we truncate the infinite series at a certain integer l, typically around 50. This leads to the matrix equation:

$$\begin{pmatrix} -\mathbf{I}_{l\times l} & \mathbf{B}_{m,n}^{(1)} \\ \mathbf{I}_{l\times l} & \mathbf{B}_{m,n}^{(2)} \end{pmatrix} \begin{pmatrix} \mathbf{a}^- \\ \mathbf{b}^+ \end{pmatrix} = \begin{pmatrix} \mathbf{a}^+ \\ \mathbf{a}^+ \end{pmatrix}, \tag{9.9}$$

where $\mathbf{I}_{l\times l}$ is the identity vector and the elements of the $\mathbf{B}$ matrices are given by:

$$B_{m,n}^{(1)} = \langle \psi_m^{(1)} | \frac{1}{\varepsilon_1(x)} | \psi_n^{(2)} \rangle \tag{9.10a}$$

$$B_{m,n}^{(2)} = \frac{\beta_n^{(2)}}{\beta_m^{(1)}} \langle \psi_m^{(1)} | \frac{1}{\varepsilon_2(x)} | \psi_n^{(2)} \rangle . \tag{9.10b}$$

The elements of $\mathbf{a}^+$ in Eq. 9.9 are known, as this is the incident field which is given by a single plane wave. Such a linear system is easily solved numerically. We can relate these mode amplitudes to the reflection and transmission coefficients through $r_{12} = a^-/a^+$ and $t_{12} = b^+/a^+$. In the case of the interface between free space and a stratified medium, these equations simplify to:

$$B_{m,n}^{(1)} = \langle \psi_m^{(1)} | \psi_n^{(2)} \rangle \tag{9.11a}$$

$$B_{m,n}^{(2)} = \frac{\beta_n^{(2)}}{k_z^{(m)}} \langle \psi_m^{(1)} | \frac{1}{\varepsilon_2(x)} | \psi_n^{(2)} \rangle , \tag{9.11b}$$

where $k_z^{(m)}$ is the component of the free space wave vector along the z direction for the mth diffracted order. The free space eigenmodes are given by:

$$|\psi_m^{(1)}\rangle = \exp(i(k_x + m\frac{2\pi}{a})x). \tag{9.12}$$

In this case the summation runs over negative indices as well, such that one sums from $m = -l/2$ to $m = l/2$ (for even l).

9.5.2 Convergence

When solving for an interface between two stratified media, this formalism often shows very poor convergence. The reason is that due to the discontinuities in the

permittivity strong Gibbs oscillations arise in the finite expansions. When expanding two discontinuous bases on each other, as is essentially done in Eq. 9.9, this leads to artificially large amplitudes for high harmonics. The rigorous coupled wave analysis formalism (RCWA) (or the Fourier modal method (FMM)), which is intricately related to the exact eigenmode expansion [320], encountered similar convergence problems for TM polarization [321]. Convergence can be improved significantly by using a basis that is not affected by the discontinuities in ε, such as Gegenbauer polynomials [322].

10

Applications

In this dissertation we have investigated how nanophotonic engineering can affect the efficiency of solar cells, and how to experimentally investigate photovoltaic devices on the nanoscale. In this chapter, we present two applications that are inspired by these themes. In Section 10.1 we present possible ways to incorporate integrating sphere microscopy into commercial systems, enhancing the ease-of-use, and propose an extension of the technique. In Section 10.2 we study the escape probability in macroscopic solar cells, and design a structure that simultaneously achieves high absorption over a broad range of wavelengths and a large escape probability for luminescence, both of which are crucial for high efficiency photovoltaics.

10.1 Integrating Sphere Microscopy in commercial systems

In Chapter 5 we introduced integrating sphere microscopy, a single nanoparticle spectroscopy technique to determine the absorption cross section quantitatively. It relies on directly measuring all of the power that is not absorbed by the nanoparticle, enabling determination of the power that is absorbed. The technique combines two elements: a long working distance objective to focus the light, and an integrating sphere to surround the sample and collect scattered light. Here we will present approaches to make integrating sphere microscopy an add-on feature in

two different commercial systems: a microscope and a ultraviolet/visible spectrometer (UV-VIS).

10.1.1 UV-VIS spectrometer

Integrating sphere measurements are commonly performed on macroscopic samples that scatter strongly, such as colloidal suspensions, powders, and textured solar cells [48, 194, 195, 211, 227, 239, 240]. Integrating spheres are often applied in an ultra-violet/visible spectrophotometer, to determine the absorbance of strongly scattering samples. A simplified schematic of a common design of a UV-VIS spectrometer is shown in Fig. 10.1a, based on the Perkin-Elmer Lambda series. Light originates from a tungsten (W) or deuterium (D_2) lamp, depending on which part of the spectrum is required. The light is monochromated by a grating monochromater and then sent through a beam splitter, with half of the incident power interacting with the sample inside the integrating sphere, and the other half is used for a reference measurement. Variations exist where a reflective chopper wheel is used to alternate illumination of the reference photodiode and the sample, or where there is no reference photodiode, and the reference has to be measured by removing the sample.

Since many UV-VIS spectrometers already ship with an integrating sphere or have it as an upgrade option, they are a natural host to accommodate integrating sphere microscopy. This requires combining the setup shown schematically in Fig. 10.1a with a long working distance (WD) objective compatible with the integrating sphere size. The Perkin-Elmer Lambda series is shipped with a 150 or 60 mm diameter integrating sphere, where the sample can be mounted on the rear (for quantitative reflectance measurements), or in the center (for absorption measurements). For the 60 mm sphere with the sample mounted in the middle a microscope objective with a working distance of at least 30 mm is required, which leaves the Mitutoyo M Plan Apo HR NIR series 5X and 10X objectives as options (WD=37.5 mm and 30.5 mm respectively). These objectives have numerical apertures of 0.14 and 0.26, enabling high spatial resolutions (depending on the coherence of the source, but this can be improved through spatial filtering). Furthermore, these objectives are wavelength-corrected from 480 to 1800 nm, so that use can be made of the large operating bandwidth of UV-VIS spectrometers.

In UV-VIS spectrometers the sample is typically mounted at a fixed position, without the ability to scan the sample position. Scanning the sample with respect to the focused spot position is crucial for integrating sphere microscopy, because it is otherwise virtually impossible to obtain an absorption measurement on a single nanoparticle. Alternatively, measurements can be obtained using wide-field excitation, but these then are typically no longer single particle, nor spatially resolved [196]. Aside from adjusting the sample mount to enable spatial scanning, it is also possible to scan the focal point position by changing the angle of incidence on the back-aperture of the objective. This is perhaps most conveniently done in a “4f” design, where a mirror is adjusted to change the angle of incidence, but two lenses

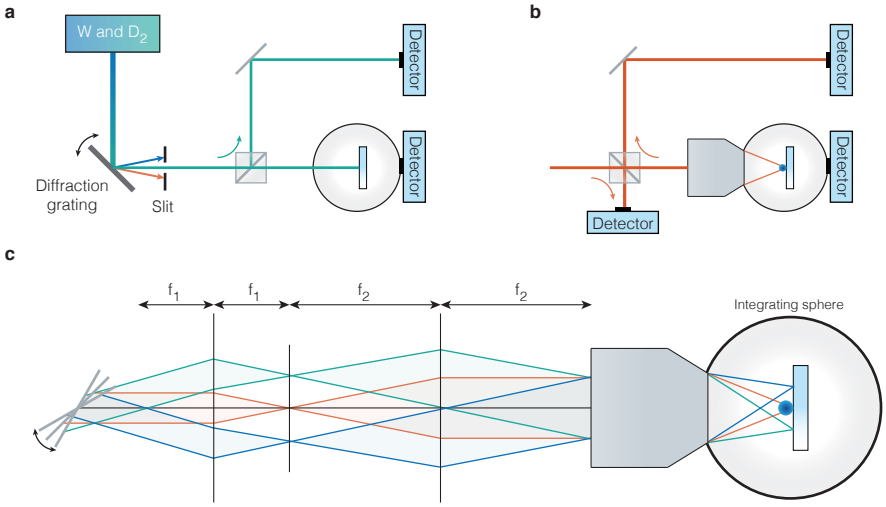

Figure 10.1: Integrating sphere microscopy in a UV-VIS spectrometer. a. A simplified schematic of a typical UV-VIS spectrometer. Light comes from a tungsten or deuterium lamp and is sent to a monochromator, after which narrow band light is sent through a beam splitter. Half of the beam goes to the integrating sphere and interacts with the species, while the other half is measured as a reference signal. **b.** The typical UV-VIS setup modified to accomodate integrating sphere microscopy. A third photodetector is required to measure the reflected signal, and a microscope objective is placed in front of the integrating sphere. **c.** To enable scanning of the focused spot a "4f" approach can be used: with a 2-axis rotating mirror and 2 lenses it is possible to change the angle of incidence on the back aperture of the objective, without changing the center position of the beam on the back aperture. Due to the change of angle of incidence the position of the focused spot in the focal plane thus changes, enabling scanning.

placed their focal distances apart ensure that the back aperture remains homogeneously filled (see Fig. 10.1c) [323]. Such an approach is sometimes also used to modulate the beam position as a means to obtain high sensitivity in extinction measurements [324].

10.1.2 Inverted microscope

The other starting point to implement integrating sphere microscopy in a commercial system is a microscope. Fig. 10.2a shows a schematic depiction of an integrating sphere mounted on an inverted microscope, which are popular for dark-field spectroscopy [81, 325], near-field spectroscopy [28, 326], extinction (transmission) spectroscopy [95, 98, 327, 328], and many other techniques. Fig. 10.2b shows a close-up schematic near the integrating sphere, with the long working distance objective visible below the integrating sphere. The top of the integrating sphere

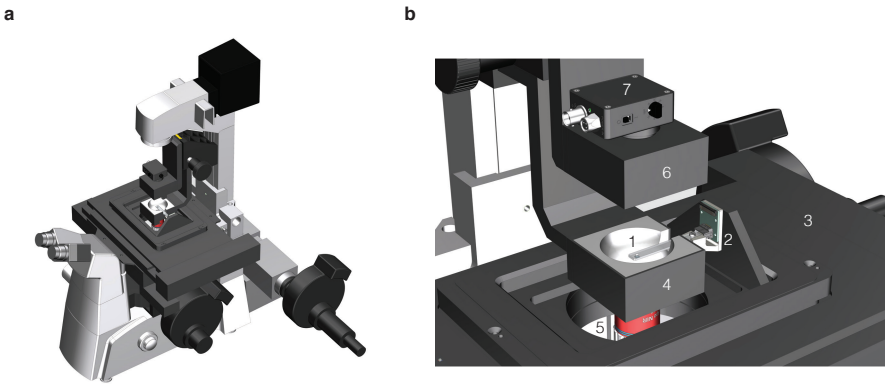

Figure 10.2: Integrating sphere microscopy in an inverted microscope. a. Perspective schematic drawing of an integrating sphere incorporated into an inverted microscope. **b.** A close-up of the area of interest. The sample (1) is attached to the sample holder (2), which itself is mounted on the microscope scanning stage (4). The bottom half of the integrating sphere (5) is mounted at a set position from the long distance microscope objective (6). The top half of the integrating sphere (7) comes down to close the integrating sphere, and a photodetector on top of the integrating sphere detects the non-absorbed intensity (8).

can be lifted to facilitate sample loading. Scanning the sample is relatively more straightforward in this scenario, as most microscopes are equipped with an electrically controlled stage.

Extinction spectroscopy

A large benefit of the inverted microscope setup is that it is straightforward to collect the excitation beam with another objective, enabling extinction or transmission spectroscopy measurements [95, 325, 327, 328]. Combining extinction measurements with an integrating sphere to collect the scattered light allows for quantitative determination of both the absorption and extinction cross section, which so far can only be done for dipolar scatterers using an interferometric technique [89]. Similar experiments have been done without an integrating sphere but with a dark-field objective, but in that case the result can only be made quantitative by making assumptions on the scattering pattern [325]. With two 37.5 mm working distance objectives there is sufficient space to fit a 60 mm integrating sphere in between, and the solid angle of excitation and collection is sufficiently low to simulate plane wave extinction (see Fig. 10.3 for a schematic drawing of a suggested approach).

For a small particle the extinction cross section is related to the collected power

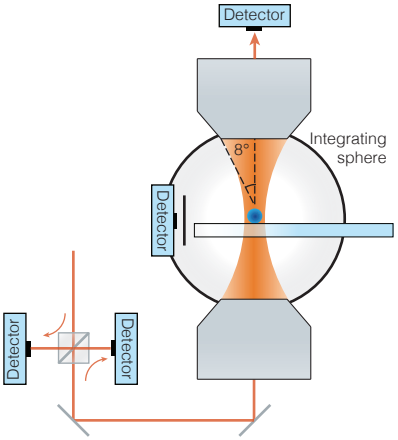

Figure 10.3: Extinction spectroscopy combined with an integrating sphere. In the common quantitative extinction spectroscopy experiment two objectives are aligned facing each other, with one objective exciting a nanoparticle, and the other objective collecting the transmitted light. From the transmitted light the extinction cross section can be determined. Here we propose combining the common extinction spectroscopy experiment with an integrating sphere (the photodetector in Fig. 10.2 has to be moved to the side). In such a setup quantitative extinction, scattering, and absorption measurements can be performed simultaneously.

in transmission via:

$$\sigma_{\text{ext}} = \frac{2P_{\text{ext}}}{\pi w^2}, \tag{10.1}$$

where the extinct power P_{ext} is determined from a reference measurement where the nanoparticle is not in the beam and w is the beam waist. A similar equation exists for the scattering cross section, but the scattered power is approximately determined as:

$$P_{\text{sca}} \approx P_{\text{R}}/P_{\text{R}}^{\text{cal}} + P_{\text{IS}}/P_{\text{IS}}^{\text{cal}} - C, \tag{10.2}$$

where C is a correction constant for the background reflection. The reflection signal is simply calibrated with a mirror, as is done in the current approach, but the integrating sphere signal is harder to calibrate as in absence of a particle the there ideally should be no signal at all. However, calibration could be done with non-absorbing scattering particles, such as silica beads. In this case the scattered power and extinction should be equal. Replacing the photodetectors by spectrometers and using a broadband laser for excitation enables rapid characterization over a broad spectral range.

10.1.3 Conclusion and discussion

We have presented two possible approaches to incorporate integrating sphere microscopy as an additional feature on existing commercial products. First we discussed UV-VIS spectrophotometers, which are frequently used to measure the absorption or extinction on macroscopic samples such as powders or colloidal suspensions over a very large bandwidth. As a result most of the infrastructure required for integrating sphere microscopy is already there: a broadband light source, an integrating sphere, and two out of three photodetectors. The largest downsides may be that scanning the sample is not straightforward, and may require modifying the integrating sphere further or adding a "4f" beam scanning system. Additionally, the coherence of the source may be an issue in achieving high spatial resolution, but at the cost of incident power the coherence can be enhanced through filtering.

The second option we discussed is to add an integrating sphere as an add-on to an inverted microscope. The largest benefit in this case is that the technique can even be extended to combine integrating sphere microscopy with extinction spectroscopy, so that direct and quantitative measurements of extinction, scattering, and absorption cross of arbitrary particles can be achieved.

10.2 Reducing photon recycling in large scale solar cells

The output power of a solar cell is given by the product of its current and voltage. To optimize the efficiency of such a device it is therefore crucial to achieve both high currents and voltages. Here we will discuss an approach to optimize the voltage of a solar cell utilizing nanophotonics, while maintaining high currents. The open-circuit voltage (V_{oc}) of a solar cell is proportional to the maximum voltage V_{oc}^{rad} according to [162, 163]:

$$V_{oc} = V_{oc}^{rad} + V_T \log(\eta_{ext}), \tag{10.3}$$

where $V_T = 25.9$ mV is the thermal voltage, and η_{ext} is the probability that a recombination event in the solar cell leads to an external photon. η_{ext} is given by [130]:

$$\eta_{ext} = \frac{\eta_{int}\overline{p}_{esc}}{1 + \overline{p}_{abs}\eta_{int}} \tag{10.4}$$

where η_{int} is the probability that a recombination event is radiative, and $\overline{p}_{esc}$ and $\overline{p}_{abs}$ are the probabilities that a photon originating from a radiative recombination event escapes or is reabsorbed. These two probabilities are related via the parasitic absorption probability, $\overline{p}_{par} + \overline{p}_{abs} + \overline{p}_{esc} = 1$, which is the probability that a photon is absorbed somewhere where it does not lead to a new electron-hole pair, such as in a metal contact or back reflector.

In planar solar cells the escape probability is lower than $\sim 1/2n^2$, where n is the refractive index of the substrate, due to trapping of the light in the high index semiconductor when it is emitted outside of the critical angle [130]. If the internal quantum efficiency is not unity, which is the case for most practical materials, this leads to significant penalties in the V_{oc}, due to increased non-radiative recombination from reabsorption events. Enhancing the escape probability can therefore lead to significant enhancements in the performance of a photovoltaics device [130, 131, 162, 329], in particular at low η_{int} where $\eta_{ext} \approx \eta_{int}\overline{p}_{esc}$.

While an increase in $\overline{p}_{esc}$ increases the V_{oc}, actually enhancing the overal conversion efficiency is harder, because the J_{sc} must be kept very high. For example, in an InP solar cell with $V_{oc} = 900$ mV a tenfold increase in $\overline{p}_{esc}$ leads to a V_{oc} increase of $\sim 6\%$. For there to be a net benefit to the conversion efficiency, the J_{sc} therefor has to remain above 94% of its initial value. Hence, for practical purposes it is crucial to demonstrate that both high J_{sc} and high $\overline{p}_{esc}$ can be achieved simultaneously.

Here we present a nanophotonic approach to simultaneously achieve very large currents and very large escape probabilities. A nanophotonic structure that demonstrates extremely high absorption over a broad wavelength range is the tapered nanowire geometry [54, 227]. Fig. 10.4a shows the dimensions of the array under consideration, together with the electric field intensity at $\lambda = 844$ nm. From the field intensity plot it is clear that even at wavelengths close to the band gap

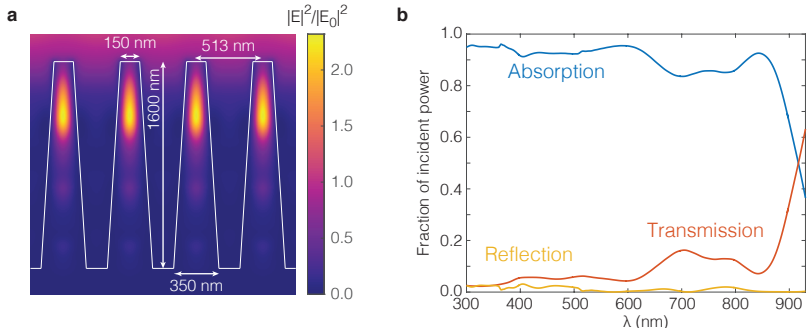

Figure 10.4: Tapered nanowire absorbers. a. Field intensity distribution at $\lambda = 844$ nm, shown with the dimensions of the array. **b.** Absorption, transmission, and reflection spectra for the array.

($\lambda_{BG} \approx 930$ nm) the light is strongly absorbed. The full absorption spectrum under normal incidence is shown in Fig. 10.4b, with absorption over 90% almost over the entire range of the solar spectrum.

10.2.1 Escape probability

We use finite-difference time-domain to investigate the escape probability of photons from recombination events in this geometry (Lumerical FDTD, [140]). We encounter two problems when attempting such a simulation: first of all, the array is infinite in size, while we are interested in the emission event corresponding to *one* dipole. It is therefore not possible to use periodic boundary conditions, although in principle this can be accounted for with an "array scanning method" [330, 331]. However, here we estimate the escape probability here by simulating 7×7 unit cells. By recording the power flow through the edge of the simulation volume we place a range of accuracy on our estimate, since that power is not yet absorbed, nor has it escaped.

The second issue with using FDTD is determining the injected power P_{inj}. While most FDTD clients have a routine to determine the injected power in lossless environments, so that for example Purcell factors can be calculated, these appear to fail when the dipole is placed in a lossy environment. Here we circumvent this problem by measuring the transmission through an imaginary box very close to the dipole (total size 40 nm), and we take this as the injected power (see inset in Fig. 10.4a). In that sense our determination of $\overline{p}_{esc}$ is thus an upper limit, ignoring reabsorption events happening very close to the emission location. More accurate results are thus obtained for smaller box sizes, but at the same time at least 5 mesh cells are required between the dipole and field monitors for converging results.

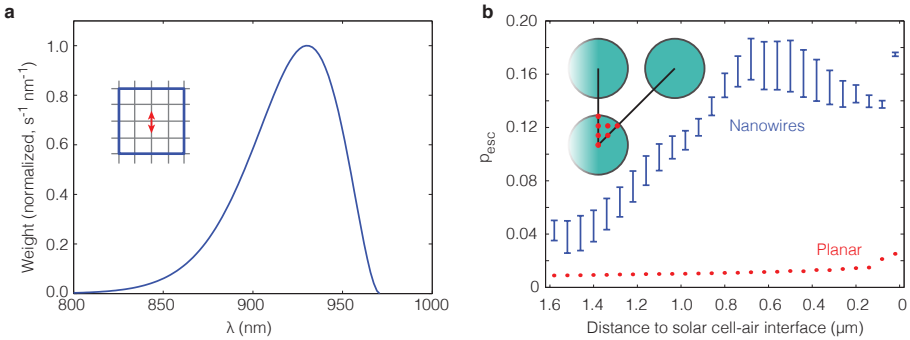

Figure 10.5: Determining the escape probability in a nanowire array. a. The weighting function used to relate escape probability simulations at different frequencies, which is the internal luminescence spectrum. The inset schematically shows how the injected power is determined: a transmission box is placed around the source, with minimal spacing, and the transmitted power is assumed to the injected power. **b.** The obtained escape probability for the nanowire array and a planar reference. The size of the bars depicts the uncertainty in our estimation due to power that was neither reabsorbed nor escaped, but entered the perfectly matched layers at the edge of the simulation volume. The inset schematically shows escape probability sampling locations, where the circles are nanowires and the red dots refer to dipole positions.

We estimate $\overline{p}_{\text{esc}}$ by calculating:

$$\overline{p}_{\text{esc}} = \int_{\omega_1}^{\omega_2} \frac{P_{\text{esc}}}{P_{\text{inj}}} W(\omega)\, d\omega \tag{10.5}$$

where ω_1 and ω_2 are the smallest and largest simulation frequency, P_{esc} is the power emitted into free space, and $W(\omega)$ is a weighting function to capture the emission spectrum, based on the van Roosbroeck-Shockley equation [179]:

$$W(\omega) = \frac{\alpha(\omega)\text{Re}\{n(\omega)\}^2}{\pi^2 c^2} \frac{\omega^2}{\exp(\hbar\omega/k_B T) - 1} \tag{10.6}$$

where α is the absorption coefficient, n is the complex refractive index, k_B is the Boltzmann constant, c is the speed of light, and T is the temperature (300 K). We calculated $\overline{p}_{\text{esc}}$ for 503 dipole positions and orientations in the single nanowire, sampling the bulk of the nanowire with 40 nm spacing as shown in the inset of Fig. 10.5b. The blue data points points show the results for the nanowire array (with the range depicting the fraction of power leaving the simulation volume through the edge). The red dots show the corresponding $\overline{p}_{\text{esc}}$ near a planar interface, which is significantly lower and is indeed close to $1/4n^2$ near the interface. The escape probability peaks at roughly 16%, an enhancement of 8 times compared to $1/4n^2$. The corresponding enhancement in η_{ext} has been verified experimentally by etch-

ing the array into an InP wafer, indeed demonstrating an enhancement in η_{ext} of a factor 14 despite the significantly increased surface area [332].

The 8-fold enhancement in $\overline{p}_{esc}$ is very large considering previously achieved enhancements. For example, an enhancement of 3.4 has been shown in organic light emitting diodes [333], and we estimate that an enhancement of roughly 4 has been achieved through random texturing in semiconductor layers [334]. The large escape probability in these nanowires may originate from the excitation of guided modes [183, 335], which are then adiabatically transformed into poorly confined guided modes *via* the tapering, facilitating transfer to free space [336, 337]. However, due to the lack of a back-reflector the escape probability is still severely limited: approximately half of the photons are emitted downward instead of up. This leads to large parasitic absorption rates in the substrate, which reduce the V_{oc}. In fact, for planar solar cells on a native substrate the recombination current is approximately $(1+n^2)$ times higher than when the solar cell is fabricated directly on a good back reflector, due to the large density of optical states in the substrate [338]. By itself this already reduces the maximum V_{oc} by 66 mV for $n = 3.5$. The back reflector is thus a crucial element in any high efficiency photovoltaic device [130, 131]. Fortunately, while nanowires are typically grown epitaxially on a substrate (or etched into a substrate), they can be transferred using a polymer peel-off procedure [237, 339–342]. Furthermore, not only the V_{oc} would benefit: from Fig. 10.4 it is clear that the largest fraction of power that is not absorbed is in fact transmitted into the passive InP substrate. Hence, replacing the substrate by a mirror can also significantly enhance the J_{sc}.

10.2.2 Conclusion and discussion

To conclude, we have shown that it is possible to achieve very high $\overline{p}_{esc}$ and high J_{sc} at the same time, both of which are crucial for high efficiency photovoltaic devices. The nanowire geometry provides a perfect platform because it facilitates more control over the direction of spontaneous emission: while in a semiconductor slab the emission is unidirectional, resulting in only a small fraction of emission within the escape cone defined by the critical angle, in nanowires spontaneous emission largely excites guided modes. These guided modes are traveling towards free space, where they experience only very little reflection, or towards the passive substrate. As a result, even larger enhancements in $\overline{p}_{esc}$ can be achieved by combining a nanowire array with a back reflector such as a mirror.

Additional mechanisms to enhance the escape probability may exist as well. For example, in Chapter 6 we saw that InP in the wurtzite crystal structure has an anisotropic refractive index. This anisotropy may be utilized to enhance the escape probability significantly, by aligning the lowest energy transitions so that they radiate towards free space.

References

[1] V. Sivaram and S. Kann, *Solar power needs a more ambitious cost target,* Nat. Energy **1**, 16036 (2016).

[2] D. Chung, C. Davidson, R. Fu, K. Ardani, and R. Margolis, *U.S. Photovoltaic Prices and Cost Breakdowns : Q1 2015 Benchmarks for Residential , Commercial , and Utility-Scale Systems,* Natl. Renew. Energy Lab. (2015).

[3] W. Shockley, *The Theory of p-n Junctions in Semiconductors and p-n Junction Transistors,* Bell Syst. Tech. J. **28**, 435 (1949).

[4] NREL, *Air Mass 1.5 (AM1.5) Global Spectrum (ASTM173-03G)*, 2008.

[5] M. B. Prince, *Silicon Solar Energy Converters,* J. Appl. Phys. **26**, 534 (1955).

[6] J. J. Loferski, *Theoretical considerations governing the choice of the optimum semiconductor for photovoltaic solar energy conversion,* J. Appl. Phys. **27**, 777 (1956).

[7] W. Shockley and H. J. Queisser, *Detailed Balance Limit of Efficiency of p-n Junction Solar Cells,* J. Appl. Phys. **32**, 510 (1961).

[8] G. Sala and I. Antón, *Photovoltaic Concentrators*, in *Handb. Photovolt. Sci. Eng.*, pages 402–451, John Wiley & Sons, Ltd, Chichester, UK, 2011.

[9] E. D. Kosten, B. M. Kayes, and H. A. Atwater, *Experimental demonstration of enhanced photon recycling in angle-restricted GaAs solar cells,* Energy Environ. Sci. **7**, 1907 (2014).

[10] E. D. Kosten, J. H. Atwater, J. Parsons, A. Polman, and H. A. Atwater, *Highly efficient GaAs solar cells by limiting light emission angle,* Light Sci. Appl. **2**, e45 (2013).

[11] A. Braun, E. A. Katz, D. Feuermann, B. M. Kayes, and J. M. Gordon, *Photovoltaic performance enhancement by external recycling of photon emission,* Energy Environ. Sci. **6**, 1499 (2013).

[12] O. Höhn, T. Kraus, G. Bauhuis, U. T. Schwarz, and B. Bläsi, *Maximal power output by solar cells with angular confinement,* Opt. Express **22**, A715 (2014).

[13] D. Timmerman, I. Izeddin, P. Stallinga, I. N. Yassievich, and T. Gregorkiewicz, *Space-separated quantum cutting with silicon nanocrystals for photovoltaic applications*, Nat. Photonics **2**, 105 (2008).

[14] O. E. Semonin, J. M. Luther, S. Choi, H.-Y. Chen, J. Gao, A. J. Nozik, and M. C. Beard, *Peak External Photocurrent Quantum Efficiency Exceeding 100% via MEG in a Quantum Dot Solar Cell*, Science **334**, 1530 (2011).

[15] D. N. Congreve, J. Lee, N. J. Thompson, E. Hontz, S. R. Yost, P. D. Reusswig, M. E. Bahlke, S. Reineke, T. Van Voorhis, and M. A. Baldo, *External Quantum Efficiency Above 100% in a Singlet-Exciton-Fission-Based Organic Photovoltaic Cell*, Science **340**, 334 (2013).

[16] N. J. L. K. Davis, M. L. Böhm, M. Tabachnyk, F. Wisnivesky-Rocca-Rivarola, T. C. Jellicoe, C. Ducati, B. Ehrler, and N. C. Greenham, *Multiple-exciton generation in lead selenide nanorod solar cells with external quantum efficiencies exceeding 120%*, Nat. Commun. **6**, 8259 (2015).

[17] M. A. Green, K. Emery, Y. Hishikawa, W. Warta, and E. D. Dunlop, *Solar cell efficiency tables (version 47)*, Prog. Photovoltaics Res. Appl. **24**, 3 (2016).

[18] A. Polman, M. Knight, E. C. Garnett, B. Ehrler, and W. C. Sinke, *Photovoltaic materials: Present efficiencies and future challenges*, Science **352**, aad4424 (2016).

[19] A. F. Koenderink, A. Alu, and A. Polman, *Nanophotonics: Shrinking light-based technology*, Science **348**, 516 (2015).

[20] N. Yu, P. Genevet, M. A. Kats, F. Aieta, J.-P. Tetienne, F. Capasso, and Z. Gaburro, *Light Propagation with Phase Discontinuities: Generalized Laws of Reflection and Refraction*, Science **334**, 333 (2011).

[21] Y. Zhao and A. Alù, *Manipulating light polarization with ultrathin plasmonic metasurfaces*, Phys. Rev. B **84**, 205428 (2011).

[22] D. Lin, P. Fan, E. Hasman, and M. L. Brongersma, *Dielectric gradient metasurface optical elements*, Science **345**, 298 (2014).

[23] K. Drexhage, *Influence of a dielectric interface on fluorescence decay time*, J. Lumin. **1-2**, 693 (1970).

[24] E. Yablonovitch, *Inhibited Spontaneous Emission in Solid-State Physics and Electronics*, Phys. Rev. Lett. **58**, 2059 (1987).

[25] S. John, *Strong localization of photons in certain disordered dielectric superlattices*, Phys. Rev. Lett. **58**, 2486 (1987).

[26] O. L. Muskens, V. Giannini, J. A. Sánchez-Gil, and J. Gómez Rivas, *Strong enhancement of the radiative decay rate of emitters by single plasmonic nanoantennas*, Nano Lett. **7**, 2871 (2007).

[27] G. M. Akselrod, C. Argyropoulos, T. B. Hoang, C. Ciracì, C. Fang, J. Huang, D. R. Smith, and M. H. Mikkelsen, *Probing the mechanisms of large Purcell enhancement in plasmonic nanoantennas*, Nat. Photonics **8**, 835 (2014).

[28] M. Frimmer, Y. Chen, and A. F. Koenderink, *Scanning Emitter Lifetime Imaging Microscopy for Spontaneous Emission Control*, Phys. Rev. Lett. **107**, 123602 (2011).

[29] J. Renger, R. Quidant, N. van Hulst, and L. Novotny, *Surface-Enhanced Nonlinear Four-Wave Mixing*, Phys. Rev. Lett. **104**, 046803 (2010).

[30] J. Lee, M. Tymchenko, C. Argyropoulos, P.-Y. Chen, F. Lu, F. Demmerle, G. Boehm, M.-C. Amann, A. Alù, and M. A. Belkin, *Giant nonlinear response from plasmonic metasurfaces coupled to intersubband transitions.*, Nature **511**, 65 (2014).

[31] A. Alù, G. D'Aguanno, N. Mattiucci, and M. J. Bloemer, *Plasmonic Brewster Angle: Broadband Extraordinary Transmission through Optical Gratings*, Phys. Rev. Lett. **106**, 123902 (2011).

[32] Y. Shen, C. W. Hsu, Y. X. Yeng, J. D. Joannopoulos, and M. Soljačić, *Broadband angular selectivity of light at the nanoscale: Progress, applications, and outlook*, Appl. Phys. Rev. **3**, 011103 (2016).

[33] Z. Ruan and S. Fan, *Superscattering of Light from Subwavelength Nanostructures*, Phys. Rev. Lett. **105**, 013901 (2010).

[34] S. A. Mann and E. C. Garnett, *Extreme Light Absorption in Thin Semiconductor Films Wrapped around Metal Nanowires*, Nano Lett. **13**, 3173 (2013).

[35] A. Alù and N. Engheta, *Achieving transparency with plasmonic and metamaterial coatings*, Phys. Rev. E **72**, 016623 (2005).

[36] J. B. Pendry, *Controlling Electromagnetic Fields*, Science **312**, 1780 (2006).

[37] P. Fan, U. K. Chettiar, L. Cao, F. Afshinmanesh, N. Engheta, and M. L. Brongersma, *An invisible metal-semiconductor photodetector*, Nat. Photonics **6**, 380 (2012).

[38] C. E. Bohren and D. R. Huffman, *Absorption and Scattering of Light by Small Particles*, John Wiley & Sons, Inc., New York, NY, USA, 1983.

[39] M. L. Brongersma, Y. Cui, and S. Fan, *Light management for photovoltaics using high-index nanostructures*, Nat. Mater. **13**, 451 (2014).

[40] O. L. Muskens, J. Gómez Rivas, R. E. Algra, E. P. A. M. Bakkers, and A. Lagendijk, *Design of light scattering in nanowire materials for photovoltaic applications*, Nano Lett. **8**, 2638 (2008).

[41] V. E. Ferry, M. A. Verschuuren, H. B. T. Li, E. Verhagen, R. J. Walters, R. E. I. Schropp, H. A. Atwater, and A. Polman, *Light trapping in ultrathin plasmonic solar cells*, Opt. Express **18**, A237 (2010).

[42] F. J. Beck, S. Mokkapati, and K. R. Catchpole, *Plasmonic light-trapping for Si solar cells using self-assembled, Ag nanoparticles*, Prog. Photovoltaics Res. Appl. **18**, 500 (2010).

[43] H. A. Atwater and A. Polman, *Plasmonics for improved photovoltaic devices*, Nat. Mater. **9**, 865 (2010).

[44] A. Polman and H. A. Atwater, *Photonic design principles for ultrahigh-efficiency photovoltaics*, Nat. Mater. **11**, 174 (2012).

[45] Z. Yu, A. Raman, and S. Fan, *Fundamental limit of nanophotonic light trapping in solar cells*, Proc. Natl. Acad. Sci. **107**, 17491 (2010).

[46] D. M. Callahan, J. N. Munday, and H. A. Atwater, *Solar cell light trapping beyond the ray optic limit*, Nano Lett. **12**, 214 (2012).

[47] S. A. Mann, R. R. Grote, R. M. Osgood Jr., and J. A. Schuller, *Dielectric particle and void resonators for thin film solar cell textures*, Opt. Express **19**, 25729 (2011).

[48] P. Spinelli, M. A. Verschuuren, and A. Polman, *Broadband omnidirectional antireflection coating based on subwavelength surface Mie resonators.*, Nat. Commun. **3**, 692 (2012).

[49] E. Garnett and P. Yang, *Light Trapping in Silicon Nanowire Solar Cells*, Nano Lett. **10**, 1082 (2010).

[50] R. R. Grote, S. J. Brown, J. B. Driscoll, R. M. Osgood, and J. A. Schuller, *Morphology-dependent light trapping in thin-film organic solar cells*, Opt. Express **21**, A847 (2013).

[51] J. Wallentin, N. Anttu, D. Asoli, M. Huffman, I. Aberg, M. H. Magnusson, G. Siefer, P. Fuss-Kailuweit, F. Dimroth, B. Witzigmann, H. Q. Xu, L. Samuelson, K. Deppert, and M. T. Borgstrom, *InP Nanowire Array Solar Cells Achieving 13.8% Efficiency by Exceeding the Ray Optics Limit*, Science **339**, 1057 (2013).

[52] S. L. Diedenhofen, G. Vecchi, R. E. Algra, A. Hartsuiker, O. L. Muskens, G. Immink, E. P. A. M. Bakkers, W. L. Vos, and J. Gómez Rivas, *Broad-band and Omnidirectional Antireflection Coatings Based on Semiconductor Nanorods*, Adv. Mater. **21**, 973 (2009).

[53] P. Krogstrup, H. I. Jørgensen, M. Heiss, O. Demichel, J. V. Holm, M. Aagesen, J. Nygard, and A. Fontcuberta i Morral, *Single-nanowire solar cells beyond the Shockley-Queisser limit*, Nat. Photonics **7**, 306 (2013).

[54] S. L. Diedenhofen, O. T. A. Janssen, G. Grzela, E. P. A. M. Bakkers, and J. Gómez Rivas, *Strong Geometrical Dependence of the Absorption of Light in Arrays of Semiconductor Nanowires*, ACS Nano **5**, 2316 (2011).

[55] E. C. Garnett, M. L. Brongersma, Y. Cui, and M. D. McGehee, *Nanowire Solar Cells*, Annu. Rev. Mater. Res. **41**, 269 (2011).

[56] G. Grzela, R. Paniagua-Domínguez, T. Barten, D. van Dam, J. A. Sánchez-Gil, and J. Gómez Rivas, *Nanowire Antenna Absorption Probed with Time-Reversed Fourier Microscopy*, Nano Lett. **14**, 3227 (2014).

[57] V. R. Almeida, Q. Xu, C. A. Barrios, and M. Lipson, *Guiding and confining light in void nanostructure*, Opt. Lett. **29**, 1209 (2004).

[58] H. R. Stuart and D. G. Hall, *Thermodynamic limit to light trapping in thin planar structures*, J. Opt. Soc. Am. A **14**, 3001 (1997).

[59] E. Yablonovitch, *Statistical ray optics,* J. Opt. Soc. Am. **72**, 899 (1982).

[60] A. Lenert, D. M. Bierman, Y. Nam, W. R. Chan, I. Celanović, M. Soljačić, and E. N. Wang, *A nanophotonic solar thermophotovoltaic device,* Nat. Nanotechnol. **9**, 126 (2014).

[61] D. M. Bierman, A. Lenert, W. R. Chan, B. Bhatia, I. Celanović, M. Soljačić, and E. N. Wang, *Enhanced photovoltaic energy conversion using thermally based spectral shaping,* Nat. Energy **1**, 16068 (2016).

[62] S. D. Lester, T. S. Kim, and B. G. Streetman, *Evidence for photon recycling in InP,* Appl. Phys. Lett. **52**, 474 (1988).

[63] R. K. Ahrenkiel, *Minority-carrier lifetime and photon recycling in n-GaAs,* J. Vac. Sci. Technol. A Vacuum, Surfaces, Film. **10**, 990 (1992).

[64] J. Parrott, *Radiative recombination and photon recycling in photovoltaic solar cells*, Sol. Energy Mater. Sol. Cells **30**, 221 (1993).

[65] V. Badescu and P. T. Landsberg, *Influence of photon recycling on solar cell efficiencies*, Semicond. Sci. Technol. **12**, 1491 (1997).

[66] J. N. Munday, *The effect of photonic bandgap materials on the Shockley-Queisser limit*, J. Appl. Phys. **112**, 064501 (2012).

[67] S. Sandhu, Z. Yu, and S. Fan, *Detailed balance analysis of nanophotonic solar cells*, Opt. Express **21**, 1209 (2013).

[68] S. Sandhu, Z. Yu, and S. Fan, *Detailed Balance Analysis and Enhancement of Open-Circuit Voltage in Single-Nanowire Solar Cells,* Nano Lett. **14**, 1011 (2014).

[69] Z. Yu, S. Sandhu, and S. Fan, *Efficiency above the Shockley-Queisser Limit by Using Nanophotonic Effects To Create Multiple Effective Bandgaps With a Single Semiconductor,* Nano Lett. **14**, 66 (2014).

[70] S. A. Mann and E. C. Garnett, *Resonant Nanophotonic Spectrum Splitting for Ultrathin Multijunction Solar Cells,* ACS Photonics **2**, 816 (2015).

[71] A. Dorodnyy, E. Alarcon-Lladó, V. Shklover, C. Hafner, A. Fontcuberta i Morral, and J. Leuthold, *Efficient Multiterminal Spectrum Splitting via a Nanowire Array Solar Cell*, ACS Photonics **2**, 1284 (2015).

[72] Y. Zeng, Q. Ye, and W. Shen, *Design principles for single standing nanowire solar cells: going beyond the planar efficiency limits,* Sci. Rep. **4**, 4915 (2014).

[73] M. Faraday, *The Bakerian Lecture: Experimental Relations of Gold (and Other Metals) to Light,* Philos. Trans. R. Soc. London **147**, 145 (1857).

[74] C. Sönnichsen, S. Geier, N. E. Hecker, G. von Plessen, J. Feldmann, H. Ditlbacher, B. Lamprecht, J. R. Krenn, F. R. Aussenegg, V. Z.-H. Chan, J. P. Spatz, and M. MoÌĹller, *Spectroscopy of single metallic nanoparticles using total internal reflection microscopy*, Appl. Phys. Lett. **77**, 2949 (2000).

[75] C. Sönnichsen, T. Franzl, T. Wilk, G. von Plessen, J. Feldmann, O. Wilson, and P. Mulvaney, *Drastic reduction of plasmon damping in gold nanorods.*, Phys. Rev. Lett. **88**, 077402 (2002).

[76] K. Lindfors, T. Kalkbrenner, P. Stoller, and V. Sandoghdar, *Detection and spectroscopy of gold nanoparticles using supercontinuum white light confocal microscopy*, Phys. Rev. Lett. **93**, 037401 (2004).

[77] F. V. Ignatovich and L. Novotny, *Real-Time and Background-Free Detection of Nanoscale Particles*, Phys. Rev. Lett. **96**, 013901 (2006).

[78] I. Sersic, C. Tuambilangana, and A. Femius Koenderink, *Fourier microscopy of single plasmonic scatterers*, New J. Phys. **13**, 083019 (2011).

[79] J. van de Groep, T. Coenen, S. A. Mann, and A. Polman, *Direct imaging of hybridized eigenmodes in coupled silicon nanoparticles*, Optica **3**, 93 (2016).

[80] B. S. Hoener, C. P. Byers, T. S. Heiderscheit, A. S. De Silva Indrasekara, A. Hoggard, W.-S. Chang, S. Link, and C. F. Landes, *Spectroelectrochemistry of Halide Anion Adsorption and Dissolution of Single Gold Nanorods*, J. Phys. Chem. C **120**, 20604 (2016).

[81] J. M. Bingham, K. A. Willets, N. C. Shah, D. Q. Andrews, and R. P. Van Duyne, *Localized Surface Plasmon Resonance Imaging: Simultaneous Single Nanoparticle Spectroscopy and Diffusional Dynamics*, J. Phys. Chem. C **113**, 16839 (2009).

[82] M. Y. Sfeir, F. Wang, L. Huang, C.-C. Chuang, J. Hone, S. P. O'Brien, T. F. Heinz, and L. E. Brus, *Probing Electronic Transitions in Individual Carbon Nanotubes by Rayleigh Scattering*, Science **306**, 1540 (2004).

[83] M. Y. Sfeir, T. Beetz, F. Wang, L. Huang, X. M. Huang, M. Huang, J. Hone, S. O'Brien, J. A. Misewich, T. F. Heinz, L. Wu, Y. Zhu, and L. E. Brus, *Optical spectroscopy of individual single-walled carbon nanotubes of defined chiral structure*, Science **312**, 554 (2006).

[84] W. M. Itano, J. C. Bergquist, and D. J. Wineland, *Laser Spectroscopy of Trapped Atomic Ions*, Science **237**, 612 (1987).

[85] A. Ashkin and J. Dziedzic, *Optical trapping and manipulation of viruses and bacteria*, Science **235**, 1517 (1987).

[86] W. E. Moerner and L. Kador, *Optical detection and spectroscopy of single molecules in a solid*, Phys. Rev. Lett. **62**, 2535 (1989).

[87] M. Celebrano, P. Kukura, A. Renn, and V. Sandoghdar, *Single-molecule imaging by optical absorption*, Nat. Photonics **5**, 95 (2011).

[88] A. Gaiduk, M. Yorulmaz, P. V. Ruijgrok, and M. Orrit, *Room-Temperature Detection of a Single Molecule's Absorption by Photothermal Contrast*, Science **330**, 353 (2010).

[89] M. Husnik, S. Linden, R. Diehl, J. Niegemann, K. Busch, and M. Wegener, *Quantitative Experimental Determination of Scattering and Absorption Cross-Section Spectra of Individual Optical Metallic Nanoantennas*, Phys. Rev. Lett. **109**, 233902 (2012).

[90] A. Crut, P. Maioli, N. Del Fatti, and F. Vallée, *Optical absorption and scattering spectroscopies of single nano-objects*, Chem. Soc. Rev. **43**, 3921 (2014).

[91] P. Zijlstra and M. Orrit, *Single metal nanoparticles: optical detection, spectroscopy and applications*, Reports Prog. Phys. **74**, 106401 (2011).

[92] J. Olson, S. Dominguez-medina, A. Hoggard, L.-y. Wang, W.-s. Chang, S. Link, J. Olson, and S. Dominguez-medina, *Optical characterization of single plasmonic nanoparticles*, Chem. Soc. Rev. **44**, 40 (2014).

[93] M. Husnik, M. W. Klein, N. Feth, M. König, J. Niegemann, K. Busch, S. Linden, and M. Wegener, *Absolute extinction cross-section of individual magnetic split-ring resonators*, Nat. Photonics **2**, 614 (2008).

[94] J.-C. Blancon, M. Paillet, H. N. Tran, X. T. Than, S. A. Guebrou, A. Ayari, A. San Miguel, N.-M. Phan, A.-A. Zahab, J.-L. Sauvajol, N. Del Fatti, and F. Vallée, *Direct measurement of the absolute absorption spectrum of individual semiconducting single-wall carbon nanotubes*, Nat. Commun. **4**, 2542 (2013).

[95] M. P. McDonald, F. Vietmeyer, D. Aleksiuk, and M. Kuno, *Supercontinuum spatial modulation spectroscopy: Detection and noise limitations*, Rev. Sci. Instrum. **84**, 113104 (2013).

[96] A. Lombardi, M. P. Grzelczak, A. Crut, P. Maioli, I. Pastoriza-Santos, L. M. Liz-Marzán, N. Del Fatti, and F. Vallée, *Optical Response of Individual Au-Ag@SiO2 Heterodimers*, ACS Nano **7**, 2522 (2013).

[97] F. Wang, D. J. Cho, B. Kessler, J. Deslippe, P. J. Schuck, S. G. Louie, A. Zettl, T. F. Heinz, and Y. R. Shen, *Observation of Excitons in One-Dimensional Metallic Single-Walled Carbon Nanotubes*, Phys. Rev. Lett. **99**, 227401 (2007).

[98] P. Billaud, S. Marhaba, N. Grillet, E. Cottancin, C. Bonnet, J. Lermé, J.-L. Vialle, M. Broyer, and M. Pellarin, *Absolute optical extinction measurements of single nano-objects by spatial modulation spectroscopy using a white lamp*, Rev. Sci. Instrum. **81**, 043101 (2010).

[99] O. L. Muskens, G. Bachelier, N. Del Fatti, F. Vallée, A. Brioude, X. Jiang, and M. P. Pileni, *Quantitative absorption spectroscopy of a single gold nanorod*, J. Phys. Chem. C **112**, 8917 (2008).

[100] P. Billaud, J.-R. Huntzinger, E. Cottancin, J. Lermé, M. Pellarin, L. Arnaud, M. Broyer, N. Del Fatti, and F. Vallée, *Optical extinction spectroscopy of single silver nanoparticles*, Eur. Phys. J. D **43**, 271 (2007).

[101] L. S. Slaughter, W. S. Chang, P. Swanglap, A. Tcherniak, B. P. Khanal, E. R. Zubarev, and S. Link, *Single-particle spectroscopy of gold nanorods beyond the quasi-static limit: Varying the width at constant aspect ratio*, J. Phys. Chem. C **114**, 4934 (2010).

[102] A. Arbouet, D. Christofilos, N. Del Fatti, F. Vallée, J. R. Huntzinger, L. Arnaud, P. Billaud, and M. Broyer, *Direct Measurement of the Single-Metal-Cluster Optical Absorption*, Phys. Rev. Lett. **93**, 127401 (2004).

[103] D. Boyer, P. Tamarat, A. Maali, B. Lounis, and M. Orrit, *Photothermal Imagin of Nanometer-Sized Metal Particles Among Scatterers,* Science **297**, 1160 (2002).

[104] S. Berciaud, L. Cognet, G. A. Blab, and B. Lounis, *Photothermal Heterodyne Imaging of Individual Nonfluorescent Nanoclusters and Nanocrystals,* Phys. Rev. Lett. **93**, 257402 (2004).

[105] A. Gaiduk, P. V. Ruijgrok, M. Yorulmaz, and M. Orrit, *Detection limits in photothermal microscopy,* Chem. Sci. **1**, 343 (2010).

[106] P. Berto, E. B. Ureña, P. Bon, R. Quidant, H. Rigneault, and G. Baffou, *Quantitative absorption spectroscopy of nano-objects*, Phys. Rev. B **86**, 165417 (2012).

[107] M. Yorulmaz, S. Nizzero, A. Hoggard, L.-Y. Wang, Y.-Y. Cai, M.-N. Su, W.-S. Chang, and S. Link, *Single-Particle Absorption Spectroscopy by Photothermal Contrast,* Nano Lett. **15**, 3041 (2015).

[108] J. Giblin, M. Syed, M. T. Banning, M. Kuno, and G. Hartland, *Experimental Determination of Single CdSe Nanowire Absorption Cross Sections through Photothermal Imaging,* ACS Nano **4**, 358 (2010).

[109] C. Ulbrich, S. Fahr, J. Üpping, M. Peters, T. Kirchartz, C. Rockstuhl, R. Wehrspohn, A. Gombert, F. Lederer, and U. Rau, *Directional selectivity and ultra-light-trapping in solar cells,* Phys. Status Solidi Appl. Mater. Sci. **205**, 2831 (2008).

[110] R. A. Pala, J. S. Q. Liu, E. S. Barnard, D. Askarov, E. C. Garnett, S. Fan, and M. L. Brongersma, *Optimization of non-periodic plasmonic light-trapping layers for thin-film solar cells,* Nat. Commun. **4**, 1 (2013).

[111] H. Tan, R. Santbergen, A. H. M. Smets, and M. Zeman, *Plasmonic Light Trapping in Thin-film Silicon Solar Cells with Improved Self-Assembled Silver Nanoparticles,* Nano Lett. **12**, 4070 (2012).

[112] Y. Xu, T. Gong, and J. N. Munday, *The generalized Shockley-Queisser limit for nanostructured solar cells,* Sci. Rep. **5**, 13536 (2015).

[113] A. Niv, M. Gharghi, C. Gladden, O. D. Miller, and X. Zhang, *Near-Field Electromagnetic Theory for Thin Solar Cells,* Phys. Rev. Lett. **109**, 138701 (2012).

[114] U. Rau, U. W. Paetzold, and T. Kirchartz, *Thermodynamics of light management in photovoltaic devices,* Phys. Rev. B **90**, 035211 (2014).

[115] L. Landau and E. Lifshitz, *Electrodynamics of Continuous Media,* Pergamon Press, Oxford, UK, 1963.

[116] G. L. Araújo and A. Martí, *Absolute limiting efficiencies for photovoltaic energy conversion,* Sol. Energy Mater. Sol. Cells **33**, 213 (1994).

[117] X. Zambrana-Puyalto and N. Bonod, *Purcell factor of spherical Mie resonators,* Phys. Rev. B **91**, 195422 (2015).

[118] L. Novotny and B. Hecht, *Principles of Nano-Optics,* Camrbidge University Press, Cambridge, UK, 2nd edition, 2012.

[119] C. E. Balanis, *Antenna Theory: Analysis and Design*, John Wiley & Sons, New York, NY, USA, 3rd edition, 2005.

[120] L. Cao, J. S. White, J.-S. Park, J. A. Schuller, B. M. Clemens, and M. L. Brongersma, *Engineering light absorption in semiconductor nanowire devices*, Nat. Mater. **8**, 643 (2009).

[121] D. R. Abujetas, R. Paniagua-Domínguez, and J. A. Sánchez-Gil, *Unraveling the Janus Role of Mie Resonances and Leaky/Guided Modes in Semiconductor Nanowire Absorption for Enhanced Light Harvesting*, ACS Photonics **2**, 921 (2015).

[122] N. Anttu and H. Q. Xu, *Efficient light management in vertical nanowire arrays for photovoltaics*, Opt. Express **21**, A558 (2013).

[123] D. van Dam, D. R. Abujetas, R. Paniagua-Domínguez, J. A. Sánchez-Gil, E. P. A. M. Bakkers, J. E. M. Haverkort, and J. Gómez Rivas, *Directional and Polarized Emission from Nanowire Arrays*, Nano Lett. **15**, 4557 (2015).

[124] Z. Ruan and S. Fan, *Temporal coupled-mode theory for light scattering by an arbitrarily shaped object supporting a single resonance*, Phys. Rev. A **85**, 043828 (2012).

[125] R. F. Harrington, *Effect of Antenna Size on Gain, Bandwidth, and Efficiency*, J. Res. Natl. Bur. Stand. - D. Radio Propag. **64D**, 1 (1960).

[126] A. Alù and N. Engheta, *Enhanced Directivity From Subwavelength Infrared/Optical Nano-Antennas Loaded With Plasmonic Materials or Metamaterials*, IEEE Trans. Antennas Propag. **55**, 3027 (2007).

[127] J. Hansen, *Spherical Near-Field Antenna Measurements*, Peter Peregrinus, Ltd., London, 1988.

[128] T. Khudiyev and M. Bayindir, *Superenhancers: Novel opportunities for nanowire optoelectronics*, Sci. Rep. **4**, 7505 (2014).

[129] Y. Yu, V. E. Ferry, A. P. Alivisatos, and L. Cao, *Dielectric Core-Shell Optical Antennas for Strong Solar Absorption Enhancement*, Nano Lett. **12**, 3674 (2012).

[130] M. A. Steiner, J. F. Geisz, I. García, D. J. Friedman, A. Duda, and S. R. Kurtz, *Optical enhancement of the open-circuit voltage in high quality GaAs solar cells*, J. Appl. Phys. **113**, 123109 (2013).

[131] V. Ganapati, M. A. Steiner, and E. Yablonovitch, *The Voltage Boost Enabled by Luminescence Extraction in Solar Cells*, IEEE J. Photovoltaics **99**, 1 (2016).

[132] I. Schnitzer, E. Yablonovitch, C. Caneau, and T. J. Gmitter, *Ultrahigh spontaneous emission quantum efficiency, 99.7% internally and 72% externally, from AlGaAs/GaAs/AlGaAs double heterostructures*, Appl. Phys. Lett. **62**, 131 (1993).

[133] A. Martí, J. L. Balenzategui, and R. F. Reyna, *Photon recycling and Shockley's diode equation*, J. Appl. Phys. **82**, 4067 (1997).

[134] M. A. Green, *Radiative efficiency of state-of-the-art photovoltaic cells*, Prog. Photovoltaics Res. Appl. **20**, 472 (2012).

[135] T. Tiedje, E. Yablonovitch, G. Cody, and B. Brooks, *Limiting efficiency of silicon solar cells*, IEEE Trans. Electron Devices **31**, 711 (1984).

[136] P. Campbell and M. Green, *The limiting efficiency of silicon solar cells under concentrated sunlight*, IEEE Trans. Electron Devices **33**, 234 (1986).

[137] Y. Shen, D. Ye, I. Celanovic, S. G. Johnson, J. D. Joannopoulos, and M. Soljačić, *Optical Broadband Angular Selectivity*, Science **343**, 1499 (2014).

[138] L. van Dijk, J. van de Groep, M. Di Vece, and R. E. I. Schropp, *Exploration of external light trapping for photovoltaic modules*, Opt. Express **24**, A1158 (2016).

[139] H. Chew, *Transition rates of atoms near spherical surfaces*, J. Chem. Phys. **87**, 1355 (1987).

[140] Lumerical Solutions, Inc., *http://www.lumerical.com/tcad-products/fdtd/*.

[141] V. Liu and S. Fan, *S^4: A free electromagnetic solver for layered periodic structures*, Comput. Phys. Commun. **183**, 2233 (2012).

[142] P. Wurfel, *The chemical potential of radiation*, J. Phys. C Solid State Phys. **15**, 3967 (1982).

[143] A. Imenes and D. Mills, *Spectral beam splitting technology for increased conversion efficiency in solar concentrating systems: a review*, Sol. Energy Mater. Sol. Cells **84**, 19 (2004).

[144] C. N. Eisler, Z. R. Abrams, M. T. Sheldon, X. Zhang, and H. A. Atwater, *Multijunction solar cell efficiencies: effect of spectral window, optical environment and radiative coupling*, Energy Environ. Sci. **7**, 3600 (2014).

[145] M. A. Green and A. Ho-Baillie, *Forty three per cent composite split-spectrum concentrator solar cell efficiency*, Prog. Photovoltaics Res. Appl. **18**, 42 (2010).

[146] Y. Ra'di, C. R. Simovski, and S. A. Tretyakov, *Thin Perfect Absorbers for Electromagnetic Waves: Theory, Design, and Realizations*, Phys. Rev. Appl. **3**, 037001 (2015).

[147] Y. Cui, Y. He, Y. Jin, F. Ding, L. Yang, Y. Ye, S. Zhong, Y. Lin, and S. He, *Plasmonic and metamaterial structures as electromagnetic absorbers*, Laser Photon. Rev. **8**, 495 (2014).

[148] M. Kuttge, F. J. García de Abajo, and A. Polman, *Ultrasmall Mode Volume Plasmonic Nanodisk Resonators*, Nano Lett. **10**, 1537 (2010).

[149] J. Yang, C. Sauvan, A. Jouanin, S. Collin, J.-L. Pelouard, and P. Lalanne, *Ultrasmall metal-insulator-metal nanoresonators: impact of slow-wave effects on the quality factor*, Opt. Express **20**, 16880 (2012).

[150] A. Chandran, E. S. Barnard, J. S. White, and M. L. Brongersma, *Metal-dielectric-metal surface plasmon-polariton resonators*, Phys. Rev. B **85**, 085416 (2012).

[151] C. Koechlin, P. Bouchon, F. Pardo, J.-l. Pelouard, and R. Haïdar, *Analytical description of subwavelength plasmonic MIM resonators and of their combination*, Opt. Express **21**, 7025 (2013).

[152] S. Adachi, *Properties of Semiconductor Alloys*, John Wiley & Sons, Ltd, Chichester, UK, 2009.

[153] R. Faggiani, J. Yang, and P. Lalanne, *Quenching, Plasmonic, and Radiative Decays in Nanogap Emitting Devices*, ACS Photonics **2**, 1739 (2015).

[154] Z. Wang, Z. Dong, Y. Gu, Y.-H. Chang, L. Zhang, L.-J. Li, W. Zhao, G. Eda, W. Zhang, G. Grinblat, S. A. Maier, J. K. W. Yang, C.-W. Qiu, and A. T. S. Wee, *Giant photoluminescence enhancement in tungsten-diselenide-gold plasmonic hybrid structures*, Nat. Commun. **7**, 11283 (2016).

[155] G. M. Akselrod, T. Ming, C. Argyropoulos, T. B. Hoang, Y. Lin, X. Ling, D. R. Smith, J. Kong, and M. H. Mikkelsen, *Leveraging Nanocavity Harmonics for Control of Optical Processes in 2D Semiconductors*, Nano Lett. **15**, 3578 (2015).

[156] C.-W. Cheng, M. N. Abbas, C.-W. Chiu, K.-T. Lai, M.-H. Shih, and Y.-C. Chang, *Wide-angle polarization independent infrared broadband absorbers based on metallic multi-sized disk arrays*, Opt. Express **20**, 10376 (2012).

[157] J. Le Perchec, Y. Desieres, N. Rochat, and R. Espiau de Lamaestre, *Subwavelength optical absorber with an integrated photon sorter*, Appl. Phys. Lett. **100**, 113305 (2012).

[158] M. G. Nielsen, A. Pors, O. Albrektsen, and S. I. Bozhevolnyi, *Efficient absorption of visible radiation by gap plasmon resonators*, Opt. Express **20**, 13311 (2012).

[159] C. Koechlin, P. Bouchon, F. Pardo, J. Jaeck, X. Lafosse, J.-L. Pelouard, and R. Haïdar, *Total routing and absorption of photons in dual color plasmonic antennas*, Appl. Phys. Lett. **99**, 241104 (2011).

[160] N. Mohammadi Estakhri and A. Alù, *Minimum-scattering superabsorbers*, Phys. Rev. B **89**, 121416 (2014).

[161] M. Gustafsson, C. Sohl, and G. Kristensson, *Physical limitations on antennas of arbitrary shape*, Proc. R. Soc. A Math. Phys. Eng. Sci. **463**, 2589 (2007).

[162] U. Rau, *Reciprocity relation between photovoltaic quantum efficiency and electroluminescent emission of solar cells*, Phys. Rev. B **76**, 085303 (2007).

[163] R. T. Ross, *Thermodynamic Limitations on the Conversion of Radiant Energy into Work*, J. Chem. Phys. **45**, 1 (1966).

[164] O. D. Miller, E. Yablonovitch, and S. R. Kurtz, *Strong Internal and External Luminescence as Solar Cells Approach the Shockley-Queisser Limit*, IEEE J. Photovoltaics **2**, 303 (2012).

[165] B. M. Kayes, H. Nie, R. Twist, S. G. Spruytte, F. Reinhardt, I. C. Kizilyalli, and G. S. Higashi, *27.6% Conversion efficiency, a new record for single-junction solar cells under 1 sun illumination*, in *2011 37th IEEE Photovolt. Spec. Conf.*, pages 4–8, IEEE, 2011.

[166] J. Balenzategui and A. Martí, *Detailed modelling of photon recycling: application to GaAs solar cells*, Sol. Energy Mater. Sol. Cells **90**, 1068 (2006).

[167] K. Joulain, R. Carminati, J.-P. Mulet, and J.-J. Greffet, *Definition and measurement of the local density of electromagnetic states close to an interface,* Phys. Rev. B **68**, 245405 (2003).

[168] W. Lukosz and R. E. Kunz, *Light emission by magnetic and electric dipoles close to a plane interface. I. Total radiated power,* J. Opt. Soc. Am. **67**, 1607 (1977).

[169] H. B. Callen and T. A. Welton, *Irreversibility and Generalized Noise,* Phys. Rev. **83**, 34 (1951).

[170] S. M. Rytov, Y. A. Kravtsov, and V. I. Tatarskii, *Principles of Statistical Radiophysics 3: Elements of Random Fields,* Springer-Verlag, Berlin, 1989.

[171] N. Yu and F. Capasso, *Flat optics with designer metasurfaces,* Nat. Mater. **13**, 139 (2014).

[172] G. W. Kattawar and M. Eisner, *Radiation from a Homogeneous Isothermal Sphere,* Appl. Opt. **9**, 2685 (1970).

[173] R. Sprik, B. A. van Tiggelen, and A. Lagendijk, *Optical emission in periodic dielectrics,* Europhys. Lett. **35**, 265 (1996).

[174] R. Baierlein, *Representing a vector field: Helmholtz's theorem derived from a Fourier identity,* Am. J. Phys. **63**, 180 (1995).

[175] R. Loudon, *The Quantum Theory of Light,* Oxford University Press, Oxford, UK, 3rd edition, 2000.

[176] L. G. Suttorp and M. Wubs, *Field quantization in inhomogeneous absorptive dielectrics,* Phys. Rev. A **70**, 1 (2004).

[177] S. M. Barnett, B. Huttner, and R. Loudon, *Spontaneous emission in absorbing dielectric media,* Phys. Rev. Lett. **68**, 3698 (1992).

[178] C.-A. Guérin, B. Gralak, and A. Tip, *Singularity of the dyadic Green's function for heterogeneous dielectrics,* Phys. Rev. E **75**, 056601 (2007).

[179] W. van Roosbroeck and W. Shockley, *Photon-Radiative Recombination of Electrons and Holes in Germanium,* Phys. Rev. **94**, 1558 (1954).

[180] S. Scheel, L. Knöll, and D.-G. Welsch, *Spontaneous decay of an excited atom in an absorbing dielectric,* Phys. Rev. A **60**, 4094 (1999).

[181] S. Karaveli and R. Zia, *Spectral Tuning by Selective Enhancement of Electric and Magnetic Dipole Emission,* Phys. Rev. Lett. **106**, 193004 (2011).

[182] K. Guo, M. A. Verschuuren, and A. Femius Koenderink, *Superresolution imaging of the local density of states in plasmon lattices,* Optica **3**, 289 (2016).

[183] J. Bleuse, J. Claudon, M. Creasey, N. S. Malik, J.-M. Gérard, I. Maksymov, J.-P. Hugonin, and P. Lalanne, *Inhibition, Enhancement, and Control of Spontaneous Emission in Photonic Nanowires,* Phys. Rev. Lett. **106**, 103601 (2011).

[184] E. Yablonovitch, T. J. Gmitter, and R. Bhat, *Inhibited and enhanced spontaneous emission from optically thin AlGaAs/GaAs Double Heterostructures*, Phys. Rev. Lett. **61**, 2546 (1988).

[185] L. M. Pazos-Outon, M. Szumilo, R. Lamboll, J. M. Richter, M. Crespo-Quesada, M. Abdi-Jalebi, H. J. Beeson, M. Vru ini, M. Alsari, H. J. Snaith, B. Ehrler, R. H. Friend, and F. Deschler, *Photon recycling in lead iodide perovskite solar cells*, Science **351**, 1430 (2016).

[186] H. F. Arnoldus, *Transverse and longitudinal components of the optical self-, near-, middle- and far-field*, J. Mod. Opt. **50**, 755 (2003).

[187] C.-T. Tai, *Dyadic Green functions in electromagnetic theory*, IEEE Press, New York, NY, USA, 1994.

[188] W. C. Chew, *Fields and waves in inhomogeneous media*, IEEE Press, New York, 1995.

[189] A. Howard, *On the longitudinal component of the Green's function dyadic*, Proc. IEEE **62**, 1704 (1974).

[190] J. D. Jackson, *Classical Electrodynamics*, Wiley, New York, NY, USA, 3rd edition, 1999.

[191] G. Baffou, P. Bon, J. Savatier, J. Polleux, M. Zhu, M. Merlin, H. Rigneault, and S. Monneret, *Thermal Imaging of Nanostructures by Quantitative Optical Phase Analysis*, ACS Nano **6**, 2452 (2012).

[192] M. L. Brongersma, N. J. Halas, and P. Nordlander, *Plasmon-induced hot carrier science and technology*, Nat. Nanotechnol. **10**, 25 (2015).

[193] C. Clavero, *Plasmon-induced hot-electron generation at nanoparticle/metal-oxide interfaces for photovoltaic and photocatalytic devices*, Nat. Photonics **8**, 95 (2014).

[194] G. F. Burkhard, E. T. Hoke, and M. D. McGehee, *Accounting for Interference, Scattering, and Electrode Absorption to Make Accurate Internal Quantum Efficiency Measurements in Organic and Other Thin Solar Cells*, Adv. Mater. **22**, 3293 (2010).

[195] S. Leyre, E. Coutino-Gonzalez, J. J. Joos, J. Ryckaert, Y. Meuret, D. Poelman, P. F. Smet, G. Durinck, J. Hofkens, G. Deconinck, and P. Hanselaer, *Absolute determination of photoluminescence quantum efficiency using an integrating sphere setup*, Rev. Sci. Instrum. **85**, 123115 (2014).

[196] D. J. Gargas, H. Gao, H. Wang, and P. Yang, *High Quantum Efficiency of Band-Edge Emission from ZnO Nanowires*, Nano Lett. **11**, 3792 (2011).

[197] X. Duan, Y. Huang, Y. Cui, J. Wang, and C. M. Lieber, *Indium phosphide nanowires as building blocks for nanoscale electronic and optoelectronic devices*, Nature **409**, 66 (2001).

[198] C. P. T. Svensson, T. Mårtensson, J. Trägårdh, C. Larsson, M. Rask, D. Hessman, L. Samuelson, and J. Ohlsson, *Monolithic GaAs/InGaP nanowire light emitting diodes on silicon*, Nanotechnology **19**, 305201 (2008).

[199] E. D. Minot, F. Kelkensberg, M. van Kouwen, J. A. van Dam, L. P. Kouwenhoven, V. Zwiller, M. T. Borgström, O. Wunnicke, M. A. Verheijen, and E. P. A. M. Bakkers, *Single Quantum Dot Nanowire LEDs*, Nano Lett. **7**, 367 (2007).

[200] M. H. Huang, S. Mao, H. Feick, H. Yan, Y. Wu, H. Kind, E. Weber, R. Russo, and P. Yang, *Room-Temperature Ultraviolet Nanowire Nanolasers*, Science **292**, 1897 (2001).

[201] M. Heiss, Y. Fontana, A. Gustafsson, G. Wüst, C. Magen, D. D. O'Regan, J. W. Luo, B. Ketterer, S. Conesa-Boj, A. V. Kuhlmann, J. Houel, E. Russo-Averchi, J. R. Morante, M. Cantoni, N. Marzari, J. Arbiol, A. Zunger, R. J. Warburton, and A. Fontcuberta i Morral, *Self-assembled quantum dots in a nanowire system for quantum photonics*, Nat. Mater. **12**, 439 (2013).

[202] Y. Yu and L. Cao, *Coupled leaky mode theory for light absorption in 2D, 1D, and 0D semiconductor nanostructures*, Opt. Express **20**, 13847 (2012).

[203] K. L. Corwin, N. R. Newbury, J. M. Dudley, S. Coen, S. A. Diddams, B. R. Washburn, K. Weber, and R. S. Windeler, *Fundamental amplitude noise limitations to supercontinuum spectra generated in a microstructured fiber*, Appl. Phys. B Lasers Opt. **77**, 269 (2003).

[204] C. Huber, S. Orlov, P. Banzer, and G. Leuchs, *Corrections to the knife-edge based reconstruction scheme of tightly focused light beams*, Opt. Express **21**, 25069 (2013).

[205] J. R. Taylor, *An Introduction to Error Analysis: The Study of Uncertainties in Physical Measurements*, University Science Books, Sausalito, California, second edi edition, 1997.

[206] T. Plakhotnik, W. Moerner, V. Palm, and U. P. Wild, *Single molecule spectroscopy: maximum emission rate and saturation intensity*, Opt. Commun. **114**, 83 (1995).

[207] E. Palik, *Handbook of Optical Constants of Solids*, Elsevier Academic Press, Waltham, MA, USA, 1985.

[208] I. Aberg, G. Vescovi, D. Asoli, U. Naseem, J. P. Gilboy, C. Sundvall, A. Dahlgren, K. E. Svensson, N. Anttu, M. T. Bjork, and L. Samuelson, *A GaAs Nanowire Array Solar Cell With 15.3% Efficiency at 1 Sun*, IEEE J. Photovoltaics **6**, 185 (2016).

[209] M. Wanlass, *Systems and methods for advanced ultra-high-performance InP solar cells (patent application US20150280042A1)*, 2015.

[210] B. Tian, X. Zheng, T. J. Kempa, Y. Fang, N. Yu, G. Yu, J. Huang, and C. M. Lieber, *Coaxial silicon nanowires as solar cells and nanoelectronic power sources*, Nature **449**, 885 (2007).

[211] M. D. Kelzenberg, S. W. Boettcher, J. A. Petykiewicz, D. B. Turner-Evans, M. C. Putnam, E. L. Warren, J. M. Spurgeon, R. M. Briggs, N. S. Lewis, and H. A. Atwater, *Enhanced absorption and carrier collection in Si wire arrays for photovoltaic applications*, Nat. Mater. **9**, 239 (2010).

[212] J. Tang, Z. Huo, S. Brittman, H. Gao, and P. Yang, *Solution-processed core-shell nanowires for efficient photovoltaic cells*, Nat. Nanotechnol. **6**, 568 (2011).

[213] J. V. Holm, H. I. Jørgensen, P. Krogstrup, J. Nygård, H. Liu, and M. Aagesen, *Surface-passivated GaAsP single-nanowire solar cells exceeding 10% efficiency grown on silicon*, Nat. Commun. **4**, 1498 (2013).

[214] J. E. Allen, E. R. Hemesath, D. E. Perea, J. L. Lensch-Falk, Z. Y. Li, F. Yin, M. H. Gass, P. Wang, A. L. Bleloch, R. E. Palmer, and L. J. Lauhon, *High-resolution detection of Au catalyst atoms in Si nanowires.*, Nat. Nanotechnol. **3**, 168 (2008).

[215] A. Nowzari, M. Heurlin, V. Jain, K. Storm, A. Hosseinnia, N. Anttu, M. T. Borgström, H. Pettersson, and L. Samuelson, *A Comparative Study of Absorption in Vertically and Laterally Oriented InP Core-Shell Nanowire Photovoltaic Devices*, Nano Lett. **15**, 1809 (2015).

[216] S. N. G. Chu, R. A. Logan, M. Geva, and N. T. Ha, *Concentration dependent Zn diffusion in InP during metalorganic vapor phase epitaxy*, J. Appl. Phys. **78**, 3001 (1995).

[217] M. De Luca, A. Zilli, H. A. Fonseka, S. Mokkapati, A. Miriametro, H. H. Tan, L. M. Smith, C. Jagadish, M. Capizzi, and A. Polimeni, *Polarized Light Absorption in Wurtzite InP Nanowire Ensembles*, Nano Lett. **15**, 998 (2015).

[218] J. K. Katahara and H. W. Hillhouse, *Quasi-Fermi level splitting and sub-bandgap absorptivity from semiconductor photoluminescence*, J. Appl. Phys. **116**, 173504 (2014).

[219] M. H. M. van Weert, O. Wunnicke, A. L. Roest, T. J. Eijkemans, A. Yu Silov, J. E. M. Haverkort, G. W. 't Hooft, and E. P. A. M. Bakkers, *Large redshift in photoluminescence of p-doped InP nanowires induced by Fermi-level pinning*, Appl. Phys. Lett. **88**, 043109 (2006).

[220] D. Magde, R. Wong, and P. G. Seybold, *Fluorescence Quantum Yields and Their Relation to Lifetimes of Rhodamine 6G and Fluorescein in Nine Solvents: Improved Absolute Standards for Quantum Yields*, Photochem. Photobiol. **75**, 327 (2007).

[221] S. Chuang, *Physics of Photonic Devices*, John Wiley & Sons, New York, NY, USA, 1995.

[222] W. Lukosz, *Light emission by magnetic and electric dipoles close to a plane dielectric interface. III. Radiation patterns of dipoles with arbitrary orientation*, J. Opt. Soc. Am. **69**, 1495 (1979).

[223] G. Grzela, R. Paniagua-Domínguez, T. Barten, Y. Fontana, J. A. Sánchez-Gil, and J. Gómez Rivas, *Nanowire Antenna Emission*, Nano Lett. **12**, 5481 (2012).

[224] C. Zhang, J. Zhang, Y. Hao, Z. Lin, and C. Zhu, *A simple and efficient solar cell parameter extraction method from a single current-voltage curve*, J. Appl. Phys. **110**, 064504 (2011).

[225] T. Mårtensson, P. Carlberg, M. Borgström, L. Montelius, W. Seifert, and L. Samuelson, *Nanowire arrays defined by nanoimprint lithography*, Nano Lett. **4**, 699 (2004).

[226] A. Pierret, M. Hocevar, S. L. Diedenhofen, R. E. Algra, E. Vlieg, E. C. Timmering, M. A. Verschuuren, G. W. G. Immink, M. A. Verheijen, and E. P. A. M. Bakkers, *Generic nano-imprint process for fabrication of nanowire arrays*, Nanotechnology **21** (2010).

[227] J. Zhu, Z. Yu, G. F. Burkhard, C.-M. Hsu, S. T. Connor, Y. Xu, Q. Wang, M. McGehee, S. Fan, and Y. Cui, *Optical Absorption Enhancement in Amorphous Silicon Nanowire and Nanocone Arrays*, Nano Lett. **9**, 279 (2009).

[228] Y. Yao, J. Yao, V. K. Narasimhan, Z. Ruan, C. Xie, S. Fan, and Y. Cui, *Broadband light management using low-Q whispering gallery modes in spherical nanoshells*, Nat. Commun. **3**, 664 (2012).

[229] J. A. Schuller, E. S. Barnard, W. Cai, Y. C. Jun, J. S. White, and M. L. Brongersma, *Plasmonics for extreme light concentration and manipulation*, Nat. Mater. **9**, 193 (2010).

[230] H. Haus, *Waves and Fields in Optoelectronics*, Prentice-Hall, Englewood Cliffs, NJ, USA, 1984.

[231] R. E. Hamam, A. Karalis, J. D. Joannopoulos, and M. Soljačić, *Coupled-mode theory for general free-space resonant scattering of waves*, Phys. Rev. A **75**, 053801 (2007).

[232] J. A. Schuller, T. Taubner, and M. L. Brongersma, *Optical antenna thermal emitters*, Nat. Photonics **3**, 658 (2009).

[233] J. A. Schuller and M. L. Brongersma, *General properties of dielectric optical antennas*, Opt. Express **17**, 24084 (2009).

[234] L. Huang, Y. Yu, and L. Cao, *General Modal Properties of Optical Resonances in Subwavelength Nonspherical Dielectric Structures*, Nano Lett. **13**, 3559 (2013).

[235] O. D. Miller, C. W. Hsu, M. T. H. Reid, W. Qiu, B. G. DeLacy, J. D. Joannopoulos, M. Soljačić, and S. G. Johnson, *Fundamental Limits to Extinction by Metallic Nanoparticles*, Phys. Rev. Lett. **112**, 123903 (2014).

[236] O. D. Miller, A. G. Polimeridis, M. T. Homer Reid, C. W. Hsu, B. G. DeLacy, J. D. Joannopoulos, M. Soljačić, and S. G. Johnson, *Fundamental limits to optical response in absorptive systems*, Opt. Express **24**, 3329 (2016).

[237] Z. Fan, H. Razavi, J.-W. Do, A. Moriwaki, O. Ergen, Y.-L. Chueh, P. W. Leu, J. C. Ho, T. Takahashi, L. A. Reichertz, S. Neale, K. Yu, M. Wu, J. W. Ager, and A. Javey, *Three-dimensional nanopillar-array photovoltaics on low-cost and flexible substrates*, Nat. Mater. **8**, 648 (2009).

[238] D. S. Hecht, L. Hu, and G. Irvin, *Emerging Transparent Electrodes Based on Thin Films of Carbon Nanotubes, Graphene, and Metallic Nanostructures*, Adv. Mater. **23**, 1482 (2011).

[239] J.-Y. Lee, S. T. Connor, Y. Cui, and P. Peumans, *Solution-Processed Metal Nanowire Mesh Transparent Electrodes*, Nano Lett. **8**, 689 (2008).

[240] J. van de Groep, P. Spinelli, and A. Polman, *Transparent Conducting Silver Nanowire Networks*, Nano Lett. **12**, 3138 (2012).

[241] T. M. Bambino, A. M. S. Breitschaft, V. C. Barbosa, and L. G. Guimarães, *Application of semiclassical and geometrical optics theories to resonant modes of a coated sphere*, J. Opt. Soc. Am. A **20**, 489 (2003).

[242] P. B. Catrysse and S. Fan, *Understanding the dispersion of coaxial plasmonic structures through a connection with the planar metal-insulator-metal geometry*, Appl. Phys. Lett. **94**, 231111 (2009).

[243] S. R. K. Rodriguez, *Classical and quantum distinctions between weak and strong coupling*, Eur. J. Phys. **37**, 025802 (2016).

[244] L. Novotny, *Strong coupling, energy splitting, and level crossings: A classical perspective*, Am. J. Phys. **78**, 1199 (2010).

[245] S. R. K. Rodriguez, Y. T. Chen, T. P. Steinbusch, M. A. Verschuuren, A. F. Koenderink, and J. Gómez Rivas, *From weak to strong coupling of localized surface plasmons to guided modes in a luminescent slab*, Phys. Rev. B **90**, 235406 (2014).

[246] R. Chikkaraddy, B. de Nijs, F. Benz, S. J. Barrow, O. A. Scherman, E. Rosta, A. Demetriadou, P. Fox, O. Hess, and J. J. Baumberg, *Single-molecule strong coupling at room temperature in plasmonic nanocavities*, Nature **535**, 127 (2016).

[247] B. Wiley, Y. Sun, and Y. Xia, *Synthesis of Silver Nanostructures with Controlled Shapes and Properties*, Acc. Chem. Res. **40**, 1067 (2007).

[248] S.-K. Kim, R. W. Day, J. F. Cahoon, T. J. Kempa, K.-D. Song, H.-G. Park, and C. M. Lieber, *Tuning Light Absorption in Core/Shell Silicon Nanowire Photovoltaic Devices through Morphological Design*, Nano Lett. **12**, 4971 (2012).

[249] S. Mubeen, J. Lee, N. Singh, S. Krämer, G. D. Stucky, and M. Moskovits, *An autonomous photosynthetic device in which all charge carriers derive from surface plasmons*, Nat. Nanotechnol. **8**, 247 (2013).

[250] F. P. García de Arquer, A. Mihi, D. Kufer, and G. Konstantatos, *Photoelectric Energy Conversion of Plasmon-Generated Hot Carriers in Metal-Insulator-Semiconductor Structures*, ACS Nano **7**, 3581 (2013).

[251] Y. Nishijima, K. Ueno, Y. Yokota, K. Murakoshi, and H. Misawa, *Plasmon-Assisted Photocurrent Generation from Visible to Near-Infrared Wavelength Using a Au-Nanorods/TiO2 Electrode*, J. Phys. Chem. Lett. **1**, 2031 (2010).

[252] Y. Takahashi and T. Tatsuma, *Solid state photovoltaic cells based on localized surface plasmon-induced charge separation*, Appl. Phys. Lett. **99**, 182110 (2011).

[253] Y. K. Lee, C. H. Jung, J. Park, H. Seo, G. A. Somorjai, and J. Y. Park, *Surface Plasmon-Driven Hot Electron Flow Probed with Metal-Semiconductor Nanodiodes*, Nano Lett. **11**, 4251 (2011).

[254] P. Reineck, G. P. Lee, D. Brick, M. Karg, P. Mulvaney, and U. Bach, *A Solid-State Plasmonic Solar Cell via Metal Nanoparticle Self-Assembly*, Adv. Mater. **24**, 4750 (2012).

[255] S. Mubeen, J. Lee, W.-R. Lee, N. Singh, G. D. Stucky, and M. Moskovits, *On the Plasmonic Photovoltaic*, ACS Nano **8**, 6066 (2014).

[256] B. K. Meyer, A. Polity, D. Reppin, M. Becker, P. Hering, P. J. Klar, T. Sander, C. Reindl, J. Benz, M. Eickhoff, C. Heiliger, M. Heinemann, J. Bläsing, A. Krost, S. Shokovets, C. Müller, and C. Ronning, *Binary copper oxide semiconductors: From materials towards devices*, Phys. status solidi **249**, 1487 (2012).

[257] F. Meillaud, A. Shah, C. Droz, E. Vallat-Sauvain, and C. Miazza, *Efficiency limits for single-junction and tandem solar cells*, Sol. Energy Mater. Sol. Cells **90**, 2952 (2006).

[258] F. Dimroth et al., *Wafer bonded four-junction GaInP/GaAs/GaInAsP/GaInAs concentrator solar cells with 44.7% efficiency*, Prog. Photovoltaics Res. Appl. **22**, 277 (2014).

[259] Z. M. Beiley and M. D. McGehee, *Modeling low cost hybrid tandem photovoltaics with the potential for efficiencies exceeding 20%*, Energy Environ. Sci. **5**, 9173 (2012).

[260] T. Minami, Y. Nishi, and T. Miyata, *High-Efficiency Cu_2O-Based Heterojunction Solar Cells Fabricated Using a Ga2O3 Thin Film as N-Type Layer*, Appl. Phys. Express **6**, 044101 (2013).

[261] Y. S. Lee, J. Heo, M. T. Winkler, S. C. Siah, S. B. Kim, R. G. Gordon, and T. Buonassisi, *Nitrogen-doped cuprous oxide as a p-type hole-transporting layer in thin-film solar cells*, J. Mater. Chem. A **1**, 15416 (2013).

[262] S. W. Lee, Y. S. Lee, J. Heo, S. C. Siah, D. Chua, R. E. Brandt, S. B. Kim, J. P. Mailoa, T. Buonassisi, and R. G. Gordon, *Improved Cu_2O-Based Solar Cells Using Atomic Layer Deposition to Control the Cu Oxidation State at the p-n Junction*, Adv. Energy Mater. **4**, 1301916 (2014).

[263] T. Oku, T. Yamada, K. Fujimoto, and T. Akiyama, *Microstructures and Photovoltaic Properties of Zn(Al)O/Cu_2O-Based Solar Cells Prepared by Spin-Coating and Electrodeposition*, Coatings **4**, 203 (2014).

[264] C.-C. Chen, L.-C. Chen, and Y.-H. Lee, *Fabrication and Optoelectrical Properties of IZO/Cu2O Heterostructure Solar Cells by Thermal Oxidation*, Adv. Condens. Matter Phys. **2012**, 1 (2012).

[265] A. T. Marin, D. Muñoz-Rojas, D. C. Iza, T. Gershon, K. P. Musselman, and J. L. MacManus-Driscoll, *Novel Atmospheric Growth Technique to Improve Both Light Absorption and Charge Collection in ZnO/Cu_2O Thin Film Solar Cells*, Adv. Funct. Mater. **23**, 3413 (2013).

[266] T. S. Gershon, A. K. Sigdel, A. T. Marin, M. F. van Hest, D. S. Ginley, R. H. Friend, J. L. MacManus-Driscoll, and J. J. Berry, *Improved fill factors in solution-processed ZnO/Cu_2O photovoltaics*, Thin Solid Films **536**, 280 (2013).

[267] T. Minami, Y. Nishi, T. Miyata, and J.-i. Nomoto, *High-Efficiency Oxide Solar Cells with ZnO/Cu_2O Heterojunction Fabricated on Thermally Oxidized Cu_2O Sheets*, Appl. Phys. Express **4**, 062301 (2011).

[268] Y. S. Lee, D. Chua, R. E. Brandt, S. C. Siah, J. V. Li, J. P. Mailoa, S. W. Lee, R. G. Gordon, and T. Buonassisi, *Atomic Layer Deposited Gallium Oxide Buffer Layer Enables 1.2 V Open-Circuit Voltage in Cuprous Oxide Solar Cells*, Adv. Mater. **26**, 4704 (2014).

[269] C.-H. Kuo, T.-E. Hua, and M. H. Huang, *Au Nanocrystal-Directed Growth of Au-Cu_2O Core-Shell Heterostructures with Precise Morphological Control*, J. Am. Chem. Soc. **131**, 17871 (2009).

[270] S. Hacialioglu, F. Meng, and S. Jin, *Facile and mild solution synthesis of Cu_2O nanowires and nanotubes driven by screw dislocations*, Chem. Commun. **48**, 1174 (2012).

[271] S. Brittman, Y. Yoo, N. P. Dasgupta, S.-I. Kim, B. Kim, and P. Yang, *Epitaxially Aligned Cuprous Oxide Nanowires for All-Oxide, Single-Wire Solar Cells*, Nano Lett. **14**, 4665 (2014).

[272] B. Sciacca, S. A. Mann, F. D. Tichelaar, H. W. Zandbergen, M. A. van Huis, and E. C. Garnett, *Solution-Phase Epitaxial Growth of Quasi-Monocrystalline Cuprous Oxide on Metal Nanowires*, Nano Lett. **14**, 5891 (2014).

[273] P. Wurfel, *Physics of Solar Cells: From Basic Principles to Advanced Concepts*, Wiley-VCH Verlag GmbH, 2009.

[274] E. E. Huber, *The effect of mercury contamination on the work function of gold*, Appl. Phys. Lett. **8**, 169 (1966).

[275] J.-D. Kwon, S.-H. Kwon, T.-H. Jung, K.-S. Nam, K.-B. Chung, D.-H. Kim, and J.-S. Park, *Controlled growth and properties of p-type cuprous oxide films by plasma-enhanced atomic layer deposition at low temperature*, Appl. Surf. Sci. **285**, 373 (2013).

[276] D. R. Lide, *CRC Handbook of Chemistry and Physics, 84th Edition, 2003-2004*, Handb. Chem. Phys. **53**, 2616 (2003).

[277] K. P. Musselman, Y. Ievskaya, and J. L. MacManus-Driscoll, *Modelling charge transport lengths in heterojunction solar cells*, Appl. Phys. Lett. **101**, 253503 (2012).

[278] Y. Liu, H. K. Turley, J. R. Tumbleston, E. T. Samulski, and R. Lopez, *Minority carrier transport length of electrodeposited Cu_2O in ZnO/Cu_2O heterojunction solar cells*, Appl. Phys. Lett. **98**, 21 (2011).

[279] A. Wagenpfahl, D. Rauh, M. Binder, C. Deibel, and V. Dyakonov, *S-shaped current-voltage characteristics of organic solar devices*, Phys. Rev. B **82**, 115306 (2010).

[280] M. Zhang, H. Wang, and C. W. Tang, *Hole-transport limited S-shaped I-V curves in planar heterojunction organic photovoltaic cells*, Appl. Phys. Lett. **99**, 213506 (2011).

[281] R. Saive, C. Mueller, J. Schinke, R. Lovrincic, and W. Kowalsky, *Understanding S-shaped current-voltage characteristics of organic solar cells: Direct measurement of potential distributions by scanning Kelvin probe*, Appl. Phys. Lett. **103**, 243303 (2013).

[282] A. Kumar, S. Sista, and Y. Yang, *Dipole induced anomalous S-shape I-V curves in polymer solar cells*, J. Appl. Phys. **105**, 094512 (2009).

[283] L. C. Olsen, R. C. Bohara, and M. W. Urie, *Explanation for low-efficiency Cu_2O Schottky-barrier solar cells*, Appl. Phys. Lett. **34**, 47 (1979).

[284] F. C. Akkari and M. Kanzari, *Optical, structural, and electrical properties of Cu_2O thin films*, Phys. status solidi **207**, 1647 (2010).

[285] S. Ryu, J. H. Noh, N. J. Jeon, Y. Chan Kim, W. S. Yang, J. Seo, and S. I. Seok, *Voltage output of efficient perovskite solar cells with high open-circuit voltage and fill factor*, Energy Environ. Sci. **7**, 2614 (2014).

[286] A. W. Hains, J. Liu, A. B. F. Martinson, M. D. Irwin, and T. J. Marks, *Anode Interfacial Tuning via Electron-Blocking/Hole-Transport Layers and Indium Tin Oxide Surface Treatment in Bulk-Heterojunction Organic Photovoltaic Cells*, Adv. Funct. Mater. **20**, 595 (2010).

[287] E. Castanié, M. Boffety, and R. Carminati, *Fluorescence quenching by a metal nanoparticle in the extreme near-field regime*, Opt. Lett. **35**, 291 (2010).

[288] V. Karanikolas, C. A. Marocico, and A. L. Bradley, *Spontaneous emission and energy transfer rates near a coated metallic cylinder*, Phys. Rev. A **89**, 1 (2014).

[289] S. K. Cushing, J. Li, F. Meng, T. R. Senty, S. Suri, M. Zhi, M. Li, A. D. Bristow, and N. Wu, *Photocatalytic Activity Enhanced by Plasmonic Resonant Energy Transfer from Metal to Semiconductor*, J. Am. Chem. Soc. **134**, 15033 (2012).

[290] J. Li, S. K. Cushing, F. Meng, T. R. Senty, A. D. Bristow, and N. Wu, *Plasmon-induced resonance energy transfer for solar energy conversion*, Nat. Photonics **9**, 601 (2015).

[291] D. R. Smith, P. Kolinko, and D. Schurig, *Negative refraction in indefinite media*, J. Opt. Soc. Am. B **21**, 1032 (2004).

[292] V. M. Shalaev, *Optical negative-index metamaterials*, Nat. Photonics **1**, 41 (2007).

[293] S. Dai, Q. Ma, T. Andersen, A. S. Mcleod, Z. Fei, M. K. Liu, M. Wagner, K. Watanabe, T. Taniguchi, M. Thiemens, F. Keilmann, P. Jarillo-Herrero, M. M. Fogler, and D. N. Basov, *Subdiffractional focusing and guiding of polaritonic rays in a natural hyperbolic material*, Nat. Commun. **6**, 6963 (2015).

[294] T. Tumkur, G. Zhu, P. Black, Y. A. Barnakov, C. E. Bonner, and M. A. Noginov, *Control of spontaneous emission in a volume of functionalized hyperbolic metamaterial*, Appl. Phys. Lett. **99**, 21 (2011).

[295] H. N. S. Krishnamoorthy, Z. Jacob, E. Narimanov, I. Kretzschmar, and V. M. Menon, *Topological transitions in metamaterials.*, Science **336**, 205 (2012).

[296] J. Kim, V. P. Drachev, Z. Jacob, G. V. Naik, A. Boltasseva, E. E. Narimanov, and V. M. Shalaev, *Improving the radiative decay rate for dye molecules with hyperbolic metamaterials*, Opt. Express **20**, 8100 (2012).

[297] X. Yang, J. Yao, J. Rho, X. Yin, and X. Zhang, *Experimental realization of three-dimensional indefinite cavities at the nanoscale with anomalous scaling laws*, Nat. Photonics **6**, 450.

[298] R. Maas, J. Parsons, N. Engheta, and A. Polman, *Experimental realization of an epsilon-near-zero metamaterial at visible wavelengths*, Nat. Photonics **7**, 907 (2013).

[299] G. Shvets, *Photonic approach to making a material with a negative index of refraction*, Phys. Rev. B **67**, 1 (2003).

[300] X. Fan, G. P. Wang, J. C. W. Lee, and C. T. Chan, *All-angle broadband negative refraction of metal waveguide arrays in the visible range: Theoretical analysis and numerical demonstration*, Phys. Rev. Lett. **97**, 1 (2006).

[301] E. Verhagen, R. De Waele, L. Kuipers, and A. Polman, *Three-dimensional negative index of refraction at optical frequencies by coupling plasmonic waveguides*, Phys. Rev. Lett. **105**, 18 (2010).

[302] R. Maas, E. Verhagen, J. Parsons, and A. Polman, *Negative Refractive Index and Higher-Order Harmonics in Layered Metallodielectric Optical Metamaterials*, ACS Photonics **1**, 670 (2014).

[303] J. A. Dionne, E. Verhagen, A. Polman, and H. A. Atwater, *Are negative index materials achievable with surface plasmon waveguides? A case study of three plasmonic geometries*, Opt. Express **16**, 19001 (2008).

[304] J. van de Groep, P. Spinelli, and A. Polman, *Single-Step Soft-Imprinted Large-Area Nanopatterned Antireflection Coating*, Nano Lett. **15**, 4223 (2015).

[305] K. X. Wang, Z. Yu, S. Sandhu, V. Liu, and S. Fan, *Condition for perfect antireflection by optical resonance at material interface*, Optica **1**, 41 (2014).

[306] M. G. Moharam and T. K. Gaylord, *Rigorous coupled-wave analysis of planar-grating diffraction*, J. Opt. Soc. Am. **71**, 811 (1981).

[307] P. Sheng, R. S. Stepleman, and P. N. Sanda, *Exact eigenfunctions for square-wave gratings: Application to diffraction and surface-plasmon calculations*, Phys. Rev. B **26**, 2907 (1982).

[308] M. G. Moharam, E. B. Grann, D. A. Pommet, and T. Gaylord, *Formulation for stable and efficient implementation of the rigorous coupled-wave analysis of binary gratings*, J. Opt. Soc. Am. A **12**, 1068 (1995).

[309] P. Lalanne and G. M. Morris, *Highly improved convergence of the coupled-wave method for TM polarization*, J. Opt. Soc. Am. A **13**, 779 (1996).

[310] B. Sturman, E. Podivilov, and M. Gorkunov, *Eigenmodes for metal-dielectric light-transmitting nanostructures*, Phys. Rev. B **76**, 125104 (2007).

[311] B. Sturman, E. Podivilov, and M. Gorkunov, *Theory of extraordinary light transmission through arrays of subwavelength slits*, Phys. Rev. B **77**, 075106 (2008).

[312] T. W. Ebbesen, H. J. Lezec, H. F. Ghaemi, T. Thio, and P. A. Wolff, *Extraordinary optical transmission through sub-wavelength hole arrays*, Nature **391**, 667 (1998).

[313] J. A. Porto, F. J. Garcia-Vidal, and J. B. Pendry, *Transmission resonances on metallic gratings with very narrow slits*, Phys. Rev. Lett. **83**, 2845 (1999).

[314] M. Foresti, L. Menez, and A. V. Tishchenko, *Modal method in deep metal-dielectric gratings: the decisive role of hidden modes*, J. Opt. Soc. Am. A. Opt. Image Sci. Vis. **23**, 2501 (2006).

[315] M. Born and E. Wolf, *Principles of Optics*, Pergamon Press, Oxford, UK, 4th edition, 1970.

[316] S. E. Kocabas, G. Veronis, D. A. B. Miller, and S. Fan, *Modal analysis and coupling in metal-insulator-metal waveguides*, Phys. Rev. B **79**, 035120 (2009).

[317] A. Zettl, *Sturm-Liouville Theory*, American Mathematical Society, Providence, Rhode Island, USA, 2005.

[318] P. St. J. Russell, T. Birks, and F. Lloyd-Lucas, *Photonic Bloch waves and photonic band gaps*, in *Confin. Electrons Photons*, edited by E. Burstein and C. Weisbuch, pages 585–633, Plenum Press, New York, NY, USA, 1995.

[319] K. B. Dossou, L. C. Botten, A. A. Asatryan, B. C. P. Sturmberg, M. a. Byrne, C. G. Poulton, R. C. McPhedran, and C. M. de Sterke, *Modal formulation for diffraction by absorbing photonic crystal slabs*, J. Opt. Soc. Am. A **29**, 817 (2012).

[320] P. St. J. Russell, *Coupled wave versus modal theory in uniform dielectric gratings*, Opt. Commun. **48**, 71 (1983).

[321] L. Li, *Use of Fourier series in the analysis of discontinuous periodic structures*, J. Opt. Soc. Am. A **13**, 1870 (1996).

[322] K. Edee, *Modal method based on subsectional Gegenbauer polynomial expansion for lamellar gratings*, J. Opt. Soc. Am. A **28**, 2006 (2011).

[323] L. Zhang, S. Aite, and Z. Yu, *Unique laser-scanning optical microscope for low-temperature imaging and spectroscopy*, Rev. Sci. Instrum. **78**, 083701 (2007).

[324] L. Oudjedi, A. N. G. Parra-Vasquez, A. G. Godin, L. Cognet, and B. Lounis, *Metrological Investigation of the (6,5) Carbon Nanotube Absorption Cross Section*, J. Phys. Chem. Lett. **4**, 1460 (2013).

[325] L. M. Payne, W. Langbein, and P. Borri, *Polarization-resolved extinction and scattering cross-sections of individual gold nanoparticles measured by wide-field microscopy on a large ensemble*, Appl. Phys. Lett. **102**, 131107 (2013).

[326] T. J. Yang, G. A. Lessard, and S. R. Quake, *An apertureless near-field microscope for fluorescence imaging*, Appl. Phys. Lett. **76**, 378 (2000).

[327] K. F. Mak, C. Lee, J. Hone, J. Shan, and T. F. Heinz, *Atomically Thin MoS_2: A New Direct-Gap Semiconductor*, Phys. Rev. Lett. **105**, 136805 (2010).

[328] R. Maas, J. van de Groep, and A. Polman, *Planar metal/dielectric single-periodic multilayer ultraviolet flat lens*, Optica **3**, 592 (2016).

[329] S. A. Mann, R. R. Grote, R. M. Osgood, A. Alù, and E. C. Garnett, *Opportunities and Limitations for Nanophotonic Structures To Exceed the ShockleyâĂŞQueisser Limit*, ACS Nano **10**, 8620 (2016).

[330] F. Capolino, D. R. Jackson, D. R. Wilton, and L. B. Felsen, *Comparison of methods for calculating the field excited by a dipole near a 2-D periodic material*, IEEE Trans. Antennas Propag. **55**, 1644 (2007).

[331] Y. Chen and A. F. Koenderink, *General point dipole theory for periodic metasurfaces: magnetoelectric scattering lattices coupled to planar photonic structures*, **19**, 15 (2015).

[332] Y. Cui, D. van Dam, S. A. Mann, N. J. J. van Hoof, P. J. van Veldhoven, E. C. Garnett, E. P. A. M. Bakkers, and J. E. M. Haverkort, *Boosting Solar Cell Photovoltage via Nanophotonic Engineering*, Nano Lett. **16**, 6467 (2016).

[333] Y. Sun and S. R. Forrest, *Enhanced light out-coupling of organic light-emitting devices using embedded low-index grids*, Nat. Photonics **2**, 483 (2008).

[334] I. Schnitzer, E. Yablonovitch, C. Caneau, T. J. Gmitter, and A. Scherer, *30% external quantum efficiency from surface textured, thin-film light-emitting diodes*, Appl. Phys. Lett. **63**, 2174 (1993).

[335] A. V. Maslov, M. I. Bakunov, and C. Z. Ning, *Distribution of optical emission between guided modes and free space in a semiconductor nanowire*, J. Appl. Phys. **99**, 024314 (2006).

[336] N. Gregersen, T. R. Nielsen, J. Claudon, J.-M. Gérard, and J. Mørk, *Controlling the emission profile of a nanowire with a conical taper.*, Opt. Lett. **33**, 1693 (2008).

[337] J. Claudon, J. Bleuse, N. S. Malik, M. Bazin, N. Gregersen, C. Sauvan, P. Lalanne, and J.-M. Ge, *A highly efficient single-photon source based on a quantum dot in a photonic nanowire*, Nat. Photonics **4**, 174 (2009).

[338] N. Anttu, *Shockley-Queisser Detailed Balance Efficiency Limit for Nanowire Solar Cells*, ACS Photonics **2**, 446 (2015).

[339] M. C. McAlpine, H. Ahmad, D. Wang, and J. R. Heath, *Highly ordered nanowire arrays on plastic substrates for ultrasensitive flexible chemical sensors*, Nat. Mater. **6**, 379 (2007).

[340] X. Dai, A. Messanvi, H. Zhang, C. Durand, J. Eymery, C. Bougerol, F. H. Julien, and M. Tchernycheva, *Flexible Light-Emitting Diodes Based on Vertical Nitride Nanowires*, Nano Lett. **15**, 6958 (2015).

[341] S. Zhang, Y. Shen, H. Fang, S. Xu, J. Song, and Z. L. Wang, *Growth and replication of ordered ZnO nanowire arrays on general flexible substrates*, J. Mater. Chem. **20**, 10606 (2010).

[342] S. Chu, D. Li, P.-C. Chang, and J. G. Lu, *Flexible Dye-Sensitized Solar Cell Based on Vertical ZnO Nanowire Arrays*, Nanoscale Res. Lett. **6**, 1 (2010).

Summary

The conversion efficiency of a solar panel is the most important lever in the cost of electricity it produces. For photovoltaics to make a significant and lasting impact as a renewable energy resource, the electricity costs have to decrease, and the conversion efficiency therefore has to increase. This is the primary goal of photovoltaic research, which combines fascinating aspects of solid state physics, materials science, thermodynamics, electrodynamics, and more recently, nanophotonics.

The field of nanophotonics aims to understand and manipulate the interaction of light and matter at the nanoscale. Since this interaction is at the heart of the photovoltaic energy conversion process, it is only natural that nanophotonics can play an important role in achieving high efficiencies. This thesis brings together experimental and theoretical contributions aimed at deepening the understanding of how nanophotonics can enhance photovoltaic conversion efficiencies. In particular, we focus on the photovoltage that a nanoscale solar cell can generate, both in the ideal case and with practical limitations.

We begin with theoretical investigations of a number of nanophotonic mechanisms that can enhance the efficiency of a photovoltaic device. We then present a new experimental technique to measure quantitatively the absorption cross section of a single nanostructure. Using our experimental technique, we characterize the limits and performance losses of a nanoscale photovoltaic device in detail. We then investigate theoretically and experimentally the optical and electrical properties of metal-semiconductor core-shell nanowires, which can have very strong absorption in very thin layers of semiconductor. Next, we design a perfect antireflection coating for a metamaterial that under normal circumstances does not permit light to enter at all. Finally, we present two applications based on central themes in this thesis.

In Chapter 2 we investigate the photovoltaic response of single nanoparticles. To do so, we extend the detailed balance framework pioneered by Shockley and Queisser to the single nanoparticle regime. We find that, contrary to expectations, a large absorption cross section is not equivalent to macroscopic concentration. A large absorption cross section by itself can therefore not be used to increase efficiency beyond the Shockley-Queisser limit. Instead, directivity in the absorption

pattern is required for nanostructures to break such a limit. This discrepancy arises due to the differences between geometric and wave optics. We continue by discussing fundamental limitations to the achievable directivity in a nanostructure, and how directive structures can be designed. Finally, we discuss how the presence of non-radiative recombination affects nanophotonic strategies to increase conversion efficiencies.

In Chapter 3 we extend the theoretical investigation of single nanostructures to periodic arrays of nanostructures. Specifically, we investigate a new architecture that directs different frequencies of sunlight into adjacent nanostructures using nanophotonic resonances. As a result, a multi-junction solar cell can be fabricated where different solar cells are placed next to each other instead of stacked on top of each other. This can help circumvent the current and lattice matching requirements that limit current multi-junction solar cells.

In Chapter 4 we investigate the photon escape probability, already introduced in Chapter 2, in more detail. The photon escape probability describes the odds that a photon originating from a recombination event inside the solar cell eventually escapes the solar cell. While this parameter is crucial to understand realistic photovoltaic devices, there was no known method to determine its value. We present a rigorous method to perform this calculation, and discuss how nanophotonic objects and their associated resonances affect the internal and external radiative efficiencies of a semiconductor material. We find that complex nanophotonic structures may offer intrinsic benefits over regular planar structures.

The photovoltaic performance of a single nanostructure is ultimately determined by its absorption cross section spectrum. In Chapter 5 we present a new experimental and quantitative technique to determine the absorption cross section of single nanoparticles. The technique, integrating sphere microscopy, is based on the combination of an integrating sphere with a microscopy objective, resulting in the direct determination of absorption with high spatial resolution. Contrary to existing methods, it can be used to determine the absorption cross section of scattering nanophotonic structures that for instance are strongly luminescent or generate photocurrent.

We apply integrating sphere microscopy in Chapter 6 to determine for the first time the internal quantum efficiency and photoluminescence quantum yield of a single nanowire solar cell. These metrics are closely related to the photocurrent and photovoltage of the solar cell, and are therefore crucial to understand the performance a photovoltaic device. We also introduce a new quantity, the collection cross section, that is the nanophotonic equivalent to the external quantum efficiency. The collection cross section has units of area, to account for the strong wavelength dependence of the effective optical area of nanostructures. Using this cross section, we determine a thermodynamic upper limit to the performance of the nanowire, which allows us to quantify the contribution of loss mechanisms such as non-radiative recombination.

In Chapter 7 we discuss the unique optical properties of metal-semiconductor core-shell nanowires, which can absorb light very strongly in only very thin layers of

semiconductors. We show that this strong absorption originates from the ability to tune resonances into the spectral window where they are most effective. Core-shell nanowires are therefore interesting candidates for photovoltaic applications, especially considering the presence of a local metal contact, which facilitates charge extraction.

We investigate these core-shell nanowires experimentally in Chapter 8. We synthesized core-shell nanowires with a Cu_2O shell and silver and gold cores using solution chemistry. We then measure the absorptance of a single core-shell nanowire with the integrating sphere microscopy technique described in Chapter 5. We find good comparison with analytical predictions, but also interesting deviations that may be due to surface roughness. Finally, we fabricate photovoltaic devices based on these core-shell nanowires, which we investigate using laser-induced current maps. The diffusion length in the Cu_2O is limited, but we show that we can enhance the extraction length by moving to a metal-semiconductor-metal geometry.

This geometry, a thin dielectric layer sandwiched between two metals, also has very interesting optical properties. For example, by alternating layers of dielectric materials and metals, a metamaterial can be realized that has a negative refractive index. However, in certain circumstances, it can be impossible to obtain transmission into these metamaterials, in particular when the optical properties rely on antisymmetric eigenmodes of the structure. In Chapter 9 we propose an approach to design anti-reflection coatings for these metamaterials. We show that, contrary to regular anti-reflection coatings, these coatings must be nanostructured to be effective. We demonstrate our approach by enhancing the transmission from 0 to 100% into a metamaterial with an antisymmetric mode with negative phase index.

Finally, Chapter 10 describes two applications that are related to the experimental and theoretical concepts in this thesis. First, we discuss how to incorporate integrating sphere microscopy into a UV-VIS spectrometer and into an inverted microscope. Secondly, we demonstrate how to achieve large photon escape probabilities in structures that at the same time maintain very large absorption over a wide range of wavelengths. Achieving both at the same time is crucial for high efficiency photovoltaic devices.

Overall, this thesis provides new fundamental insights into nanoscale photovoltaics. We have explored limiting efficiencies and various loss mechanisms from a theoretical perspective, and developed an experimental technique to quantify these limits and losses in nanoscale devices. Our findings strengthen the role of nanophotonics in photovoltaics, and may also be applied in other optoelectronic devices such as light emitting diodes.

Samenvatting

Zonnepanelen zijn te duur om een speler te zijn in de mondiale transitie naar een duurzame energievoorziening. Het rendement waarmee een zonnepaneel zonlicht omzet in elektrisch vermogen is de belangrijkste factor in deze kosten. Alleen door zonnepanelen te maken met een hoger rendement, kan de elektriciteit goedkoper worden geproduceerd. Het behalen van hogere rendementen is dan ook het voornaamste doel van onderzoek naar zonnecellen, waarin fascinerende aspecten van vastestoffysica, materiaalkunde, thermodynamica, elektrodynamica en sinds kort ook nanofotonica gecombineerd worden. Het onderzoeksgebied nanofotonica bestudeert en beïnvloedt de interactie tussen licht en materialen op nanoschaal. Deze interactie vormt het hart van het conversieproces in een zonnecel en daarom kan nanofotonica een belangrijke rol spelen in het behalen van hogere rendementen.

Dit proefschrift bundelt experimentele en theoretische inzichten in hoe nanofotonica die rol precies kan vervullen. We richten ons in het bijzonder op het voltage dat een nanozonnecel kan genereren, zowel in ideale als in realistische scenario's. Het proefschrift begint met theoretische beschouwingen van een aantal nanofotonische mechanismes die het rendement van een zonnecel kunnen verbeteren. We presenteren daarna een nieuwe experimentele techniek om kwantitatief de absorptiedoorsnede van een individuele nanostructuur te kunnen meten. Met deze experimentele techniek beschrijven we vervolgens in detail de verliesmechanismes en fundamentele operationele limieten van een enkele nanodraadzonnecel.

In het volgende deel van het proefschrift onderzoeken wij de optische en elektrische eigenschappen van een nieuw soort nanodraad, zowel theoretisch als experimenteel. Deze nanodraden hebben een kern van metaal en een schil van halfgeleider. Ze kunnen licht zeer sterk absorberen, zelfs in een heel dunne laag van halfgeleider. Daarna ontwerpen wij een ideale antireflectieve laag voor een metamateriaal, die onder normale omstandigheden helemaal geen licht toelaat. Tot slot presenteren wij twee toepassingen gebaseerd op centrale thema's in dit proefschrift.

In hoofdstuk 2 onderzoeken wij de fotovoltaïsche eigenschappen van individuele nanodeeltjes. Om dat te kunnen doen vertalen wij het raamwerk van Shockley en Queisser naar enkele nanodeeltjes. In tegenstelling tot wat men zou verwachten,

volgt hieruit dat een grote absorptiedoorsnede niet gelijk is aan “concentratie” zoals met een lens. Een grote absorptiedoorsnede alleen kan dus niet gebruikt worden om rendementen boven de zogenaamde Shockley-Queisser limiet te behalen. In tegendeel, voor nanostructuren is directiviteit in de absorptiedoorsnede nodig om deze limiet te verbreken. Deze tegenstelling komt voort uit verschillen in geometrische optica en golfoptica. We bespreken fundamentele limieten van de directiviteit en hoe structuren ontworpen kunnen worden die sterke directiviteit in hun absorptiepatroon hebben. Tot slot bespreken we hoe niet-stralende recombinatie de nanofotonische strategieën voor hoge rendementen beïnvloedt.

In hoofdstuk 3 verbreden we onze blik door naar periodieke roosters van nanodeeltjes te kijken. We onderzoeken een nieuwe architectuur voor zonnecellen, waarin zonlicht van verschillende golflengtes naar verschillende nanostructuren wordt geleid. Als resultaat hiervan kan een tandemzonnecel gemaakt worden waarvan de verschillende zonnecellen niet op elkaar liggen, maar juist naast elkaar zijn geplaatst. Bestaande problemen in tandemzonnecellen, zoals dat de stroom in elke laag hetzelfde moet zijn, of dat de kristalroosters dezelfde grootte moeten hebben, kunnen hiermee worden opgelost.

In hoofdstuk 4 onderzoeken we hoe waarschijnlijk het is dat een foton dat uit recombinatie in een bepaalde halfgeleider volgt, die halfgeleider ook verlaat. Hoewel deze “ontsnappingskans” cruciaal is om realistische zonnecellen te begrijpen, was er nog geen methode bekend om deze waarde te berekenen. Wij bespreken hoe resonanties in nanofotonische structuren die ontsnappingskans kunnen beïnvloeden en presenteren in dit hoofdstuk een methode om deze kans te berekenen. Het blijkt dat nanofotonische structuren zoals resonante bollen intrinsieke voordelen hebben ten opzichte van de normale planaire structuren.

De fotovoltaische eigenschappen van een enkele nanostructuur worden gelimiteerd door zijn absorptiespectrum. In hoofdstuk 5 presenteren wij een nieuwe kwantitatieve experimentele techniek om de absorptiedoorsnede van een enkele nanostructuur te bepalen. Deze techniek is gebaseerd op de combinatie van een integrerende bol met een microscoopobjectief. Hiermee kan de absorptie van licht direct bepaald worden, met hoge ruimtelijke resolutie. In tegenstelling tot bestaande technieken kan deze methode ook gebruikt worden om de absorptiedoorsnede te bepalen van verstrooiende nanostructuren die bijvooorbeeld sterk luminesceren of stroom genereren.

We gebruiken deze nieuwe techniek in hoofdstuk 6 om voor de eerste keer de interne kwantumefficiëntie en fotoluminescentie kwantumefficiëntie van een enkele nanodraad zonnecel te meten. Deze eigenschappen zijn sterk verbonden aan het voltage en de stroom die een zonnecel genereert en zijn daarom cruciaal om het gedrag van een zonnecel te kunnen verklaren. Bovendien introduceren we een nieuwe eigenschap, de collectiedoorsnede, die het equivalent is van de externe kwantumefficiëntie in macroscopische zonnecellen. Op basis van de collectiedoorsnede bepalen we de thermodynamische limiet op het voltage van de nanozonnecel en kunnen we de rol van verschillende verliesmechanismes kwantificeren.

In hoofdstuk 7 bespreken we de unieke optische eigenschappen van nanodra-

den met een metalen kern en een halfgeleider schil. Deze kern-schil nanodraden kunnen licht zeer sterk absorberen in een hele dunne laag halfgeleider. Daarnaast kan de metalen kern dienst doen als een lokale elektrode. Dit maakt kern-schil nanodraden zeer interessante kandidaten voor dunne zonnecellen. Wij laten zien dat de sterke absorptie van licht voortkomt uit de mogelijkheid om de spectrale positie van resonanties te kunnen beïnvloeden. Hierdoor kunnen meerdere resonanties overlappen in het spectrale gebied waarin zij het meest efficient zijn en zo de absorptie verhogen.

We onderzoeken deze kern-schil nanodraden experimenteel in hoofdstuk 8. We hebben daartoe kern-schil nanodraden gemaakt met een kern van zilver of goud en een schil van koper(I)oxide (Cu_2O). Met integrerende bol microscopie hebben we het absorptiespectrum van een enkele zilver-koper(I)oxide kern-schil nanodraad gemeten, zoals beschreven in hoofdstuk 5. Vervolgens fabriceren we nanodraad-zonnecellen van goud-koper(I)oxide kern-schil nanodraden en onderzoeken deze zonnecellen op basis van laser-geïnduceerde stroommetingen. De diffusielengte in koper(I)oxide beperkt de kwaliteit van de zonnecel, maar de extractie van ladingsdragers kan verbeterd worden door de andere elektrode over de lengte van de kern-schil nanodraad te draperen en zo een metaal-halfgeleider-metaalgeometrie te creëren.

Deze geometrie, een diëlektrische laag tussen twee metalen, heeft ook zeer interessante optische eigenschappen. Door bijvoorbeeld lagen van een diëlektricum af te wisselen met metaal kan een zogenaamd metamateriaal gevormd worden dat een negatieve brekingsindex heeft. In sommige gevallen is het echter onmogelijk om van die negatieve brekingsindex gebruik te maken, omdat licht niet toegelaten wordt tot het metamateriaal. Dit is met name het geval als de optische eigenschappen van het metamateriaal gebaseerd zijn op eigenmodes met een antisymmetrisch veldprofiel. In hoofdstuk 9 stellen we een aanpak voor om antireflectieve lagen te ontwikkelen voor zulke metamaterialen. We tonen aan dat, in tegenstelling tot normale antireflectieve lagen, deze laag uit nanostructuren moet bestaan. Ter demonstratie verhogen we de transmissie van 0 naar 100% in een metamateriaal met een antisymmetrische eigenmode met negatieve fase-index.

Tot slot, hoofdstuk 10 bespreekt twee toepassingen gebaseerd op experimentele en theoretische concepten in dit proefschrift. We beschrijven eerst hoe de experimentele techniek uit hoofdstuk 5 een toepassing kan vinden in een UV-VIS spectrofotometer en in een geïnverteerde microscoop. Daarna demonstreren we numeriek dat het mogelijk is om nanostructuren te creëren die sterk absorberen en de kans vergroten dat een foton volgend uit recombinatie ontsnapt. Om een zonnecel met heen hoog rendement te maken is het cruciaal dat aan beide voorwaarden tegelijkertijd voldaan wordt.

Deze dissertatie presenteert nieuwe fundamentele inzichten in zonnecellen op nanoschaal. We hebben vanuit theoretisch perspectief de fundamentele limieten en verliesmechanismes van zonnecellen op nanoschaal onderzocht en een experimentele techniek ontwikkeld die deze limieten en verliezen kan kwantificeren. Onze bevindingen versterken de rol die voor nanofotonica in zonnecellen is wegge-

legd, maar kunnen ook toegepast worden in andere opto-elektronische apparaten zoals leds.

List of publications

This thesis is based on the following publications:

- *Opportunities and limitations for nanophotonic structures to exceed the Shockley-Queisser limit*, S.A. Mann, R.R. Grote, R.M. Osgood, Jr., A. Alù, and E.C. Garnett, ACS Nano **10** (9), pp. 8620-8631, 2016. **(Chapter 2)**
- *Resonant nanophotonic spectrum splitting for ultrathin multijunction solar cells*, S.A. Mann and E.C. Garnett, ACS Photonics **2** (7), pp. 816-821, 2015. **(Chapter 3)**
- *Rigorous calculations of the photon recycling probability*, S.A. Mann and E.C. Garnett, in preparation. **(Chapter 4)**
- *Integrating sphere microscopy for direct absorption measurements of single nanostructures*, S.A. Mann, B. Sciacca, Y. Zhang, J. Wang, E. Kontoleta, H. Liu, and E.C. Garnett, submitted. **(Chapter 5)**
- *Quantifying losses and thermodynamic limits in nanophotonic solar cells*, S.A. Mann*, S.Z Oener*, A. Cavalli, J.E.M. Haverkort, E.P.A.M. Bakkers, and E.C. Garnett, Nature Nanotechnology, 2016. doi:10.1038/nnano.2016.162 **(Chapter 6)**
- *Extreme light absorption in thin semiconductor films wrapped around metal nanowires*, S.A. Mann and E.C. Garnett, Nano Letters **13** (7), pp. 3173-3178, 2013. **(Chapter 7)**
- *Solution-phase epitaxial growth of quasi-monocrystalline cuprous oxide on metal nanowires*, B. Sciacca, S.A. Mann, F.D. Tichelaar, H.W. Zandbergen, M.A. van Huis, and E.C. Garnett, Nano Letters **14** (10), pp. 5891-5898, 2014. **(Chapter 8)**
- *Au-Cu_2O core-shell nanowire photovoltaics*, S.Z. Oener, S.A. Mann, B. Sciacca, C. Sfiligoj, J. Hoang, and E.C. Garnett, Applied Physics Letters **106** (2), pp. 023501, 2014. **(Chapter 8)**
- *Generalized antireflection coatings for complex bulk metamaterials*, R. Maas*, S.A. Mann*, D.L. Sounas, A. Alù, E.C. Garnett, and A. Polman, Physical Review B **93** (19), pp. 195433, 2016. **(Chapter 9)**

- *Boosting solar cell photovoltage via nanophotonic engineering*, Y. Cui*, D. van Dam*, S.A. Mann, N.J.J. van Hoof, P.J. van Veldhoven, E.C. Garnett, E.P.A.M. Bakkers, and J.E.M. Haverkort, Nano Letters **16** (10), pp. 6467-6471, 2016. **(Chapter 10)**

Other publications by the author:

- *Dielectric particle and void resonators for thin film solar cell textures*, S.A. Mann, R.R. Grote, R.M. Osgood, Jr., and J.A. Schuller, Optics Express **19** (25), pp. 25729-25740, 2011.
- *The energy payback time of advanced crystalline silicon PV modules in 2020: a prospective study*, S.A. Mann, M.J. de Wild-Scholten, V.M. Fthenakis, W.G.H.J.M. van Sark, and W.C. Sinke, Progress in Photovoltaics: Research and Applications **22** (11), pp. 1180-1194, 2012.
- *Nanoscale spatial coherent control over the modal excitation of a coupled plasmonic resonator system*, T. Coenen, D.T. Schoen, S. A. Mann, S.K.R. Rodriguez, B.J.M. Brenny, A. Polman, and M.L. Brongersma, Nano Letters **15** (11), pp. 7666-7670, 2015.
- *Direct imaging of hybridized eigenmodes in coupled silicon nanoparticles*, J. van de Groep, T. Coenen, S. A. Mann, and A. Polman, Optica **3** (1), pp. 93-99, 2016.
- *Indirect to direct bandgap transition in methylammonium lead halide perovskite*, T. Wang*, B. Daiber*, J. Frost, S.A. Mann, E.C. Garnett, A. Walsh, B. Ehrler, submitted.
- *Super-resolution imaging of light-matter interactions near single semiconductor nanowires*, E. Johlin, J. Solari, S.A. Mann, J. Wang, T. Shimizu, and E.C. Garnett, submitted.
- *Dipole transition rates near and inside infinite cylinders*, E. Johlin, S.A. Mann, and E.C. Garnett, in preparation.
- *Fundamental limits to broadband absorption in thin-film solar cells*, F. Monticone, S.A. Mann, E.C. Garnett, A. Alù, in preparation.
- *Nano-antenna enhanced two-focus fluorescence correlation spectroscopy*, L. Langguth, A. Szuba, S.A. Mann, E.C. Garnett, G. Koenderink, A.F. Koenderink, in preparation.
- *Highly tunable hybrid nanowire-quantum dot nanostructure for optoelectronic applications*, L. van de Waart, R. Bosma, S.A. Mann, B. Sciacca, L. Yang, E.C. Garnett, and B. Ehrler, in preparation.

Acknowledgements

This thesis could not have been possible without the help, support, and encouragement of many. In the following I would like to express my gratitude to those who have contributed, scientifically or otherwise.

First of all, my advisor Erik: I'm very grateful for the opportunity to do a PhD in your group. You got me started on great projects, but also always gave me the freedom and means to work on whatever I liked. Moreover, you gave me the opportunity to visit many conferences and get to know the field and expand my network. And even though the group expanded rapidly, you were always available to discuss anything. I greatly appreciate these things, and am very happy to have had this experience.

I'm also very happy to have been a member of the Nanoscale Solar Cells group. It was fun to do science with Sebastian, Beniamino, Eric, Sarah, Linda, Jenny, Parisa, Jia, Cristina, and John, but also outside of work it was great to be a part of this group. Thanks to all group members for the good times! The group trip to Sicily is an absolute highlight of my time at AMOLF.

In the beginning of my PhD, when Sebastian and I were the only students in our group, we found a home in Albert Polman's group. To this day, we still happily tag along for daily lunch dates and join forces at conferences. Albert, thank you for making us feel at home, proofreading this dissertation, and for a number of very nice outings. Jorik and Ruben: thanks for many fun and productive collaborations and conferences! Benjamin, thanks for always being willing to help (or chat).

AMOLF has been a fantastic environment to do a PhD, and I'm grateful to all of those who have contributed to this. In terms of technical support I think AMOLF is unparalleled in at least this corner of the universe, and I'm particularly grateful to Marco Seynen, Henk-Jan Boluijt, Duncan Verheijde, Jan Zomerdijk, Jan van Elst, Wiebe de Boer, and all others at the mechanical workshop, electrical and software engineering, and ICT.

The nanophotonics department has been an excellent scientific setting to investigate nanophotonic solar cells. I have learned more from the nanophotonics colloquium than I could have ever learned from a book, and I'm supremely grateful to those organizing it and maintaining its quality over the years: Femius

Koenderink, Kobus Kuipers, Ewold Verhagen, Jaime Gómez Rivas, Albert Polman, Ad Lagendijk, Erik Garnett, Bruno Ehrler, and Esther Allarcon Llado. Within the department I am glad to have had the opportunity to collaborate with Ruben, Jorik, Toon, Said, Benjamin B and Benjamin D, Albert, Tianyi, Bruno, Lutz, and Femius. Andrea, Dimitrios, and Francesco: it was a pleasure to collaborate while you were visiting AMOLF.

I have also learned a lot from scientists outside of AMOLF. I have enjoyed our collaboration with the TU Eindhoven: Dick, Alessandro, Jos, and Erik: dank! Scientists abroad: I would like to thank Rich Grote, Jon Schuller, and Martijn Wubs. Rich, I'm sorry for bothering you all the time with things that I find weird, funny, smart, unclear, cool, or obtuse, but our discussions have been elucidating. Jon, thanks for teaching me Mie theory: I liked it so much I ended up doing a PhD on nanowires. Martijn, thank you for your enthusiasm and insightful comments.

Finally, I would like to thank my friends and family. Jan, oude vriend, I'm extremely indebted to you for letting me use your computer for the past two years. This entire thesis was written on it, and almost all calculations and data analysis were done on it as well. Sebastian, it has been a lot of fun sharing the experience of doing a PhD with you: thanks for many beers of joy and grief, games of squash, helping me find the smallest weight in the gym, and some OK collaborations.

Het was (en is) heel leuk om in Amsterdam te wonen dankzij velen, maar met name wil ik Kayleigh, Ludo, Wiegertje, Mus, Yannick en Floor bedanken voor de vele maaltijden, drankjes en feestjes die ik met liefde met ze heb verorberd. Bobby, bedankt voor alle leuke tripjes! Johan, ik kijk altijd uit naar de knipselkrant.

Ik ben heel dankbaar voor alle steun en liefde van mijn ouders, zusje, en verdere familie. Lausie, jij was onmisbaar toen ik mijn sleutelbeen gebroken had. Jael, zonder jouw grapjes en liefde was er niks gekomen van deze twee-drietjes, sphericity bubbles, en infinity cubes. ♡

About the author

Sander Mann was born in 's-Gravenzande, The Netherlands, on July 12th, 1987. He studied physics and energy science at Utrecht University, and graduated cum laude in 2012. To complete his Master's degree he spent a year at Columbia University, NY, to write two theses: one on energy payback time projections for crystalline silicon solar cells (supervised by prof. dr. Vasilis Fthenakis and prof. dr. Wim Sinke), and one on Mie resonators for enhanced absorption in thin film solar cells (supervised by prof. dr. Jon Schuller). He then started a PhD in the research group of dr. Erik Garnett at FOM Institute AMOLF in Amsterdam, The Netherlands, the results of which are presented in this dissertation.

The work described in this thesis was performed at the FOM-Institute AMOLF, Science Park 104, 1098 XG Amsterdam, The Netherlands.